



**HAL**  
open science

# Quantum-confined nanocrystals for infrared optoelectronics: carrier dynamics and intraband transitions

Clément Livache

► **To cite this version:**

Clément Livache. Quantum-confined nanocrystals for infrared optoelectronics: carrier dynamics and intraband transitions. Materials Science [cond-mat.mtrl-sci]. Sorbonne Université, 2019. English. NNT: . tel-02436321

**HAL Id: tel-02436321**

**<https://hal.science/tel-02436321>**

Submitted on 13 Jan 2020

**HAL** is a multi-disciplinary open access archive for the deposit and dissemination of scientific research documents, whether they are published or not. The documents may come from teaching and research institutions in France or abroad, or from public or private research centers.

L'archive ouverte pluridisciplinaire **HAL**, est destinée au dépôt et à la diffusion de documents scientifiques de niveau recherche, publiés ou non, émanant des établissements d'enseignement et de recherche français ou étrangers, des laboratoires publics ou privés.

**THÈSE DE DOCTORAT  
DE SORBONNE UNIVERSITÉ**

**Spécialité : Physique**

**École doctorale 397 : Physique et Chimie des Matériaux**

réalisée

au **Laboratoire de Physique et d'Étude des Matériaux (ESPCI Paris)**  
et à l'**Institut des Nanosciences de Paris (Sorbonne Université)**

présentée par

**Clément LIVACHE**

pour obtenir le grade de :

**DOCTEUR DE SORBONNE UNIVERSITÉ**

Sujet de la thèse :

**Quantum-confined nanocrystals for infrared optoelectronics:  
Carrier dynamics and intraband transitions**

**soutenue le 18 octobre 2019**

devant le jury composé de :

Mme. Angela VASANELLI (LPENS, Paris)	Rapportrice
M. Olivier GRAVRAND (CEA LETI, Grenoble)	Rapporteur
Mme. Vanessa WOOD (ETH, Zürich)	Examinatrice
M. Jérôme TIGNON (LPENS, Paris)	Examineur
M. Benoit DUBERTRET (LPEM, Paris)	Directeur de thèse
M. Emmanuel LHUILLIER (INSP, Paris)	Invité



"Jamais vu une noix aussi dure."  
André Franquin, *Gaston Lagaffe*

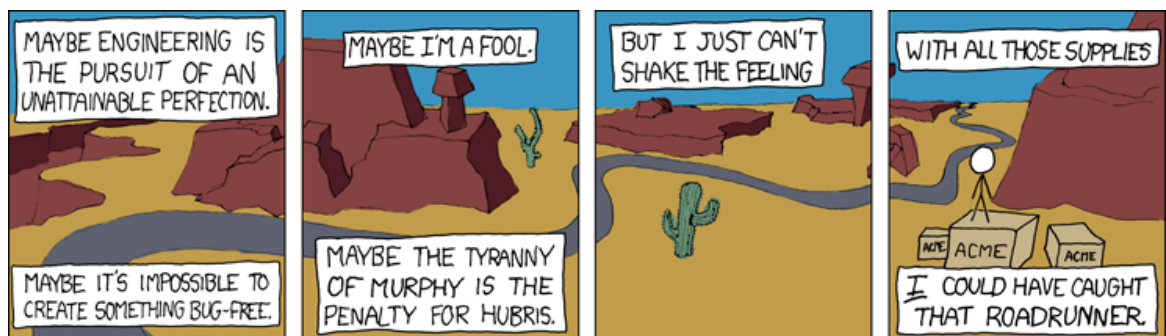


Fig. 0.1 The true reason why I'm going to New Mexico. Randall Munroe, xkcd 319



## Remerciements

Trois années et demi se terminent dans ces pages, et il est déjà l'heure de se dire à bientôt. J'ai rencontré Emmanuel et Benoit pour la première fois un matin de novembre à l'ESPCI : on a parlé mercure, infrarouge et boîtes quantiques et j'étais convaincu. Le groupe d'Emmanuel, c'était alors trois personnes : Adrien, thésard en rédaction, Emmanuel, tout juste arrivé au CNRS, et moi. Durant ces trois années, j'ai vu le groupe grossir et évoluer. En le quittant aujourd'hui, je suis convaincu d'avoir fait le bon choix, et je suis fier d'avoir participé à la genèse d'un groupe dynamique, dans lequel il fait bon vivre et travailler.

Mes premiers remerciements iront aux membres du jury, et en particulier aux deux rapporteurs, Olivier Gravrand et Angela Vasanelli. Merci d'avoir pris le temps de discuter avec moi, et merci infiniment de l'attention avec laquelle vous avez lu mon manuscrit. Excusez-moi encore pour les (trop) nombreuses fautes, et mille mercis pour les corrections. Merci à Vanessa Wood et à Jérôme Tignon d'avoir accepté d'évaluer mon travail, et pour vos questions pertinentes.

Je remercie ensuite les membres de l'équipe QD du LPEM, où j'aurais surtout passé du temps durant mon stage (comprenez que je les ai plus vus au bar qu'à la paillasse). Merci aux chefs : Nicolas, Sandrine, Thomas et Alexandra pour cette atmosphère chaleureuse, vous êtes super cools (Nicolas un peu plus parce qu'il m'a emmené faire du planeur). Merci à Xiangzhen pour la microscopie électronique et tes délicieuses contributions culinaires durant nos pots. Merci aussi à Sophie et Marie-Claude, à Ricardo et à toute l'équipe des physiciens. Merci bien-sûr aux thésards du groupe QD pour la bonne ambiance, les super matériaux et les moult activités extra-doctorales : merci à Marion pour sa nonchalance légendaire, à Manon pour les fréquences inaudibles, à Eva pour le Pastis et les plaquettes. Merci aussi aux plus vieux : Ye, Jamila, Michele, Alexis et Fatima ; ainsi qu'à ceux qui prennent la relève : Mogha, Antoine, Sheila, Subha et Fanny. Sandrine, merci d'être si forte et de compenser toutes les lacunes d'Emmanuel. Bon courage pour l'HDR et encore bravo pour l'argent.

Merci à tous les membres, passés ou présents, du groupe d'Emmanuel. Merci en particulier à Bertille pour ces trois années de collaboration. On a commencé, on était deux petits thésards, Emmanuel faisait encore des devics et on devait traverser le 5e pour aller prendre un spectre FTIR. Merci à Adrien qui m'aura appris tant de choses, de la synthèse de HgSe aux manips de bruit. Nicolas, merci pour tout tes matériaux, ton temps et ton expertise. Tu es passé de l'or au mercure avec une facilité déconcertante, y'a tellement de choses qu'on n'aurait jamais pu faire sans toi. Ça n'a malheureusement pas été vraiment reconnu à sa juste valeur par les grandes instances du CNRS et de l'université, mais ça ne t'a pas arrêté. J'espère pour toi que ça va s'arranger, et pour le groupe que tu continueras à t'intéresser aux petits gaps. Junling: you're the true wizard of the lab, please continue being awesome, and take good care of Charlie so he doesn't die too soon. Charlie, Audrey, vous êtes presque bientôt des vieux thésards, je vous laisse les clés de la boutique. Vous allez faire des belles choses, j'espère bien d'ici deux ans voir des photos de profil Google Scholar dans le moyen infrarouge. Je compte sur vous pour continuer à mélanger HgSe avec des trucs même si Emmanuel est pas d'accord. Prenez bien soin des manips, et quand vous casserez des trucs n'oubliez pas de préciser que ça marchait quand Clément est parti. Frank, t'es trop frais. Julien, tout le monde t'a déjà oublié au labo. Cheh. Thanks Prachi for the good laughs, and good luck with your nasty perovskites. Sang-Soo, welcome in the group, have fun here!

Merci infiniment à Emmanuel. J'ai croisé suffisamment de thésards pas heureux pour comprendre que l'encadrement, ça n'allait pas de soi. Tu as su depuis le début comment nous orienter, dosant subtilement pour chacun de nous supervision et liberté. En travaillant avec toi je me suis senti à la fois ingénieur, jeune chercheur, chimiste, physicien et même parfois conquérant de l'inutile : la science qu'on fait dans ton groupe est un savant mélange de trucs très appliqués, de trucs à la mode, et de trucs qu'on fait parce que ça nous amuse, quand bien même ça n'intéresse personne. J'ai pu goûter à tout, et j'en suis très content. Tu m'auras appris énormément de choses (notamment qu'il y a autant de salaires que de tarauds), je te remercie encore pour ces trois années et quelques. Benoit, je te

remercie pour ta confiance et pour nos discussions toujours intéressantes.

Merci évidemment à tous les thésards de l'INSP avec qui on partage des repas, des bières, et parfois même des échantillons. Je pense notamment, par ordre d'apparition, à la team vieux qui nous ont montré la voie : Romain, Cyril, Pierre-Yves, Lise, Mathia et Nathalie ; les éternels "deuxième année" Suzanne, Lounès, Alberto (l'homme le plus classe du monde, on a rien pu faire), Danilo (morticia), Léo (le meilleur d'entre nous), Louis et William. Viennent ensuite tous les "jeunes" : Camille, Suniva, Raphaël, Medhi, Violette, Ronan, Samuel (☺), Cyrine, Dan, Pedro, Kai, Hélène... J'en oublie certainement, j'espère que vous ne m'en tiendrez pas rigueur.

Merci à toute l'équipe PhySuf' pour votre accueil et votre gentillesse. Merci à Hervé pour les nuits à Soleil, les bières et les ragots. Merci mille fois à Séba(s)tien, pilier de l'équipe, pour ton aide précieuse et pour tous ces outils "empruntés" que tu ne retrouveras plus. Tu seras parfait quand tu auras une thèse. Merci Denis pour les conseils en électronique.

Je voudrais aussi remercier Jean-Louis de nous avoir cédé son précieux matériel de manip'. Un grand merci à Yoann pour la chimie, à Loïc et Erwan de la salle blanche à l'INSP, ainsi qu'à Maxime pour son aide à l'atelier de mécanique (le meilleur endroit sur terre). Merci à Corinne et François pour leur gentillesse et leur réactivité, à Raka pour les pots et à Christophe de la mécanique pour les nombreux coups de main.

J'ai pendant cette thèse passé pas mal de temps au synchrotron, cet espace de non-droit où tout n'est que café, accumulation de données et promenades nocturnes. Merci à Mathieu de nous avoir accueilli de nombreuses fois sur TEMPO, et merci à Debora pour ta patience et ta pédagogie quand tu nous expliquais à 4 heures du matin et pour la 7ème fois que  $KE + BE + W_F = h\nu$ . Merci aussi à Francesco de la ligne SMIS : on partait vraiment pas gagnants avec nos échantillons pleins de mercure, mais ça a étonnement bien marché.

Merci à tous mes amis grenoblois, parisiens, grenoblo-parisiens ou autres, et notamment Valentin, Laurent, Albin, Cholé & Abdel, Yanis, Florian, Coline, Christophe & Lulu, Jojo, Clément et Kévin, Bubu, Max, Bob et Sophie.

Enfin, merci à mes parents, mes sœurs, mes grands-parents, mes super cousins/cousines et ma famille en général. Vous êtes top. Merci en particulier à Elodie, qui me supporte au jour-le-jour dans tous les sens du terme : on part maintenant vers d'autres aventures qui, j'en suis sûr, seront pleines de bonheur, de surprises, de serpents à sonnette et de Dunkin' Donuts.

# Contents

<b>Notations and abbreviations</b>	<b>ix</b>
<b>Introduction</b>	<b>xi</b>
<b>1 Infrared Photodetection with Nanocrystals</b>	<b>1</b>
1.1 Colloidal nanocrystals . . . . .	2
1.1.1 Nanocrystals and quantum confinement . . . . .	2
1.1.2 Colloidal nanocrystals: size and shape control . . . . .	5
1.1.3 Exciton dynamics . . . . .	9
1.1.4 Wave-function engineering in heterostructures . . . . .	12
1.2 Transport in nanocrystal arrays . . . . .	14
1.2.1 Hopping transport . . . . .	14
1.2.2 Controlling the tunnel barrier: effect of ligands . . . . .	16
1.2.3 Field-effect transistors . . . . .	18
1.2.4 Energy spectrum of nanocrystal arrays . . . . .	21
1.2.5 Principles of photodetection . . . . .	23
1.3 Addressing infrared with nanocrystals . . . . .	29
1.3.1 The infrared range: interest and applications . . . . .	29
1.3.2 Infrared detectors . . . . .	30
1.3.3 Narrow-bandgap nanocrystals . . . . .	33
1.3.4 NC-based detectors: toward low-cost, efficient detectors in SWIR and MWIR . . . . .	38
<b>2 Probing dynamics in Mercury Telluride nanoplatelets</b>	<b>41</b>
2.1 Transport dynamics: an alternative to transient spectroscopies . . . . .	42
2.1.1 Limitations of transient optical spectroscopies . . . . .	42
2.1.2 Probing dynamics at the device scale . . . . .	43
2.2 HgTe nanoplatelets: a 2D material for Near-Infrared with tunable majority carrier . . . . .	45
2.2.1 HgTe nanoplatelets: synthesis and optical properties . . . . .	45

2.2.2	Majority carrier tunability through ligand exchange . . . . .	46
2.2.3	DC transport in photoconductive devices . . . . .	48
2.3	Probing low-frequency phototransport dynamics under gate control . . . . .	49
2.3.1	A first experimental setup to probe photocurrent dynamics in the low frequency range . . . . .	49
2.3.2	Transport dynamics in HgTe NPL under gate control . . . . .	50
2.4	Time-resolved photoemission . . . . .	51
2.4.1	Principle and experiment . . . . .	51
2.4.2	HgTe NPL: probing electron and hole relaxation . . . . .	54
2.4.3	Toward more complex heterostructures and limitations . . . . .	57
2.5	Conclusions . . . . .	58
<b>3</b>	<b>Photocurrent dynamics and carrier multiplication in HgTe MWIR nanocrystals</b>	<b>59</b>
3.1	Mercury Telluride nanocrystals for Mid-Wave Infrared photodetectors . . . . .	60
3.1.1	Optical properties and energy levels . . . . .	60
3.1.2	DC transport in MWIR-sensing photoconductive devices . . . . .	61
3.2	Band-edge dynamics and multiple exciton generation in Mid-Wave Infrared HgTe devices	62
3.2.1	MHz dynamics at the band-edge of MWIR HgTe nanocrystal-based devices . .	62
3.2.2	Detection of Multiple Exciton Generation (MEG) . . . . .	64
3.3	Transient photocurrent measurements . . . . .	67
3.3.1	A new, versatile setup to probe transient photocurrent with a large dynamic range	67
3.3.2	A tool to probe trap distribution at the device scale in NCs arrays . . . . .	68
3.4	Probing dynamics in perovskite photodetectors: toward efficient carrier transport . . .	70
3.4.1	A new material for visible optoelectronics: perovskite nanocrystals . . . . .	70
3.4.2	Transient photocurrents and exciton dissociation in perovskite nanocrystals arrays	71
3.5	Conclusion . . . . .	72
<b>4</b>	<b>Intraband photodetection with self-doped nanocrystals</b>	<b>73</b>
4.1	HgSe nanocrystals for intraband photodetection: material and early results . . . . .	74
4.1.1	Self-doped HgSe nanocrystals . . . . .	74
4.1.2	Transport, photodetection and key limitations of pure HgSe nanocrystal arrays	77

---

4.1.3	HgSe under gate control: toward faster photoresponse? . . . . .	78
4.1.4	The need for uncoupling optical and transport properties in intraband materials	80
4.2	HgSe/HgTe heterostructures: a step toward improved performances . . . . .	81
4.2.1	Simulation of the core/shell phase diagram . . . . .	81
4.2.2	Growth of HgSe/HgTe heterostructures . . . . .	84
4.2.3	Transport and improved MWIR performances in HgSe/HgTe heterostructures .	85
4.2.4	Perspectives for HgSe/HgTe nanocrystals . . . . .	88
4.3	Effect of pressure on narrow-bandgap materials . . . . .	88
4.3.1	Evaluation of the interfacial pressure in HgSe/HgTe nanocrystals . . . . .	89
4.3.2	Fourier-transform Infrared Spectroscopy under pressure at Soleil synchrotron . .	89
4.3.3	HgTe nanocrystals under pressure: a story of gap-opening . . . . .	91
4.3.4	HgSe intraband nanocrystals under pressure . . . . .	95
4.4	Designing a new narrow-bandgap energy landscape: toward colloidal QDIP . . . . .	97
4.4.1	Reproducing the QDIP energy landscape by mixing nanocrystals: building the CQDIP . . . . .	97
4.4.2	Optimization of the hybrid material for intraband photodetection in the MWIR	100
4.4.3	Reduction of apparent doping in the HgSe/HgTe CQDIP . . . . .	103
4.5	A multi-spectral, intraband-based MWIR photodiode . . . . .	104
4.5.1	Building a mid-wave infrared vertical device . . . . .	104
4.5.2	An intraband-based MWIR diode with an unipolar barrier . . . . .	106
4.5.3	Spectral characterization . . . . .	109
4.5.4	First attempts at thermal sensing . . . . .	111
	<b>Conclusions and perspectives</b>	<b>115</b>
	<b>A Material and Methods</b>	<b>117</b>
	<b>List of publications</b>	<b>121</b>
	<b>References</b>	<b>125</b>



# Notations and abbreviations

## Constants

Symbol	Value	Description
$e$	$1.609 \times 10^{-19} \text{ C}$	Electron charge
$c$	$299\,792\,458 \text{ ms}^{-1}$	Speed of light
$h$	$6.62 \times 10^{-34} \text{ Js}$	Planck constant
$\hbar$	$1.05 \times 10^{-34} \text{ Js}$	Reduced Planck constant
$k_B$	$1.38 \times 10^{-23} \text{ JK}^{-1}$	Boltzmann constant
$m_0$	$9.11 \times 10^{-31} \text{ kg}$	Rest electron mass
$\epsilon_0$	$8.85 \times 10^{-12} \text{ m}^{-3}\text{kg}^{-1}\text{s}^4\text{A}^2$	Vacuum permittivity

## Abbreviations

Abbreviation	Signification
NC, NCs	Nanocrystal, Nanocrystals
CQD, CQDs	Colloidal Quantum Dot, Colloidal Quantum Dots
NPL, NPLs	Nanoplatelet, Nanoplatelets
TEM, SEM	Transmission Electron Microscopy, Scanning Electron Microscopy
VB, CB	Valence Band, Conduction Band
PLQY	Photoluminescence Quantum Yield
MBE	Molecular Beam Epitaxy
IR, NIR	Infrared, Near-Infrared
SWIR, E-SWIR	Short-Wave Infrared, Extended Short-Wave Infrared
MWIR	Mid-Wave Infrared
LWIR, FIR	Long-Wave Infrared, Far Infrared
FTIR	Fourier-Transform Infrared Spectroscopy
FET	Field-Effect Transistor
XPS, UPS	X-Ray Photoemission Spectroscopy, UV Photoemission Spectroscopy
SPV	Surface Photo-Voltage
QCL	Quantum Cascade Laser
MEG	Multiple Exciton Generation
QW, QWIP	Quantum Well, Quantum Well Infrared Photodetector
QDIP	Quantum Dot Infrared Photodetector
cQDIP	Colloidal Quantum Dot Infrared Photodetector
EDT	Ethanedithiol
DDT	Dodecanthiol
TOP	Tri-octylphosphine
PEG	Polyethylene glycol
NMF	N-methyl formamide
DMF	Di-methyl formamide
DTGS	Deuterated Triglycerin Sulfate

## Notations

Symbol	Description
$T$	Temperature
$h\nu$	Photon energy
$k$ or $\mathbf{k}$	Wavevector
$\lambda$	Wavelength
$R$	Nanocrystal radius
$E_{\text{bulk}}$	Bulk bandgap
$E_G$	Nanocrystal bandgap
$E_C$	Quantum confinement energy
$m_e^*, m_h^*$	Electron and hole effective masses
$\eta_{PL}$	Photoluminescence quantum yield
$\tau_{\text{hop}}$	Hopping time
$D, L_D$	Diffusion coefficient, diffusion length
$E$	Electric field
$\mu$	Mobility
$V_{DS}$	Drain-source bias voltage
$I_{DS}$	Drain-source current
$V_{GS}$	Gate-source voltage
$I_{GS}$	Gate leak current
$E_F$	Fermi level
$\Phi$	Work function
$KE$	Electron kinetic energy, measured in photoemission experiments
$BE$	Electron binding energy, measured in photoemission experiments
$VB - E_F$	Valence band to Fermi level energy distance
$\phi_0$	Photon flux
$\phi_d$	Photon flux density
$P_{\text{opt}}$	Optical incident power
$n_d, n_l$	Electron density in the conduction band in the dark and under illumination
$p_d, p_l$	Hole density in the valence band in the dark and under illumination
$I_{\text{dark}}$	Dark current
$I_{\text{light}}$	Current under illumination
$I_{\text{photo}}$	Photocurrent $I_{\text{light}} - I_{\text{dark}}$
$E_A$	Dark current activation energy
$\eta, g$	Quantum efficiency and photoconductive gain
$\mathcal{R}$	Device responsivity
$S_I$	Dark current spectral density
$D^*$	Device detectivity
$\Delta\nu$	Device bandwidth
$\sigma$	Nanocrystal absorption cross-section
$\langle N_X \rangle$	Average number of injected excitons
$P$	Pressure
$Y_{\text{HgTe}}, B_{\text{HgTe}}, \nu_{\text{HgTe}}$	Young modulus, Bulk modulus and Poisson coefficient of HgTe
$a_{\text{HgTe}}$	Lattice parameter of HgTe
$\varepsilon$	Strain
$\Delta E$	HgSe 1P <sub>e</sub> to HgTe 1S <sub>e</sub> energy difference in our cQDIP material
$\Delta L$	Average distance between two HgSe nanocrystals in our cQDIP material
$x_{\text{HgSe}}$	Fraction of HgSe nanocrystals in our cQDIP material

# Introduction

We owe the first prediction of what is today known as *infrared radiation* to Émilie du Châtelet in *Dissertation sur la nature et la propagation du feu*, in 1737 [1]. She understood that red light heats more than blue light, and that there are "des corps qui brûlent la main qui s'en approche, et qui ne donnent aucune lumière" ("some objects burn the hand that approaches them without emitting any light"). Herschel was the first to experiment with infrared by using a crude monochromator and a thermometer in 1800 [2]: he noticed that beyond the red part of the visible light, "something", that behaved just like light does, was still able to heat up his detector. In 1880, Samuel Pierpont Langley invents the bolometer, the first actual infrared detector [3]. Langley's bolometer was built from two platinum strips covered in carbon black and connected to a Wheaton bridge. Under infrared absorption, platinum wires would heat up and the change in resistance was measured with a precise galvanometer. With such a crude device, Langley was capable of detecting infrared radiation emitted by a cow 400 meters away. Bolometers were improved over almost 100 years before the apparition of a competing technology. They were especially developed for the military, because of the key strategic advantage they offer to gather intelligence on an enemy's position and movement. Interestingly, bolometer-like systems also exist in nature: some snakes (boas, python and rattlesnakes) possess "pit-organs" that are basically biological bolometers [4]. Those organs allow their hosts to sense infrared radiation emitted by their prey, and enable night hunting.

The first apparition of infrared *quantum* detectors, sensitive to a *photon* flux rather than to an *energy* flux, came from the development of narrow-bandgap semiconductors such as InSb and HgCdTe in the 1950's. At the same time, Albert Rose proposed an extensive explanation of the photoconduction processes in semiconductors with a detailed analysis of both electron and hole carriers importance [5]. His work enabled the rise of semiconductor photodetectors in the visible, UV and infrared ranges, that quickly overperformed other historical technologies.

The main issue with this approach is that the number of available narrow-bandgap semiconductors is very limited, even if alloying narrow-bandgap materials with other elements (HgTe with Cd in mercatel, for example) offers a bit of flexibility. In the 1970's, thanks to the development of molecular beam epitaxy, a whole new playground opens with the demonstration of the first semiconductor heterostructure by Leo Esaki [6]. This concept allow to design low energy transitions at the device level thanks to the exploitation of quantum confinement. In those heterostructures, it is possible to engineer intraband transitions with doped semiconductors, to build barrier layers filtering one specific carrier, or even control the wave-functions of electrons and holes over the whole device. It is a major paradigm shift compared to traditional narrow-bandgap-based detectors: instead of changing the bulk material bandgap through metallurgy and alloying, transitions can now be engineered on-demand in heterostructures thanks to quantum simulation and well-controlled epitaxial growth.

Despite the technological progresses, infrared imagery is still not accessible to the wide public, due to the prohibitive cost of detectors arrays. Consequently, semiconductor-based Short Wave, Mid-Wave and Long-Wave technologies are limited to military, scientific or spatial applications. Bolometers, while being a cheaper alternative, present the major drawback of being limited to slow-speed detection, incompatible with the developing needs of high framerate cameras for self-driving cars, high-speed material sorting or infrared LIDAR development.

Colloidal semiconductor nanocrystals appeared at the beginning of the 1990's [7], and quickly benefited from the epitaxial semiconductor community background. Synthesized in apolar solvent using inorganic chemistry concepts, their mass production is much easier than that of epitaxial heterostructures, and they have already found a number of applications based on their photoluminescence properties. They are notably used as down-converters for TV screens (in Samsung QLED series,

for example), or as chlorophyll-optimized solar concentrators for greenhouse passive lighting. Their integration into efficient opto-electronic devices such as LEDs, solar cells and photodetectors is still challenging. The field of infrared sensing with colloidal nanomaterial has been active since almost tens years and has already encountered some success with the development of several start-ups. Among them InVisage, producing lead sulfide nanocrystals for the extension of CMOS sensors to the Near Infrared, was recently bought by Apple. Thermal imaging with nanocrystals is the next big step, with increasing reports of high performance devices.

My PhD work was conducted between two labs. The Quantum Dots (QD) team of Benoit Dubertret in "Laboratoire de Physique et d'Étude des matériaux" at ESPCI Paris focuses in the design, synthesis and characterization of colloidal nanomaterials for optics, optoelectronics and biological applications. Most of the syntheses for my PhD work were performed at LPEM, as well as a lot of early device characterization. In the physical chemistry team of "Institut des Nanosciences de Paris", at Sorbonne University, the group of Emmanuel Lhuillier builds devices, and especially infrared-sensing devices, from colloidal nanocrystals. During my three years of PhD, I progressively set up the lab, and this is where most of my work on device characterization was performed.

During this project, I focused on probing material properties at the device scale, using opto-electronic characterization techniques. A significant part of my work was also dedicated to the design, development and building of such experiments.

## Organisation of the manuscript

This manuscript is divided in four chapters. The **first chapter** is dedicated to a presentation of the background of my PhD work, from the synthesis of colloidal nanocrystals to their integration in infrared-sensing devices. I also introduce how transport occurs in arrays of colloidal nanoparticles, as well as the relevance of carrier dynamics study.

In the **second and third chapters**, I am interested in photo-transport dynamics in systems of decreasing bandgap. Starting from the Near Infrared with colloidal mercury telluride nanoplatelets in the **second chapter**, I give a picture of the opto-electronic properties of this new promising 2D material, then I present two ways of probing the dynamics of photo-excited carriers in arrays of this material. In the **third chapter**, I switch to a Mid-Wave Infrared absorbing material: mercury telluride quantum dots. For the first time, we probe the photocurrent dynamics at the band-edge of devices made from such narrow-bandgap materials. Doing so, we are able to study hot carrier effects, under illumination with photon energies far above the material absorption band-edge. Finally, I develop a new technique based on transient photocurrent with a high dynamic range, allowing to develop a better understanding of carrier lifetime.

The **fourth chapter** is dedicated to the understanding and exploitation of intraband transitions in self-doped mercury selenide nanocrystals. During three years of work on this material, the group built a deep understanding of this material. I present my early, exploratory work around intraband-based Mid-Wave Infrared sensing devices, which allowed to identify the major drawbacks of this material. Since this material is an electron-doped semiconductor featuring intraband transitions, we were inspired by Quantum Well and Quantum Dot Infrared Photodetectors based on III-V materials, and looked for ways to uncouple optical absorption and charge transport in HgSe-based devices. I present the design and growth of core-shell structures of HgSe/HgTe, allowing to dramatically improve devices performances. In those heterostructures, the understanding of the interface between the core and the shell is crucial to control the electronic properties, so we studied the effect of pressure on the optical spectra of our narrow-bandgap nanomaterials. I then present a new approach, where we reproduce the energy landscape of III-V detectors using a binary mix of two nanocrystal populations: this allows to design an heterostructure at the device level rather than at the nanoparticle scale. Finally, I integrate this hybrid material into the first intraband-based multicolor photodiode.

# Chapter 1

## Infrared Photodetection with Nanocrystals

---

<b>1.1</b>	<b>Colloidal nanocrystals</b> . . . . .	<b>2</b>
<b>1.2</b>	<b>Transport in nanocrystal arrays</b> . . . . .	<b>14</b>
<b>1.3</b>	<b>Addressing infrared with nanocrystals</b> . . . . .	<b>29</b>

---

### Related articles

- C. Livache, B. Martinez, N. Goubet, J. Ramade and E. Lhuillier, "Road Map for Nanocrystal Based Infrared Photodetectors", *Frontiers in Chemistry* 6, 575 (2018)
- A. Jagtap, C. Livache, B. Martinez, J. Qu, A. Chu, C. Gréboval, N. Goubet and E. Lhuillier, "Emergence of Intraband Transitions in Colloidal Nanocrystals", *Optical Materials Express* 8, 1174-1183 (2018)

## 1.1 Colloidal nanocrystals

### 1.1.1 Nanocrystals and quantum confinement

We start by considering a simple model of Quantum Dot (QD): a semiconductor particle in a box. In this model, electrons and holes of the semiconductor material are described by two parabolic dispersion relations, one for the Conduction Band (CB) and one for the Valence Band (VB). Assuming that our semiconductor features a direct bandgap at the wavevector  $\Gamma = 0$ , those bands are separated in energy at the  $\Gamma$  point by the material bulk bandgap energy:  $E_{\text{bulk}}$ . Dispersion relations for the electron (*i.e.*, conduction band) and for the hole (*i.e.*, valence band) are then:

$$E_{CB}(k) = E_{\text{bulk}} + \frac{\hbar^2 k^2}{2m_e^*} \text{ and } E_{VB}(k) = -\frac{\hbar^2 k^2}{2m_h^*} \quad (1.1)$$

Where  $\hbar$  is the reduced Planck constant,  $k$  is the wavevector and  $m_e^*$  and  $m_h^*$  are the effective electron and hole masses, respectively. Those parabolic bands are represented in Figure 1.1.

Upon absorption of light in this semiconductor, an electron from the valence band is promoted to the conduction band. This process occurs for  $\Delta k = 0$ , so the photon energy  $h\nu$  must be greater than the energy bandgap in order to be absorbed. The electron/hole pair created by this process is bounded by the Coulombic interaction and called *exciton*. The average distance between the two bound photo-generated charges is given by the Bohr model and called the exciton Bohr radius:

$$a_0 = \frac{4\pi\epsilon_0\epsilon_r\hbar^2}{m_0 m_{eh}^* e^2} \quad (1.2)$$

Where  $\epsilon_r$  is the semiconductor dielectric constant and  $m_{eh}^*$  is the reduced mass:  $(m_{eh}^*)^{-1} = (m_e^*)^{-1} + (m_h^*)^{-1}$ . Table 1.1 presents the Bohr radii for several semiconductor materials that will be discussed in this work. Whenever one dimension of the semiconductor particle falls below the exciton Bohr radius, quantum confinement arises in this direction.

Material	$E_{\text{bulk}}$ (eV)	$m_e^*$ (in $m_0$ unit)	$m_h^*$ (in $m_0$ unit)	$a_0$ (nm)	Reference
CdSe	1.73	0.12	0.9	5.6	[8]
CdTe	1.48	0.09	0.8	7.3	[8]
PbS	0.42	0.087	0.083	21	[8]
HgTe	0	0.03	0.7	40	[9]
HgSe	0	0.04	0.78	17	[10]

Table 1.1: Electronic parameters for few semiconductor materials

In the case of a square box of dimensions  $L_x < a_0$ ,  $L_y < a_0$ ,  $L_z < a_0$  with infinite potential barriers, solving the Schrodinger equation for one band results in confined, discrete states of wavefunction:

$$\Phi(x, y, z) = \sqrt{\frac{8}{L_x L_y L_z}} \sin\left(\frac{n_x \pi x}{L_x}\right) \sin\left(\frac{n_y \pi y}{L_y}\right) \sin\left(\frac{n_z \pi z}{L_z}\right) \quad (1.3)$$

And each state indexed by  $n_x$ ,  $n_y$ ,  $n_z$  has the energy:

$$E_{n_x, n_y, n_z} = \frac{\hbar^2 \pi^2}{2m^*} \left( \frac{n_x^2}{L_x^2} + \frac{n_y^2}{L_y^2} + \frac{n_z^2}{L_z^2} \right) \quad (1.4)$$

Where  $m^*$  is either the effective electron ( $m_e^*$ ) or hole ( $m_h^*$ ) mass.

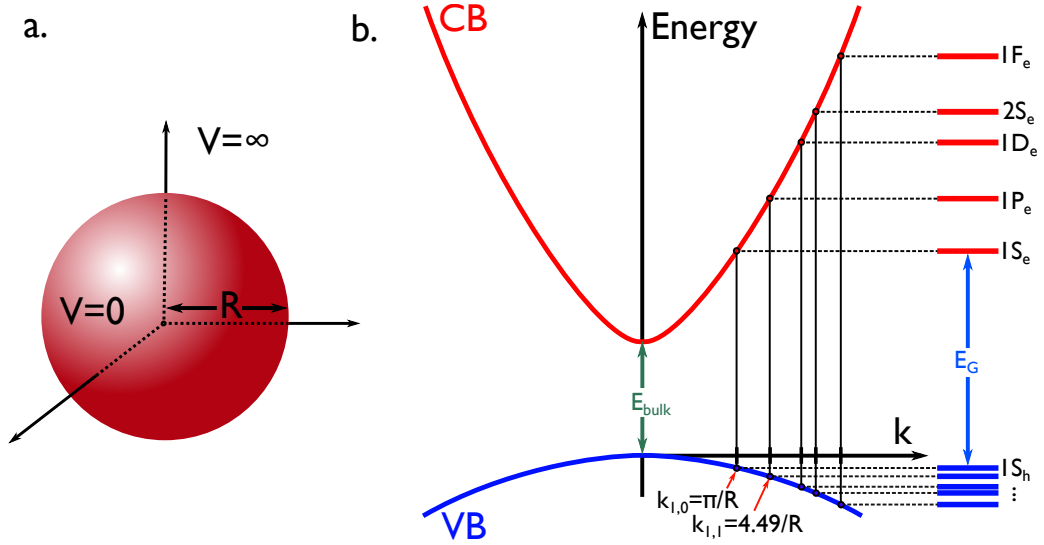


Fig. 1.1 Effect of quantum confinement for a spherical particle of semiconductor. **a.** Semiconductor particle with infinite spherical barriers. **b.** Band diagram of a semiconductor in the parabolic approximation (thick lines). Quantum confinement transforms the parabolic bands in discrete, non-dispersive levels.

Now, if we consider a spherical box of radius  $R < a_0$ , like the one presented in Figure 1.1a, the geometry of the problem changes but the fundamental effect of the confinement on the semiconductor particle energy states stays the same: we obtain discrete levels indexed by quantum numbers  $n$ ,  $M$  and  $L$ . The levels wave-functions are given in spherical coordinates by [11]:

$$\Phi_{n,L,M}(r, \theta, \varphi) = \frac{\sqrt{2}}{R^3} \frac{j_L(\phi_{n,L} r/R)}{j_{L+1}(\phi_{n,L})} Y_{L,M}(\theta, \varphi) \quad (1.5)$$

Where  $j_L$  are the spherical Bessel functions,  $Y_{L,M}$  are the spherical harmonic functions and  $\phi_{n,L}$  is the  $n$ -th root of the Bessel function  $j_L$ . The discrete states energies are then given by:

$$E_{n,L,M} = \frac{\hbar^2 \phi_{n,L}^2}{2m^* R^2} \quad (1.6)$$

Where again,  $m^*$  is either the effective electron or hole mass. Those energies are degenerated relatively to  $M$  and the corresponding states are usually noted  $nL$  with  $n = \{1, 2, \dots\}$  and  $L = \{S, P, D, F, \dots\}$ . As shown on Figure 1.1b, those energy states can be seen as discrete cuts into the bulk semiconductor bands, at wavevectors  $k = \phi_{n,L}/R$ .

As pictured in Figure 1.1b, the density of states in the valence band is usually much higher than the density of states in the conduction band. This is due to the strong difference between electron and hole effective masses, making that the dispersion of the valence band is usually much lower than that of the conduction band. As a result, the discrete levels of the valence band can often be seen as a quasi-continuum of states.

The bandgap energy of the newly obtained nanostructure is directly obtained by taking the energy difference between the ground states of the conduction band ( $1S_e$ ) and the valence band ( $1S_h$ ):

$$E_G = E_{1S_e} - E_{1S_h} = E_{\text{bulk}} + \frac{\hbar^2 \phi_{1,0}^2}{2m_e^* R^2} - \left( -\frac{\hbar^2 \phi_{1,0}^2}{2m_h^* R^2} \right) = E_{\text{bulk}} + \frac{\hbar^2 \pi^2}{2m_e^* R^2} + \frac{\hbar^2 \pi^2}{2m_h^* R^2} = E_{\text{bulk}} + \frac{\hbar^2 \pi^2}{2m_{eh}^* R^2} \quad (1.7)$$

Where  $m_{eh}^{-1} = m_e^{-1} + m_h^{-1}$  is the electron-hole reduced mass. At that point, we see that the signature of quantum confinement apart from the quantization of states is the appearance of a *confinement energy* that is added to the bulk bandgap energy of the semiconductor:

$$E_C(R) = \frac{\hbar^2 \pi^2}{2m_{eh}^* R^2} \quad (1.8)$$

Which scales as  $1/R^2$ , meaning that the smaller the particle, the higher its bandgap energy.

The optical bandgap of the nanocrystal defines the absorption band-edge of the material, and is obtained by renormalizing the bandgap with the Coulombic interaction between the photo-generated electron and hole [12]:

$$E_G^{\text{op}} = E_{\text{bulk}} + \frac{\hbar^2 \pi^2}{2m_{eh}^* R^2} - \frac{1.8e^2}{\epsilon_{\infty} R} \quad (1.9)$$

Where  $\epsilon_{\infty}$  is the dielectric constant of the material.

Since the absorption band-edge of the nanocrystal depends on its size, so does its *emission* properties. Indeed, as pictured in Figure 1.2, a photo-excited quantum dot will emit light upon recombination of the electron-hole pair. Because of energy conservation, the wavelength of the emitted photon will correspond to the bandgap of the nanocrystal. Moreover, since a quantum dot have flat, non-dispersive states, it features a direct bandgap (*i.e.* the top of the valence band and the minimum of the conduction band are found at the same wavevector). This makes that all quantum dots should be capable of light emission, even if the material they are made with features an indirect bandgap in the bulk form. This is notably the case for silicon nanocrystals [13].

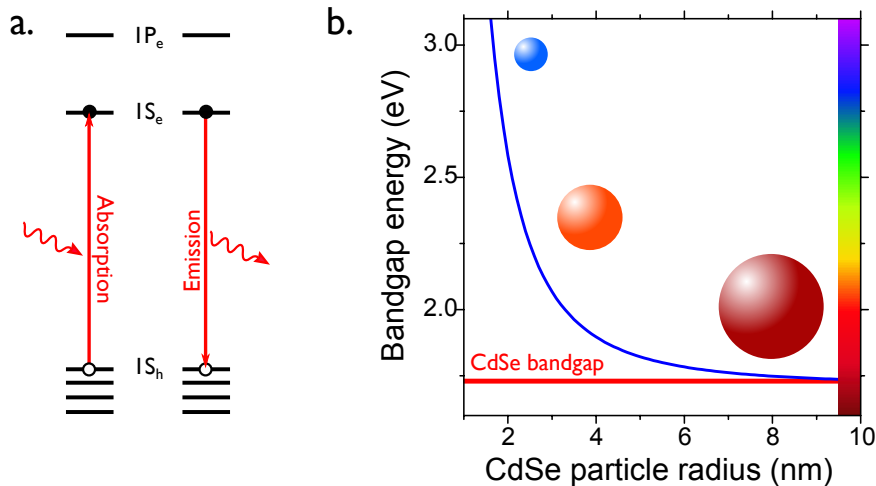


Fig. 1.2 Optical properties of a CdSe spherical quantum dot **a.** Schematic description of an interband absorption process (left) and emission process (right) in a CdSe QD. **b.** Optical bandgap of a CdSe quantum dot when the particle size is tuned from 1 to 10 nm. The red line indicates the bulk bandgap of the material.

It is of course possible to observe quantum confinement in other geometries than the sphere. Figure 1.3 provides examples of 1D, 2D and 3D confinement. In the case of 3D confinement, we often

speak about 0D object, and of 2D objects in the case of 1D confinement. Structures confined in only one dimension were the first to be studied, and are usually called Quantum Wells (QW), when those confined in two dimensions are called Quantum Wires, or nanowires. The density of states (*i.e.*, the probability to find an electron (or a hole) state at a given energy) is also given in Figure 1.3.

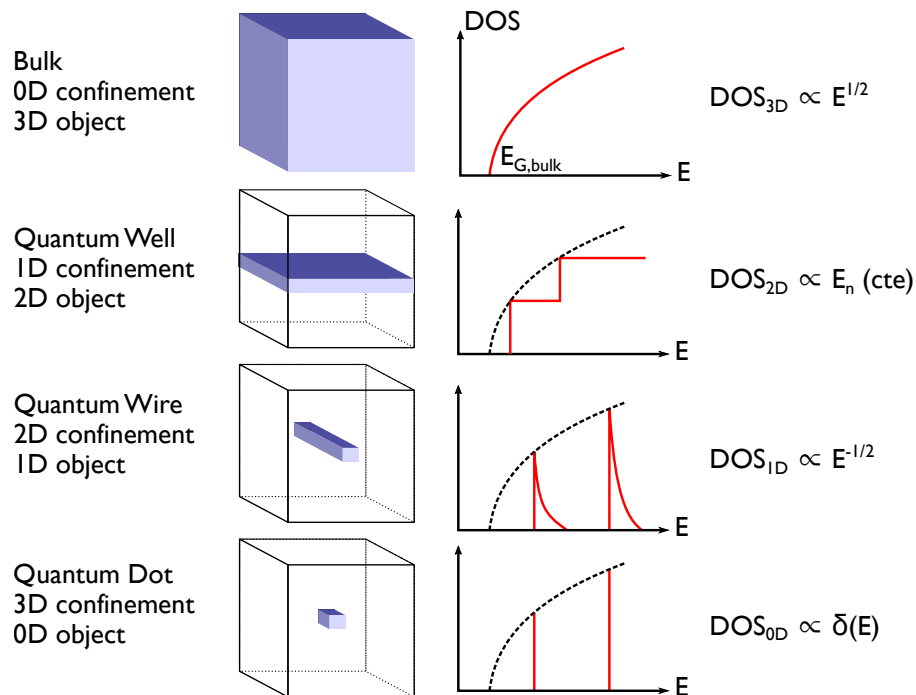


Fig. 1.3 Confinement can be observed in 1, 2 or 3 dimensions. The density of states of the semiconductor nanoparticle depends strongly on the degrees of freedom of the charge carriers in the material.

### 1.1.2 Colloidal nanocrystals: size and shape control

The introduction of quantum confined structures in the semiconductor world allowed for a paradigm shift: controlling the optical properties of a material could now be achieved by carefully tuning its size. As a result, different absorption or emission properties can be realized with the same material without the need of alloying or doping. The first realization of those quantum confined structures were obtained by Esaki using molecular beam epitaxy (MBE) [6]. During epitaxial growth, materials are deposited atom after atom on a substrate with the best possible lattice parameter match. Hence, the growth of a thin layer of GaAs between two AlGaAs barriers effectively produces a Quantum Well structure [14], confined in the direction of the material growth. The first quantum dots were also grown using this epitaxial technique: by growing a thin enough InAs layer on GaAs, the lattice mismatches cannot be relaxed and the layer dewets, forming small islands of InAs embedded in a GaInAs matrix. [15, 16].

#### Colloidal Quantum Dots (CQDs)

As the epitaxial growth of nanostructures have found a number of industrial applications, notably for the growth of III-V semiconductors, colloidal synthesis of semiconductor nanoparticles have been developed since the 1990s. In 1993, Murray, Norris and Bawendi demonstrated the first synthesis of II-VI nanocrystals using wet chemistry approach [7]. In this paper, they demonstrated the growth of CdSe (see Figure 1.5a), CdTe and CdS nanocrystals in an apolar, coordinating solvent. Starting from a hot solvent under inert atmosphere, they conduct a pyrolysis reaction by quickly injecting

the cadmium and chalcogenide precursors, ensuring a fast decomposition followed by nucleation of small nanoparticle seeds called *monomers*. The subsequent growth of those seed is mostly controlled by the temperature of the flask, the duration of the reaction and the presence of ligands [17]. The reaction is stopped either by introducing a large amount of organic ligands to prevent the monomers to access the nanoparticle, or quickly cooling down the flask. The reaction is followed by critical washing steps where the nanocrystals are precipitated and redispersed several times to eliminate any excess of precursors or ligands. Colloidal synthesis allows the production of massive amounts of quantum dots for a cheap price, compared to epitaxial techniques that require heavy equipment.

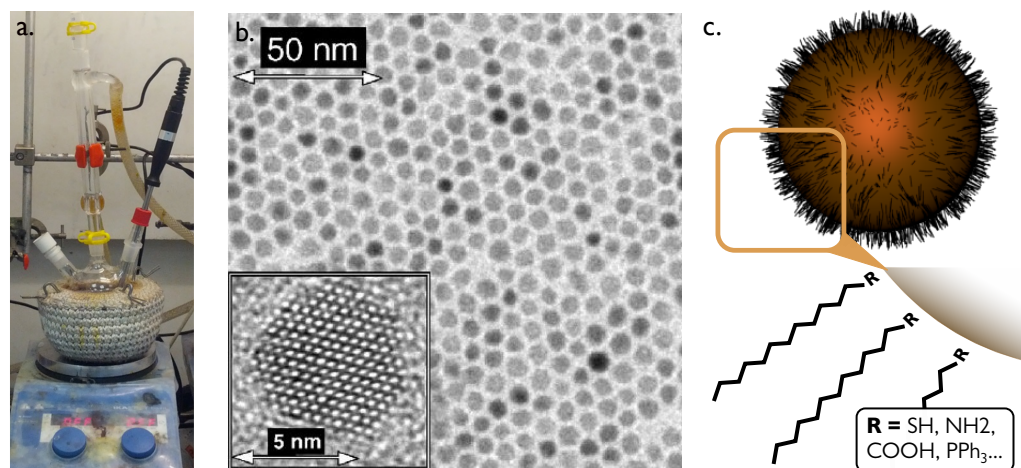


Fig. 1.4 Colloidal Quantum Dots synthesis. **a.** Typical chemistry setup for one-pot synthesis of metal chalcogenide CQDs. Atmosphere of the flask can be switch to air, vacuum or argon. **b.** TEM picture of CdSe CQD capped with trioctylphosphine oxide (TOPO) ligands. Inset: High-resolution TEM picture of a single CdSe CQD showing the crystalline structure of the material. From ref. [18]. **c.** Scheme of a single CQD capped with organic ligands. Those ligands consist typically of a long alkyle chain functionalized to allow hybridation with the CQD's surface.

Most synthesis of II-VI nanocrystals follow the same major principles with a dissolution of the precursor, a fast nucleation followed by a controlled growth of particles. Figure 1.4a shows the typical chemistry setup used to perform such a synthesis, and an example of CdSe Colloidal Quantum Dots (CQDs) seen using Transmission Electron Microscopy (TEM). TEM imaging allows the observation of ensemble of nanoparticles as well as single objects, and reveals the crystalline character of the material (here, the zinc-blende structure characteristic of CdSe nanocrystals).

It is very important to understand that the key parameter that made the nanocrystal synthesis as successful as they are today is the ability to produce monodisperse objects. Indeed, access to the physics of discrete states is only possible if the energy dispersion of these levels at the batch scale is low enough in front of the level spacing, to ensure that there is no overlap. In other terms, the inhomogeneous broadening brought by the size dispersion of the particles in a batch must stay low to be able to observe the effect of quantum confinement in an ensemble measurement. As pictured in Figure 1.5a, the synthesis reported by Murray, Norris and Bawendi was able to reach a level of dispersion good enough to observe a quantum confinement effect, as the size of the obtained nanocrystals has a real impact on the optical absorption of the solution.

One key parameter making colloidal QDs different from their epitaxial counterpart is the presence of ligands at the surface of the nanoparticles, see Figure 1.4c. Those ligands, at the synthesis level, usually consists in long alkyle chains (from C<sub>10</sub> to C<sub>18</sub>) terminated with a function allowing them to bind to the surface of the nanoparticle. They have three main purpose:

- They regulate the formation of nanocrystals by forming micelles around the nanoparticle seeds

and slowing down the reaction, allowing for a controlled growth rate. A slow, controlled growth rate, as opposed to fast and explosive growth, is the key to maintain a reasonable size dispersion at the batch scale.

- They stabilize the colloidal solution by ensuring that the nanocrystals are spatially separated from each other, preventing aggregation.
- They passivate the surface of the particles by binding to dangling bonds at the surface of the nanocrystal. Another way of seeing this mechanism is considering that the ligands can hybridize with in-gap trap states, effectively pushing them outside of the bandgap by creating new binding and non-binding states located inside the conduction and valence band, respectively [19].

The first target application for CQDs was based on their bright light emission, see Figure 1.5b. Figure 1.5c presents the emission spectrum of a CdSe CQD solution. With an average size around 3 nm, those nanocrystals emit green light upon excitation in the UV. There is a notable red-shift between the absorption and the emission spectrum maxima of the nanocrystals: this is called the *Stokes shift* and is due to the coupling between light emission and acoustic phonons at the nanoparticle scale [20].

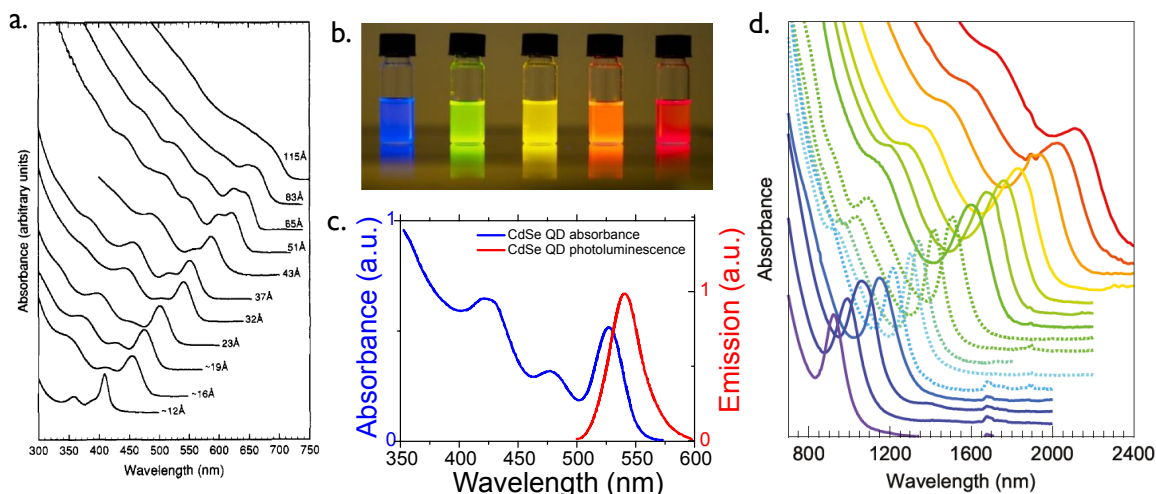


Fig. 1.5 Optical properties of CQDs. **a.** Absorbance spectra of spherical CdSe CQDs ranging from 1.2 nm to 11.5 nm with absorption and emission in the visible range. From ref. [7]. **b.** CdSe CQDs of different sizes in in solution, illuminated with UV light (©Nexdot). **c.** Absorption and emission spectra of  $\sim 3$  nm CdSe CQDs. **d.** Absorbance spectra of PbS CQDs with absorption and emission in the near-infrared range. From ref. [21].

Over more than 30 years, a wide variety of quantum confined nanomaterials have been developed. Starting from cadmium chalcogenides, other II-VI materials have been explored as ZnS [22] or mercury chalcogenides [23–28]

Same synthesis principles can also be applied to IV-VI materials: lead chalcogenides, as example, can be prepared and have been extensively used for solar cell applications thanks to their controllable absorption in the near-infrared range, see Figure 1.5d [29–31].

The developpement of this new material class raised a number of questions about their toxicity. In addition to be in nanoparticle form (allowing to bypass a fair number of barriers), a significant share of those new materials are made of toxic compounds as cadmium, mercury, lead, selenide... This can be a serious concern for a wide range of biological applications as well as applications needing a large amount of material. Developpement of non-toxic materials have been pushed since 2000, including InP, Si and Ge nanocrystals for the visible range [32] and ternary I-II-VI materials as CuInSe in the near infrared [33–35].

## Nanoplatelets

In 2006, the group of Taeghwan Hyeon in Korea introduced a synthetic pathway to obtain 2-dimensional *nanoribbons* of CdSe in the wurtzite structure [36]. In 2008, Ithurria and Dubertret presented the first synthesis of two-dimensional nanocrystals with zinc-blende structure, confined in only one spatial dimension [37]. By introducing cadmium acetate during the growth of the nanoparticles, they were able to template the monomers assembly and to force the growth to happen preferentially in certain crystallographic directions. As a result, the growth along the [100] axis is self-limited [38], and the resulting objects present a large lateral extension (from 10 to 100 nm, see Figure 1.6) when their thickness is the only confined direction. By changing the reaction parameters (time, temperature, ratio of precursors), it is possible to control the final thickness of the 2D objects down to the monolayer, one monolayer being defined as one plane of anion plus one plane of cation. This results in a change of confinement, as can be seen on Figure 1.6a: thicker NPLs are less confined and feature a lower energy optical band edge.

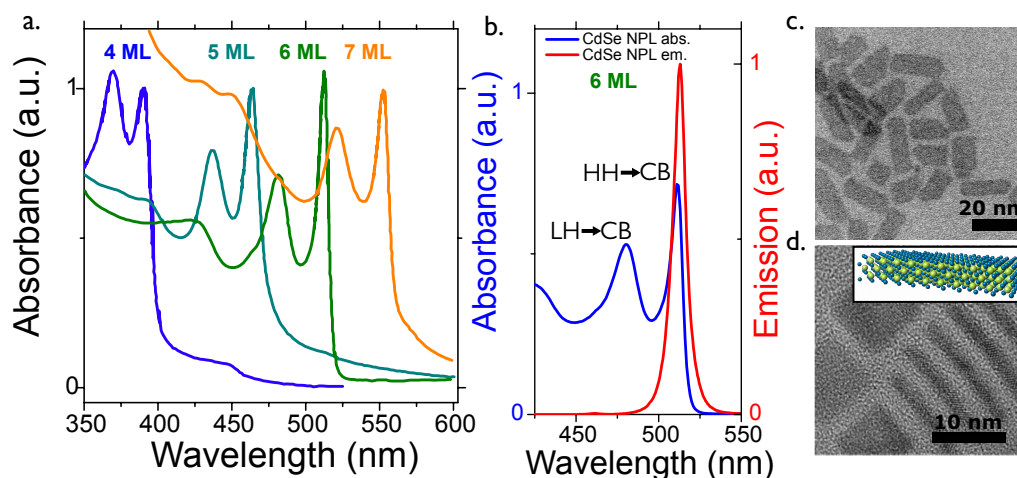


Fig. 1.6 Colloidal nanoplatelets (NPL). **a** Absorbance spectra of CdSe NPL from 4 monolayers (1.2 nm) to 7 monolayers (2.1 nm). Adapted from [39]. **b** Absorbance and photoluminescence spectra of 6 monolayers CdSe NPL. **c** TEM picture of CdSe NPL laying flat. **d** TEM picture of CdSe NPL laying on the side, from [37]. Inset: scheme of a single NPL.

The two peaks observed in absorption spectrum (see Figure 1.6a) are attributed, in a 2D quantum well model, to transitions from the heavy-hole band to conduction band (reddest peak) and from the light-hole band to conduction band (bluest peak) [38]. As can be seen on Figure 1.6b, the absorption and emission features of NPL are considerably narrower than those of CQDs at the same wavelength (see Figure 1.5d). In nanoplatelets, the control of the thickness is atomically accurate, meaning that NPL are atomically flat objects. As a result, all objects in a batch have the same thickness, and since the thickness is the only confined dimension, all the objects have the same optical properties. This is a real difference between NPL and CQDs: CQD batch, as good as they can be, will always feature some size dispersion that is responsible for a heterogeneous broadening of the ensemble optical properties. In a NPL batch, since all the quantum wells have the same thickness, the spectrum of the ensemble is the same as the single object one [40]. The linewidth of the emission spectrum of NPL ensembles have been measured to be  $\simeq 2kT$ , indicating that it is indeed limited by homogeneous broadening due to non-zero temperature.

## Applications

As mentioned before, the first interest of CQDs was their bright luminescence in the visible range. Nanocrystals have now reached a maturity where they are readily used as phosphor in high-end television products. Samsung QLED products include heavy-metal free InP CQDs as down-converters

to produce green and red light, and a number of small and medium companies sell CQDs for lighting or biological labeling. As pictured in Figure 1.7, there are several ways to achieve light emission with nanocrystals. In the simplest applications, CQDs are optically pumped by a blue source (see Figure 1.7a). For lasing application (Figure 1.7b), CQDs are enclosed in a cavity and optically pumped under sufficient power to achieve population inversion and stimulated emission [41–45]. Light emission under electrical injection in LED devices (Figure 1.7c) have also been developed [46–49] and should see first applications in high contrast, extended gammut screens in the next few years [50].

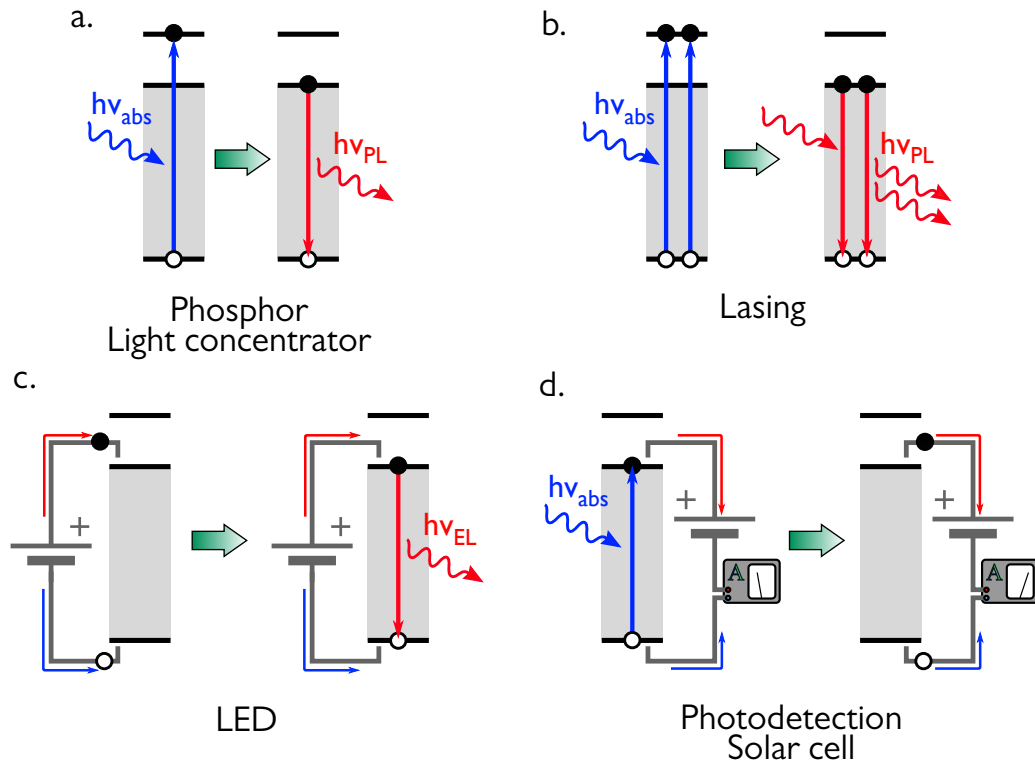


Fig. 1.7 Applications of colloidal nanocrystals. **a.** Light conversion. **b.** Lasing. **c.** Light Emitting Diodes (LEDs) with electrical injection. **d.** Photodetectors and solar cells. Inspired from [17].

This manuscript will not focus on light emission but rather on applications around light absorption and transduction in electrical signals (Figure 1.7d). This is the underlying principle of photodetectors and solar cells: converting incident photons into current, either to measure the incident light flux (photodetector) or to produce power (solar cells). In this sense, nanocrystals are interesting because their tunable bandgap allows for precise matching to the incident photon energy and because of the simplification of device building compared to traditional semiconductor technologies.

Colloidal nanoplatelets have also encountered a reasonable success among academic research. Recent realisation with NPLs include lasing of nanoplatelets under optical excitation [51–53], LEDs, NPL doping [54, 55] and the development of objects with absorption and emission in the infrared range [56].

### 1.1.3 Exciton dynamics

As mentioned in the precedent section, light emission motivated most of the first works on CQDs. In order to optimize the material for any desired application, one must understand what happens in a nanocrystal after excitation. Upon absorption of an incident photon of higher energy than the bandgap of the material ( $h\nu_i > E_G$ ), an electron-hole pair (or exciton) is created. This exciton can then recombine in different ways, pictured in Figure 1.8a.

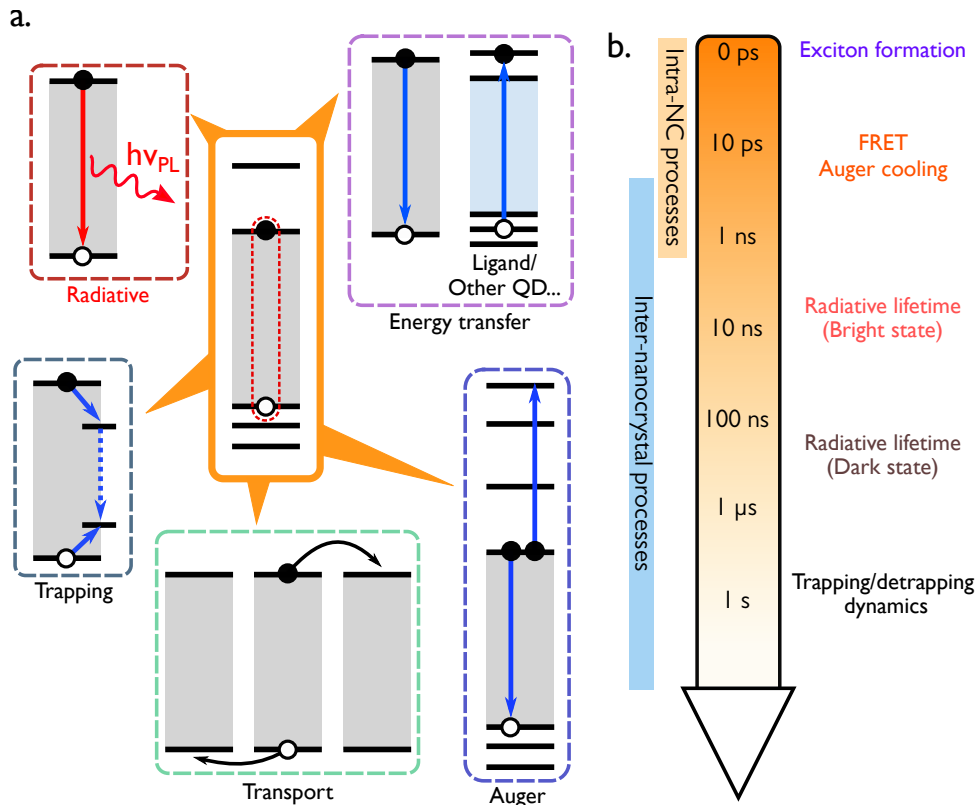


Fig. 1.8 The fate of an exciton in a nanocrystal. **a** Different recombination pathways for an electron-hole pair (exciton) in a nanocrystal. **b** Schematic timescale of the different processes involved in the recombination of an electron-hole pair.

- The exciton can recombine *radiatively* via a photoluminescence process: the electron-hole pair annihilates and a photon of energy  $h\nu_{PL}$  is emitted.
- One or both of the carriers can be *trapped* in a non-radiative state, preventing or slowing down the emission of light. In this case, the energy is mostly dissipated as thermal losses.
- If another carrier is present in one of the bands (case of a charged exciton or of multiple excitons), the exciton can undergo Auger recombination. In this case, the electron-hole pair recombines through the gap of the material and the energy is transferred to the third carrier, which will ultimately undergo thermal cooling.
- Under certain conditions, the energy of the exciton can be transferred to ligands or to a neighbor particle *via* non-radiative processes (FRET).
- Finally, under specific conditions the excitonic pair can be split and each carrier transferred to a neighbor nanocrystal: this is the first step toward carrier transport in nanocrystal films, that will be discussed later.

The figure of merit used to describe how good a material is for light emission is the *photoluminescence quantum yield*, or PLQY. The *external* PLQY describes the probability for an incident photon to be absorbed by the material and create an electron-hole pair that will undergo radiative recombination. The *internal* PLQY describes the same phenomenon, but only considers absorbed photons (*i.e.* is independent from the material absorbance). The internal PLQY  $\eta_{PL}$  can be defined as:

$$\eta_{PL} = \frac{\Gamma_r}{\sum_i \Gamma_i} \quad (1.10)$$

Where  $\Gamma_r$  is the rate of radiative recombination and  $\sum_i \Gamma_i$  is the sum of the rates of all the decay processes. If we consider the characteristic time of each of the process  $t_i = 1/\Gamma_i$ , one can conclude that in order to maximize the PLQY of any material the radiative recombination has to be the fastest recombination process.

Exciton dynamics in nanocrystals are usually probed using optical spectroscopy technique. The easiest way to probe photoluminescence dynamics is to use a time-resolved spectroscopy setup where excitation is provided by a pulsed (50 ps, typically) laser. Photoluminescence of the sample is collected and sent into a fast photodetector able to measure the real-time decay of the photoluminescence signal after excitation. Figure 1.9a shows a typical time-resolved photoluminescence trace from HgTe nanoplatelets in the near-infrared [56]. Being based on the photoluminescence of the sample, this techniques does not allow to easily probe non-radiative decay. More insight can be obtained using ultrafast transient absorption in pump-probe configuration. In this experiment, absorption of a sample is measured before and after its excitation by an intense, ultrafast (few tens of fs) laser pulse (the *pump*). Measurement of absorption is performed using a delayed fs pulse (the *probe*). The absorption bleach at the pulse wavelength reflects the population of the matching transition, and by scanning the delay of the probe relatively to the pump, it is possible to measure a level occupation as a function of time, as pictured in Figure 1.9b.

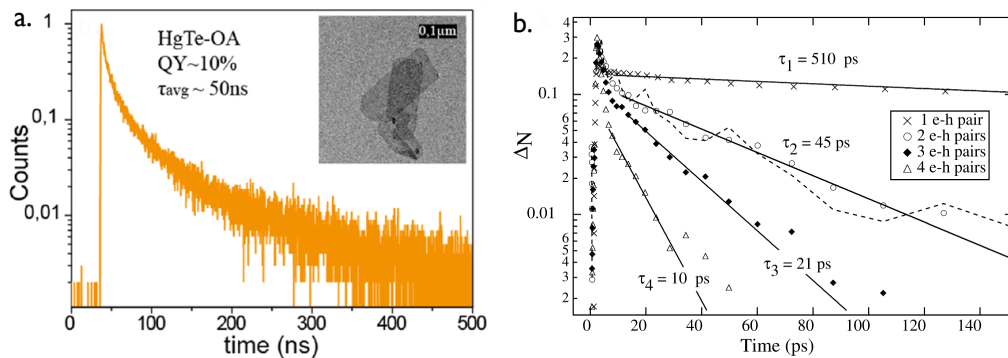


Fig. 1.9 Exciton lifetimes measured by optical spectroscopy. **a** Time-resolved photoluminescence signal at 828 nm after excitation by a 50 ps, 355 nm laser. The extracted radiative average lifetime is around 50 ns. Inset: TEM image of the nanoplatelets. From [56]. **b** Dynamics of the exciton population measured by transient absorption in CdSe CQDs under various excitation power. Each set of data points correspond to injection of 1 ( $\times$ ), 2 ( $\circ$ ), 3 ( $\diamond$ ) or 4 ( $\triangle$ ) excitons per nanocrystal. From [57].

Figure 1.8b provides some orders of magnitude for the dynamics of the different decaying processes. The photoluminescence lifetime usually spans from a few ns to 1  $\mu$ s, depending on the selection rules associated with the transition. As it can be seen on Figure 1.9a, the photoluminescence decay is rarely a single-exponential process because of the variety of pathways leading to radiative recombination, especially at the ensemble level. Trapping can be as fast as a few hundreds of fs [58, 59], but *de-trapping* (*i.e.* release of the carrier from their traps) can extend over very long time scales. Energy transfer such as Förster energy transfer (FRET) are usually sub-ns processes [60], as well as Auger processes. The particular case of Auger recombination have been extensively studied by the group of Klimov in Los Alamos National Laboratories [57, 61], and one example is given in Figure 1.9b. Because Auger recombination needs an additional electron in the conduction band (or hole in the valence band) to occur, it is usually not observed under illumination leading to injection of  $<1$  exciton per CQD. Upon higher fluence though, Auger decay prevails over photoluminescence since it occurs much faster than the multiexciton radiative decay. There is a universal trend for Auger decay in colloidal quantum dots: regardless of the material, the lifetime of Auger processes seems to be proportionnal to the particle volume ( $R^3$  scaling) [17, 57, 62].

In order to match a certain material to an application, it is mandatory to control the lifetime of those different radiative or non-radiative processes. Applications around light emission will need to

control the non-radiative channels to improve the PLQY. Auger decay have to be tamed to perform CQD lasing, intrinsically needing strong excitation to achieve population inversion. In another hand, applications around light detection or solar energy conversion needs for the radiative recombination (as well as faster processes) to be slowed down or suppressed to ensure efficient charge extraction. This level of control is usually not achievable with core-only objects, and requires the need for heterostructures.

#### 1.1.4 Wave-function engineering in heterostructures

Heterostructuration of colloidal materials came from the need to have a higher control over the optical and electrical properties of the nanocrystals. With core-only objects and with a given material, the optical properties of a CQD can only be affected by the size of the material (and, to a small extent, by its surface chemistry). The introduction of a shell made from another material allows to switch from bandgap engineering to wave-function engineering in nanocrystals.

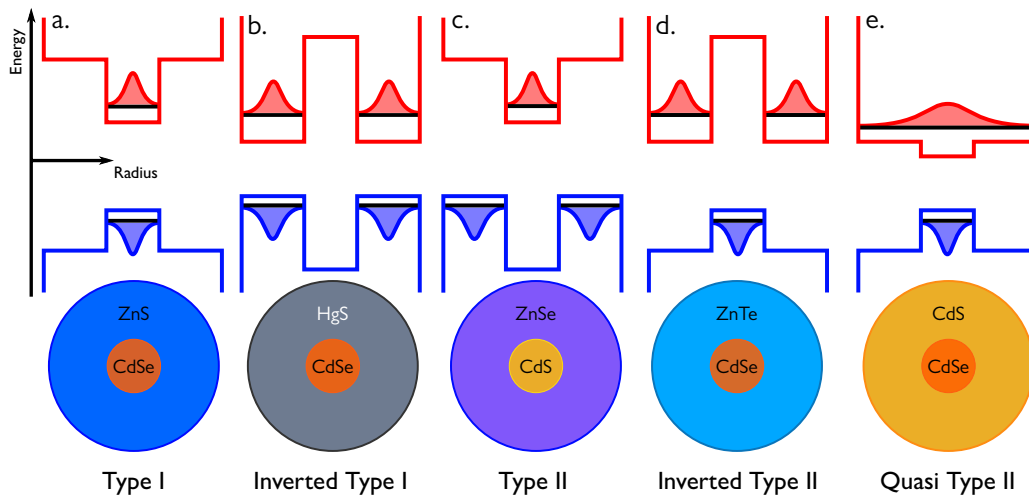


Fig. 1.10 The different types of band alignment in core-shell materials. In each band structure, valence band of the bulk materials are depicted in blue and conduction bands in red. Confined levels are displayed in black, and electron and hole ground states wave-functions are pictured in red and blue, respectively. **a.** Type-I band alignment: hole and electron wave-functions are confined in the core structure, protected by the shell from the surrounding medium. **b.** Inverted Type I: both the electron and hole wave-functions are localized in the shell. **c.** Type II band alignment: the two carriers are spatially separated, the electron being confined in the core while the hole is delocalised in the shell. **d.** Inverted Type II: the hole is confined in the core and the electron delocalized in the shell. **e.** Quasi-Type II band alignment. If the conduction band mismatch between core and shell material is small enough, one of the carriers can be confined in the core while the other is delocalized other the entire structure. Inspired from [17].

By carefully choosing the materials of the core and the shell, it is possible to produce different kinds of band alignments, presented in Figure 1.10. By choosing a shell material with a larger bandgap than the core material, see Figure 1.10a, the wave-function of the carriers localizes only in the core. This does not affect the absorption nor the emission energy of the material, but shields the core material from oxydation and the exciton from external perturbation and trapping at the surface states. Indeed, since the shell growth is epitaxial, the core/shell interface can present less surface defects than the core/ligand interface. This type-I configuration is mostly used for application where a high photoluminescence quantum yield is needed. Experimentally, a small red-shift of the excitonic properties is observed when growing type-I core-shell objects. Indeed, the wave-function extension in the core is always larger for a semiconductor/semiconductor epitaxial interface rather than for a semiconductor/ligands interface, making the effective diameter of the core slightly bigger

when the large-bandgap shell is grown. CdSe/ZnS heterostructures are the most popular example of type-I heterostructures [29, 63], but this kind of structure is also encountered for infrared materials with PbS/CdS [64, 65] and HgSe/CdS [66, 67].

Inverted type-I heterostructures (Figure 1.10b), where the electron and the hole localize in the shell, are mostly studied as models to understand shell growth and carrier localization because the addition of the shell is very easy to follow by optical spectroscopy. Indeed, because of the strong bandgap difference between the core and the shell, a strong red-shift of the optical properties is expected as the shell is added to the core nanocrystal [68].

In type-II configurations (Figure 1.10c), an asymmetry is introduced by choosing a shelling material with a similar bandgap as the core material, but presenting a strong band offset. This way, the electron and the hole localize in different parts of the nanostructure. This configuration is particularly interesting for application where the electron-hole pair needs to be split. Spectrally speaking, the band-edge of the optical absorption is defined by the narrowest bandgap. Since the electron and the hole localize very quickly after absorption, the emission is strongly affected. Emission of light now requires a transition from the shell to the core, which is associated to a low oscillator strength because of the poor spatial overlap of the electron and hole wave-functions. As a result, lifetime of the radiative transition is dramatically extended and can reach several  $\mu\text{s}$ . Examples of this heterostructure include CdTe/CdSe core-shell particles [69], CdS/ZnSe [70] and PbSe/PbS [71, 72].

In quasi-type II heterostructure, the situation is somewhat between type-I and type-II alignments. The two materials have quasi-resonant conduction (or valence) bands and one of the carriers is confined while the other is delocalized over the whole structure. The main example of this structure are CdSe/CdS particles [73].

More complicated shelling schemes have been explored for boosting CQDs emission properties like cascading shells [74, 75], graded shells using quasi-continuous alloys [76, 77], or asymmetric shells to induce strain in the heterostructure [44, 78].

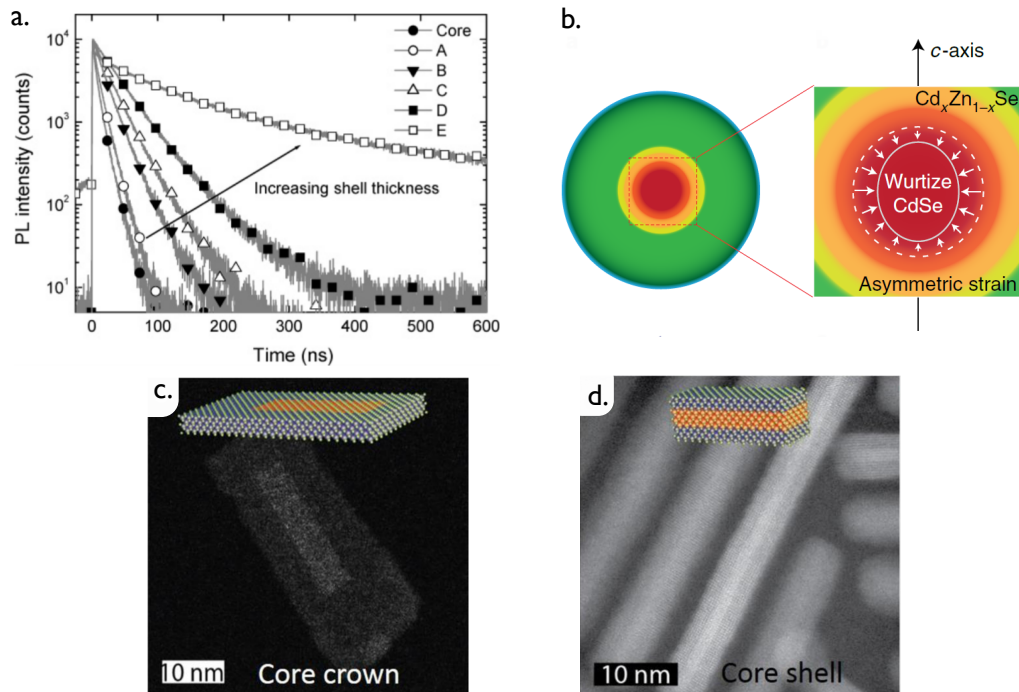


Fig. 1.11 **a.** Effect of type-II band alignment shelling on the radiative lifetime of CdTe/CdSe CQDs, from [79] **b.** An example of a graded, asymmetrical shell for Auger decay suppression, from [78] **c.** TEM picture and scheme of core-crown nanoplatelets, from [39]. **d.** TEM picture and scheme of core-shell nanoplatelets, from [39].

Heterostructures of nanoplatelets have also been developed [39, 80]. Because of their 2D geometry, there are two alternative strategies to build an heterostructure around a nanoplatelet: core-crown structure, where the second material is grown in the lateral direction (see 1.11c); and core-shell structure, where the second material is added in the thickness (*i.e.* in the confined direction, see Figure 1.11d).

## 1.2 Transport in nanocrystal arrays

Previous section introduced a number of important concepts about colloidal nanocrystals and their applications. In this section, we will be interested in the transport properties of an assembly of nanocrystals in densely packed films. Being able to conduct charges in a solid made of independent NCs is the first step towards the creation of devices being able to transduce optical absorption into charge motion. A critical point that will be addressed throughout this section is the notion of *inter-nanocrystal coupling*, and how it is possible to control it using physical chemistry.

### 1.2.1 Hopping transport

We consider an array of nanocrystals randomly distributed on a plane surface. The film is connected to two electrodes, commonly called *source* and *drain* electrodes. A potential difference  $V_{DS}$  is applied to the electrodes (see Figure 1.12a), and we study how the charges (electrons and holes) can be transported inside the nanocrystal film.

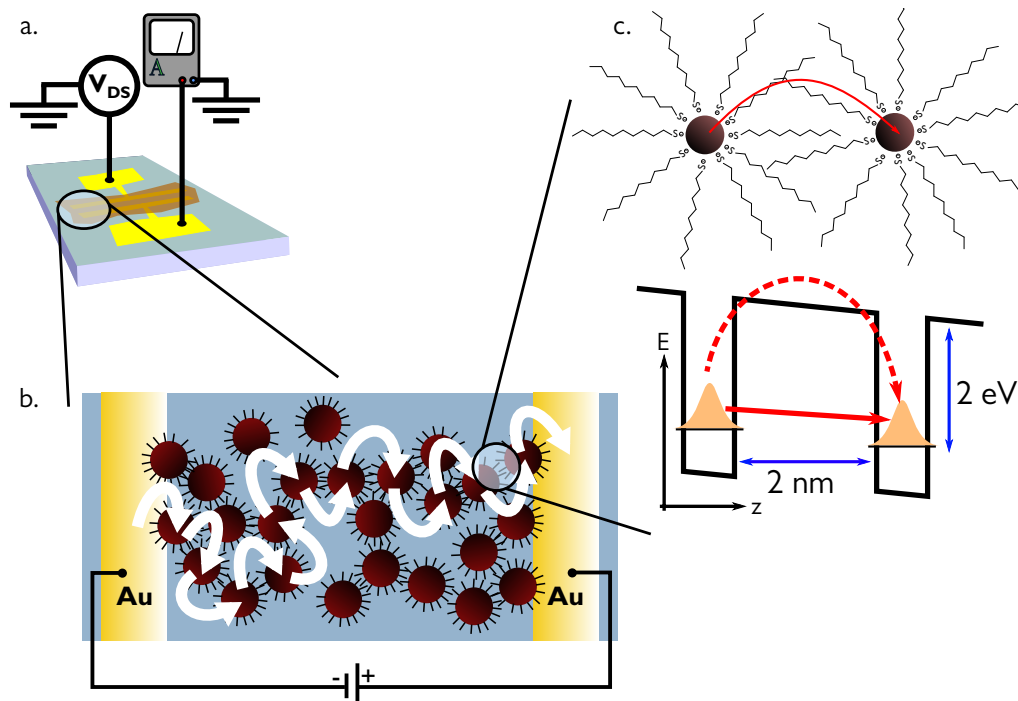


Fig. 1.12 Hopping transport in a nanocrystal film. **a.** Scheme of a nanocrystal film deposited on gold electrodes, connected to a bias source and to a current-meter. **b.** Transport of an electron *via* multiple hopping steps in a nanocrystal film. **c.** Sketch of two neighbor nanocrystals, separated by long organic ligands. The ligands constitute a barrier for a charge to hop from one nanocrystal to the other. The electron can either tunnel through the barrier (plain arrow) or be thermally activated over the barrier (dashed arrow).

Because the nanocrystals are capped with long organic ligands, they are separated from each other by a few nanometers. As a result, they are poorly electrically coupled. In order to be transported from

one electrode to the other, a charge has to follow a percolation path through the film, *hopping* from nanocrystal to nanocrystal (Figure 1.12b). Another vision is to consider the wave-function extension of the ground states of a nanocrystal: the overlap between the wave-functions of two neighbor crystals is weak (see Figure 1.12c), so each hopping step can be either a thermally activated transfer above the barrier, or a tunnel event through the barrier formed by the medium separating two nanocrystals (mostly composed of ligands). This is referred to as *hopping transport*.

### Fundamentals of hopping transport

In hopping transport, the key parameter driving the carriers mobility is the tunnel barrier between two sites (*i.e.* two nanocrystals). The transparency of the barrier can be written as [81]:

$$\mathcal{T} = \exp\left(-2l\sqrt{\frac{2m^*V_B}{\hbar^2}}\right) = \exp(-\beta l) \quad (1.11)$$

Where  $l$  is the barrier length,  $V_B$  the barrier height and  $m^*$  the effective mass of the carrier.  $\beta$  describes the extension of the wave-function in the barrier. Using a diffusive model in three dimensions, we can express the mobility of a carrier using Einstein's equations by:

$$D = \frac{\mu k_B T}{e} = \frac{R^2}{6\tau_{\text{hop}}} \Leftrightarrow \mu = \frac{eR^2}{6\tau_{\text{hop}}k_B T} \quad (1.12)$$

Where  $D$  is the diffusion coefficient associated to charge transport,  $\mu$  is the charge mobility,  $R$  is the nanocrystal size,  $k_B T$  the thermal energy and  $\tau_{\text{hop}}$  is the hopping time. Each hopping step being a tunnel event, the hopping time can be written as a function of the interdot barrier transparency:

$$\tau_{\text{hop}}^{-1} \simeq \frac{2E_a}{\hbar} \mathcal{T} \exp(-E_a/k_B T) \quad (1.13)$$

Where  $E_a$  is the activation energy of the hopping process, depending on the nanocrystal charging energy and on the energetic disorder. It is of the order of 50 meV for semiconductor nanocrystal films [81].

The electronic mobility for one channel can then be expressed as:

$$\mu = \frac{eR^2}{3\hbar k_B T} \exp(-\beta l - E_a/k_B T) \quad (1.14)$$

Transport in films is controlled by the hopping events from one electrode to the other. Depending on the electrodes spacing, there is between 10 (for  $\simeq 100$  nm spaced electrodes) and a few thousands hopping steps (for  $\simeq 10$   $\mu\text{m}$  electrodes). Charge transport is hence a diffusive process, with charges flowing through multiple percolation paths that are susceptible to change with current, temperature and film aging.

### Effect of size dispersion

As our system consists in confined particles, any size dispersion in the nanocrystal population results in a dispersion of particle bandgap at the film level. Hence, bigger particles with narrower-than-average bandgap act as trap states for hopping transport [81]: a carrier arriving in this site will

see a much higher barrier to go toward the next nanocrystal, see Figure 1.13a. As a result, carriers falling in these larger nanocrystals will statistically stay longer than on smaller sized crystals, because their probability of hopping is lower.

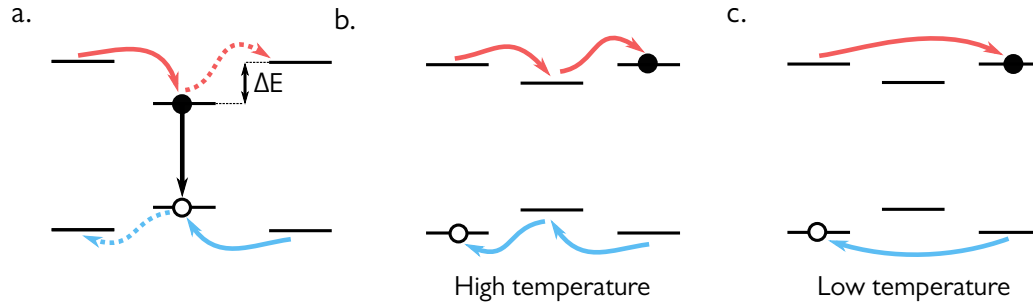


Fig. 1.13 Effect of polydispersity on transport at the film level. **a.** Energy levels of three neighbor nanocrystals. The middle-one acts as a traps state and recombination center for transport, reducing the overall mobility of the film. **b.** Nearest-neighbor hopping transport prevails in a semiconductor nanocrystal film at high temperature. **c.** Variable-range hopping prevails at low temperature because it minimizes the energy losses in the transport process.

There are mostly two channels for hopping transport in disordered films: nearest-neighbor hopping (NNH) and variable-range hopping (VRH). Both channels are always active, but their relative contribution is tuned by temperature and density of states.

In nearest-neighbor hopping, the limiting factor is thermal activation over the barrier length: the carrier will hop to the closest center, even if the transition is not perfectly resonant (Figure 1.13b). This mode of hopping is mostly observed for transport at high temperature, where the thermal activation is sufficient to absorb the cost of non-resonant transitions. This is notably the observed hopping mode at high temperature for arrays of weakly-coupled metal chalcogenide nanocrystals.

Variable-range hopping has been firstly described by Neville Mott [82] and later by Efros and Shklovskii [83]. In this mode, the limiting parameter is the energy difference between the initial and final states (Figure 1.13c). Simply stated, in VRH it is more energetically favorable to hop to a site which is not the nearest, but for which the energy cost is minimal. VRH drives the conductivity in semiconductor nanocrystal films at low-temperature [84].

Hopping transport in nanocrystal films is driven by the inter-particle coupling and strongly impacted by the disorder, both spatial and energetical, of the film. Control of the nanoparticle coupling must be precise, because there is a trade-off between low coupling, where the film mobility is too low to be useful; and high interparticle coupling where the wave-functions are no longer confined inside a nanocrystal. The latter case is also detrimental because the optical properties of the nanocrystals, and of the film, depend on the confinement. The next section will present how we can achieve precise control over the inter-particle barrier length by tuning their surface chemistry.

## 1.2.2 Controlling the tunnel barrier: effect of ligands

As explained above, in order to be transported in a film of nanocrystals, charges have to hop from one nanocrystal to a neighbor. Each hopping step is essentially a tunnel event through the ligands. The tunnel barrier corresponds to the medium between two nanocrystals, that we assume in our case to be constituted only with ligands. The organic ligands capping the nanocrystals will hence define the length and height of the tunnel barrier, as pictured in Figure 1.12c and Figure 1.14.

Because they are synthesized using long organic ligands, as-deposited films of nanocrystals are usually insulating, the mobility of carriers being too low to observe any collective effect at the film scale. The first approach was to perform ligand strip-off procedures [85, 86]. Those procedures were

effective and led to conductive films (*i.e.*, improved film mobility), but had to be performed on thin films in order to effectively strip-off a significant number of long ligands. However, because charges have to go from one nanocrystal to another, the hopping transport is extremely sensitive to the surface of the nanocrystals. Removing the organic ligands at the nanocrystals surface is very effective to ensure a close packing of particles, but affects their surface passivation, which is highly detrimental for transport.

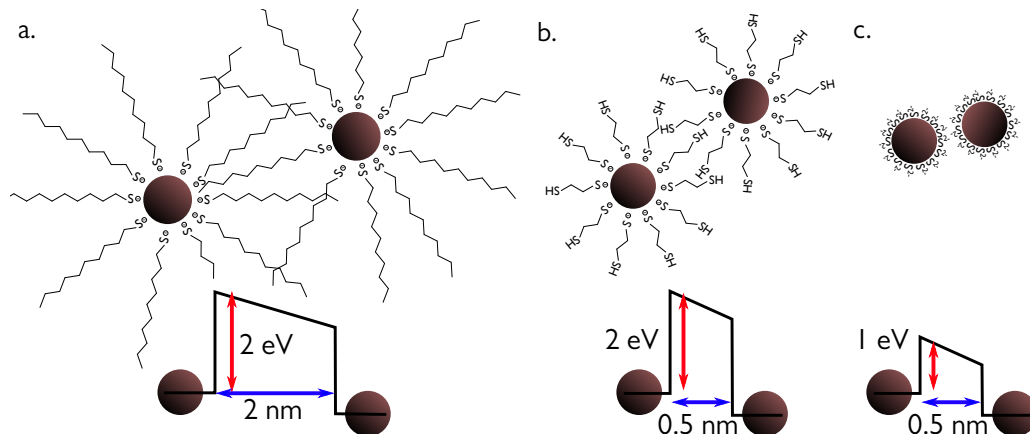


Fig. 1.14 Effect of the capping ligands on interparticle tunneling barrier. **a.** Dodecanthiol-capped nanocrystals: long alkane chains. **b.** Ethanedithiol (EDT)-capped nanocrystals: short alkane chains. **c.** Sulfide-capped nanocrystals: atomic charged ligands with electrostatic repulsion.

Following these attempts, ligand exchange procedures have been developed [87, 88]. The idea is to remove the long organic ligands and replace them by shorter ones, allowing for a better inter-particle coupling while keeping an efficient surface passivation. Examples of short organic ligands include hydrazine [88] and short thiols as ethanedithiol. Figures 1.14a and b illustrate the idea behind ligand exchange: by tuning the length of the alkyl chain from 12 to 2 carbons, here in the case of dodecanthiol (DDT) and ethanedithiol (EDT), the length of the tunnel barrier is decreased from  $\approx 2$  nm to  $\approx 0.5$  nm [89]. This ligand exchange toward shorter organic molecules can be done at the film level, as pictured in Figure 1.15a. A film of the nanocrystals capped with long ligands is dipped in a solution of the new, shorter ligand (typically, 1% in mass in ethanol). In solution, there is an equilibrium between ligands at the surface of the crystals and free, solvated ligands. Because of the high concentration of new ligands, this equilibrium is displaced in favor of new ligand, as pictured in Figure 1.15a. This ligand exchange process is nevertheless limited to thin films (few nanocrystals layers, typically), as the ligands can not diffuse efficiently into thick films. The macroscopic quality of the film is also affected: as the nanocrystals get closer to each other, the volume of the film contracts and cracks are forming [90]. Both these issues are partly solved by repeating the deposition and exchange process several times to fill the developing cracks and build thicker films. The ligand exchange can be followed by infrared spectroscopy (FTIR) by looking at the C-H absorption bands: the efficiency of the process is typically around 80%.

Other proposed approaches proposed by groups of Talapin, Kagan or Sargent was to use small inorganic molecules as  $\text{Sn}_2\text{S}_6^{4-}$  [91, 92], or even small ions [93] as sulfide  $\text{S}^{2-}$ , thiocyanate  $\text{SCN}^-$  [94] or halides  $\text{Cl}^-$ ,  $\text{I}^-$  [95]. In this case, the effect on the tunnel barrier is double: the length of tunnel barrier is reduced thanks to their small size, and the height of the barrier is reduced by  $\approx 1$  eV when compared with aliphatic chains, see Figure 1.14c. Those ions are only stable in polar solvents, which led to the development of liquid-phase transfer ligand exchange processes. This procedure is pictured in Figure 1.15b. The nanocrystals are introduced with their long capping ligands in their apolar solvent (hexane or toluene, typically). The new ligands are introduced in a polar solvent (formamide, typically), and upon agitation the exchange surface between the two phases increases and the ligand exchange process can occur. The ion-capped nanocrystals are then stabilized by the polar solvent: a

Ligand	$l$ (nm)	$\beta$ ( $\text{\AA}^{-1}$ )	Transparency $\mathcal{T}$	Hopping time	Mobility $\mu$ ( $\text{cm}^2\text{V}^{-1}\text{s}^{-1}$ )
DDT	2	0.9-1.2 [89]	$10^{-9}$	10 $\mu\text{s}$	$10^{-8}$
EDT	0.5	0.9-1.2 [89]	$10^{-2}$	10 ps	$10^{-2} - 10^{-1}$
Ions ( $\text{S}^{2-}$ ...)	0.2	0.4-0.6 [93]	$10^{-1}$	1 ps	1

Table 1.2: Orders of magnitude of electronic mobilities for different nanocrystal surface chemistry. Calculated for  $E_a = 25$  meV,  $R = 5$  nm and  $k_B T = E_a$  with equations 1.11, 1.13 and 1.14

phase transfer is observed while the long organic ligands remain in the apolar phase. This process is more efficient than solid-state ligand exchange (the exchange is complete), and allows the preparation of nanocrystal inks that can be directly deposited without any post-processing.

With the development of nanocrystal-based solar cells and devices, surface chemistry engineering of NC have been pushed to remarkably high levels. Advanced surface passivation strategies have been developed to efficiently bind to all coordinating sites of a nanocrystal using hybrid schemes [96–99].

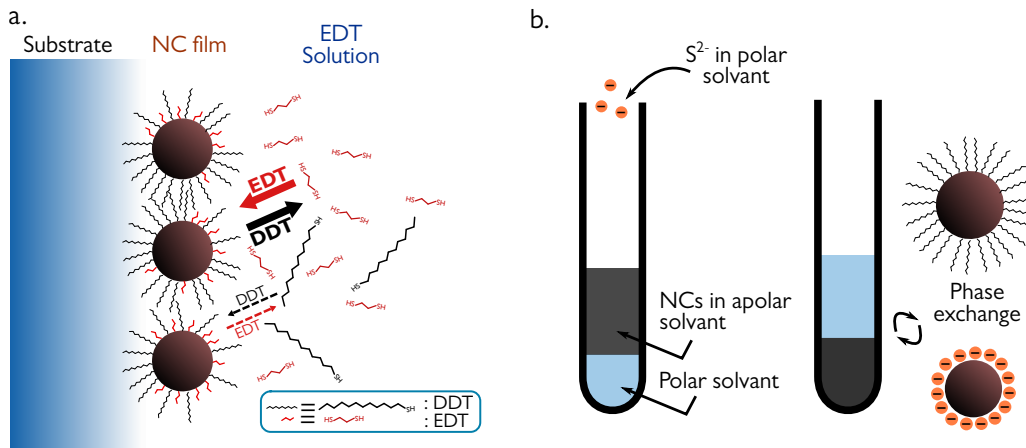


Fig. 1.15 Ligand exchange strategies. **a.** Solid-state ligand exchange (SSLE). Nanocrystals are deposited with their synthesis ligand (here, dodecanthiol, DDT) and exchanged in a solution of the new ligand (here, ethanedithiol, EDT). Arrows indicates transfer of ligands from solution to the film and back. The equilibrium is displaced in favor of the new ligand because of its high concentration in the exchange solution. **b.** Phase-transfer ligand exchange. Nanocrystals in apolar solvent are introduced to ionic ligands in polar solvent. Ion-capped nanocrystals are stabilized by the polar solvent, allowing them to change phase.

Table 1.2 provides orders of magnitude for the expected mobilities of nanocrystal films capped with different ligands, using the equations and parameters defined in the previous section. Mobilities obtained experimentally with solid-state ligand exchange are of the order of  $10^{-4}$  to  $10^{-2}$   $\text{cm}^2\text{V}^{-1}\text{s}^{-1}$  with solid state ligand exchange [89] and can reach 1 to 100  $\text{cm}^2\text{V}^{-1}\text{s}^{-1}$  with ionic ligands. Record mobilities of around 400  $\text{cm}^2\text{V}^{-1}\text{s}^{-1}$  have been reported by the Talapin group using "molecular solders", *i.e.* ligands with the same atomic composition as the nanocrystal film itself ( $[\text{Cd}_2\text{Se}_3]^{2-}$  ligands on CdSe NCs) [100].

### 1.2.3 Field-effect transistors

After the first demonstrations of conductive films of NCs, a tool to change the carrier density at the nanocrystal level was needed to get more insight about the carriers nature and mobility. In a film of nanocrystals under an electric field  $E$ , the current density  $j$  is given by:

$$j = e(n_e\mu_e + p_h\mu_h)E \quad (1.15)$$

Where  $n_e$ ,  $p_h$ ,  $\mu_e$ ,  $\mu_h$  are the electron (resp. hole) densities and mobilities in the film. In the bulk semiconductor community, the carrier densities and mobilities are usually extracted from Hall effect experiments, where a device is exposed to a magnetic field. There is a few reports that exploit Hall effect measurements in nanocrystal films [101, 102], nevertheless the mobilities at play in those devices are fairly low compared to that of bulk semiconductors (usually around  $1 \text{ cm}^2\text{V}^{-1}\text{s}^{-1}$  or below), and this technique remains tricky. As a result, the wide majority of the community prefers using a Field Effect Transistor (FET) geometry to evaluate carrier mobilities in films of coupled nanocrystals.

A FET is an electronic device where the conductance of a channel can be tuned by application of a control signal. A classical FET device is shown in Figure 1.16a. In this device, a film of nanocrystals is deposited between two electrodes, called *source* and *drain* electrodes. This defines a channel: by applying a bias  $V_{DS}$  between source and drain electrodes, a current  $I_{DS}$  flows in the nanocrystal film. The substrate of this device is a doped silicon wafer with a thin layer of insulating silicon dioxide  $\text{SiO}_2$ : it can be seen as a capacitor, as pictured in Figure 1.16b. Upon application of a positive bias  $V_{GS} > 0$  between the gate and the source electrode, electrons are injected in the NC film to screen the positive charges appearing at the surface of the dielectric. Under negative bias  $V_{GS} < 0$ , holes are injected in the film. The evolution of the channel conductance (under constant  $V_{DS}$ ) as a function of the gate voltage (*i.e.* as a function of carrier injection) is called a *transfer curve* and allows to determine the majority carrier in a material. If conduction in a material increases under electron injection (for  $V_{GS} > 0$ ), electrons are the majority carriers and the material is said to be *n-type*. Respectively, conduction under hole injection (for  $V_{GS} < 0$ ) indicates that holes are the majority carriers, and the material is said to be *p-type*. A material with conductivity increasing under both electron and hole injection is called *ambipolar*.

For a channel of length  $L$  and width  $W$  under a bias  $V_{DS}$ , the mobility  $\mu_e$  of the electron (or that of the hole) can be retrieved from the slope of the transfer curve in the region of interest:

$$\mu_e = \frac{1}{C_S V_{DS}} \times \frac{L}{W} \times \left[ \frac{\partial I_{DS}}{\partial V_{GS}} \right]_{V_{DS}=\text{cst}} \quad (1.16)$$

Where is  $C_S$  is the surface capacitance of the gate. For a classical FET device as pictured in Figure 1.16a and b,  $C_S = \epsilon_0\epsilon_r/d$  with  $\epsilon_r$  the dielectric constant of  $\text{SiO}_2$  and  $d$  the gate thickness.

Because of their low gate capacitance ( $10^{-8} \text{ F/cm}^2$  for 400 nm of  $\text{SiO}_2$ ), classical back-gated FETs are not efficient for injecting charges in nanocrystal films. Indeed, assuming a 64% density (random close packing) for a film of spherical 5 nm NCs, the density of particles is around  $n_p = 10^{18} \text{ cm}^{-3}$ . Injection of one electron per nanocrystal requires the application of an electrical field  $E_G = en_p/C_S \simeq 10^8 \text{ Vcm}^{-1}$ , far above the dielectric breakdown of the  $\text{SiO}_2$ . Moreover, the gate effect for this back-gate geometry only occurs in the first 20 to 40 nm of the NC film thickness, making the gating of thick NC films impossible. In practice, back-gated transistor are used as a tool to measure the mobility of thin films of nanocrystals, but applications where the carrier densities need to be strongly tuned are not achievable.

An alternative possibility is to use a top-gated, ion-gel FET geometry [103]. Presented in Figure 1.16c and d, this configuration employs an electrolytic gate made of lithium and perchlorate ions ( $\text{Li}^+$ ,  $\text{ClO}_4^-$ ) embedded in a drop of polyethylene glycol (PEG). Appendix A gives more details about the preparation of such devices. As pictured in Figure 1.16d, under positive gate bias the  $\text{Li}^+$  ions percolate into the film and form an electrostatic layer around the nanocrystals, leading to injection of electrons in the NCs in order to screen the positive charges. The capacity of this gate is orders of magnitude above that of solid-state dielectric gates (around  $10^{-6} \text{ F/cm}^2$ ) allowing to strongly tune the carriers densities and making it a tool of choice to probe transport in NC films [104–106]. By

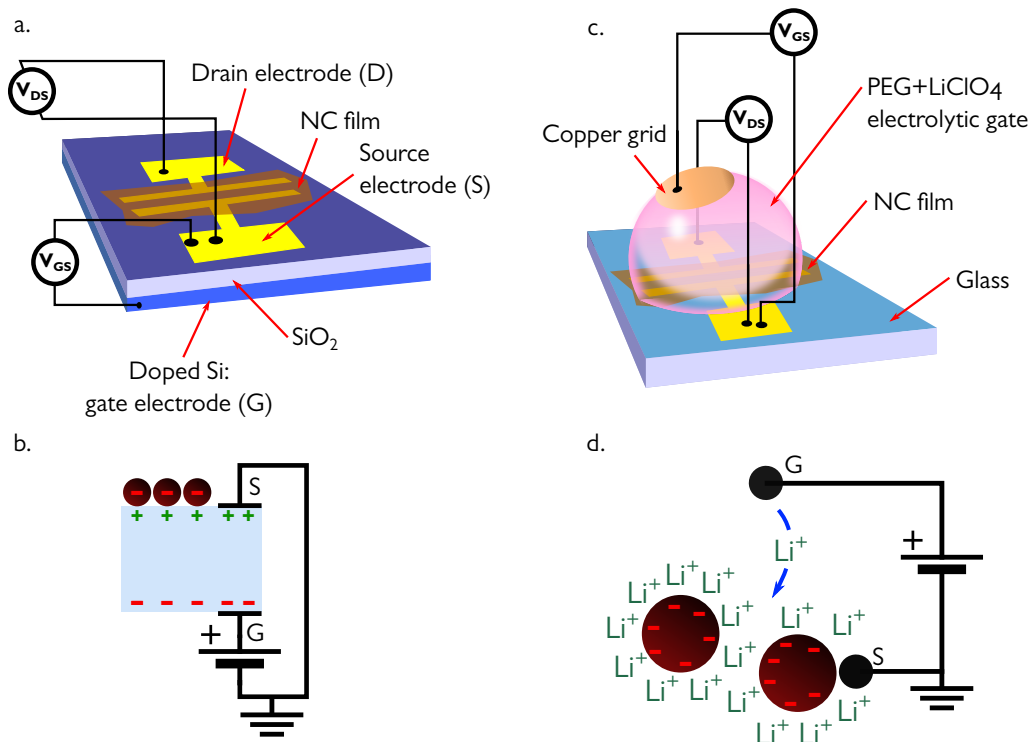


Fig. 1.16 Field effect transistor devices. **a.** Classical solid-state field-effect transistor (FET) in a back-gate configuration with a dielectric SiO<sub>2</sub> gate. **b.** Principle of action: under positive gate voltage, electrons are injected in the film to screen the positive charges in the dielectric. **c.** Ion-gel top-gate FET device with an electrolytic gate. **d.** Principle of action: under positive gate voltage, Li<sup>+</sup> ions percolate in the film and electrons are injected in the nanocrystal to screen their charge.

carefully choosing the molar mass of the matrix polymer, this gate can be made semi-solid, allowing for easy-to-use devices. Moreover, this electrolytic transistor configuration allows to gate thick films, but suffers from a few drawbacks:

- The range of operable gate bias is restricted to the electrolyte electrochemical stability window ( $-3$  to  $3$  V for in our case) to avoid electrochemical reactions within the electrolyte.
- Because the ions must diffuse into the film and because of the high density of the PEG matrix, the scanning steps must stay slow ( $\simeq 1$  mV/s) and the transistor does not work at low temperatures.
- The gate capacitance is not well defined, so the carrier mobility can only be estimated with a large error bar. This drawback could be partly solved by adding a fourth terminal to act as a reference, hence transforming our transistor measurement into an electrochemistry setup.

Examples of transfer curves obtained with this configuration of transistor are given in Figure 1.17. As a part of my project, I studied transport in nanoplatelets of mercury telluride (HgTe NPLs) [56], and found that the nature of their majority carrier can be tuned by the choice of the capping ligand [107]. Figure 1.17b shows the transfer curve of a S<sup>2-</sup>-capped NPL device, with a clear n-type conduction indicating that electrons are the majority carriers. When the ligand is switched to EDT, as pictured in Figure 1.17c, the transfer curve shows p-type conduction, indicating that holes are now the majority carriers. In black are given the *leakage currents*  $I_{GS}$  of the transistors: this is the current that flows from the film to the gate due to non-ideal insulating character of the gate. This current must always stay well below the channel current  $I_{DS}$ .

One can also think of the FET as a tool to move the Fermi level around its rest position in the nanocrystal energy diagram. Under positive gate bias, the relative position of bands and Fermi level

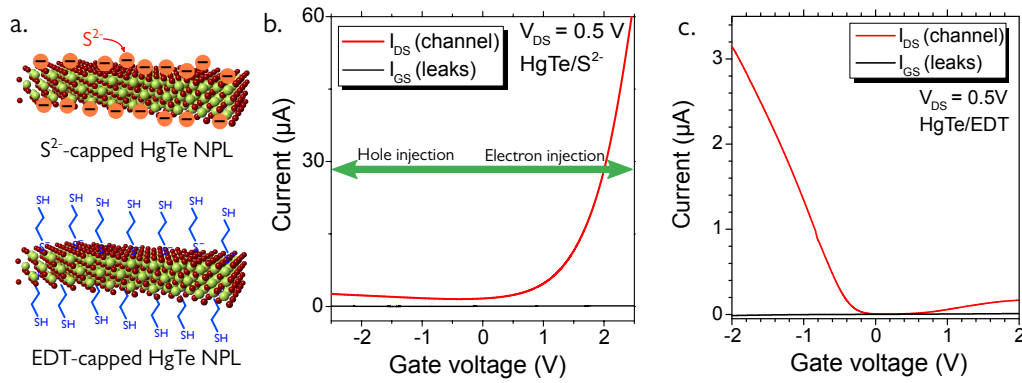


Fig. 1.17 Field-effect transistor: transfer curves on HgTe nanoplatelets films. **a.** HgTe nanoplatelets capped with either sulfide ions ( $S^{2-}$ , top) or ethanedithiol (EDT) ligands (bottom). **b.** FET transfer curve (*i.e.*, channel current as a function of gate voltage) of a film of HgTe NPLs capped with sulfide ions, showing n-type conduction. **c.** FET transfer curve of a film of HgTe NPLs capped with EDT, showing p-type conduction.

are modified and the Fermi level is shifted to higher energies, when under negative gate bias it moves closer to the valence band. As a result, the transfer curve allows to probe the effect of this Fermi level movement on the carrier densities  $n_e$  and  $n_h$ , and informs on the rest position of the Fermi level in the nanocrystal bandgap.

#### 1.2.4 Energy spectrum of nanocrystal arrays

To get an accurate picture of the energy levels in a nanocrystal array, transistor measurements are not sufficient, because they do not offer any quantitative information on the exact Fermi level position. Figure 1.18a shows a typical nanocrystal band diagram with flat levels. The position of the Fermi level in this diagram will set the majority carrier and/or the doping of the nanocrystal, as indicated on the right of the figure. For most nanocrystals, the Fermi level  $E_F$  lies inside the bandgap (grey area). Materials with a Fermi level situated at mid-gap are said to be *intrinsic*. Low electron or hole doping will bring the Fermi level higher in energy (or lower, respectively), making the material n-type or p-type. For degenerate electron doping, the Fermi level lies above the  $1S_c$  level of the conduction band and for very high degenerate doping (more than 20 electrons per dot [108, 109]), the nanocrystals behave as metal nanoparticles. As discussed in the previous section, one can determine the approximate position of the Fermi level through transistor measurements, but other strategies are needed to measure precisely the relative positions of Fermi level inside the band diagram.

Another information of high interest is the work function  $\Phi_{NC}$  of the nanocrystals. The work function is the energy needed to remove an electron from the Fermi level of the nanocrystal and bring it to vacuum, and defines the absolute energy of the nanocrystal bands. This parameter is of utmost importance to build devices, because it will define how the different material bands aligns in an heterojunction. The simple case of a contact between a metal and a n-type NC film is pictured in Figure 1.18b and c. If the work function of the metal  $\Phi_M$  is higher than that of the NCs  $\Phi_{NC}$ , the contact between the two leads to the formation of a Schottky barrier (1.18b). This barrier is highly detrimental for the injection of electrons from the metal to the film because a high bias is required to overcome the barrier. On the contrary, if  $\Phi_M < \Phi_{NC}$ , the metal and the NC film align to form an ohmic contact (1.18c), for which injection of electrons from the metal can be realized at very low bias.

A possible way to get this information is to use electrochemistry [110–112]. Using a 4-electrodes cells, it is possible to measure the position of the bands and of the Fermi level relatively to a reference electrode (typically, a saturated calomel electrode), hence allowing to construct the band diagram in absolute energy scale.

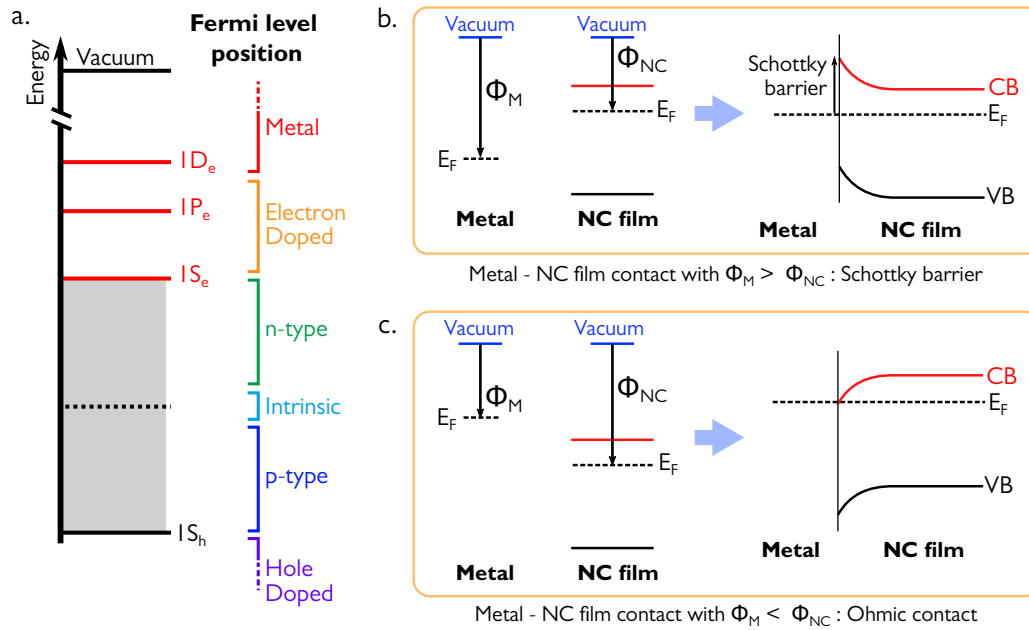


Fig. 1.18 Energy spectrum of a nanocrystal and its consequences for building devices. **a.** Energy levels of a nanocrystal. The position of Fermi level in this spectrum determines the nanocrystal nature and doping. **b.** Scheme of contact alignment between a metal and a n-type NC film, with the work function  $\Phi_M$  larger than that of the nanocrystals  $\Phi_{NC}$ . Left: materials before contact. Right: levels alignment after contact leads to the formation of a Schottky barrier. **c.** Scheme of contact alignment between a metal and a n-type NC film, with the work function  $\Phi_M$  smaller than that of the nanocrystals  $\Phi_{NC}$ . Left: materials before contact. Right: levels alignment after contact leads to the formation of an ohmic contact.

The classical method used to probe the band diagram of semiconductors is X-ray or ultraviolet photoemission (XPS or UPS): this technique is also suitable for films of nanocrystals. In photoemission, a sample kept under ultra-high vacuum is illuminated with high energy photons (from UV to soft X-rays). Due to photoelectric effect, electrons are stripped from the sample and collected into a spectrometer, which discriminates electrons with their kinetic energy (see inset of Figure 1.19a). Due to energy conservation, the binding energy  $BE$  of the electron in the material can be expressed as  $BE = h\nu - KE$  where  $h\nu$  is the photon energy and  $KE$  is the measured kinetic energy. Figure 1.19 presents how XPS performed at Soleil Synchrotron allows us to reconstruct the absolute energy diagram of CdSe/ZnS core-shell nanoplatelets [113]. A typical full-scale photoemission spectrum consists in three parts:

- At low kinetic energy (*i.e.* high binding energy), we observe the secondary electrons, which experienced a lot of collisions and exit the material with a very low energy. This is what is presented in Figure 1.19a for CdSe/ZnS NPLs. The cut-off of this graph corresponds to the energy which is necessary to bring those low-energy electrons into vacuum: this is the definition of the work function  $\Phi_{NC}$ .
- For intermediary energies, electrons are coming from the core levels of the materials, *i.e.* levels deep in the valence band of the nanocrystals. They are useful for determination of the material composition and oxidation states.
- At high kinetic energies (*i.e.* low binding energies), electrons are coming from the valence band of the nanocrystals. Figure 1.19b presents this kind of spectrum for CdSe/ZnS NPL. The "zero" of binding energies corresponds to electrons stripped from the Fermi level, so the cut-off of the signal (where electrons from the top of the valence band start to be extracted) corresponds to the energy difference  $VB - E_F$ .

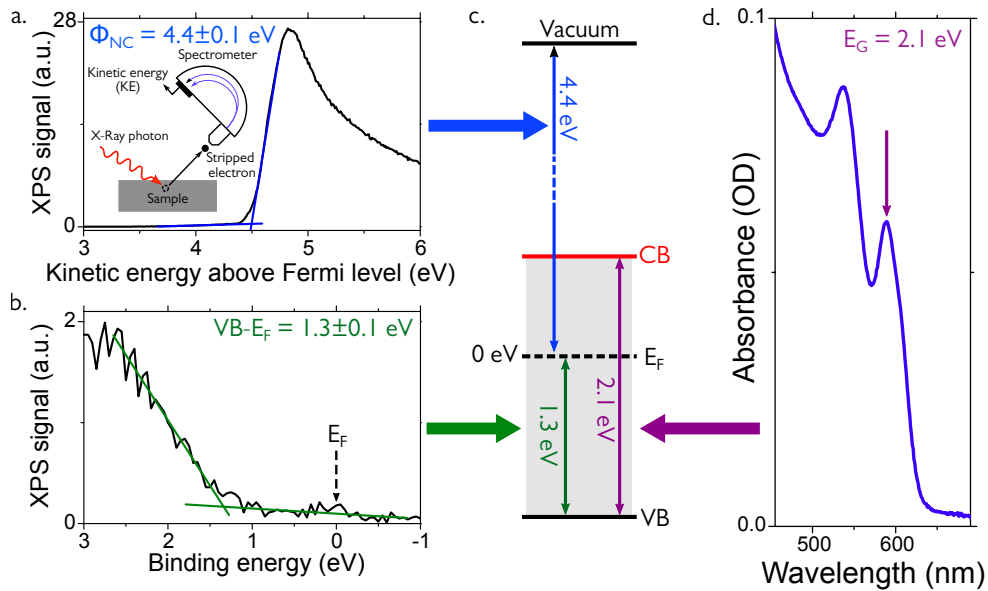


Fig. 1.19 Reconstruction of a nanocrystal energy spectrum in absolute energy scale: an example with CdSe/ZnS core-shell nanoplatelets **a**. Photoemission spectrum centered at low kinetic energies of a film of CdSe/ZnS NPLs. Pictured here is the cut-off of the secondary electrons, allowing the determination of the NPLs work function  $\Phi_{NC}$  (blue lines). Inset: principle of photoemission spectroscopy. **b**. Photoemission spectrum centered at high kinetic energies to collect electrons coming from the valence band of the nanocrystals. The energy difference between the top of the valence band and the Fermi level  $VB - E_F$  can be extracted (green lines). **c**. Reconstructed energy spectrum for CdSe/ZnS NPLs in absolute energy scale using information from panels a, b, and d. **d**. Optical spectrum of a film of CdSe/ZnS NPL. Optical bandgap  $E_G$  is extracted at the energy of the first exciton (purple arrow).

Photoemission allows the extraction of  $\Phi_{NC}$  and the energy difference  $VB - E_F$ , so by setting the Fermi level to  $E_F = 0$  eV, valence band position  $E_{VB}$  and vacuum level  $E_{vac}$  can be located in absolute energy, see Figure 1.19c. Photoemission can only observe filled states, so a complimentary method must be used to determine the energy of conduction band. We use optical spectroscopy: the optical bandgap of the nanocrystals is extracted from an absorption spectrum, see Figure 1.19d, and the electrical bandgap is obtained by renormalizing the optical gap by the Coulomb interaction using equation 1.9:  $E_G^{el} = E_G^{op} + E_C$ .  $E_C$  is of the order of 10 meV for small nanocrystals. Position of the conduction band in the energy spectrum is then obtained using  $E_{CB} = E_{VB} + E_G^{el}$ , and the diagram is complete.

### 1.2.5 Principles of photodetection

In a film of nanocrystals, or in a semiconductor in general, the transitions between the different energy levels of a nanocrystal impact the carrier densities in those energy levels. Those difference of carrier densities can be exploited to build *photodetectors*, that transduce optical absorption into electrical signals (current or voltage). There are two main types of photodetectors: *photoconductors* and *photodiodes*.

#### Photoresponse of a photoconductor

In a nanocrystal photoconductor, a film of nanocrystals is connected to two contacts and biased by a voltage source, as pictured in Figure 1.20a. Upon illumination, photons are absorbed by the NC

film, creating electrons and holes that get transported toward the two electrodes (Figure 1.20b), thus increasing the current flowing in the detector [114].

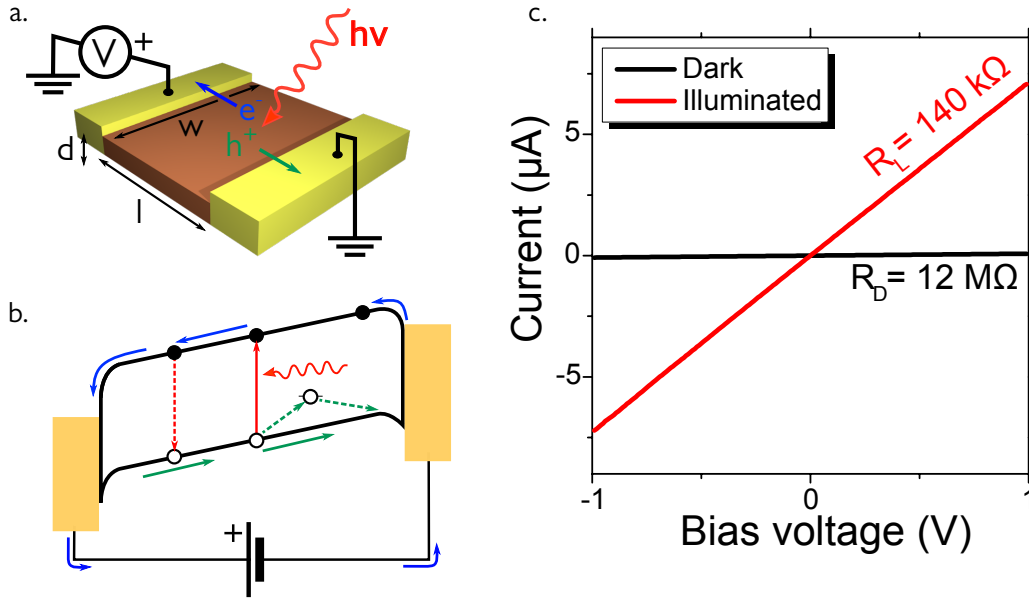


Fig. 1.20 A photoconductive device made from nanocrystals. **a.** Scheme of a photoconductive device consisting in a NC film (brown) connected to two metal contacts (gold). Illumination is provided from the top, and a bias is applied on the film to extract the photogenerated carriers. **b.** Simplified band diagram of a photoconductive device under bias. Gain effect is shown: electrons are allowed to circulate as long as the hole is trapped. **c.** Current-voltage characteristics of a photoconductive device made of HgTe nanoplatelets [107], showing ohmic behavior. The conductance of the device is greatly increased under illumination by 808 nm light.

We consider a film of dimensions  $w \times l \times d$  illuminated from the top with a photon flux  $\phi_0$ , along the  $z$  axis (Figure 1.20). Assuming an absorption coefficient  $\alpha$  for the film, the photon flux in the NC film is:

$$\phi(z) = \phi_0 e^{-\alpha z} \quad (1.17)$$

Absorbed photons generate electron-hole pairs: if  $n_l$ ,  $n_d$  and  $p_l$  and  $p_d$  are the densities of electrons and holes under illumination and in the dark, we have:

$$\Delta n_{\text{photo}} = n_l - n_d \quad \text{and} \quad \Delta p_{\text{photo}} = p_l - p_d \quad (1.18)$$

The generation rate of those electron-hole pairs per unit of volume is given by:

$$G_{\text{ex}}(z) = \alpha \phi_0 e^{-\alpha z} \quad (1.19)$$

For a p-type NC film, we have  $p_0 \gg n_0$  and we can assume that only  $\Delta n$  (*i.e.*, the electrons) will contribute significantly to the photocurrent. Hence, assuming a lifetime  $\tau_n$  for the electron, the rate equation associated with photo-carrier generation and recombination is:

$$\frac{\Delta n(z)}{\tau_n} - D_n \frac{d^2}{dz^2} \Delta n = \alpha \phi_0 e^{-\alpha z} \quad (1.20)$$

Assuming that diffusion along the  $z$  axis is negligible (thin device), and integrating the previous equation over the thickness  $d$  of the device, we get:

$$\Delta n = \frac{\phi_0 \tau_n}{d} (1 - e^{-\alpha d}) \quad (1.21)$$

The internal quantum yield  $\eta_i = (1 - e^{-\alpha d})$  expresses how many photons are converted into electrons in the device. The external quantum efficiency  $\eta = (1 - R)(1 - e^{-\alpha d})$  includes the reflectance  $R$  of the device. The electron density is then:

$$\Delta n = \frac{\phi_0 \tau_n}{d} \eta \quad (1.22)$$

We apply an electric field perpendicularly to the  $z$  axis, like pictured in Figure 1.20a. The photocurrent is then given by:

$$I_{\text{photo}} = j_{\text{photo}} \times w \times d = \Delta n e \mu_e E \times w d = (\phi_0 \tau_n \eta) \times (e \mu_e E) \times w \quad (1.23)$$

The *responsivity*  $\mathcal{R}$  is defined by the ratio of the photocurrent to the incident power illuminating the device on the area  $w \times l$ , and expressed in A/W:

$$\mathcal{R} = \frac{I_{\text{photo}}}{P_{\text{opt}}} = \frac{e \mu_e \tau_n \eta E}{h\nu \times l} = \frac{g \eta e}{h\nu} \quad (1.24)$$

Where  $g$  is the *photoconduction gain*:

$$g = \frac{\tau_n \mu_e E}{l} = \frac{\tau_n}{\tau_{\text{transit}}} \quad (1.25)$$

We can understand the transit time  $\tau_{\text{transit}}$  as the time taken by an electron to cross the channel from one electrode to another. If its lifetime  $\tau_n$  is longer than the transit time, the photoconductive gain takes values above unity: one electron can loop around the polarization circuit several times before recombination, hence contributing multiple times to the photocurrent. The common picture is that one of the carriers get trapped, allowing circulation of the other one to long as its counterpart is not available for recombination [5]. High gain values come at the price of a slow time response, since the recombination time  $\tau_n$  is large: this is the gain/bandwidth trade-off. Another way to observe gain is to use devices where the transit time is short due to a narrow channel, as in nanoscale devices featuring electrodes spaced by a few tens of nanometers [115, 116].

Figure 1.20c presents  $I(V)$  characteristics of a photoconductive film of HgTe nanoplatelets in the dark and under illumination by a 808 nm laser [107]. The device shows an ohmic behavior (*i.e.*, linear I-V characteristics) and its conductance is strongly increased under illumination, as  $n_l \gg n_d$ . The main issue with photoconductors is that they have to be operated under non-zero bias and always feature *dark current* (*i.e.* current flowing in the detector when it is not illuminated), which can contribute to a significant part of the total device current, especially in narrow-bandgap materials absorbing in the infrared range.

## Photoresponse of a photodiode

A photodiode, or photovoltaic detector, relies on an heterojunction to absorb photons and separate the photogenerated charges. The working principle is exactly the same as a solar cell, but photodiodes are optimized for *detection* rather than power generation. In a photodetector, an asymmetry is introduced in the device, allowing to strongly suppress the dark current in the structure. A scheme of a simple heterojunction device is shown in Figure 1.21a. When a p-doped and a n-doped semiconductors are brought together to form an heterojunction, a depletion region (or space-charge region, SCR) forms at the interface of the two materials. Electron-hole pairs created in this region are immediately separated due to the high built-in electric field, and pairs created outside of the depletion region can still be separated if they diffuse to the SCR [114]. As pictured in Figure 1.21b, generated carriers are collected at the top and bottom contacts, hence creating a current in the device. This kind of devices are built layer-by-layer, and one of the metallic contact should be transparent to allow illumination of the heterojunction. This is usually realized by using doped oxides as tin-doped indium oxide (ITO) or fluorine-doped tin oxide (FTO). An example of an actual NC-based device is presented in Figure 1.21c: the heterojunction is realized using two films of PbS nanocrystals treated by different ligands, leading to n-type and p-type films [117]. In addition, this device incorporates TiO<sub>2</sub> and MoO<sub>3</sub> layers to act as electron transport layer (ETL) and hole blocking layer (HBL) on the TiO<sub>2</sub> side, and hole transport layer (HTL) / electron blocking layer (EBL) on the MoO<sub>3</sub> side.

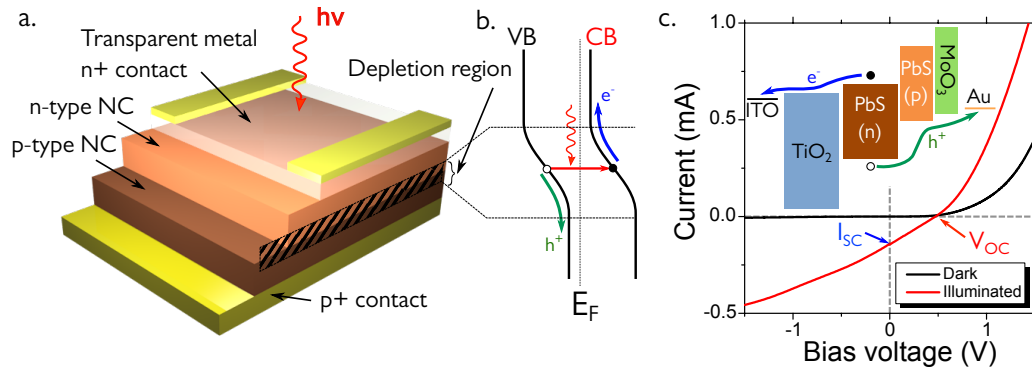


Fig. 1.21 A photovoltaic device from nanocrystals. **a.** Scheme of a simple photovoltaic device based on an heterojunction between p-type and n-type NC films. The depletion region is shown in stripes. **b.** Energy diagram of the heterojunction of the device shown in (a). Photocarriers generated in this region are transported toward top contact (electrons) and bottom contacts (holes) thanks to the built-in electric field. **c.** Current-voltage characteristics of a photovoltaic device made of PbS nanocrystals. The structure of the device is ITO/TiO<sub>2</sub>/n-type PbS NCs/p-type PbS NCs/MoO<sub>3</sub>/Au as shown in the band diagram inset. The  $I(V)$  curve shows rectifying behavior. Short-circuit current  $I_{SC}$  and open-circuit voltage  $V_{OC}$  under illumination have been highlighted.

As shown in the current-voltage  $I(V)$  characteristics shown in Figure 1.21, a photovoltaic device shows rectifying behavior: the  $I(V)$  curve is strongly asymmetric. This results from the strong asymmetry of the band alignment: injection of electrons from ITO side is easy since  $\Phi_{ITO} < \Phi_{Au}$ , allowing the carriers to flow easily under positive bias. Under negative bias though, injection of electrons from the gold side and of hole from the ITO side is prevented by the large barriers, resulting in a very low dark current. As a result, thanks to this strong asymmetry, photodiodes can be operated at zero bias (photocurrent mode where the signal is given by the short-circuit current  $I_{SC}$ ) or zero current (photovoltage mode where the signal is the open-circuit voltage  $V_{OC}$ ).

The total current density in the diode under illumination is given by [114] :

$$J = J_{\text{sat}} \left( e^{qV/k_B T} - 1 \right) - J_{\text{photo}} \quad (1.26)$$

Where  $V$  is the applied bias and  $J_{\text{sat}}$  is the saturation current, depending on the materials used and band alignment in the diode structure. The photocurrent density  $J_{\text{photo}}$  is:

$$J_{\text{photo}} = -e\eta\phi_0 \quad (1.27)$$

Where  $\phi_0$  is the illumination flux and  $\eta = (1 - R) \left( \frac{1 - e^{-\alpha d}}{1 + \alpha L_D} \right)$  is the external quantum efficiency of the device.  $d$  is the thickness of the SCR and  $L_D$  is the diffusion length of the photogenerated carriers created outside of the SCR. The main difference with photoconductors is that there is no gain effect in a photodiode.

In zero bias operation (photocurrent mode), the short-circuit current  $I_{SC}$  is  $I_{SC} = A \times J_{\text{photo}}$  with  $A$  the detector surface area.

In zero current operation (photovoltage mode), the open-circuit voltage  $V_{OC}$  is:

$$V_{OC} = \frac{k_B T}{e} \log \left( 1 + \frac{J_{\text{photo}}}{J_{\text{sat}}} \right) \quad (1.28)$$

Finally, the responsivity of a photodiode with a surface  $A$  is given by:

$$\mathcal{R} = \frac{J_{\text{photo}} A}{P_{\text{opt}}} = \frac{\eta q}{h\nu} \quad (1.29)$$

Since here electrical and illuminated sections are the same: carrier and photon fluxes are parallel.

## Noise and detectivity

The responsivity of a photodetector describes its ability to transduce incoming photons into an electrical current, but does not take into account the *noise* of the detector. In the infrared range, because photon (and bandgap) energies become small, thermal activation of carriers is competing with optical excitation of the material. As a result, infrared detectors present much more *noise* than their visible counterparts. This is the main reason why those infrared detectors are generally operated at cryogenic temperatures. The ultimate figure of merit for a photodetector is its *signal to noise* ratio, usually expressed as the detectivity  $D^*$ . The noise in a photodetector is intrinsically linked to its dark current. The signal to noise ratio indicates how well a photodetector is able to discriminate a current generated by incoming photons (signal) from the dark current.

In a perfect detector, noise have two main sources [114]:

- Thermal noise (also called Johnson noise) is related to the mobility fluctuation of carriers due to thermal agitation. For a semiconductor of resistance  $R_0$  operating in the electrical bandwidth  $\Delta\nu$  (i.e. with an integration time of  $1/(2\Delta\nu)$ ) at the temperature  $T$ , the thermal noise is given by:

$$i_{\text{Johnson}}^2 = \frac{4k_B T}{R_0} \Delta\nu \quad (1.30)$$

- Generation-recombination noise (G-R noise) is due to the carrier density fluctuations due to spontaneous creation and annihilation of electron-hole pairs in the semiconductor. For a photoconductor operated in the electrical bandwidth  $\Delta\nu$ , this noise depends on the average dark current  $I_{\text{dark}}$  and on the gain of the detector  $g$  through:

$$i_{\text{GR}}^2 = 4eI_{\text{dark}}\Delta\nu \quad (1.31)$$

For our nanocrystal-based devices, those two analytical formulas for noise only provide a idea of the best possible device. Indeed, noise is never thermal or generation-recombination-limited in NC-based devices, and always has to be experimentally measured. This is due to the presence of a low-frequency  $1/f$  noise, attributed to the disordered aspect of the conductive matrix [118–120]. Figure 1.22a presents an experimental setup used to measure the current spectral density  $S_I$  on an NC-based device kept at low temperature. The noise spectral density can then be obtained as  $S_n = S_I^2$ . Figure 1.22b shows the results of this measurement on a HgSe/HgTe NC device (see chapter 4), with a  $1/f^{0.5}$ -limited current spectral density. The noise values measured for this device are well above the calculated thermal noise, indicating that the noise is indeed  $1/f$  limited. The thermal activation of the noise seen in this example reflects the thermal activation of the dark current, and is the reason why certain detectors have to be operated at cryogenic temperatures to ensure a good signal-to-noise ratio.

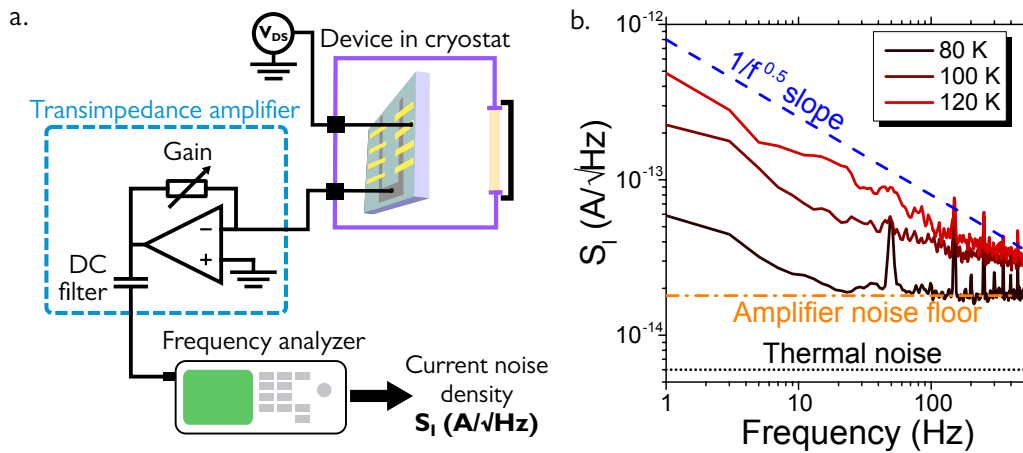


Fig. 1.22 Noise in nanocrystal-based devices **a.** Scheme of a temperature-resolved noise measurement on a NC-based device. The device is enclosed in a cryostat, in the dark and under bias. The current from the device is acquired using a transimpedance amplifier (a Femto DLPCA-200 amplifier, typically) and the output is fed into a frequency analyser. The measured quantity is the current spectral density  $S_I$  in  $\text{A}/\sqrt{\text{Hz}}$ . **b.** Current spectral density  $S_I$  for a NC-based device (HgSe/HgTe, see chapter 3) at low temperature. In black dots is shown the calculated device thermal noise at 80 K.

A good figure of merit expressing a signal to noise ratio for a photodetector is the *Net Equivalent Power* or NEP: it corresponds to the lowest optical power that is possible to measure with the device. It is given by:

$$\text{NEP} = \frac{S_I \times \sqrt{\Delta\nu}}{\mathcal{R}} \quad (1.32)$$

Where  $S_I$  is the measured noise current density,  $\Delta\nu$  is measurement bandwidth (*i.e.* the integration time  $1/2\Delta\nu$ ) and  $\mathcal{R}$  is the device responsivity. The NEP is expressed in W, and the lowest the NEP, the better the detector.

The detectivity  $D^*$  is the ultimate figure of merit for a photodetector. It is obtained by:

$$D^* = \frac{\sqrt{A\Delta\nu}}{\text{NEP}} = \frac{\mathcal{R}\sqrt{A}}{S_I} \quad (1.33)$$

Where  $A$  is the device area. The detectivity is expressed in  $\text{cm}\cdot\text{Hz}^{1/2}\cdot\text{W}^{-1}$ , or Jones.

## 1.3 Addressing infrared with nanocrystals

### 1.3.1 The infrared range: interest and applications

The infrared range of wavelength is historically associated with military applications. Indeed, armies have identified since the beginning of the XX<sup>th</sup> century that mastering light emission and imaging in various ranges of the infrared brings a serious strategic advantage over an enemy that does not possess this kind of technology. This is mainly due to the fact that infrared light is invisible to the naked eye.

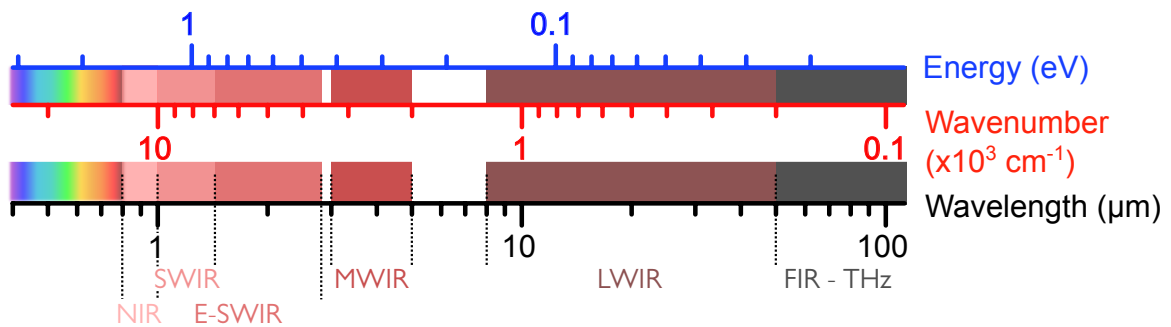


Fig. 1.23 The subdivisions of the infrared range. Top axis and middle axis give the associated photon energy (in eV) and wavenumber (in  $\text{cm}^{-1}$ ).

The infrared range extends from 800 nm to 100  $\mu\text{m}$  and Figure 1.23 presents the different regions of interest. There are several ways of dividing the infrared range in regions, we present here on that is commonly used by academics and industry because it is based on sensor response. Starting from the red part of the visible range:

- The **Near-Infrared (NIR)** spans from 800 nm to 1  $\mu\text{m}$ . Because of its proximity to visible range, NIR is relatively accessible and offers plenty of applications. It is the range of choice for solar-cell materials thanks to the possibility to harvest the whole visible spectrum of the sun, plus a significant part of its infrared spectrum. The existence of relatively cheap and powerful lasers in the NIR (AlGaAs around 808 nm, Nd:YAG at 1.064  $\mu\text{m}$ ) makes it very useful for range-finding and laser guidance, in combination with a well suited detector. This range of wavelength is also of strong interest for biology, as tissues are transparent to wavelengths around 900 nm.
- The **Short-Wave Infrared (SWIR)** extends from 1  $\mu\text{m}$  to 1.7  $\mu\text{m}$ . In this region, objects and bodies are, just like in the visible range, secondary sources: they reflect and diffuse light. Imaging in this range is performed using illumination by a powerful source (LEDs or lasers), and sometimes referred to as *active imaging*. Atmospheric transparency over the whole SWIR range and high performance of sources and detectors in this region allow long-range imaging, at nighttime and in adverse meteorologic conditions. Telecommunication wavelengths also fall in SWIR, as the lowest attenuation in glass-based telecom optical fibers is achieved around 1.5  $\mu\text{m}$ . Extended SWIR, sometimes denoted E-SWIR, extends up to 2.7  $\mu\text{m}$ .
- The **Mid-Wave Infrared (MWIR)** spans from 3  $\mu\text{m}$  to 5  $\mu\text{m}$ . As seen in Figure 1.24a, this corresponds to an atmospheric transparency window. Around 3  $\mu\text{m}$ , the black body emission of objects starts to prevail over the reflection of secondary sources. Black body emission for an object at the temperature  $T$  is given by:

$$L(\lambda, T) = \frac{2hc^2}{\lambda^5} \frac{1}{e^{hc/(\lambda k_B T)} - 1} \quad (1.34)$$

Where  $L(\lambda, T)$  is the spectral radiance in  $\text{W}\cdot\text{m}^{-3}\cdot\text{sr}^{-1}$ ,  $c$  is the speed of light and  $\lambda$  is the wavelength. Relative black body emission is shown in Figure 1.24b. As a result, the MWIR range allows *thermal imaging*, or passive imaging of the photons emitted by *hot* (*i.e.* above  $0^\circ\text{C}$ ) objects and bodies. As it does not require an external source, imaging in the MWIR is perfectly stealthy. As shown in Figure 1.24b, the MWIR is more suited to image hot ( $>100^\circ\text{C}$ ) objects than room-temperature ones. As a result, MWIR detectors are perfect for missile and airplane-seeking in military applications. The MWIR range is also widely used for gas sensing and spectroscopy, since there is large number of molecules with absorption in this range of wavelength ( $\text{CO}_2$  at  $2349\text{ cm}^{-1}$ ,  $\text{C}-\text{H}$  at  $2900\text{ cm}^{-1}$ ).

- The **Long-Wave Infrared (LWIR)** corresponds to wavelengths between  $8\text{ }\mu\text{m}$  and  $12\text{ }\mu\text{m}$ . As pictured in Figure 1.24, the maximum of emission of a  $300\text{ K}$  body is around  $10\text{ }\mu\text{m}$ , in the middle of LWIR range. LWIR is the preferential domain to conduct thermal imaging of room-temperature objects.
- The **Far-Infrared (FIR)** extends between  $12\text{ }\mu\text{m}$  and  $100\text{ }\mu\text{m}$ . Since cold objects emit in the FIR, this range is of interest for astronomy. FIR overlaps with the THz range, and can be used for surveillance since it penetrates much deeper than other wavelengths without any ionizing hazard.

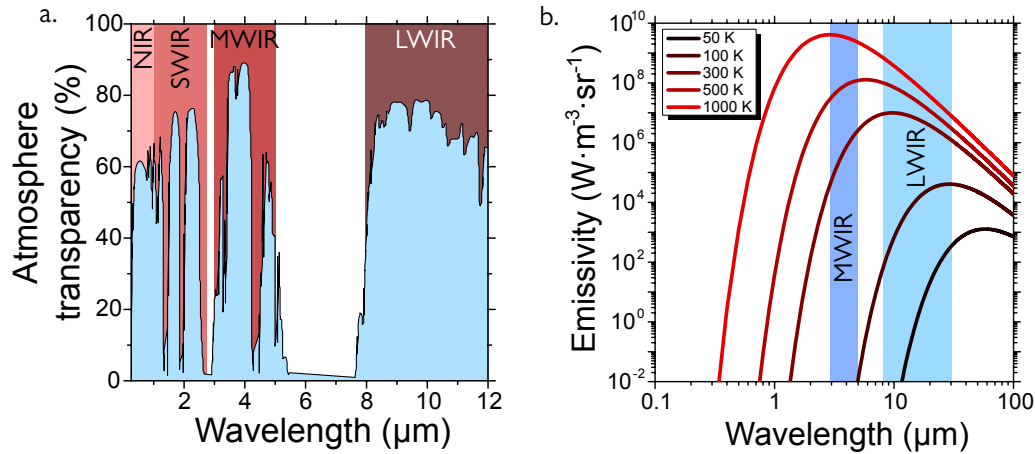


Fig. 1.24 Infrared for thermal imaging. **a.** Atmosphere transparency between  $0.2$  and  $12\text{ }\mu\text{m}$ . NIR, SWIR, MWIR and LWIR ranges have been reported on the graph. **b.** Black-body spectral radiance for cold, room-temperature and hot objects.

### 1.3.2 Infrared detectors

The division of the infrared range proposed in the precedent section was based on different detector response. We will present here the current technologies and materials used to detect infrared light. Figure 1.25 presents the most widespread technologies. It is important to distinguish between the two different types of detectors used in the infrared: photodetectors and thermal detectors [121, 122].

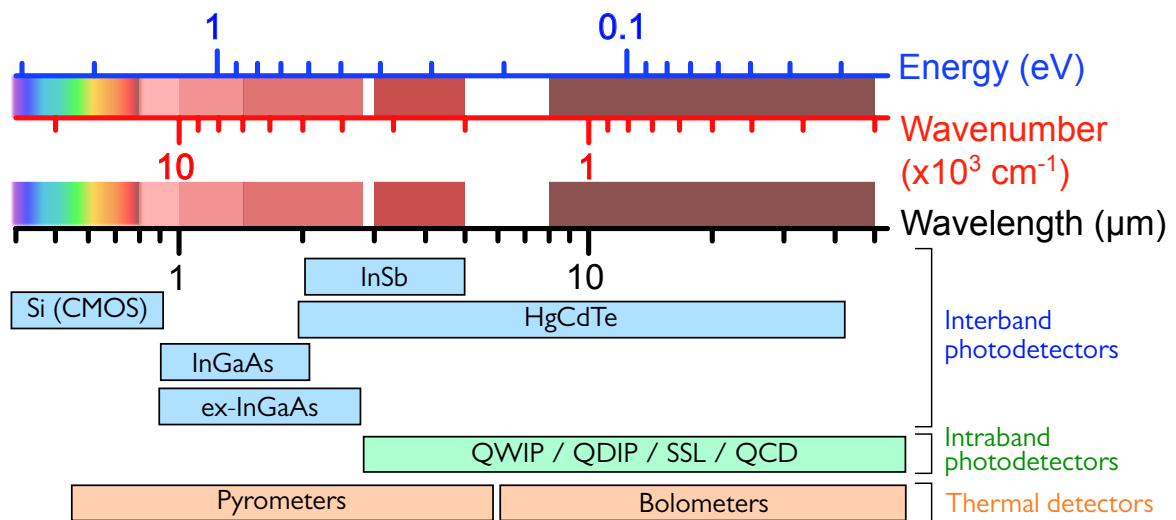


Fig. 1.25 Overview of the different technologies of detectors in the infrared range from 0.7  $\mu\text{m}$  to 14  $\mu\text{m}$ . ex-InGaAs: extended InGaAs. QWIP: Quantum Well Infrared Photodetector. QDIP: Quantum Dot Infrared Photodetector. SSL: Strained Superlattices. QCD: Quantum Cascade Detector.

## Infrared photodetectors

Photodetectors, sometimes called *quantum detectors*, are based on transitions between bands or levels in semiconductor materials (see section 1.2.5). Upon photon absorption in the active material, an electron-hole pair is created. The electron, the hole, or both of the carriers, are then transported in the material due to an electric field (applied or built-in), hence creating a *photo-current*. Because the energies associated with infrared photons are low, the involved transitions have to be of low energy. In MWIR, the optical transitions start to be competing with the thermal energy  $k_B T$ : a significant number of electron-hole pairs can be created due to thermal activation. As a result, MWIR and LWIR detectors have to be cooled down to increase their signal-to noise ratio. Their operating temperature is usually around 150 K for MWIR detectors and 77 to 90 K for LWIR detectors. Photodetectors are sensitive to a photon flux  $\phi_0$ .

**Interband photodetectors** are based on materials featuring transitions between a valence band and a conduction band. Figure 1.26a shows a simple sketch of a typical interband photoconductor made of Mercury Cadmium Telluride (MCT). Low energy interband transitions can be achieved either by using a narrow bandgap semiconductor (Ge in SWIR, InSb in MWIR) or by alloying two semiconductors of similar lattice parameters ( $\text{In}_{1-x}\text{Ga}_x\text{As}$  in the NIR to SWIR, or  $\text{Hg}_{1-x}\text{Cd}_x\text{Te}$  in the MWIR to LWIR).

In the NIR, silicon-based CMOS detectors are sensitive up to  $\simeq 1 \mu\text{m}$ , allowing for cheap, high performance imaging in this range. In particular, any CMOS-based camera (DSLR, smartphone...) is able to see in the near-infrared once its low-pass filter is removed. They can be used for active imaging, in combination to a powerful NIR light source.

In the SWIR, the main technology is based on InGaAs ternary alloy. InGaAs detectors achieve very high performances, with detectivities  $> 10^{12}$  Jones at room temperature, very low dark currents and ps time response. Epitaxially grown on InP substrate, the active layer has to be hybridized to a Read-Out Integrated Circuit (ROIC) using indium beads. The presence of the InP substrate limits their operation to 900 nm for the high energy cutoff, and the band-gap of the material limits the lower energy cut-off to 1.7  $\mu\text{m}$ . Extended-InGaAs can reach up to 2.7  $\mu\text{m}$  using strained material. Because of the complex material processing and multiple micro-fabrication steps, they remain expensive detectors, especially for large Focal Plane Arrays (FPA). Other examples of less-sensitive detectors are PbS, PbSe

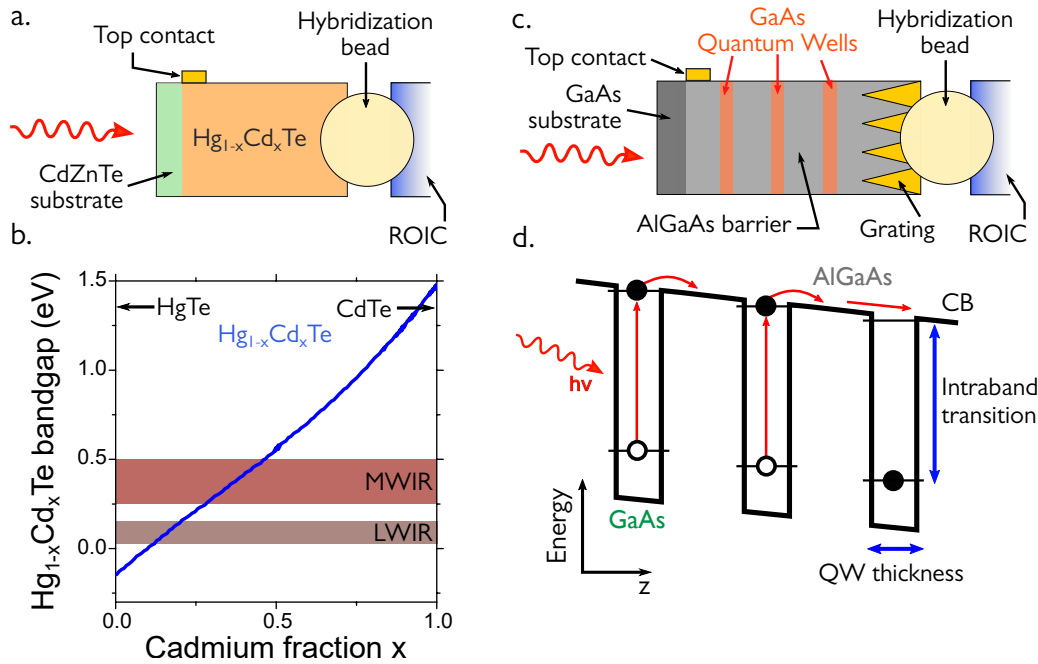


Fig. 1.26 Exploiting interband and intraband transitions for infrared photodetectors. **a.** Simple scheme of a Mercury Cadmium Telluride ( $\text{HgCdTe}$ , MCT) interband photoconductor. The interband MCT active material is grown on CdZnS substrate and hybridized on a Read-Out Integrated Circuit (ROIC) using an indium bead. **b.** Interband bandgap of  $\text{Hg}_{1-x}\text{Cd}_x\text{Te}$  (MCT) for different cadmium fractions. MWIR and LWIR bands have been highlighted. **c.** Simple scheme of a Quantum-Well Infrared Photodetector (QWIP) made of doped GaAs quantum wells separated by an AlGaAs barrier. **d.** Schematic band diagram of the conduction band of a QWIP. Energy of the intraband transitions in the doped GaAs quantum wells is controlled with the well thickness. Electrons promoted to the excited levels of the QW are collected and transported in the AlGaAs conduction band.

and Ge detectors.

There are two competing interband technologies in the MWIR: InSb and HgCdTe. Indium antimonide is a III-V semiconductor with a 230 meV ( $5.4 \mu\text{m}$ ) bandgap at 80 K. Usually grown by Metal-Oxide Chemical Vapor Deposition (MOCVD), InSb has the largest electronic mobility known for III-V semiconductors, leading to very high quantum efficiency. InSb detectors are very sensitive with detectivities around  $10^{11}$  Jones at  $5 \mu\text{m}$  and at cryogenic temperatures, but cannot be spectrally tuned due to their fixed bandgap. On the contrary, the interband bandgap of mercury cadmium telluride ( $\text{HgCdTe}$ , MCT) can be tuned over a large range by changing the cadmium content, see Figure 1.26b. As a result, MCT detectors can address either the MWIR or the LWIR [123]. Grown on CdZnTe using liquid-phase epitaxy, MCT also have to be operated at cryogenic temperatures to ensure good signal-to-noise ratios. Recent MCT detectors are found in the form of unbiased homo- and hetero-junctions photodiodes [124]. Detectivities of few  $10^{10}$  to  $10^{11}$  Jones are achievable in the MWIR and LWIR. Generally speaking, MWIR photodetectors are expensive and controlled (because of their strategical aspect) pieces of technology, with a cost around 20 000 to 100 000 € for a camera.

LWIR interband photodetectors are usually MCT detectors with low cadmium content, operated at cryogenic temperatures with detectivities of a few  $10^{10}$  Jones. Because of the high mercury content in the ternary alloy, the active material is quite soft, leading to inhomogeneities at the FPA scale. The lack of alternative interband material in the LWIR led to the development of detectors based on intraband and intersubband transitions.

**Intraband photodetectors** represent a change of paradigm in the field of infrared detection: instead of trying to obtain narrow interband transitions through metallurgy, alloying and bandgap en-

gineering, wave-function engineering in heterostructured semiconductors is used to achieve transitions in the upper levels of the conduction band.

The best example of an intraband detector is the Quantum Well Infrared Photodetector, or QWIP [125, 126]. Using molecular beam epitaxy (MBE), thin layers ( $\simeq 10$  nm) of doped GaAs are grown successively, separated by barriers of AlGaAs. A scheme of a device is shown in Figure 1.26c, and the conduction band alignment of the two materials is sketched in Figure 1.26d. Because they are doped, the GaAs quantum wells are populated with electrons in the ground level of their conduction band. Upon absorption of light, intraband transition occurs in the GaAs QWs. Because the upper level is aligned with the AlGaAs conduction band, the electron can be transferred to the barrier and be extracted at the contacts. As a result, QWIP are narrow-band, adjustable photodetectors: by adjusting the aluminum content and the thickness of the wells, it is possible to tune the energy of the intraband transition over the MWIR and LWIR. Quantum Dots Infrared Photodetectors are the 0-D counterpart of QWIP, relying on non-lattice matched materials to create isolated, nanoscale island of confined quantum dots to provide optical absorption [126].

Wave-function engineering can be pushed to the device level to build more complex structures: in Quantum Cascade Detectors (QCD), several quantum wells of different thicknesses are weakly coupled to funnel photogenerated electrons toward the contacts using a cascading effect [127]. In superlattices, the arrangement of quantum wells is engineered to create *subbands* and *minibands*, allowing optical transitions between two subbands (inter-subband photodetector) [128, 129].

Despite having good performances, intraband-based photodetectors still have to be operated at cryogenic temperatures and usually suffer from a higher dark current than their interband counterpart. Moreover, optical selection rules in 2D and 0D structures makes that absorption is forbidden at normal incidence. As a result, a grating have to be etched at the surface of the detector to ensure a good optical coupling, see Figure 1.26c.

## Thermal detectors

Thermal detectors detect an energy flux instead of a photon flux. Their active material consists in a material that heats up upon absorption of infrared light: this heating effect is measured and the absorbed power is deduced. Bolometers and pyrometers are examples of thermal detectors. In bolometers, the absorber material is connected to a thermal reservoir at constant temperature through a thermal conductance  $G$ . The measurement of the absorber temperature change (with a precise resistive thermometer) allows to extract the incident power:  $P = \Delta T \times G$ . Thermal detectors are sensitive to the incident power  $h\nu \times \phi_0$  rather than the incident photon flux  $\phi_0$ . Thermal detectors are cheaper than photodetectors and are intrinsically broadband detectors. They are usually operated at room-temperature with a detectivity of around  $10^8$  to  $10^9$  Jones, but can be cooled down to achieve higher performances (especially at long wavelengths). One of the key limitations of bolometers is their low refresh rate: because they are based on heating/cooling of absorbers, they are usually limited to bandwidth around 10 Hz.  $\text{VO}_x$  microbolometers arrays are commercially available to the general public and equip most of the cheap thermal imagers. Deuterated Triglycerin Sulfate (DTGS) is another example of a thermal detector widely used for Fourier-transform infrared spectroscopy.

### 1.3.3 Narrow-bandgap nanocrystals

Because traditional infrared photodetectors remain based on complex, epitaxially grown materials, they remain expensive pieces of technology. As soon as conduction in films of NCs was achieved, using semiconductor nanocrystals films as active infrared material was proposed. Addressing the infrared with nanocrystals seems rather counter-intuitive at first glance. Indeed, as stated in section 1.1.1, quantum confinement in nanocrystals leads to an increase of the bandgap energy compared to the

bulk material. As a result, narrow-bandgap nanocrystals can only be obtained with narrow-bandgap bulk materials. The first historical example of nanocrystals with optical properties in the NIR are lead sulfide nanocrystals (PbS), which were discussed in section 1.1.2. PbS having a bulk bandgap of 370 meV, optical absorption and emission of quantum-confined PbS NCs fall in the near-infrared (see Figure 1.5b). After several years of investigation for solar cells, they are a promising material for a new generation of NIR photodetectors.

Another strategy to build nanocrystal with narrow energy bandgap is to start with a bulk material with a zero bandgap, *i.e.*  $E_{\text{bulk}} = 0$ . By looking back at the simple spherical particle model provided in section 1.1.1 and Equation 1.7, the bandgap energy of a nanocrystal of size  $R$  ( $1S_h$  to  $1S_e$  transition) is then given by:

$$E_G = E_{1S_e} - E_{1S_h} = E_{\text{bulk}} + \frac{\hbar^2\pi^2}{2m_{eh}^*R^2} = \frac{\hbar^2\pi^2}{2m_{eh}^*R^2} \quad (1.35)$$

With  $m_{eh}^*$  is the electron-hole reduced mass. The nanocrystal bandgap is then only controlled by the confinement energy, which can theoretically be as small as desired for very large nanoparticles. This zero bulk bandgap is notably the signature of *semi-metals*. This section will concentrate on nanocrystals made from two semi-metals: mercury telluride (HgTe) and mercury selenide (HgSe).

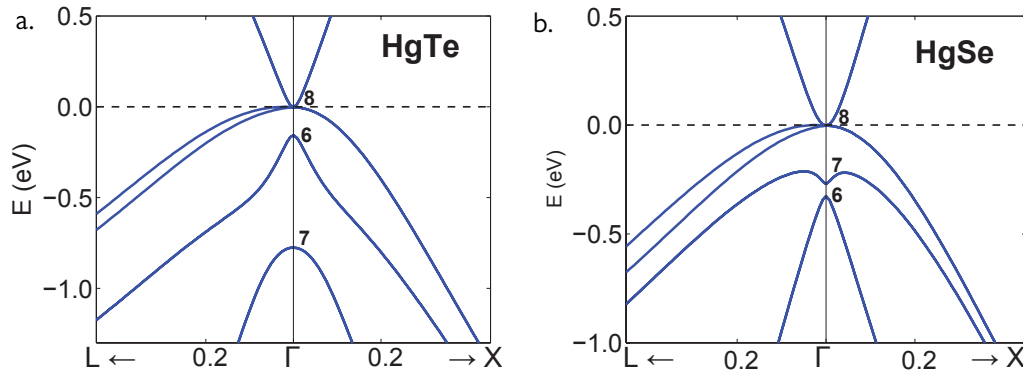


Fig. 1.27 Calculated bands structure of HgTe (a) and HgSe (b), from [130]. The horizontal axis ticks are  $2\pi/a$  with  $a = 6.47 \text{ \AA}$  for HgTe and  $a = 6.08 \text{ \AA}$  for HgSe.

Calculated band structure of bulk HgTe and HgSe are presented in Figure 1.27 [130]. The first observation on those band diagrams is that the band ordering is reversed compared to classical semi-conductors: for both HgTe and HgSe, the first conduction band is a  $\Gamma_8$  band (which is usually a valence band), and the  $\Gamma_6$  band (usually a conduction band) is found deep below the first valence bands. The classical definition of the bandgap being the energy between  $\Gamma_6$  and  $\Gamma_8$  bands at the center of the Brillouin zone, this leads to the attribution of a *negative bandgap* to HgSe and HgTe. The first valence band is also a  $\Gamma_8$  band and is degenerated for both cases. An important point is that valence and conduction  $\Gamma_8$  bands touch at the center of the Brillouin zone. Fermi levels of the materials lie between conduction and valence bands, making that both materials are semi-metals with a zero effective bandgap. Graphene is another example of a semi-metal with valence and conduction bands touching at the  $\Gamma$  point.

### Infrared interband transitions in HgTe nanocrystals

Synthesis of HgTe nanocrystals was first developed by Rogach *et al.* [23] in aqueous medium with a gaseous  $H_2Te$  precursors. Kovalenko *et al.* [24] improved the synthesis and introduced size tunability, before Keuleyan *et al.* provided a more straightforward synthesis in organic solvents [27]. In this approach, mercury is introduced as  $HgCl_2$  salt in an organic medium and heated around

80 to 100°C, and a tri-octylphosphine:tellurium complex (TOP:Te) is injected in the hot solution. After a few minutes, reaction is quenched using dodecanthiol (DDT). The nanocrystals mean size is controlled by adjusting injection temperature and reaction length. The detailed synthesis procedures can be found in appendix A.

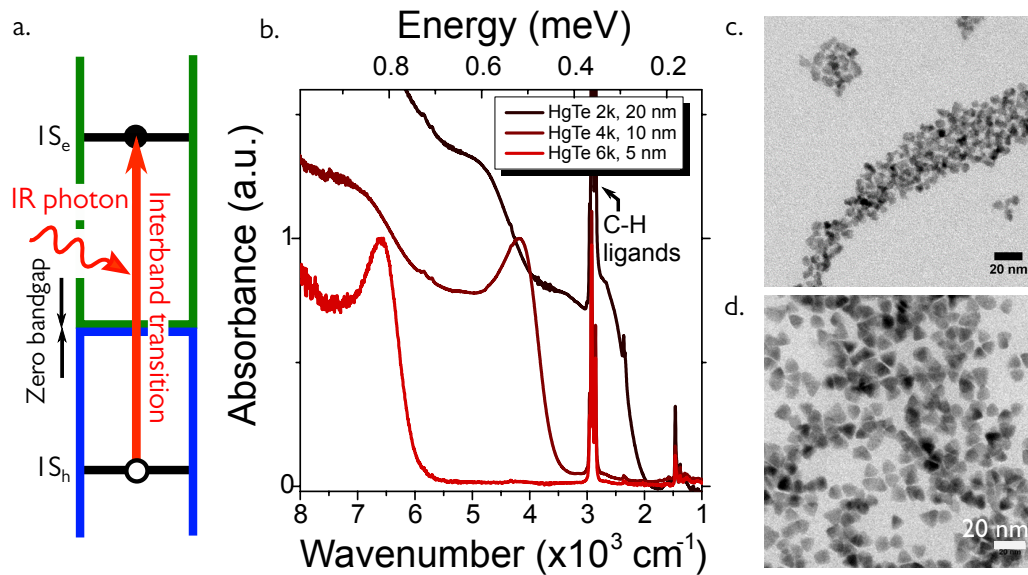


Fig. 1.28 Mercury Telluride nanocrystals with interband absorption in the SWIR to MWIR. **a.** Sketch of HgTe NC band diagram. Low energy interband transition occurs between  $1S_h$  and  $1S_e$  levels. **b.** Absorption spectra (room temperature) of three sizes of HgTe NCs displaying a size-tunable bandgap from SWIR to MWIR. "6k", "4k" and "2k" refers to the absorption band-edge of the nanocrystals, respectively around  $6000\text{ cm}^{-1}$ ,  $4000\text{ cm}^{-1}$  and  $2000\text{ cm}^{-1}$ . **c.** TEM picture of HgTe 4k NCs showing tetrapodic-shaped particles. **d.** TEM picture of HgTe 2k NCs showing tetrahedral-shaped particles.

Because of the gapless character of HgTe, the resulting nanocrystals feature an interband bandgap ( $1S_h \rightarrow 1S_e$  transition, see Figure 1.28a) whose energy is only controlled by the quantum confinement, hence by the size of the nanocrystal. Figure 1.28b presents the optical spectra of three sizes of HgTe NCs with bandgaps around  $6000\text{ cm}^{-1}$  ( $1.6\text{ }\mu\text{m}$ , SWIR),  $4000\text{ cm}^{-1}$  ( $2.5\text{ }\mu\text{m}$ , E-SWIR) and  $2000\text{ cm}^{-1}$  ( $5\text{ }\mu\text{m}$ , MWIR). Those three sizes of HgTe nanocrystals will be respectively called "HgTe 6k", "HgTe 4k" and "HgTe 2k" throughout the manuscript. Those spectra show well-defined band-edges as well as excitonic features, which is an indication of a controlled ( $< 10\%$ ) size dispersion. One particularity of those absorption spectra is that they show a fine, intense structure around  $2900\text{ cm}^{-1}$ : this is the signature of C – H bonds in the 12-C long DDT ligands. As pictured in Figures 1.28c and d, HgTe nanocrystals deviate quite strongly from the spherical shape. They are found to be tetrapodic for small sizes, before switching to a more regular tetrahedral shape for larger sizes [131].

With strong, spectrally tunable interband absorption from the SWIR to MWIR, HgTe nanocrystals have encountered quite a lot of success for their integration into optoelectronic devices for infrared photodetection, starting in the Guyot-Sionnest group in Chicago [27, 118, 132] and in the Rogach group in Hong Kong [133]. Recent progresses in this direction will be discussed in the next section.

Along with optical absorption in the infrared, HgTe nanocrystals also feature interband emission [27, 134–136]. Because of the presence of numerous non-radiative decay paths in the infrared, the photoluminescence quantum yield of those nanocrystals remains low, but electroluminescent devices have been demonstrated [137] as well as continuous-wave lasing under optical excitation [45].

Another recent achievement that will be relevant for the next parts of this manuscript was the synthesis of 2-dimensional HgTe nanoplatelets. Using a cation-exchange approach, Izquierdo *et al.* were able to prepare HgTe NPLs from CdTe NPLs, effectively replacing each  $\text{Cd}^{2+}$  cation by a  $\text{Hg}^{2+}$

one while preserving the NPL structure. Those objects are nevertheless very confined (3 monolayers, 1.1 nm total thickness), with optical absorption and emission in the NIR [56].

### Intraband transitions in self-doped systems

Just as we demonstrated in section 1.3.2 that infrared absorption can be realized in epitaxial devices by engineering intraband or inter-subband transitions in doped systems, it is possible to obtain doped nanocrystals featuring intraband absorption in the IR. In nanocrystals, intraband absorption can be observed in the form of transitions between the first levels of the conduction band, see Figure 1.29a. If the ground level of the conduction band is occupied by one or more electrons (*i.e.* the nanocrystal is degenerately electron-doped), transitions from the  $1S_e$  and  $1P_e$  are authorized. First realizations of intraband absorption was obtained by heavily doping CdSe [138] or HgTe [110] nanocrystals using electrochemistry, or in nanocrystals under strong optical excitation such as in PbSe [139] or CdS [140].

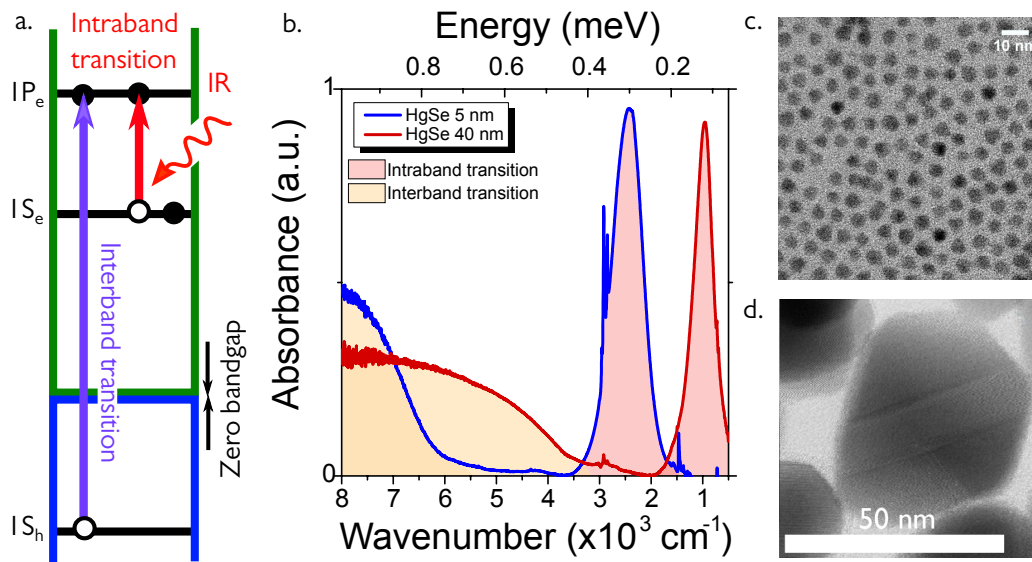


Fig. 1.29 Self-doped Mercury Selenide nanocrystals with intraband absorption in the MWIR to LWIR. **a.** Sketch of HgSe NC band diagram. Since the NCs are doped, the  $1S_e$  level is populated and intraband transitions from  $1S_e$  to  $1P_e$  levels is possible. The interband (VB $\rightarrow$ CB) transition is likely to occur between  $1S_h$  and  $1P_e$  levels because of the first level saturation. **b.** Absorption spectra of two sizes of HgSe NCs. Intraband transitions appear as a size-tunable narrow feature in MWIR to LWIR. Interband transition is observed as a broad feature in the SWIR. **c.** TEM picture of small, spherical HgSe NCs ( $\approx 5$  nm). **d.** High-resolution TEM picture of a single  $\approx 40$  nm HgSe NC.

In 2014, the Guyot-Sionnest group demonstrated self-doped mercury selenide (HgSe) nanocrystals, in which the first level of the conduction band is occupied in the steady state [141]. The synthesis was refined by Lhuillier *et al.* with spectral tunability of the  $1S_e \rightarrow 1P_e$  transition other the MWIR to LWIR ranges [142]. The procedure is very similar to that of HgTe NCs synthesis, but uses mercury oleate  $\text{Hg}(\text{OAc})_2$  as a  $\text{Hg}^{2+}$  precursor. It is described in appendix A.

Optical spectra of medium and large HgSe nanocrystals are provided in Figure 1.29b. Two absorption features are observed for each size: the low-energy, narrow peak in the MWIR to LWIR (pale red) corresponds to intraband  $1S_e \rightarrow 1P_e$  transition, when the higher energy broadband feature (pale yellow) corresponds to interband transition. Both absorption features red-shift when the mean size of the nanocrystal increases, as a result of confinement loss. As seen in TEM pictures (Figures 1.29c and d), HgSe NCs are much more spherical than their HgTe counterparts.

The mechanism of doping in those nanocrystals is believed to be linked to NC reduction by the environment. Indeed, the work function of HgSe NCs in presence of long ligands is high enough for the first level of the conduction band to be below the  $O_2/H_2O$  redox couple, located around 5 eV. As a result, water acts as a reducer and the HgSe NCs are negatively charged in their steady state [143]. Interestingly, the self-doped character of this material has been observed down to the single-particle level [116].

In recent work, the precise nature of the low energy feature for the big nanocrystals has been attributed to plasmonics rather than to pure intraband transition due to the level of doping of the big HgSe NCs ( $> 20$  electrons per NC). This indicates that as the narrow absorption feature red-shifts, its intrinsic nature continuously transitions from intraband to plasmonic [109]. Interestingly, similar effects have also been observed in coupled epitaxial quantum wells [144].

The same self-doping character has also been found in mercury sulfide HgS nanocrystals, despite HgS being a gapped semiconductor [145, 146]. More recently, intraband absorption in HgTe was demonstrated in the steady-state using iodine-doped HgTe nanocrystals [147], or high temperature synthesis [131]. In this last approach, temperatures well above the classical synthesis (max.  $120^\circ\text{C}$ ) are used to obtain big, unconfined HgTe microcrystals with intraband/plasmonic absorption up to the THz range. This material is currently the reddest colloidal material ever reported.

To conclude on HgTe and HgSe nanocrystals, Figure 1.30 presents the available materials between  $1\ \mu\text{m}$  and  $100\ \mu\text{m}$ , from small HgTe interband nanocrystals in the SWIR to self-doped intraband HgSe in the MWIR and heavily doped HgTe microcrystals in the FIR/THz.

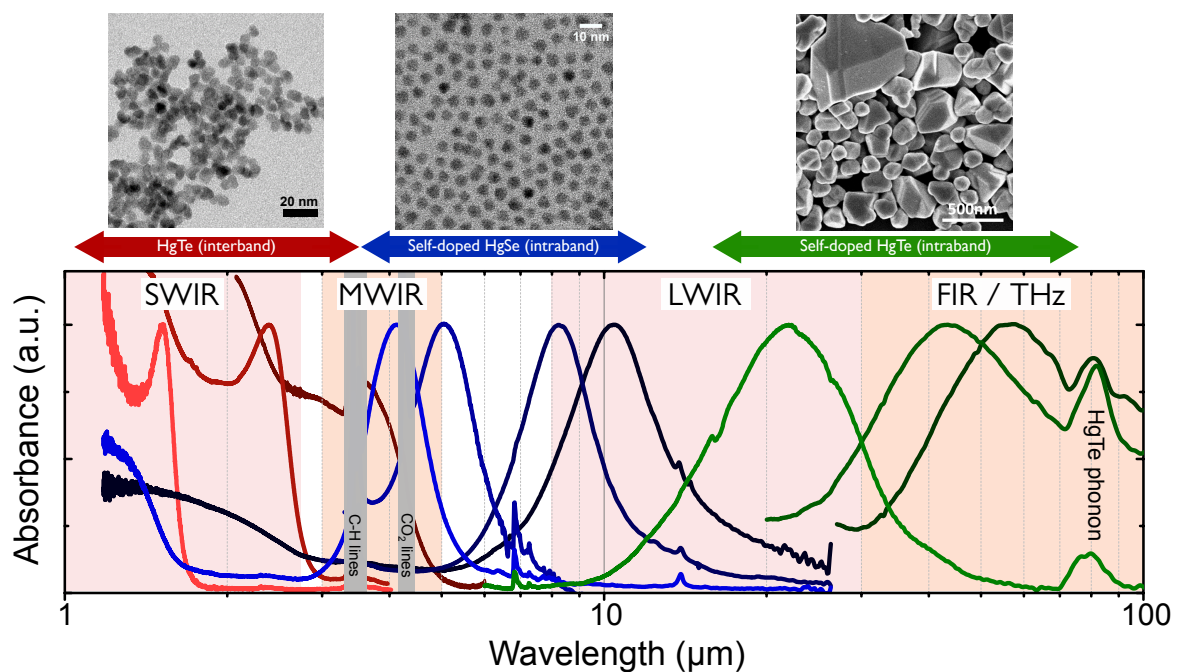


Fig. 1.30 State-of-the-art of the HgTe and HgSe nanocrystals available in the group. In red are pictured interband HgTe NCs, in blue intraband HgSe NCs and in green intraband HgTe NCs. The different IR ranges have been highlighted.

### Toward non-toxic infrared nanomaterials

An obvious objection to the use of HgTe and HgSe materials as active materials for a new generation of infrared detectors is the toxicity of those materials. Indeed, mercury compounds are quite dangerous to handle, especially under nanoparticle form. A major counter-argument would be that exposure is very limited when the material is embedded in a Focal Plane Array (FPA). Moreover,

as opposite to solar cells, only a very small amount of material is needed in an infrared detector ( $\simeq 1 \text{ cm}^2$ ). As a result, we estimated that only 50 kg of HgTe material would be needed to equip every car sold in Europe in one year with a HgTe-based infrared camera, even assuming a 90% loss during deposition process [148].

Nevertheless, heavy-metal free alternative should be explored. As narrow bandgap is associated with large density of state, and so with heavy elements, no viable alternative have been reported for infrared interband nanocrystals yet. There is more promises for intraband materials with notably silver selenide ( $\text{Ag}_2\text{Se}$ ) nanocrystals featuring intraband/plasmonic absorption in the same range as HgSe [149–152]. They nevertheless do not reach the level of maturity of mercury-based compounds.

### 1.3.4 NC-based detectors: toward low-cost, efficient detectors in SWIR and MWIR

To conclude this introductory chapter, we will summarize the different progresses that have been achieved in almost 10 years of mercury chalcogenide nanocrystal-based infrared photodetection. The first devices were reported in the SWIR by the Wolfgang Heiss group [153], using inkjet-printed photoconductive devices. First reports on MWIR detectors were brought by the Guyot-Sionnest group in Chicago, with HgTe-based photoconductive detectors fabricated by drop-casting [27, 132]. Figures 1.31a and b give I-V characteristics as well as photocurrent spectra of such early devices. Major improvements were brought by tuning the surface chemistry of the nanocrystals to improve mobility [154] or improving the film quality by switching to cleaner deposition methods [133]. The experimental measurement of the noise in those devices was a huge step in rationalizing the performances of those IR-sensitive devices and bring them to a more mature stage of development [118, 119].

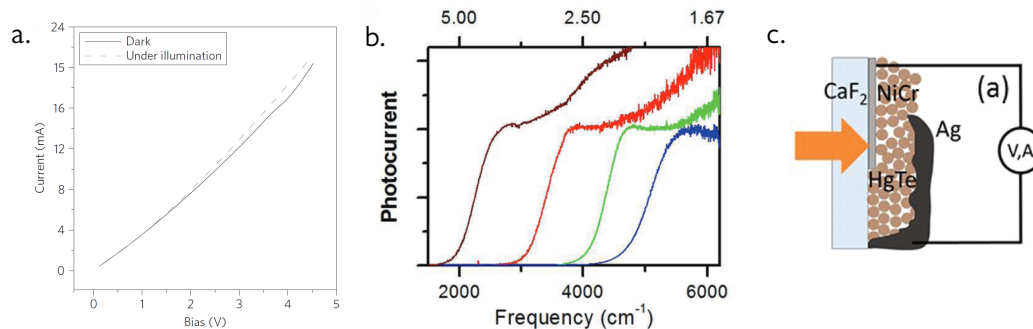


Fig. 1.31 First generation of HgTe infrared photodetectors. **a.** I-V characteristics of a  $5 \mu\text{m}$  HgTe photoconductive device in the dark and under illumination, from [132]. **b.** Photocurrent spectra of four HgTe photoconductive devices from SWIR to MWIR, from [27]. **c.** Scheme of the first HgTe photovoltaic device, demonstrating background-limited infrared photodetection (BLIP) at 90 K. From [155].

More recent photoconductive devices have demonstrated higher performances thanks to material improvement. The integration of the HgTe active material in a field-effect transistor allowed to build efficient phototransistors in the SWIR [156]. Very high responsivities above  $100 \text{ mA/W}$  were reported using  $\text{As}_2\text{S}_3$ -capped HgTe NCs [154, 157, 158]. Another interesting strategy to improve photoconductor was the hybridation of HgTe NCs in a  $\text{MoS}_2$  2D device [159]. Responsivities as high as  $10^6 \text{ A/W}$  have been reported, but overall performances of those devices remain very limited due to their slow time response and high dark current.

A huge step forward was the introduction of photovoltaic devices. Being able to build a photodiode from nanocrystals requires to have a mature active material, since the band alignment of the different diode constituents will have a strong impact on the device performance. Moreover, a vertical device requires to be able to build thick, smooth and pinhole-free NC films to prevent any electrical shorts. The first MWIR HgTe-based diode was a Schottky NiCr/HgTe/Ag paste stacking, see Figure 1.31c.

This diode demonstrated in 2015 background-limited infrared photodetection (BLIP) at 90 K [155]. An improved structure was proposed by Ackerman *et al.* in 2018, using an ITO/HgTe/Ag<sub>2</sub>Te/Au. The heterojunction is formed between the n-type HgTe NCs and the p-type Ag<sub>2</sub>Te NCs. A sketch of this diode is provided in Figure 1.32a, as well as an image acquired at 80 K by scanning a lens in front of the detector to simulate multiple pixels. The introduction of plasmonic structures to boost the optical coupling in HgTe devices has been studied since 2014 [160], and was introduced to photovoltaic device in 2018 by Tang *et al.* to improve the performances of the diode presented in 1.32a [161]. Figures 1.32c and d present the structure of the diode incorporating gold plasmonic discs to boost its absorption in the MWIR, as well as an image of a Peltier cooler taken with this improved diode.

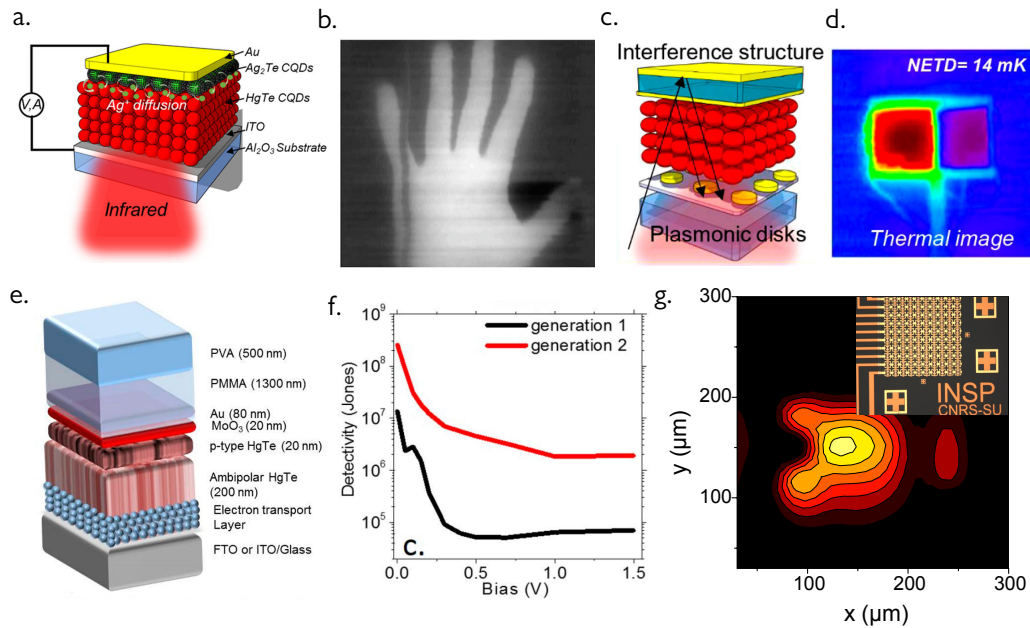


Fig. 1.32 Recent achievements for photodetection with HgTe NCs in the MWIR and SWIR. **a.** Scheme of a MWIR photodiode based on a HgTe/Ag<sub>2</sub>Te junction with high detectivity at 90 K [162]. **b.** Thermal image obtained with the diode shown in (a) by scanning a lens in front of the detector. [162]. **c.** Scheme of a plasmonic-enhanced HgTe diode with improved absorption in the MWIR [161]. **d.** Thermal image obtained with the diode shown in (c) by scanning a lens in front of the detector, allowing to measure a 14 mK Net Equivalent Temperature Difference (NETD) [161]. **e.** Scheme of a HgTe-based E-SWIR photodiode incorporating an unipolar barrier made of smaller HgTe NCs to filter dark current [163]. **f.** Detectivity of the diode shown in (e) with unipolar barrier, compared to the same diode structure without the unipolar filtering barrier (in black) [163]. **g.** Demonstration of a 10×10 pixels FPA based on HgTe nanocrystals in the E-SWIR. The image shows a focused laser beam. Inset shows the home-made FPA before NC deposition [164].

The first extended short-wave (ESWIR) HgTe diode was introduced by our group using a ITO/TiO<sub>2</sub>/HgTe/Au stack [165]. The dark current in this diode was still fairly high, and we introduced the concept of unipolar barrier to filter out the electronic dark current in this structure. Practically speaking, this unipolar barrier consists in a thin layer of a higher bandgap HgTe NCs, see Figure 1.32e. The performance of this diode was improved by more than one order of magnitude with the addition of the unipolar barrier, see Figure 1.32f. More recently, the Guyot-Sionnest group reported a flexible HgTe-based SWIR diode with higher detectivity [166]. Our last development around SWIR HgTe was the demonstration of a fully-homemade 10×10 pixels FPA in photoconductive configuration. Figure 1.32g shows an image of a focused 1.5 μm laser beam acquired with such a FPA [164]. Finally, we recently demonstrated active imaging in the NIR using a PbS-based photodiode, with devices sensitive enough to detect diffused light at distances up to 180 m [167].

Finally, multi-spectral devices start to be demonstrated. Multi-band detection is very useful for

applications where spectral contrast is needed and to build versatile detectors able to produce images in two very different IR ranges. Visible/ESWIR multispectral detection have been demonstrated in electrolytically-gated devices containing both CdSe/CdS nanoplatelets and infrared-absorbing HgTe nanocrystals [104]. A multicolor photoconductive device consisting in three sub-pixels in the MWIR (4.8  $\mu\text{m}$  and 6  $\mu\text{m}$ ) and LWIR (9.5  $\mu\text{m}$ ) have been proposed by Tang *et al.* [157]: he uses a stamping strategy to successively transfer the three HgTe films to the final device, see Figure 1.33. A dual-band SWIR-MWIR photodiode device has also been reported, with two HgTe diodes built back-to-back [168]. Thanks to this back-to-back configuration, the bias on the device controls which one of the diode is operated.

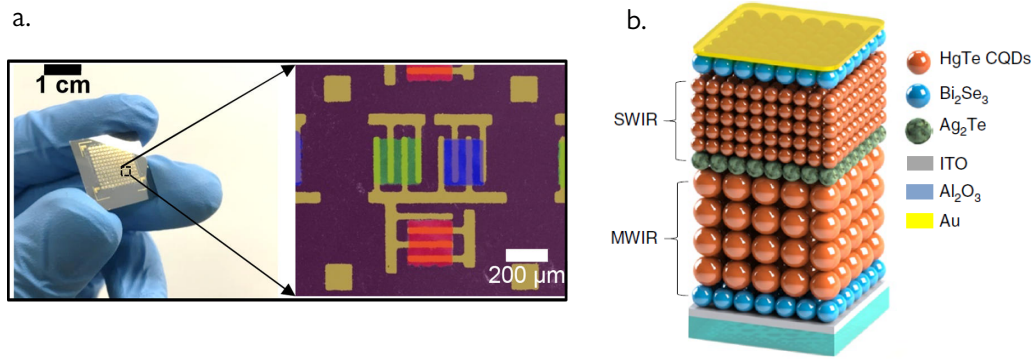


Fig. 1.33 Multi-spectral, HgTe-based photodetectors. **a.** Multispectral photoconductive HgTe detector with three wavelengths in the MWIR (4.8  $\mu\text{m}$  and 6  $\mu\text{m}$ ) and LWIR (9.5  $\mu\text{m}$ ) [157]. **b.** Scheme of a dual-band SWIR-MWIR HgTe photodiode. The device consist in two diodes built back-to back, and the polarization bias allows to switch between MWIR and SWIR sensitivity.

# Chapter 2

## Probing dynamics in Mercury Telluride nanoplatelets

---

<b>2.1</b>	<b>Transport dynamics: an alternative to transient spectroscopies . . . . .</b>	<b>42</b>
<b>2.2</b>	<b>HgTe nanoplatelets: a 2D material for Near-Infrared with tunable majority carrier . . . . .</b>	<b>45</b>
<b>2.3</b>	<b>Probing low-frequency phototransport dynamics under gate control . . . . .</b>	<b>49</b>
<b>2.4</b>	<b>Time-resolved photoemission . . . . .</b>	<b>51</b>
<b>2.5</b>	<b>Conclusions . . . . .</b>	<b>58</b>

---

### Related articles

- C. Livache, E. Izquierdo, B. Martinez, M. Dufour, D. Pierucci, S. Keuleyan, H. Cruguel, L. Becerra, J.L. Fave, H. Aubin, E. Lacaze, M.G. Silly, B. Dubertret and E. Lhuillier, "Charge Dynamics and Optoelectronic Properties in HgTe Colloidal Quantum Wells", *Nano Letters* 17, 4067-4074 (2017)
- E. Izquierdo, M. Dufour, A. Chu, C. Livache, B. Martinez, D. Amelot, G. Patriarche, N. Lequeux, E. Lhuillier, S. Ithurria, "Coupled HgSe Colloidal Quantum Wells through a Tunable Barrier: A Strategy To Uncouple Optical and Transport Band Gap", *Chemistry of Materials* 30, 4065-4072 (2018)
- C. Gréboval, E. Izquierdo, C. Livache, B. Martinez, M. Dufour, N. Goubet, N. Moghaddam, J. Qu, A. Chu, J. Ramade, H. Aubin, H. Cruguel, M. G. Silly, E. Lhuillier, S. Ithurria, "Impact of Dimensionality and Confinement on the Electronic Properties of Mercury Chalcogenide Nanocrystals", *Nanoscale* 11, 3905-3915 (2019)

### Related communications

- "Charge Dynamics and Optoelectronic Properties of HgTe Colloidal Quantum Wells"
  - MRS Spring Meeting 2018, Phoenix AZ, USA.
  - NanoTN Conference 2018, Marrakech, Morocco.

In this chapter and the next one, I will present alternative strategies to probe carrier dynamics in narrow bandgap semiconductor nanocrystals. Because we are interested in detectors, we want to get insights on transport dynamics at the device scale, which are not usually probed with classical, optical techniques. As a result, a significant experimental effort must be done to develop time-resolved techniques that are compatible with device operation and give information on relevant time scales. This first result chapter is dedicated to NIR material, and as we go toward longer wavelengths in the next chapter, specific methods have to be developed.

This chapter is centered around a new material for near-infrared: mercury telluride 2D nanoplatelets. In the first section, we discuss the intrinsic limitations of optical time-resolved spectroscopy techniques to probe device dynamics, which typically spans over long time scales and involves inter-nanocrystal processes. We present in the second section optical and transport properties of the material of interest for this study, HgTe nanoplatelets. The two last sections are focused on probing the carrier dynamics by two different means: time-resolved photocurrent measurements at low frequency, and time-resolved photoemission spectroscopy.

## 2.1 Transport dynamics: an alternative to transient spectroscopies

### 2.1.1 Limitations of transient optical spectroscopies

Dynamics in colloidal nanomaterials are usually studied by means of (ultra)-fast optical spectroscopies as time-resolved photoluminescence or transient absorption. Time resolved photoluminescence spectroscopy allows studying the radiative excitonic decay, while transient absorption is a pump-probe technique that measures the change in absorption in a material a few ps to ns after excitation of the material by an intense, ultrashort laser pulse.

A first limitation of those transient optical spectroscopies is that they usually resolve only intra-nanocrystal processes: photoluminescence occurs at the nanocrystal level and pump-probe techniques are usually limited to timescales of a few ns at best. Indeed, for this kind of experiment, scanning the delay between pump and probe requires to physically move a set of two mirrors while ensuring no drift of the beam at the sample location. As a result, a 1 ns delay requires a 30 cm displacement, which is already difficult to achieve. A rough timeline of relaxation and transport processes is given in Figure 2.1: processes relevant for transport typically occur in the 100 ps to ms range, the fastest process being the hopping time. As a result, inter-nanocrystal processes are usually never probed with classical optical spectroscopy techniques.

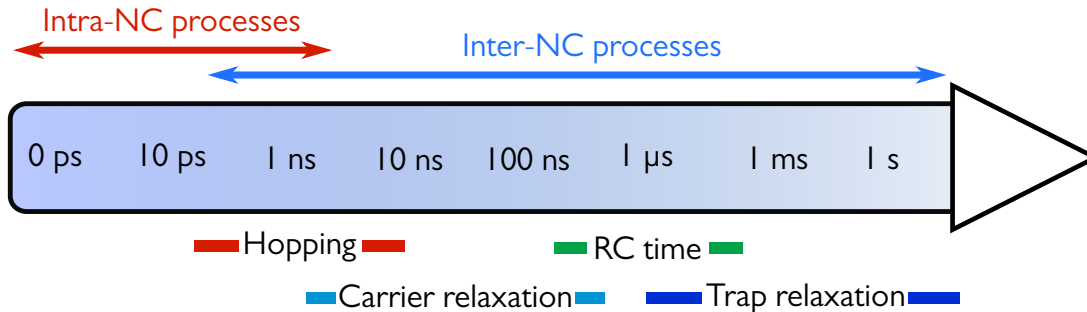


Fig. 2.1 Schematic timescale of intra- and inter-nanocrystals processes.

In the infrared, time-resolved photoluminescence spectroscopy techniques, relying on the observation of PL decay after a short optical excitation of the nanocrystals, are also way more complicated to setup than in the visible range. This is due to the very weak photoluminescence quantum yield of infrared nanocrystals: in the first chapter, we introduced the PLQY as  $\eta_{PL} = \Gamma_{\text{rad}}/(\Gamma_{\text{rad}} + \Gamma_{\text{nr}})$ . The

radiative rate  $\Gamma_{\text{rad}}$  scales as the cube of the transition energy  $h\nu$ , making that PLQY is inevitably reduced in the infrared. Moreover, non-radiative decay processes become very important in the infrared range, strongly affecting  $\Gamma_{\text{nr}}$ . Energy transfer toward organic ligands is notably very efficient because of the multiple absorption lines of those ligands in the SWIR, MWIR and LWIR. Figure 2.2 presents the work of Keuleyan *et al.* [135], who calculated theoretical radiative and non-radiative exciton decay rates in HgTe nanocrystals capped with DDT ligands (see Figure 2.2a). Resulting theoretical PLQY, shown in Figure 2.2b, is already only around 10% at 6000  $\text{cm}^{-1}$  (0.75 eV), and drops around 1% for 4000  $\text{cm}^{-1}$  material (0.5 eV). In the MWIR ( $< 0.3$  eV), theoretical PLQY falls to even lower values. Those values are PLQY maximum expected values for a colloidal suspension of well-passivated HgTe quantum dots. At the device scale, where nanocrystals are close-packed and where long ligands are exchanged toward shorter ones to allow charge transport, PLQY is strongly quenched due to the increased inter-particle coupling and degradation of traps passivation.

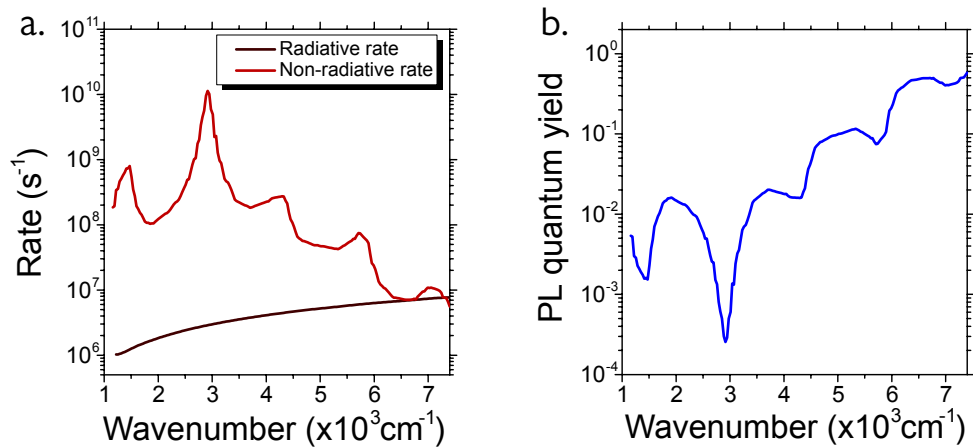


Fig. 2.2 Calculated decay rates and photoluminescence quantum yield of HgTe nanocrystals. **a.** Calculated radiative (black) and non-radiative (red) decay rates for an exciton in dodecanethiol-capped HgTe nanocrystals. Reproduced from [135]. **b.** Calculated photoluminescence quantum yield (PLQY) of DDT-capped HgTe nanocrystals. Reproduced from [135].

Another issue affecting the potency of time-resolved spectroscopies is the availability of efficient sources and detectors in the infrared range: ultrafast optical setups are widely spread in the visible to NIR range, but get a lot more complex and expensive in the SWIR and MWIR. Generation of high power fs pulses requires either the use of parametric amplifiers or of completely new laser oscillators [169]. Fast and efficient detectors in this range (typically, InGaAs in the SWIR and MCT in the MWIR) are also a lot more expensive than their silicon counterpart in the visible range. Because of that, time-resolved spectroscopy is difficult to conduct with our infrared materials, especially at the band-edge of MWIR nanocrystals. Moreover, probing narrow-bandgap nanocrystals with higher photon energy (say, at 800 nm) leads to non-trivial mechanisms due to the fact that the photon energy is several times the bandgap of the material. Hot carrier generation can notably undergo non-classical cooling leading to carrier multiplication, that will be discussed later in the next chapter [17, 170].

### 2.1.2 Probing dynamics at the device scale

Alternative techniques to probe dynamics at the nanocrystal-based device scale have been reported in the last decade. Interestingly, a lot of them are inspired by transient electrical measurement techniques developed during the last century to study carrier dynamics in semiconductors and their heterojunctions [171, 172]. We present here a few of them that motivated our work in this direction.

A lot of the reported approaches uses the photocurrent as a probe of the carriers dynamics in the nanocrystal solid. Among them, Gao and Fidler from Klimov group in Los Alamos showed that

ultrafast photocurrent measurements can be used as an alternative to transient spectroscopies to measure the intra-nanocrystal excitonic decay from an ensemble measurement at the device level. As pictured in Figure 2.3a, they use an Auston-switch configuration [173] with carefully matched impedance and a classical fs-pulsed laser. They were able to detect Auger decay [174] and multiple exciton generation [175] (see Figure 2.3b) through the photocurrent temporal traces in photoconductive PbS samples.

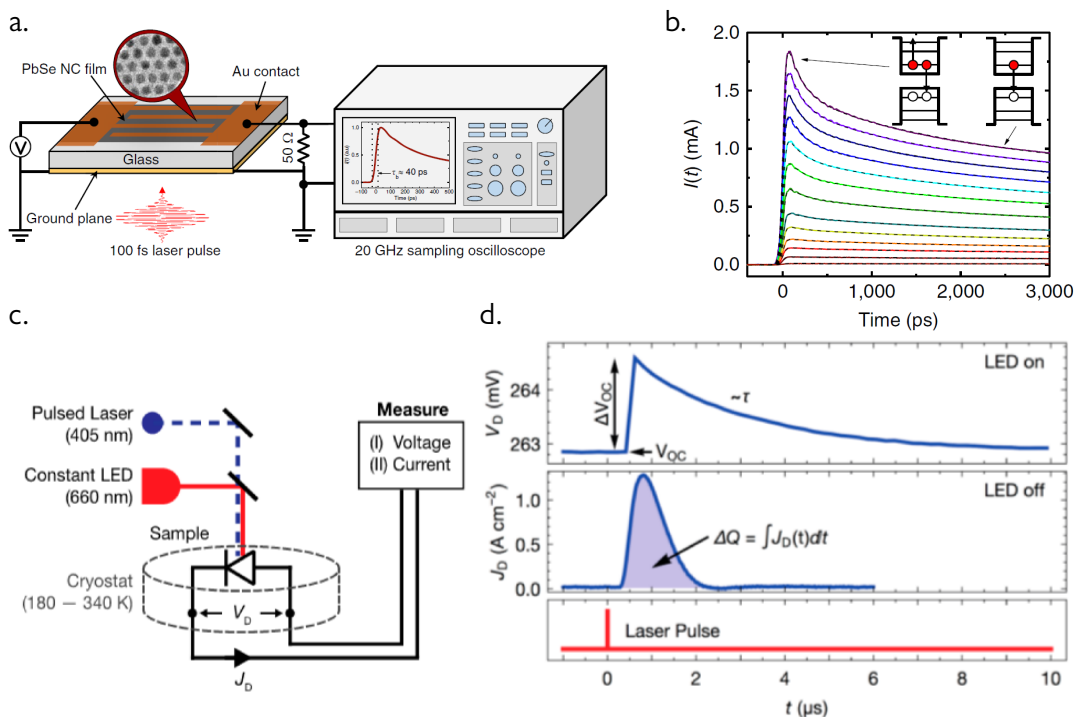


Fig. 2.3 Two examples of device-scale experiments based on transient electrical measurements. **a.** Scheme of a multi-GHz transient photocurrent setup used to detect Auger recombination and multiple exciton generation at the device scale in a PbS photoconductive device. Reproduced from [175]. **b.** Transient photocurrent traces obtained from the setup shown in (a), with increasing excitation power. Reproduced from [175]. **c.** Scheme of a MHz time-resolved setup to probe the open circuit voltage and photocurrent transient evolution in a PbS-based solar cell. CW illumination is provided by a visible LED while transient excitation is provided by a pulsed UV laser. Reproduced from [176]. **d.** Temporal traces of open circuit voltage (under illumination) and current density (without CW illumination) in the solar-cell device. Reproduced from [176].

Another interesting approach was introduced by the team of Vanessa Wood in Zürich, which presented transient photovoltage measurements on PbS solar cells [176]. Their experiment is schematized in Figure 2.3c: a pulsed (50 ps) blue laser excites a sample under bias and illumination by a CW LED, hence using the pulsed excitation as a small perturbation of the device electrical characteristics. Photocurrent and photovoltage transients, presented in Figure 2.3d, are interpreted as RC circuit decays and used to provide insights about charge trapping, recombination and capacitive effects in the solar cell device. Unfortunately, the bandwidth of their electrical setup does not allow to precisely resolve dynamics below 1  $\mu$ s.

A last aspect around device-scale dynamics is brought by spatially-resolved experiments. Using time-resolved photoluminescence spectroscopy with a sub-wavelength resolution, the Zamkov group in Bowling green [177] and Tisdale group in MIT [178] were able to map the exciton transfer as well as its spatial and temporal decay in assemblies of PbS.

## 2.2 HgTe nanoplatelets: a 2D material for Near-Infrared with tunable majority carrier

The nanomaterial we are going to investigate throughout this chapter is mercury telluride nanoplatelets (HgTe NPLs). With optical properties in the near-infrared (NIR) and availability of a wide characterization toolbox for II-VI nanocrystals, this new material is an interesting platform to start the development of new experiments around carrier dynamics. Moreover, the NIR range is, while belonging to the infrared domain, close enough to the visible range. This makes that:

- NIR devices feature reasonable signal to dark ratios without requiring cryogenic cooling,
- Light sources (continuous and pulsed) are still widely available.

### 2.2.1 HgTe nanoplatelets: synthesis and optical properties

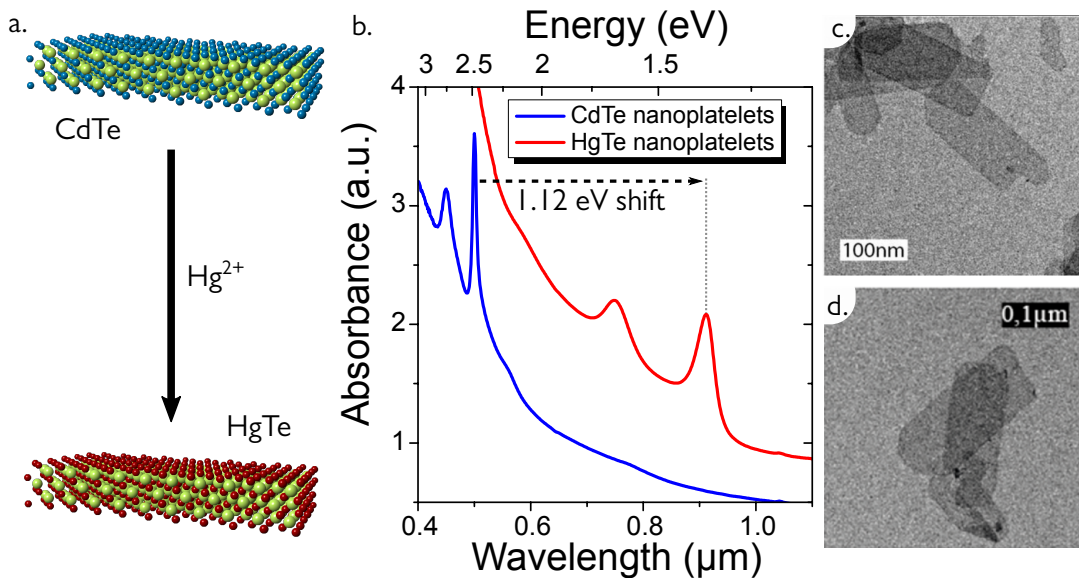


Fig. 2.4 Synthesis and optical properties of HgTe nanoplatelets. **a.** Scheme of the cation exchange procedure used to obtain HgTe NPLs from CdTe NPLs. The shape of the nano-objects is not affected during the cation exchange. **b.** Absorption spectra of CdTe nanoplatelets before cation exchange (blue) and HgTe nanoplatelets after cation exchange (red). **c.** Transmission Electron Microscopy (TEM) image of CdTe nanoplatelets [56]. **d.** TEM image of HgTe nanoplatelets [56].

The synthesis of HgTe nanoplatelets have been developed in 2016 by Izquierdo *et al.* [56]. We explained in the first chapter that synthesis of II-VI nanoplatelets was enabled by the introduction of acetate during synthesis: it is nevertheless not possible to directly obtain HgTe NPLs. The strategy developed by E. Izquierdo and S. Ithurria at LPEM (ESPCI) was to synthesize thin (3 monolayers) CdTe nanoplatelets, and to use a cation exchange procedure, as pictured in Figure 2.4a. The optical spectrum of CdTe NPL is given in Figure 2.4b, and features sharp excitonic features in the visible range around 2.5 eV (500 nm). By introducing the platelets in a solution of  $\text{Hg}(\text{OAc})_2$  in oleylamine, it is possible to exchange the  $\text{Cd}^{2+}$  cations for  $\text{Hg}^{2+}$  over the whole nanoplatelet while preserving their 2D shape. Figure 2.4b also gives the absorption spectra of the platelets after the cation exchange, showing excitonic features around 1.4 eV (900 nm). The 1.12 eV red-shift between CdTe and HgTe NPLs is explained by the combination of bulk bandgap difference (CdTe have a 1.44 eV bandgap when HgTe is a zero bandgap semi-metal) and effective masses changes affecting the confinement energy. The resulting HgTe nanoplatelets are extremely confined objects, with an optical bandgap resulting

from pure confinement:  $E_C \simeq 1.4$  eV. The fact that the excitonic features are preserved in the HgTe material is a first proof that the cation exchange process does not affect the platelet structure, *i.e.* that the anion network stays untouched and that the 2D shape stays unaffected. Another evidence is given by the TEM images of the material before and after exchange, as shown in Figures 2.4c and d.

It is worth noting that the same procedure can be applied to CdSe nanoplatelets to create HgSe nanoplatelets with similar optical properties. For both HgTe and HgSe NPLs, the cation exchange process is nevertheless limited to the first 1 to 2 monolayers: 3 monolayers (ML) platelets can be fully exchanged, but the same procedure conducted over  $\geq 4$ ML NPLs lead to hybrid materials where only the external layers are effectively exchanged [179].

### 2.2.2 Majority carrier tunability through ligand exchange

HgTe NPLs are provided in the form of a colloidal dispersion in an organic, apolar solvent. The solvent is switched to a hexane:octane mixture (9:1 in volume) to ensure an homogeneous drying process. Films are obtained through drop-casting onto pre-patterned interdigitated gold electrodes on glass (see appendix A). Without any ligand exchange procedure, the films are insulating due to the long oleylamine ligands capping each individual platelet. Those ligands are exchanged toward shorter ones using solid-state ligand exchange approach (see section 1.2.2). The film is dipped into a diluted solution of the new ligands in acetone for 90 seconds, then rinsed in clean acetone. Once the film is dry, another layer of material is deposited and ligand-exchanged. The process is repeated five to six times to build a  $\simeq 100$  nm film. A quick, 10 s annealing at 120°C is then performed to dry the sample. The ligands we use in this study are ethanedithiol (EDT) and sulfide ions ( $S^{2-}$ ), from  $Na_2S$ . Upon ligand exchange, the main absorption features red-shifts to 1.35 eV ( $\simeq 920$  nm), consistent with a small delocalization of the wave-functions and of an increased inter-platelet coupling.

The films of EDT-capped and sulfide-capped HgTe NPLs are then integrated into a top-gate electrolytic field-effect transistor (FET) configuration, see section 1.2.3. Typical transfer curves for those two samples are given in Figures 2.5a and b. Those two curves show that conductance in EDT-treated films is maximized under hole injection, indicating a p-type behavior. On the contrary, conductance is maximized under electron injection for sulfide-treated films, indicating a n-type behavior. The two transfer curves are actually ambipolar: the conductance rises under both hole and electron injection, but the majority carrier mobility for both materials (linked to the slope of the curve, see Equation 1.16) is at least ten times higher than that of the minority carrier. It is hence possible to tune the majority carrier in HgTe NPL films by choosing the capping ligand: EDT leads to holes being the majority carriers while sulfide leads to electrons being the majority carriers.

Using photoemission on the Tempo beamline of Soleil synchrotron, we were able to reconstruct the energy diagram of both materials in absolute energy scale, see Figure 2.5c. In the case of EDT-treated films, we find the Fermi level just below the middle of the gap, in good agreement with the slight p-type behavior observed in FET measurements. The Fermi level of sulfide-capped material is found almost resonant with the conduction band, again in perfect agreement with the strong n-type doping suggested by the FET data. Interestingly, the work function is found to be quite similar for both materials, around 4.4 eV.

X-ray photoemission is also used to probe the core levels of the material, and especially the mercury core levels. The mercury 4f levels appear as a doublet  $4f_{5/2} - 4f_{7/2}$  with a  $\simeq 4$  eV spin-orbit splitting, and centered around a binding energy of 102 eV, see Figure 2.5. Mercury core levels from the sulfide-treated film are found at a slightly lower binding energies than those of EDT-treated films ( $\simeq 200$  meV shift), indicating that mercury states in sulfide-capped NPLs are relatively more electron-rich, again in agreement with the observed trend. As the top-surface (large exposed facet) of our HgTe NPLs are terminated with  $Hg^{2+}$  cations, the doping origin is likely due to a strong hybridization of mercury surface states with the ligands in the case of sulfide ions: when for EDT-capping, the sulfur

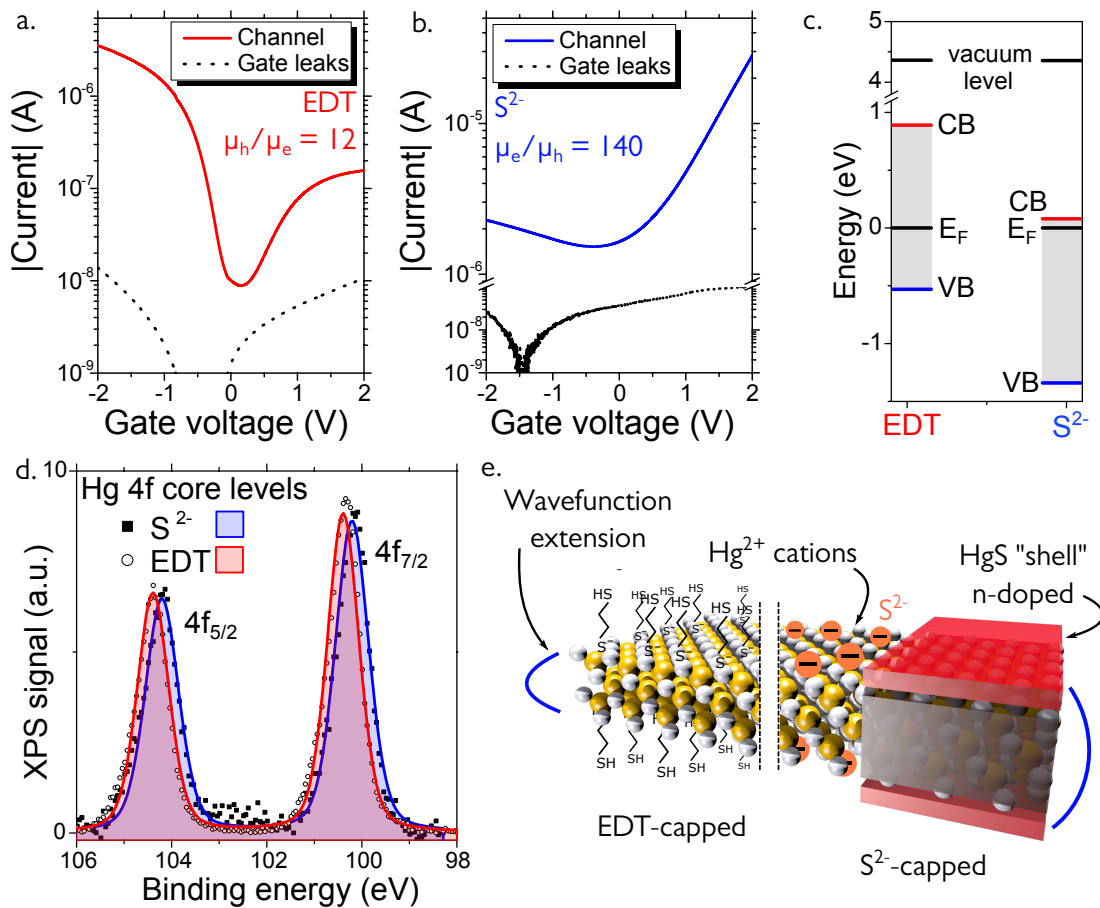


Fig. 2.5 Effect of ligand exchange on electrical properties of HgTe nanoplatelets arrays. **a.** Transfer curve of an EDT-treated HgTe NPL film showing an ambipolar behavior with a strong p-type character. Source-drain voltage is 0.5 V. **b.** Transfer curve of an  $S^{2-}$ -treated HgTe NPL film showing an ambipolar behavior with a strong n-type character. Source-drain voltage is 0.5 V. **c.** Energy spectra of both EDT (left) and  $S^{2-}$ -treated films (right) in absolute energy scale, reconstructed using a combination of photoemission and absorption spectroscopy. **d.** Photoemission spectra of mercury 4f core levels, for films of EDT- (red) and  $S^{2-}$ -treated (blue) HgTe NPLs. The peaks are fitted to a single contribution. The lower relative binding energy for the case of  $S^{2-}$ -capped films indicates that the mercury states are more electron-rich. **e.** Scheme of an HgTe nanoplatelet explaining the difference of doping between EDT and sulfide-capped material. The hybridization of sulfide ions with surface mercury cations is much stronger than the hybridization with sulfur atoms in the EDT chains, leading to the formation of a HgS "shell" at the surface of the platelet.

atoms bind weakly with the surface of the platelets, sulfide ions can hybridize strongly with the surface mercury cations, effectively leading to the formation of an electron-rich HgS monolayer "shell", as pictured in Figure 2.5e. This is interesting to note that introducing anions on cation-terminated nanocrystals is the first step of colloidal Atomic Layer Deposition (c-ALD), a technique used to grow layer-by-layer shells on nanocrystals in solution [180]. Nevertheless, this dramatic change of carrier density is not usually observed on HgTe quantum dots (spherical nanocrystals): in the NPL form, the exposed facets are not the same as in the 0D case, and notably the perfect flatness of the [100] top and bottom surfaces allows for a much higher ligand coverage and binding. In combination with the low thickness of the nanoplatelet, ligands capping those surfaces are indeed expected to have a strong effect on the nanoplatelet.

### 2.2.3 DC transport in photoconductive devices

EDT- and sulfide-capped HgTe NPL films show photoconductivity when exposed to 808 nm light (*i.e.* just above the band-edge of the material), see Figure 2.6a. Indeed,  $I(V)$  curves at room temperature show ohmic behavior and positive photoresponse for both surface chemistries, but the observed modulation ( $I_{\text{Photo}}/I_{\text{Dark}}$ ) is much stronger in the case of EDT-capped material than in the case of sulfide. This is due to the almost degenerative doping of sulfide-capped material. For EDT-capped material, the Fermi level lie in the middle of the gap and the density of thermally activated holes  $p_{\text{dark}}$  is low. As a result, under illumination the injected density of holes is much higher than the thermal one, resulting in a strong modulation of the hole density  $\Delta p = p_{\text{light}} - p_{\text{dark}} \simeq p_{\text{light}}$ . In the case of sulfide-capped material, the Fermi level lies just below the conduction band, so the thermally activated electron density is high. As a result, illumination of this sample in the same conditions than the previous one leads to much weaker current modulation, because  $\Delta n = n_{\text{light}} - n_{\text{dark}} \simeq n_{\text{dark}}$ .

In the following, we mainly focus on EDT-capped devices because they present the best photoconduction performances. Cooling down those devices allows to extract the activation energy of this material. In this experiment, the device is enclosed in a closed-cycle Helium cryostat and cooled down. Every 25 K,  $I(V)$  curves in the dark and under illumination by a 808 nm laser are acquired, and the extracted current under 1 V bias is reported in Figure 2.6. The dark current in an infrared-sensing device is thermally activated through the activation of majority carrier density: this can be expressed by an Arrhenius law:

$$I_{\text{dark}}(T) \propto \exp\left(\frac{-E_A}{k_B T}\right) \quad (2.1)$$

An exponential fit of the dark current evolution with temperature at high temperature (typically between 300 K and 100 K) allows to extract this carrier density activation energy, here found around 250 meV. This value is expected to be around half the bandgap energy for a perfect semiconductor. Under illumination, we can write that the current is given by:

$$I_{\text{light}} = (p_{\text{dark}} + p_{\text{light}}) \times \mu_h e E \quad (2.2)$$

Under the reasonable approximation that  $p_{\text{dark}} + p_{\text{light}} \simeq p_{\text{light}}$  under intense illumination, the current under illumination  $I_{\text{light}}$  is expected to stay constant while the material is cooled down. Figure 2.6 shows that it is actually decreasing with temperature: this is a signature of *mobility activation*, mainly related to hopping activation in our disordered arrays of nanocrystals. As for the dark current, we can write an Arrhenius law for the hole mobility:

$$\mu_h(T) \propto \exp\left(\frac{-E_{A,\mu}}{k_B T}\right) \quad (2.3)$$

And a high temperature fit of the current under illumination yields a value of  $E_{A,\mu} = 20$  meV for the hole mobility activation.

Now that we have the confirmation that transport and DC phototransport can be realized with films of ligand-exchanged HgTe nanoplatelets, we desire to investigate the dynamics of these processes. To do so, we need time-resolved techniques that we can apply at the device scale.

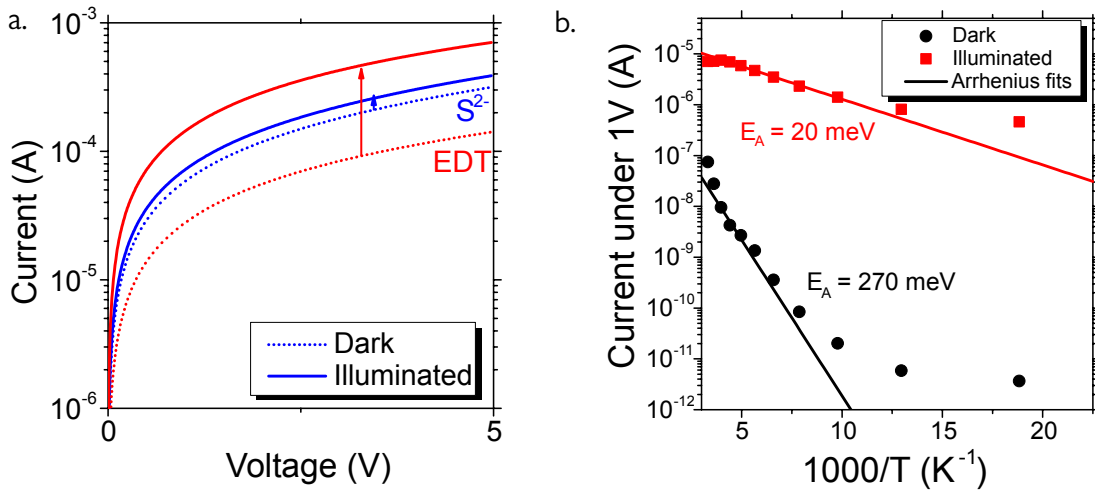


Fig. 2.6 HgTe NPLs film characterization under illumination. **a.** I-V characteristics of EDT- (red) and sulfide-capped (blue) HgTe NPL films in the dark (dashed lines) and under illumination by a few mW of 808 nm laser, at room temperature. **b.** Characterization of an EDT-capped HgTe NPL film at low temperature. Current under 1 V bias is extracted from the  $I(V)$  curves in the dark and under illumination, allowing to extract the thermal activation of the dark carrier density as well as the thermal activation of the mobility.

## 2.3 Probing low-frequency phototransport dynamics under gate control

As a first step toward the study of device and carrier dynamics, I focused on the development of experimental setups to probe the photocurrent dynamics in a low frequency range, that is in the continuous to 10 kHz range. Those experiments are always a good starting point to explore the photo-carrier dynamics in films of nanomaterials, because they give access to a glimpse of temporal resolution without the need of complex pump-probe configuration. From this point of view, those experiments are very unambiguous, and offer a lot of additional information compared to DC measurements.

The addition of the gate control gives an additional knob to tune the material properties: by injecting holes or electrons in a nanocrystal film, we can probe the effect of those additional carriers on the photocurrent dynamics.

### 2.3.1 A first experimental setup to probe photocurrent dynamics in the low frequency range

An experimental setup offering time resolution as well as carrier injection control through field effect is presented in Figure 2.7. In this setup, we use the typical ion-gel gating strategy presented earlier. The device is built on a glass slide with interdigitated electrodes, on which are deposited a film of ligand-exchanged nanocrystals. The gate consists in a drop of polyethyleneglycol (PEG) containing  $\text{Li}^+$  and  $\text{ClO}_4^-$  ions, brushed on top of the film and dried overnight. This semi-solid gate enables the gating of thick films in air, using low biases due to the very large gate capacitance, as described previously in section 1.2.3. Because this PEG gate is poorly transparent, illumination of the device must be provided from the back-side, through the glass substrate.

Illumination is provided by a laser source which is either optically or electrically chopped. Gate and drain bias are controlled by a dual-channel source-meter. The current is either measured directly by the source-meter if the chopping frequency is below 5 Hz, or fed into a transimpedance amplifier and acquired with an oscilloscope. Because the device is in a field-effect transistor configuration, the

drain bias must stay low compared with the gate bias. Practically speaking, we usually use a 100 mV drain bias, while the gate bias is scanned between -2 V to 2 V.

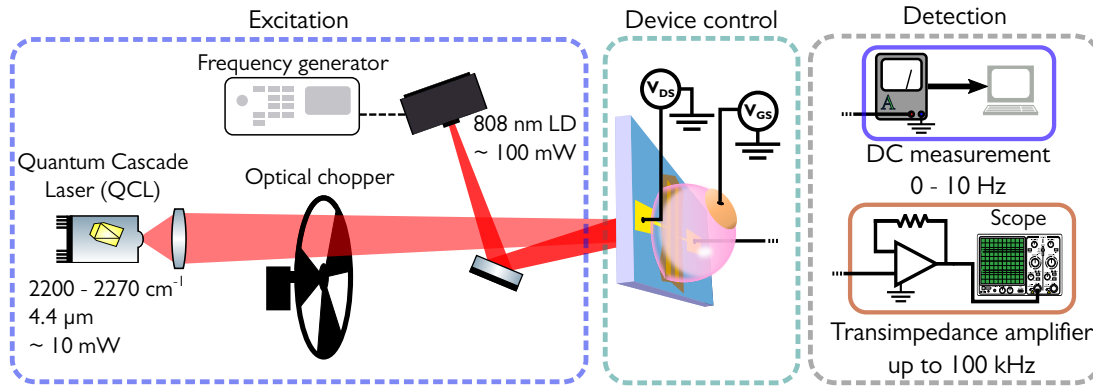


Fig. 2.7 An experimental setup to probe photocurrent dynamics under gate control at low frequency. The source is here either a 808 nm laser diode (up to 100 mW) or a 4.4  $\mu\text{m}$  optically chopped Quantum Cascade Laser (QCL). The sample is illuminated from the back side, under gate and drain bias. Photocurrent is measured directly by the source-meter (for modulations < 10 Hz) or through a transimpedance amplifier connected to an oscilloscope (for modulations between 10 Hz and 100 kHz).

### 2.3.2 Transport dynamics in HgTe NPL under gate control

The material we studied in the configuration were EDT-capped HgTe nanoplatelets, because they present the best DC modulation under illumination. Using a 808 nm laser source, we excite the interband transition of HgTe NPL. Data obtained under gate control and for a 100 Hz modulated light are presented in Figure 2.8a. The photoresponse dynamics of this material is clearly tuned under gate bias: under electron (*i.e.* minority carrier) injection at positive gate biases, the response of the device is strongly accelerated compared to the dynamics observed under hole (*i.e.* majority carrier) injection. Evolution of the rising and falling times, measured on photocurrent traces with exponential fits, are provided in Figure 2.8b. The holes can circulate in this material as long as they do not get trapped in the shallow hole trap states above the valence band. Under negative gate biases, the hole trap states get filled by injected holes, increasing the lifetime of photo-generated holes in the conduction band and slowing the photoresponse of the material. Under electron injection though, those traps are emptied, allowing for a fast photocurrent dynamics. Under large electron injection, photocurrent dynamic start to be slower because electrons are now the majority carrier, and their traps are filled [106, 115]. The time response as a function of gate bias (Figure 2.8b) actually reproduces almost perfectly the transfer curve of the device (see Figure 2.5a). In this configuration, the photocurrent dynamics are measured to be as fast as 100  $\mu\text{s}$ .

The current modulation brought by the light, defined by the ratio  $I_{\text{light}}/I_{\text{dark}}$ , is also extracted from the temporal traces of the photocurrent as pictured in Figure 2.8. Its evolution is monotonic under the range of explored gate voltages: the modulation (which scales as the detectivity of the device) is higher under electron injection. This is mostly an effect of dark current reduction under electron injection. A simple model, only relying on majority carrier densities, can be used to reproduce the observed current modulation. The thermally activated hole density can be expressed as:

$$p = \frac{m^*}{\pi\hbar^2} E_C \exp\left(-\frac{E_A}{k_B T}\right) \simeq 7 \times 10^{13} \text{cm}^{-2} \quad (2.4)$$

Where  $m^*/(\pi\hbar^2)$  is the 2D density of states,  $E_C$  the confinement energy (1.35 eV) and  $E_A$  the measured activation energy for dark current, see Figure 2.6b. Taking the response time at 0 V gate

bias to  $\tau = 1$  ms as the majority carrier (hole) lifetime and the absorption coefficient at 808 nm to  $\alpha = 7000 \text{ cm}^{-1}$  for a  $L = 1$  nm-thick platelet, the photogenerated hole density under a  $\phi_0$  photon flux is:

$$p_{\text{light}} = \phi_0 \tau \alpha L \simeq 2.6 \times 10^{13} \text{ cm}^{-2} \quad (2.5)$$

These estimations yields  $(p_{\text{light}} + p)/p = 1.4$ , which is in the same range as what is measured in Figure 2.8c.

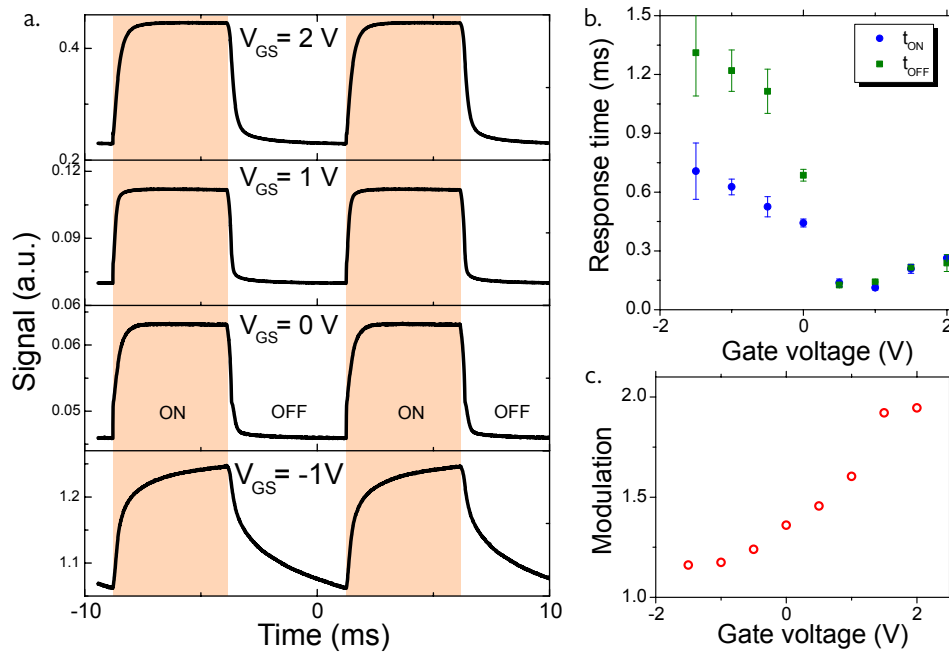


Fig. 2.8 Gate control of photocurrent dynamics in EDT-capped HgTe NPLs. **a.** Temporal traces of the photocurrent under electron injection ( $V_{GS} > 0$ ) and hole injection ( $V_{GS} < 0$ ). Orange sections corresponds to intervals where the film is illuminated by the 808 nm, 100 Hz-pulsed laser. **b.** Evolution of rise and fall times of the photocurrent, extracted from exponential fits of the temporal traces, under gate control. **c.** Evolution of the modulation (*i.e.*,  $I_{\text{light}}/I_{\text{dark}}$  ratio) under gate control.

We then wondered if that measured dynamics were limited by the material itself or by the device configuration: at that point, we needed another way to measure more intrinsically the carrier dynamics in a HgTe film.

## 2.4 Time-resolved photoemission

An alternative, unconventional technique to probe the carrier dynamics in films of nanomaterials is to use time-resolved photoemission spectroscopy. In this experiment, conducted at the Tempo beamline of Soleil synchrotron, we perform photoemission spectroscopy under pulsed laser excitation.

### 2.4.1 Principle and experiment

Time-resolved photoemission is a *pump-probe* technique where a sample is optically pumped by a laser excitation, and the probe consists in the photoelectrons resulting from the continuous X-ray illumination [181, 182].

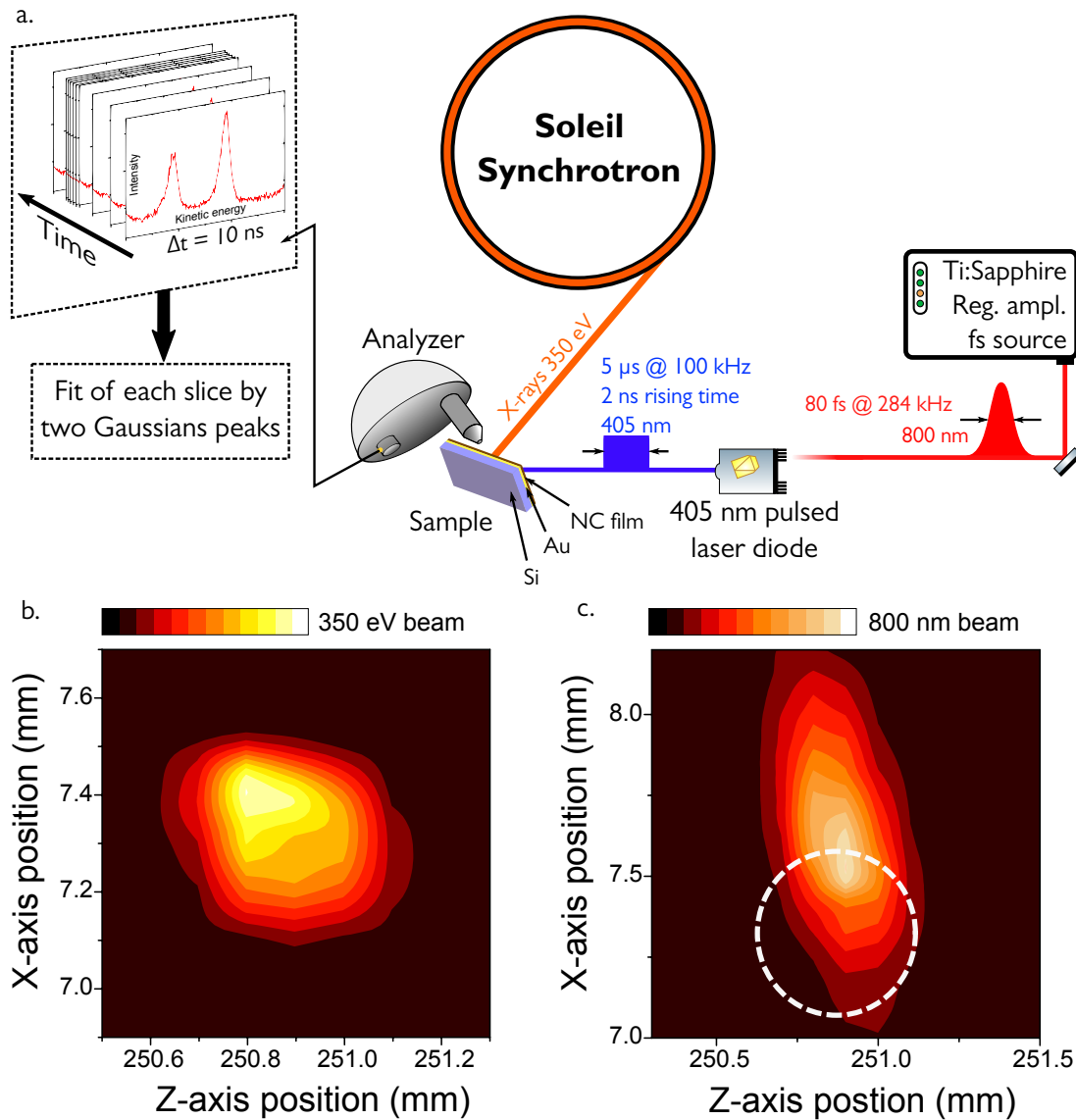


Fig. 2.9 Time-resolved photoemission spectroscopy experiment on the Tempo beamline of Soleil Synchrotron. **a.** Scheme of the setup. Sample is kept under ultra-high vacuum and illuminated by X-rays from the synchrotron source as well as by a pulsed laser. Photoelectrons are collected by the analyzer with a resolution of 10 ns. Laser source is either a blue,  $\mu\text{s}$ -pulsed blue (405 nm) laser source or a regeneratively-amplified Ti:sapphire ultrafast source around 800 nm producing 80 fs pulses. **b.** Intensity profile of the 350 eV X-ray synchrotron beam at the sample location. **c.** Intensity profile of the 800 nm, 80 fs laser at the sample location. The white dotted circle indicates the position and size of the X-ray beam.

The experimental setup for time-resolved photoemission spectroscopy is given in Figure 2.9a. The core of this experiment is a typical X-ray photoemission spectroscopy (XPS) setup, consisting in our case of a chamber under ultra-high vacuum, equipped with additional windows to allow the sample exposure to both X-rays and a laser beam. The X-ray source is a 350 eV monochromated beam from Soleil synchrotron. Just as in any XPS measurement, the sample is illuminated by X-rays and generated photoelectrons are collected by the analyzer, which discriminates them in energy before sending them onto a detector plate. We look here at the XPS signal coming from the core-levels of the material, *i.e.* at occupied states deep inside the valence band of our nanomaterials. A typical mercury core-level spectrum (obtained under regular XPS measurements on HgTe NPLs) was given previously in Figure 2.5d.

The sample is repeatedly pumped by an optical source, sending it in an excited level. In our experiment, we used either a blue, 405 nm electrically-pulsed laser diode or an ultrafast,  $\simeq 800$  nm regeneratively-amplified Ti:Sapphire laser. The blue diode produces square signals of 50% duty cycle at 100 kHz (that is 5  $\mu$ s pulses with 2 ns rising time), when the Ti:Sapphire laser delivers 80 fs pulses at 284 kHz. The two sources operates in the same range of continuous-wave average power (1 mW - 200 mW), but the peak power is obviously much higher for the femtosecond pulses.

The key difference between regular XPS and time-resolved XPS is that here, the electron detector plate is time-resolved: it is capable of acquiring an electron spectrum snapshot every 10 ns, as pictured in Figure 2.9a. The detector is synchronized with laser excitation, so it can deliver core-level spectra before and after the pump with a 10 ns resolution. It is worth mentioning that higher resolution ( $\simeq 50$  ps) can be obtained by using the temporal structure of the electron bunches in the synchrotron when the ring is working in a non-continuous mode. This strongly reduces the X-ray flux as well as requires to achieve temporal synchronization of the synchrotron ring with the laser [183].

The key step for this experiment to work is to realize a good pump-probe overlap at the sample position. This is done by carefully aligning the laser on the X-ray beam. As shown in Figure 2.9b, the X-ray spot can be located by using a single-pixel Si photodiode in the sample holder. By scanning its position around the sample location and monitoring the current, we retrieve the shape and position of the X-ray beam. We do the same thing for the laser beam, and as pictured in Figure 2.9c, and map the shape and position of the optical beam at the sample location (here, the fs laser). The beam appears elongated due to its rather wide angle of incidence with the sample plane. The spatial overlap between the two beams is realized by moving the laser beam and acquiring multiple maps until the beam positions look coincident enough, as pictured in Figure 2.9c.

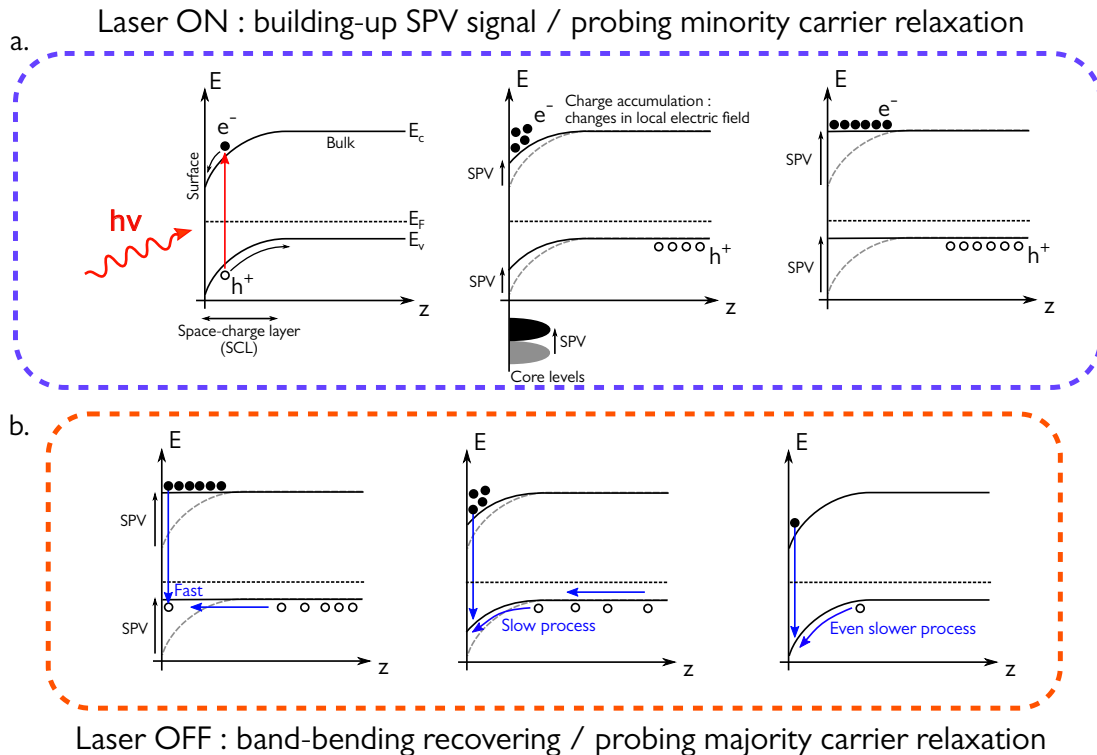


Fig. 2.10 Surface photovoltage process for a film of p-doped semiconductor such as EDT-capped HgTe nanoplatelets. **a.** Establishment of the surface photovoltage signal (SPV) when the laser source is turned on. **b.** Relaxation of the SPV when the laser source turns off.

In a classical semiconductor, time-resolved photoemission is a *surface photovoltage* (SPV) measurement. Figure 2.10 explains its principle in terms of band bending and photocarriers diffusion, for a p-type semiconductor. As pictured in Figure 2.10a, a p-type semiconductor features downward

band bending at the film/vacuum interface. The spatial extension of this band bending in the film thickness is called the *space-charge layer* (SCL). Upon illumination of the film, electron-hole pairs are created in the whole film. Because of the downward band bending, electrons will locate preferentially in the SCL when hole will diffuse from the SCL toward the bulk of the film. The electron accumulation in the SCL changes the local electrical field, which opposes the band bending: this is the *surface photovoltage*, or SPV. As pictured in the center panel of Figure 2.10a, the SPV can be seen as a surface voltage shifting the energy of the bands at the material/vacuum interface, and reducing the band bending. This SPV shift is *rigid*, meaning that the whole band structure of the material at the vacuum interface is shifted by the same amount as the conduction band. As a result, one can measure this SPV shift on the core levels of the materials: this is what time-resolved XPS aims at. This SPV shift will increase as the number of excitons in the film increases, the electron lifetime being here the limiting process. During the SPV signal building, it is then possible to probe the minority carrier relaxation: the faster the minority carrier relaxes, the faster the SPV signal saturates. The signal saturation occurs whenever the generation rate equals the recombination rate, or if the surface charge density is sufficient to achieve a flat band.

When the light is switched off, the SPV signal will disappear progressively as carriers recombine. Figure 2.10b pictures what occurs in a p-type semiconductor. As soon as electron-hole pair generation stops, the number of photo-generated carriers will decrease and the band bending will recover, localizing the electrons in the SCR. As a result, the photo-generated holes, mostly localized in the bulk of the film, have to diffuse up to the SCR to recombine with an electron. This process is self-decelerating, because the barrier seen by the holes gets higher as the carriers recombine and the band-bending is recovered. As a result, the relaxation of the SPV signals is related to the majority carrier diffusion and lifetime.

For our applications, it is worth mentioning that band bending is not occurring at the nanocrystal scale, because the characteristic size of the nanocrystals is much smaller than the depletion width, as it has been shown for several 2D or layerer materials [184–186]. The observed band bending with films of weakly coupled nanocrystals is more likely to occur at the film level. While its exact origin is unclear, it can be due to charge transfer between nanocrystals at the interface and nanocrystals from the bulk of the film.

### 2.4.2 HgTe NPL: probing electron and hole relaxation

The first material we investigated with time-resolved photoemission spectroscopy were HgTe nanoplatelets. Using the blue, 5  $\mu\text{s}$  pulsed laser source, we were able to observe SPV signal from both ethanedithiol- and sulfide-capped HgTe NPLs films. For these two samples, we looked at the mercury 4f core levels. As explained earlier, we take spectra snapshots every 10 ns and, as the detection is synchronized with the laser pulses, we average the signal over four to eight hours to maximize the signal-to-noise ratio. Each averaged Hg 4f spectra snapshot is then fitted with two Gaussian peaks ( $4f_{7/2}$  and  $4f_{5/2}$  contributions). Figure 2.11a and b presents the actual time-resolved SPV data: the binding energy of the  $4f_{7/2}$  peaks extracted from the fits, as a function of time during a full cycle of the laser.

In the case of EDT-capped HgTe NPLs, presented in Figure 2.11a, the Hg 4f core levels shift toward *lower* binding energies under illumination. A lower binding energy means that the photoelectrons extracted from this core level have a higher kinetic energy ( $BE + KE = h\nu$ ), hence that the core levels are shifting upward in absolute energy scale. In other words, this is exactly the situation describes in Figure 2.10a: EDT-capped HgTe NPLs behave just as a p-type semiconductor, confirming again what was observed using transistor (Figure 2.5a) and photoemission (Figure 2.5c) measurements.

On the contrary, data obtained on sulfide-capped films of HgTe nanoplatelets show a shift of the Hg  $4f_{7/2}$  core-level toward *higher* binding energy, that is a shift of the core-levels away from the Fermi

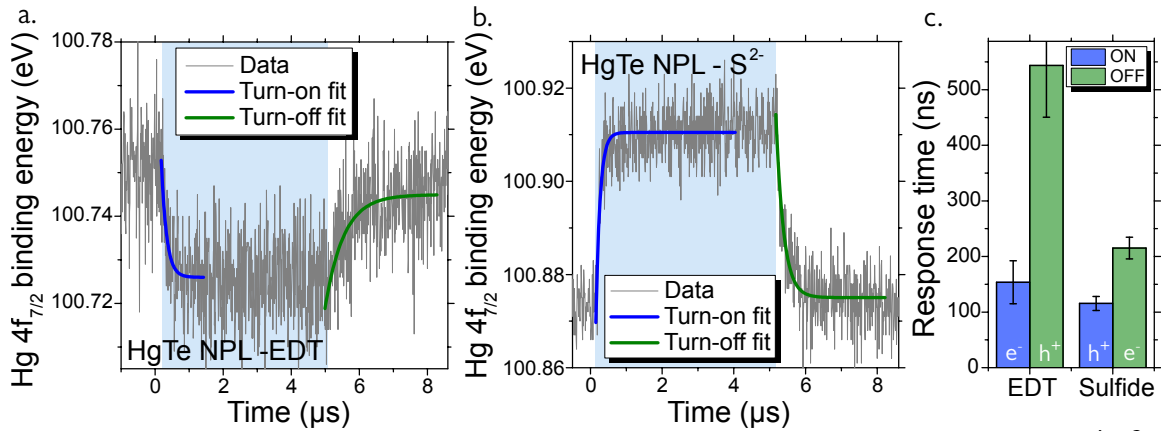


Fig. 2.11 Time-resolved photoemission with HgTe nanoplatelets under 200 kHz illumination. **a.** Binding energy of the Hg  $4f_{7/2}$  core level under illumination by a 405 nm laser ( $\approx 100$  mW) for a EDT-capped HgTe NPL film. The core levels shifts toward lower binding energies under illumination. Single-exponential fits of the signal rise (related to minority carrier) and fall (majority carrier) are given in blue and green, respectively. **b.** Binding energy of the Hg  $4f_{7/2}$  core level under illumination by a 405 nm laser ( $\approx 100$  mW), for a  $S^{2-}$ -capped HgTe NPL film. The core levels shifts toward higher binding energies under illumination. Single-exponential fits of the signal rise and fall are given in blue and green, respectively. **c.** On- and off-times extracted from the exponential fits of the SPV signal. For each material, the corresponding majority and minority carriers have been indicated.

energy. This is what would be expected for a n-type semiconductor, which features upward band bending in the SCR. This is again a proof that the majority carrier can be tuned from hole to electron in HgTe NPLs by choosing either EDT or  $S^{2-}$  as a capping ligand.

In this regime of illumination, we can clearly define a rising time and a decay time of the SPV signal for both materials. Exponential fits are given in Figures 2.11a and b, and the corresponding characteristic times are provided in Figure 2.11c. For both materials, the turn-on time, relating to minority carrier relaxation, is fitted around 100 to 150 ns. This characteristic time is much shorter than the one measured in photocurrent traces (around 100  $\mu$ s, see Section 2.3.2 and Figure 2.8). The ratio  $\sim 1000$  between the two measurements can be related to the ratio of transport scale. In photocurrent measurement, transport occurs in the film plane between two electrodes separated by 20  $\mu$ m, while in SPV measurement it occurs in the thickness of the film (from the surface of the film toward the bulk). The typical film thickness for XPS measurements is around 50 nm: there is indeed a ratio  $\sim 1000$  between the transport length in the two experiments. Taking a diffusion length of  $L_d = 50$  nm, we can also estimate the material mobility:  $\mu = L_d^2 e / (\tau_{SPV} k_B T) = 10^{-2}$   $\text{cm}^2 \text{V}^{-1} \text{s}^{-1}$ , in good agreement with the typically reported values of  $10^{-3} - 10^{-2}$   $\text{cm}^2 \text{V}^{-1} \text{s}^{-1}$  for mobility of EDT-capped nanocrystals solids. This also suggests that devices with much faster photoresponse could eventually be built by taking advantage of a device size reduction toward the diffusion length.

We then probed the SPV response of EDT-capped HgTe NPL films under illumination with the 800 nm, 80 fs ultrafast laser. As stated earlier, the time resolution of our experiment is given by the time resolution of the electron detector,  $t_{\text{detector}} = 10$  ns. Here, the pump pulse length  $t_{\text{pump}} = 80$  fs  $\ll t_{\text{detector}}$ , so we cannot resolve any rising time of the SPV signal. Under those conditions, we consider the pump pulse as an instantaneous way of injecting a large number of electron-hole pairs, and that we only observe their decay with a 10 ns resolution. Just as what was presented in the previous set of data, Figure 2.12a shows the temporal traces of the Hg  $4f_{7/2}$  core level binding energy, for different pump power. The observed core-level shift is again negative here, as we found when using the blue laser source on EDT-treated films.

The key observation from those experiment is that the decay time of the SPV signal, fitted by

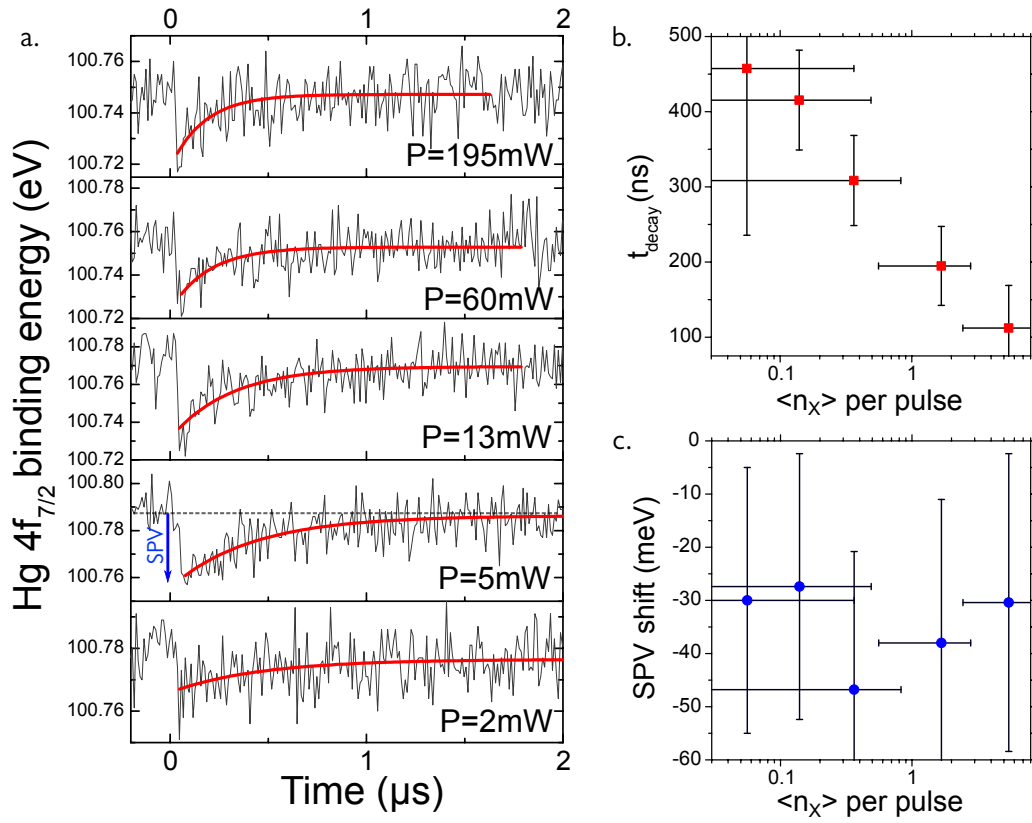


Fig. 2.12 Time-resolved photoemission with HgTe nanoplatelets under ultrafast excitation. **a.** Temporal traces of the Hg  $4f_{7/2}$  core level binding energy in a EDT-capped HgTe NPL film, for different illumination power. A single-exponential fit of the SPV signal decay is provided in red. Intensity of the SPV signal is indicated by the blue arrow. **b.** SPV decay time extracted from the exponential fit of the data. The illumination power have been converted into an average number of excitons injected by the 800 nm, 80 fs pulse. **c.** Intensity of the SPV signal (*i.e.* binding energy shift after the laser pulse) for the different regimes of illumination.

exponentials in Figure 2.12a, seems to be strongly dependent on the illumination power. It is measured to be around 450 ns at 2 mW of average power, in good adequation with the 500 ns measured with the blue laser excitation, but is strongly reduced as the incident power is increased, down to 100 ns under 195 mW of average power. An explanation of this observation can be provided by considering the average amount of excitons created in a nanoplatelet under optical excitation by the two lasers.

Under illumination by the 5  $\mu$ s-pulsed , 405 nm laser, we can estimate the average number of injected excitons per NPL by:

$$\langle N_X \rangle = \sigma_{\text{NPL}} \phi_d \tau_X \quad (2.6)$$

Where  $\sigma_{\text{NPL}}$  is the absorption cross-section of a NPL,  $\phi_d$  the photon flux density and  $\tau_X$  the exciton lifetime, taken at 10 ns with a very conservative assumption. Throughout this manuscript, we will approximate the absorption cross-section of HgTe nanocrystals to be around  $\sigma_{\text{NPL}} \sim \sigma_{\text{HgTe}} \approx 10^{-14} \text{ cm}^{-2}$ . The actual value is probably slightly higher for HgTe NPL and slightly lower for HgTe quantum dots, but this approximation allows to consistently evaluate the order of magnitude of injected excitons for several experiments and materials. Reported values of this cross-section in relevant nanomaterials are around  $10^{-13} \text{ cm}^{-2}$  for 4 monolayers, 200 nm<sup>2</sup> CdSe NPL [187] and around  $5 \times 10^{-15} \text{ cm}^{-2}$  for 0D HgTe quantum dots [188]. Under the flux densities used in the previous experiment (with the blue laser), we find an average of  $\langle N_X \rangle = 10^{-3}$  exciton per NPL, well below unity.

On the other hand, for the ultrafast laser, since  $t_{\text{pump}} \ll \tau_X$ , the average number of injected excitons per NPL and per pulse is:

$$\langle N_X \rangle = \sigma_{\text{NPL}} \frac{E_{\text{pulse}}}{h\nu} \quad (2.7)$$

Where  $E_{\text{pulse}}$  is the pulse energy per  $\text{cm}^2$ , calculated from the average power density  $P_{\text{CW}}$ , the pulse length  $t_{\text{pulse}}$  and the repetition frequency  $f_{\text{rep}}$ :  $E_{\text{pulse}} = P_{\text{CW}} \times t_{\text{pulse}} f_{\text{rep}}$ . As indicated in the x-axis of Figure 2.12b, an average power of 2 mW leads to  $\langle N_X \rangle \simeq 10^{-2}$  exciton per NPL and per pulse. As a result, under a few mW of fs-laser, we are typically in the same sub-exciton per NPL regime as when using the blue laser.

Under higher excitation power though, the average number of injected excitons per pulse  $\langle N_X \rangle$  can exceed one and reach values of around 5 excitons per NPL, so one can expect multi-excitonic Auger recombination to become important. As a result, the measured relaxation time being an average over a large number of NPLs, the increasing probability of Auger multi-excitonic decay at high excitation leads to an apparent reduction of the observed lifetime. The intensity of the SPV signal does not change dramatically with the pump intensity, as pictured in Figure 2.12c, which might indicate that the flat band (total compensation of the band bending) is achieved even under low excitation.

### 2.4.3 Toward more complex heterostructures and limitations

More recently, we investigated other materials with the same time-resolved photoemission technique. Notably, we wanted to investigate the impact of dimensionality and barrier confinement on the photocarrier dynamics in HgTe material. Using HgTe NPLs (1.4 eV bandgap) as a reference material, we measured in the same conditions samples made of HgTe/CdS type I core-shell nanoplatelets (1 eV bandgap) and of HgTe quantum dots with a similar bandgap around 0.9 eV. Figure 2.13a and b gives a scheme of the materials as well as their schematic band diagram. All materials are capped with ethanedithiol (EDT) ligands.

Core-shell nanoplatelets are grown using colloidal-Atomic Layer Deposition (c-ALD), where the shell is built layer-by-layer by alternatively exposing the platelets to the shell anions ( $\text{S}^{2-}$ ) and cations ( $\text{Cd}^{2+}$ ), until a thickness of 3 monolayers is reached. Resulting objects feature red-shifted optical properties when compared to the core-only HgTe NPLs: this is due to a loss of confinement, the wave-function extension being much higher in the high bandgap shell than in the ligands of the core objects [189].

Figure 2.13c shows the temporal traces of the mercury  $4f_{7/2}$  core-level, measured under optical excitation with the 800 nm Ti:sapphire laser. The incident power is set to be in the  $\simeq 1$  exciton per nanocrystal regime. In this regime, both the SPV relaxation times of HgTe NPLs and HgTe QDs are measured to be around 250 ns. The relaxation time of HgTe/CdS nanoplatelets, on the other hand, appears much longer, measured here around 850 ns. In other words, the change of nanocrystal dimension (from 2D to 0D) does not seem to affect the majority carrier (holes) relaxation, while the presence of a wide bandgap CdS shell have a much stronger impact. This is due to the fact that in those HgTe/CdS NPLs, absorption occurs in the core of the object (because the wide bandgap shell does not absorb at 800 nm), and that the SPV relaxation occurs through majority carrier diffusion in the film. An increased SPV relaxation time indicates that the photogenerated holes localize in the core of the platelet, and that wide-bandgap shell acts as an additional barrier for the carrier hopping, decreasing the hopping time and diffusion length.

As powerfull and interesting as it is, this time-resolved XPS technique seems nevertheless limited to a narrow range of nanomaterials. Despite having tried this experiment on numerous samples, we only obtained exploitable results (with a significant signal-to-noise ratio) with nanomaterials featuring

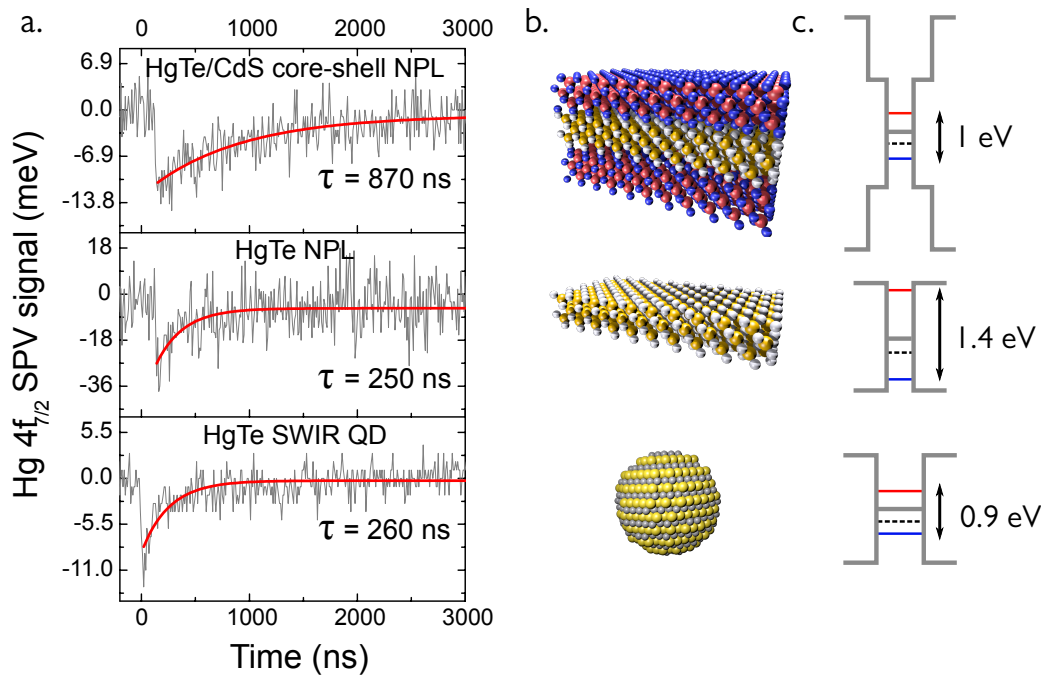


Fig. 2.13 Time-resolved photoemission with HgTe nanocrystals: effect of shelling and dimensionality. **a.** Temporal traces of the Hg  $4f_{7/2}$  core level binding energy for three HgTe-based, EDT-capped nanomaterials. Top: HgTe/CdS core-shell nanoplatelets. Middle: HgTe nanoplatelets (3 MLs). Bottom: small HgTe quantum dots with absorption in the SWIR. For the three materials, a single-exponential fit of the data is given in red. **b.** Scheme of each material. **c.** Scheme of the materials band diagram. The bulk band alignment is given in grey, and position of discrete confined levels is indicated as measured with XPS (blue is VB, red is CB). The Fermi level position (determined with XPS) is indicated with a dashed black line.

bandgaps around 1 eV to 1.5 eV. In narrower bandgap materials (HgTe, HgSe nanocrystals), the observed shifts are too small ( $<5$  meV when observed) to be significant, when higher bandgaps materials (CdSe NPLs, CsPbBr<sub>3</sub> cubes) are usually susceptible to charging effects.

## 2.5 Conclusions

In this first result chapter, we used mercury telluride nanoplatelets as a platform to investigate photocurrent and carrier dynamics at the device scale. This new material might offer promising opportunities for near-infrared detecting or emitting devices, especially as an alternative to lead sulfide nanocrystals. I showed that in this two-dimensional material, the capping ligands have a dramatic effect on the transport properties, and we were able to tune the majority carriers to obtain n- or p-type devices just by choosing different capping ligands. I then studied the photocurrent dynamics using a rather straightforward experiment, and found that the time response of the device can be tuned over one order of magnitude by applying a gate bias. In this configuration, the fastest dynamics were measured to be around  $\sim 100$   $\mu$ s, and we wondered if we could relate this time to the carriers lifetime in the film. To answer this question, we used time-resolved photoemission spectroscopy in Soleil synchrotron, and measured the hole and electron lifetime to be around 100 to 500 ns, respectively. We also applied this unusual experimental technique to other 2D and 0D nanomaterials.

In the next chapter, we continue to be interested in transport and carrier dynamics in nanocrystal-based devices, but shift to a *redder* material, with optical properties in the Mid-Wave Infrared.

# Chapter 3

## Photocurrent dynamics and carrier multiplication in HgTe MWIR nanocrystals

---

<b>3.1</b>	<b>Mercury Telluride nanocrystals for Mid-Wave Infrared photodetectors . . . . .</b>	<b>60</b>
<b>3.2</b>	<b>Band-edge dynamics and multiple exciton generation in Mid-Wave Infrared HgTe devices . . . . .</b>	<b>62</b>
<b>3.3</b>	<b>Transient photocurrent measurements . . . . .</b>	<b>67</b>
<b>3.4</b>	<b>Probing dynamics in perovskite photodetectors: toward efficient carrier transport . . . . .</b>	<b>70</b>
<b>3.5</b>	<b>Conclusion . . . . .</b>	<b>72</b>

---

### Related articles

- C. Livache, N. Goubet, B. Martinez, A. Jagtap, J. Qu, S. Ithurria, M.G. Silly, B. Dubertret and E. Lhuillier, "Band Edge Dynamics and Multiexciton Generation in Narrow Band Gap HgTe Nanocrystals", *ACS Applied Materials and Interfaces* 14, 11880-11887 (2018)
- B. Martinez, C. Livache, N. Goubet, A. Jagtap, H. Cruguel, A. Ouerghi, E. Lacaze, M.G. Silly and E. Lhuillier, "Probing Charge Carrier Dynamics to Unveil the Role of Surface Ligands in HgTe Narrow Band Gap Nanocrystals", *Journal of Physical Chemistry C* 122, 859-865 (2018)
- W.J. Mir, C. Livache, N. Goubet, B. Martinez, A. Jagtap, A. Chu, N. Coutard, H. Cruguel, T. Barisien, S. Ithurria, A. Nag, B. Dubertret, A. Ouerghi, M.G. Silly and E. Lhuillier, "Strategy to Overcome Recombination Limited Photocurrent Generation in CsPbX<sub>3</sub> Nanocrystal Arrays", *Applied Physics Letters* 11, 113503 (2018)

### Related communications

- "Transport and GHz Phototransport Reaching Recombination-Limited Dynamics in CsPbX<sub>3</sub> Quantum Dots Solids", MRS Spring Meeting 2018, Phoenix AZ, USA.
- "Alternative Time-Resolved Techniques to Probe Dynamics in Narrow Bandgap Nanocrystals" Colloidal Nanocrystal Workshop 2018, Sorbonne University, Paris.

This chapter is written in the same spirit as the the previous one: probing carrier dynamics with transport-based experiments, at the device scale. This time, we go deeper in the infrared as we focus on Mid-Wave Infrared-absorbing mercury telluride nanocrystals: we want to understand the band-edge dynamics of this materials and to explore the photophysics of such narrow-bandgap nanocrystals. The first section presents the material and DC transport and phototransport experiments. In the second section, I present the study of photocurrent dynamics at the band-edge of the material, as well as carrier multiplication effects in HgTe MWIR sensing devices. Finally, in the last section I present a new experiment to probe transient photocurrents in a wide variety of photoconductive samples, allowing to extract material-related properties and to get deeper insights on the electronic structure from a transport measurement.

## 3.1 Mercury Telluride nanocrystals for Mid-Wave Infrared photodetectors

As previously presented in section 1.3.3, the infrared range can be addressed using interband HgTe nanocrystals. Featuring low energy  $1S_h \rightarrow 1S_e$  transitions around  $2000 \text{ cm}^{-1}$  ( $\simeq 300 \text{ meV}$ ), HgTe "2k" nanocrystals are an interesting platform to probe photocarrier dynamics in the Mid-Wave Infrared (MWIR). Those nanocrystals are currently the most advanced nanomaterials for integration into MWIR-sensing devices: material and devices have been continuously improved since the first device report in 2011 [132], and the most recent works achieve near unity quantum efficiency and detectivities of  $10^9 \text{ Jones}$  at 230 K at 4 to 5  $\mu\text{m}$  ( $2500\text{-}2000 \text{ cm}^{-1}$ ) using this material [162].

### 3.1.1 Optical properties and energy levels

HgTe 2k nanocrystals are synthesized by Nicolas Goubet using a procedure described in appendix A. Figure 3.1a shows the typical absorption spectrum of those nanocrystals capped with their long dodecanethiol (DDT) ligands. Because of their large size (see Figure 3.1b), the colloidal stability of those nanocrystals is quite poor, and they are particularly not stable in the hexane:octane mixture typically used for drop-casting. The films are then obtained by dip-coating the pre-patterned gold interdigitated electrodes on glass into the NC suspension in chloroform. The ligands are then exchanged toward ethanedithiol (EDT) by dipping the film in a solution of EDT in ethanol for 90 s, then rinsing in ethanol. The process is repeated six times to build a  $\simeq 100 \text{ nm}$  smooth film. All this process is conducted in a nitrogen-filled glove box. Figure 3.1a also shows how the optical spectrum of HgTe 2k is affected by the ligand exchange: there is a notable red-shift, consistent with wave-function delocalization, as well as a broadening of the optical features. The strongly reduced intensity of the C – H absorption peaks around  $2800 \text{ cm}^{-1}$  is a signature of the ligand-exchange process effectiveness.

Field-effect transistor measurements, presented in Figure 3.1b, indicates an ambipolar conduction (conduction under both electron and hole injection), with a strong n-type doping. This is confirmed by photoemission: the energy diagram of the material is reconstructed in Figure 3.1c, and shows that the Fermi level lies just below the  $1S_e$  conduction band level. The narrowness of the gap, combined with the potency of the electrolytic gate, allows the Fermi level to be tuned over the whole material bandgap under  $-2$  to  $2 \text{ V}$  gate bias: this is the reason why we observe an ambipolar character even if the material is found to be strongly n-type with XPS. Interestingly, the combination of those two measurements allows to evaluate the potency of the electrolytic gate. Considering that the charge neutrality point (*i.e.* the gate voltage for which the channel current is minimum) in the transfer curve corresponds to a situation where the effective Fermi level lies in the middle of the HgTe NCs bandgap, we can estimate the leverage effect of the gate on the Fermi level position. The charge neutrality point is found at  $V_N = -670 \text{ mV}$  in Figure 3.1, when the energy distance from the Fermi level at zero gate bias and the middle of the gap is measured to be  $\Delta E = -120 \text{ meV}$ . As a result, the leverage effect

of the gate on the Fermi level position is around  $\Delta E/V_N \simeq 0.2$  eV/V. In other words, applying 1 V on the gate of our device allows to tune the Fermi level position by roughly 200 meV in the HgTe nanocrystals.

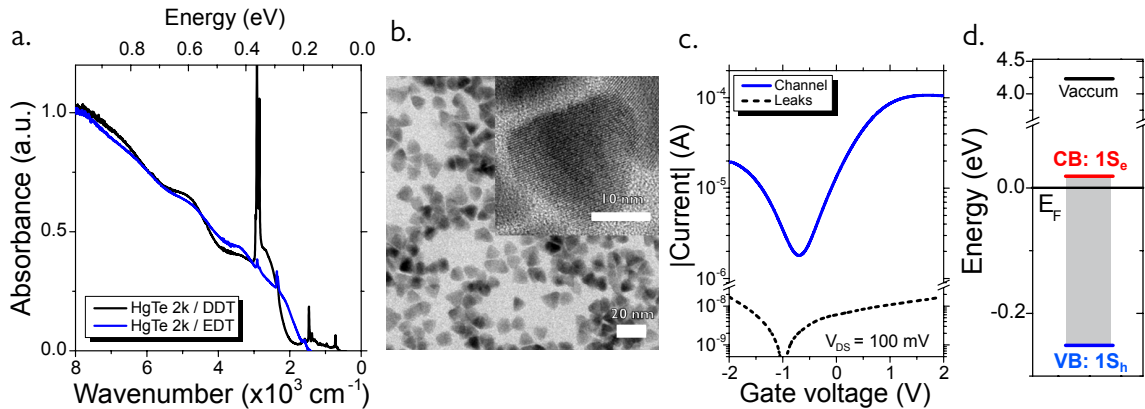


Fig. 3.1 HgTe Quantum Dots for Mid-Wave Infrared photodetection. **a.** Infrared absorption spectra of a film of HgTe NCs with a bandgap around  $2000\text{ cm}^{-1}$  (HgTe 2k) before and after ligand exchange from dodecanethiol (DDT, black curve) to ethanedithiol (EDT, blue curve). **b.** TEM picture of HgTe 2k material showing tetrahedral shape. Inset: High-resolution TEM image. **c.** Transfer curve of an EDT-capped HgTe 2k film in an electrolytic FET configuration, showing ambipolar character with a strong n-type behavior. Source-drain voltage is 0.1 V. **d.** HgTe 2k levels positions in absolute energy scale, reconstructed from XPS and infrared spectroscopy.

### 3.1.2 DC transport in MWIR-sensing photoconductive devices

Because it features a narrow interband bandgap, HgTe 2k films are photoresponsive to Mid-Wave Infrared light. In our study, we use a  $4.4\text{ }\mu\text{m}$  ( $2250\text{ cm}^{-1}$ ) Quantum Cascade Laser (QCL) as a MWIR source. Because we are interested in carrier dynamics and photophysics of the material, the devices are not tailored for high performances. Illumination with a QCL source offers a good flexibility in terms of light flux, allows pulsed operation and is relatively easy to set-up. Activation of the carrier density is pictured in Figure 3.2a: an Arrhenius fit of the dark current at high temperature gives a value of 90 meV for the dark current activation energy. Again, this value is below  $E_G/2$ , indicating the presence of traps. At low temperature ( $< 25\text{ K}$ ), the dark current can be fitted with an Efros-Shklovskii variable-range hopping law  $\exp\left((T/T_0)^{-1/2}\right)$ , which is typical for low-temperature hopping transport in disordered films of nanocrystals with a high density of states.

Figure 3.2 shows the current under  $V_{DS} = 1\text{ V}$ , extracted from  $I(V)$  curves in the dark and under few mW of QCL illumination. This graph shows the dramatic effect of temperature on the device signal-to-noise ratio, and is a good illustration of the need for cryogenic operation for infrared detectors. The photocurrent  $I_{\text{photo}} = I_{\text{light}} - I_{\text{dark}}$  is also provided: it stays roughly constant over the whole temperature range, but features a maximum around 175 K. This bell-shape of the photocurrent is often observed in disordered narrow-bandgap chalcogenides semiconductors [190], and is explained by the change of recombination mechanism. At high temperature, there is a large number of available thermally excited electrons for the photo-generated holes to recombine with: this is a *monomolecular* process where  $n_{\text{dark}} > n_{\text{light}}$ . As cooling down reduces the number of thermally activated recombination centers, the lifetime of the hole increases and the overall detector gain increases as well. When the thermal electron density  $n_{\text{dark}}$  becomes comparable to the photo-generated electron density  $n_{\text{light}}$ , recombination of the photo-generated hole now occurs with the photo-generated electron: the recombination is now a *bimolecular* process. In this regime, the photocurrent depends on the carriers mobility, which decreases with decreasing temperature.

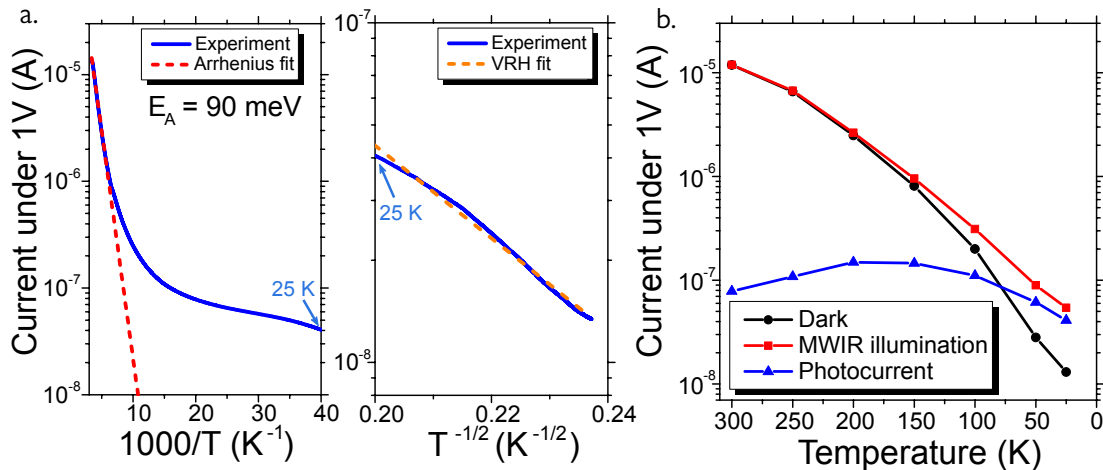


Fig. 3.2 Electrical properties of HgTe 2k films. **a.** Evolution of the current under  $V_{DS} = 1$  V while cooling down the device. Left: between 300 K and 25 K. The current evolution is fitted to Arrhenius law at high temperatures. Right: between 25 K and 15 K, the current can be fitted to Efros-Schklovski variable range hopping law. **b.** Current under  $V_{DS} = 1$  V, extracted from  $I(V)$  curves in the dark (black circles) and under illumination by a  $4.4 \mu\text{m}$  ( $2250 \text{ cm}^{-1}$ ) Quantum Cascade Laser (QCL) MWIR source (red squares). The photocurrent  $I_{\text{photo}} = I_{\text{light}} - I_{\text{dark}}$  is given in blue triangles.

## 3.2 Band-edge dynamics and multiple exciton generation in Mid-Wave Infrared HgTe devices

In the second part of this chapter, we are interested in carrier dynamics in HgTe quantum dots (0D nanocrystals) with an optical bandgap in the MWIR. We desire to probe the true device dynamics at the band-edge of the material. Indeed, previous reports about HgTe-based devices always provide photocurrent dynamics measured with high-energy photons (800 nm or 1064 nm, typically), because of a lack of a fast optical source in the MWIR. This can be quite detrimental for the comprehension of the system, because of the narrow-bandgap nature of our materials: it is very easy to provide illumination with photon energies several times bigger than the bandgap (in the MWIR, a 800 nm photon is already at least  $5 \times E_G$ ). As a result, one could expect a lot of non-desired effect to occur under such illumination, such as hot carrier generation and carrier multiplication, that might strongly affect the observed carrier dynamics.

### 3.2.1 MHz dynamics at the band-edge of MWIR HgTe nanocrystal-based devices

In our experiment, MWIR photons are provided by a  $4.4 \mu\text{m}$  Quantum Cascade Laser from the French company MirSense. This laser is electrically pulsed, with the pulse length being tunable from 20 ns to 495 ns. In the typical experiment, we use a  $5 \mu\text{s}$  repetition rate, allowing the laser to work with a 0.4% to 10% duty cycle. Figure 3.3a presents the optical and electrical setup used for this experiment. The device is enclosed in a cryostat, and illumination from the QCL is provided through an optical window. The laser is focused to be around  $1 \text{ mm}^2$  around the device area. Bias is provided by a 9 V battery, and photocurrent is acquired through a  $50 \Omega$  current shunt. The voltage drop at the shunt is amplified using a Femto DUPVA GHz voltage amplifier with a 50 dB gain, then fed into a 12 GHz sampling oscilloscope.

Because the QCL driver was extremely electrically noisy at the time of this study, special care was taken during these experiments to reduce the impact of this noise on measurements. Particularly, coaxial cables are reduced to their minimal length, signal amplification is performed directly

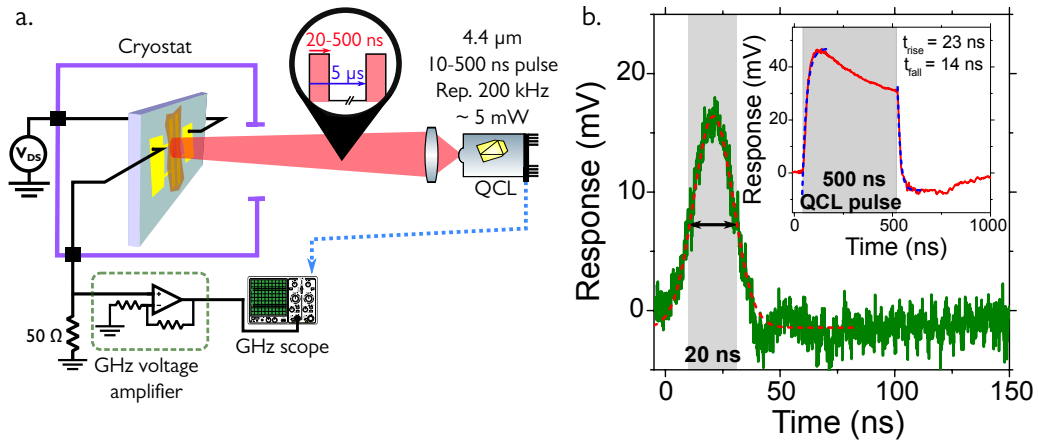


Fig. 3.3 Fast band-edge dynamics in HgTe MWIR photodetectors. **a.** Scheme of the experiment. The HgTe photoconductive sample is enclosed in a cryostat under 9 V bias and illuminated by a MHz-pulsed Quantum Cascade Laser. Pulses are 20 to 500 ns long with a  $\simeq 10$  ns rising time, repeated every 5  $\mu$ s. Photocurrent is acquired through a 50  $\Omega$  current shunt and a GHz voltage amplifier. **b.** Electrical response of the device under MHz optical excitation by a 20 ns long pulse. Dashed red line is a Gaussian fit showing a 20.1 ns FWHM. Inset: response of the device under excitation by a 500 ns pulse, allowing extraction of  $\simeq 20$  ns rise and fall times.

at the cryostat output, and we try to minimize ground loops and to symmetrize the cable lengths. Impedance matching starts to be important at these frequencies, and use of higher values of current shunt resistances leads to appearance of ringing effect.

Figure 3.3b shows photocurrent temporal traces measured with this experimental setup at room temperature. A 495 ns pulse is well resolved with rising and falling times measured to be of 23 ns and 14 ns, respectively. This is the same order of magnitude than the laser rising time, indicated to be of 10 ns in the laser specification. A 20 ns pulse is also resolved as a Gaussian-shaped peak with a 20.1 ns FWHM, indicating that the laser pulse is indeed well reproduced. As a result, we can estimate the bandwidth of our HgTe MWIR detector to be at least 50 MHz.

Because this kind of device is usually operated at cryogenic temperatures, I investigated how the device dynamics are affected under cooling. This is presented in Figure 3.4. Electrical noise produced by the QCL driver is very detrimental in this experiment, because it affects strongly the response of the device *via* the cryometric lines in the cryostat (temperature sensors and heaters). Figure 3.4a gives the device photocurrent traces under illumination by 500 ns QCL pulses from 300 K down to 15 K. 300 K and 15 K traces appear less noisy because cryometric lines are unplugged, reducing the sample exposition to QCL driver electrical noise. Nevertheless, we can observe that the photocurrent dynamics barely evolves with temperature, with no particular acceleration nor lengthening of the photoreponse. The magnitude of the photocurrent, extracted from the temporal traces, is provided in Figure 3.4b. It features a bell-shaped evolution with temperature with a maximum around 200 K, very similar to what is observed under continuous excitation, see Figure 3.2b. Moreover, when accounting for the difference in photon flux between the two experiments (there is a 10% duty cycle), we measure a similar responsivity of around 0.1 mA/W for the two experiments (at 4.4  $\mu$ m and under a  $\sim$  mW CW average power). This is a good indication that we are indeed probing with short pulses the same photoconductive behavior that we measure in CW conditions (*i.e.*,  $I(V)$  curves under illumination).

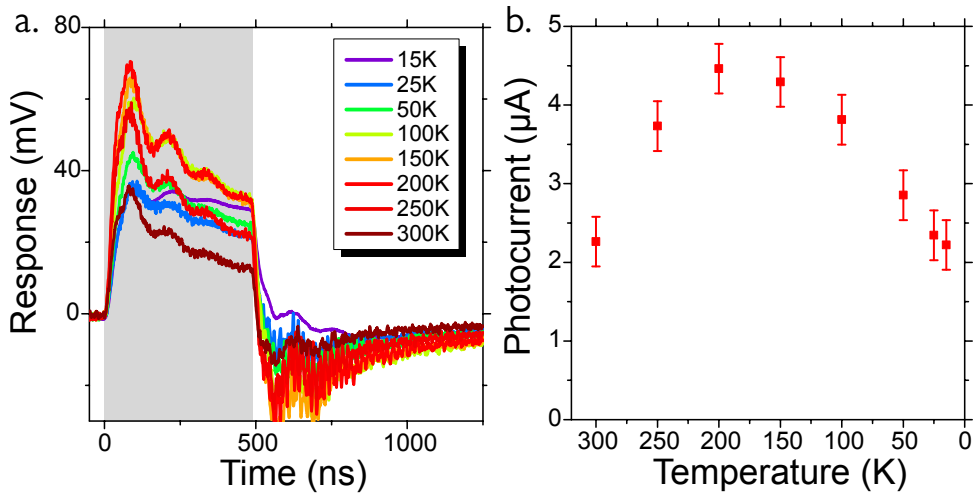


Fig. 3.4 MHz photocurrent in HgTe: effect of temperature. **a.** Electrical response of the device under MHz optical excitation by a 500 ns long pulse with varying temperature. **b.** Photocurrent evolution with temperature. Photocurrent is calculated from temporal traces.

### 3.2.2 Detection of Multiple Exciton Generation (MEG)

In the introduction of this chapter, we mentioned that narrow-bandgap materials are susceptible to undergo carrier multiplication when illuminated with photon energies much higher than their bandgap. This process, known as Multiple Exciton Generation (MEG), has been known since the 1950s for bulk materials and is presented in Figure 3.5a. Upon absorption of a photon of high energy  $h\nu > 2E_G$ , an electron is promoted far in the conduction band of the nanocrystal: it is usually called a *hot* electron. This hot carrier usually decays thermally (*via* phonon-assisted transitions) down to the first level of the conduction band, where it can recombine with its hole. There is however another decay pathway for this hot carrier: if its energy is high enough, an energy transfer from this hot carrier toward another electron of the valence band can occur, allowing the hot carrier to decay toward the band-edge while a second electron is promoted in the conduction band. The final yield of this process is two electrons at the band-edge for the price of one absorbed photon, hence the term of *carrier multiplication*. The maximum theoretical yield for this process is a stair-case function, pictured in Figure 3.6c: one exciton is created for  $E_G \leq h\nu < 2E_G$ , two excitons for  $2E_G \leq h\nu < 3E_G$ , three excitons for  $3E_G \leq h\nu < 4E_G$ , and so forth [17, 191].

In the bulk, this process is nevertheless very inefficient because of the availability of a large number of phonon pathway decays and the fact that the energy transfer process occurs with conservation of translational momentum. As a result, MEG occurs in the bulk with a large threshold of 6 to  $7 \times E_G$ , typically. In 0D confined nanostructures though, phonon losses are reduced due to an increase of level splitting [192], and the conservation of momentum is relaxed thanks to non-dispersive, atom-like states, making that MEG occurs with a much lower threshold than in the bulk state, closer to the ideal value of  $2E_G$ . As a result, it is possible using narrow-bandgap nanocrystal to observe carrier multiplication under illumination with photon energies that are easily accessible [193]. Particularly, MEG is sometimes presented as the key process to go above the Shockley-Queisser limit in photovoltaics by taking advantage of the high-energy photons in the solar spectrum: PbS-based solar cells with internal quantum efficiency above 120% under 3 eV illumination ( $\simeq 3.5E_G$ ) have been demonstrated [194].

Our HgTe nanocrystals feature a bandgap of 280 meV: reaching photon energies of multiple times the bandgap is then very easy. Even at 800 nm, photon energy is already  $5.5 \times E_G$ . Al-Otaify *et al.* reported a MEG threshold around  $2.5E_G$  for HgTe nanocrystals with bandgap at 1 eV [195], so we expect to see a manifestation of MEG around this kind of excitation. We want to see if we detect the signature of MEG in the photocurrent of a HgTe-based device. The experiment is schematized in Figure 3.5b: the device is kept under vacuum at room temperature, and is biased with 1 V.

We use three different laser sources at 4400 nm ( $h\nu = E_G$ ), 1550 nm ( $h\nu \simeq 2.9E_G$ ) and 808 nm ( $h\nu \simeq 5.5E_G$ ). Each laser is either electrically or optically chopped, and the photocurrent in the device is acquired with three different techniques depending on the chopping frequency. Below 2 Hz, photocurrent can be measured in real time with the source-meter used to bias the sample. Below 100 kHz, photocurrent is amplified by a DLPCA 200 transimpedance amplifier which output fed into an oscilloscope. Above 100 kHz, photocurrent is measured through a  $50 \Omega$  current shunt and amplified with a high bandwidth voltage amplifier. Being able to explore a large range of excitation frequencies and fluxes allows to probe the device response in a wide range of configurations, and to be more confident in the measurements.

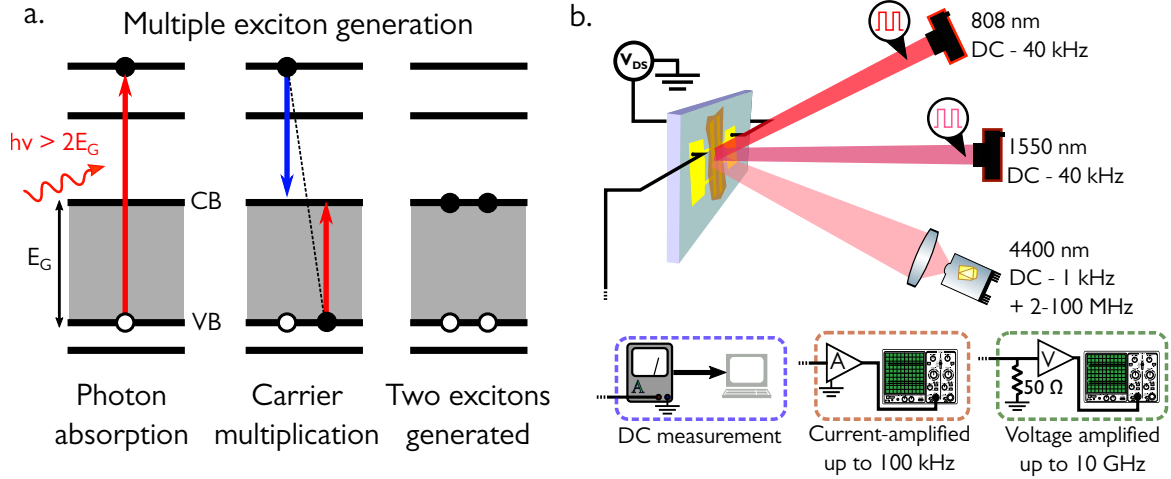


Fig. 3.5 Multiple exciton generation in HgTe MWIR nanocrystals: principle and experiment. **a.** Principle of multiple exciton generation (MEG). Upon absorption of a photon with energy  $h\nu > 2E_G$  (left panel), the hot electron can cool down by transferring its excess energy to another electron of the valence band (middle panel). This process yields two electron/hole pairs for one absorbed photon (right panel). **b.** Scheme of the experiment: the sample is bias and three sources are alternatively used: one 4400 nm QCL resonant with the bandgap ( $h\nu = E_G$ ), one 1550 nm laser ( $h\nu \simeq 3 \times E_G$ ) and one 808 nm laser ( $h\nu \simeq 5.5 \times E_G$ ). The resulting photocurrent is measured with three different setups depending on the excitation frequency.

We need an intrinsic efficiency parameter to be able to quantitatively evaluate the efficiency of the detector under illumination by the different photon sources. We choose to plot the *relative gain*, the gain of the photoconductor detector normalized by the detector gain under illumination at 4.4  $\mu\text{m}$ . The gain of a photoconductive detector has been defined earlier by:

$$g = \frac{\mathcal{R}h\nu}{e\eta} \quad \text{where } \mathcal{R} = \frac{I_{\text{photo}}}{P_{\text{opt}}} \quad (3.1)$$

Where  $\mathcal{R}$  is the device responsivity (ratio of photocurrent  $I_{\text{photo}}$  over incident light power  $P_{\text{opt}}$ ) and  $\eta$  is the internal quantum yield of the device. This internal quantum yield scales as the film absorption, and since everything is going to be normalized anyway, we choose to replace  $\eta$  by  $\eta_\lambda$ :

$$\eta_\lambda = \frac{A(\lambda)}{A(4400 \text{ nm})} \quad (3.2)$$

Where  $A(\lambda)$  is the absorption of the device at the wavelength  $\lambda$  and  $A(4400 \text{ nm})$  is the absorption of the device at the band-edge. Those quantities are determined using a FTIR spectrum of a film of EDT-capped HgTe nanocrystals. We can then write  $g_\lambda$  as a function of the incident photon flux  $\phi_0$ :

$$g_\lambda = \frac{\mathcal{R}h\nu}{e\eta_\lambda} = \frac{I_{\text{photo}}}{e\eta_\lambda \phi_0} \quad (3.3)$$

The gain  $g_\lambda$  hence describes the effect of one absorbed photon of wavelength  $\lambda$  on the photocurrent. In a two-band model where multi-exciton generation does not occur, a photon with  $h\nu > E_G$  should have the same effect on the photocurrent regardless of its energy, since a quantum detector is not sensitive to the photon energy. Any effect of carrier multiplication should then be characterized by an increase of  $g_\lambda$  compared to the band-edge gain  $g_{4400 \text{ nm}}$ .

To make sure that the observed effect is not due to generation of multiple exciton under multiple photon absorption, we can estimate the average number of injected excitons in each HgTe nanocrystal. With an absorption cross-section of  $\sigma_{\text{QD}} = 6 \times 10^{-15} \text{ cm}^2$  at  $5 \mu\text{m}$  [188], we have  $\langle N_X \rangle = \sigma_{\text{QD}} \phi_d \tau_X$ , see Equation 2.6. Using a typical value of  $\phi_d = 10^{19} \text{ s}^{-1} \text{ cm}^{-2}$  for the photon flux density and a conservative assumption of 10 ns for the exciton lifetime, we get  $\langle N_X \rangle = 6 \times 10^{-5}$  exciton per nanocrystal, far below unity.

To avoid any experimental error, all laser spot sizes and optical powers are measured at the sample location to correctly evaluate the photon flux. The latter is tuned by changing the lasers optical power. Relative transparency of the cryostat window is also accounted for in presented data.

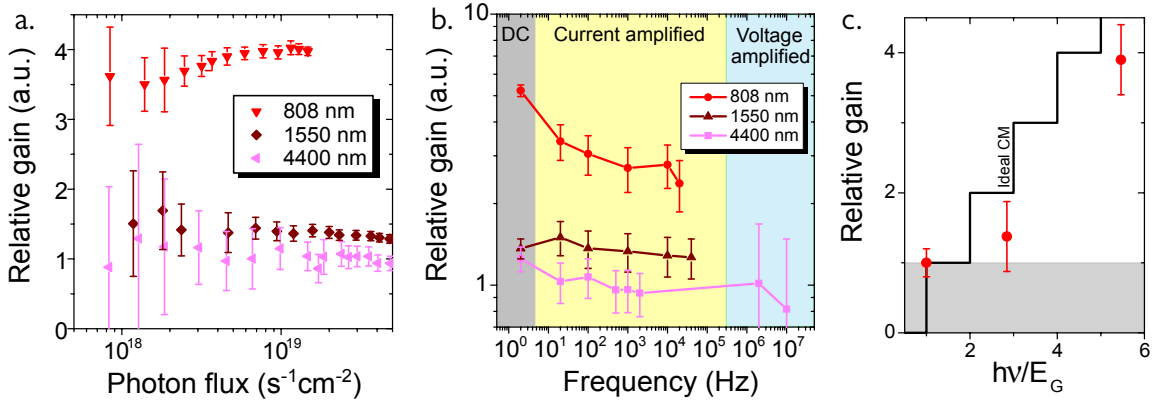


Fig. 3.6 Multiple exciton generation in HgTe MWIR nanocrystals: results. **a.** Relative gain  $g_\lambda = I_{\text{ph}}/\eta_\lambda e\phi$  (set to one for illumination at 4400 nm, see text) of the HgTe MWIR detector under illumination with varying flux of the three light sources. The three sources are optically chopped at 1 kHz and the sample bias is set to 1 V. **b.** Frequency dependence of the relative gain for the three laser illumination (around  $10^{19} \text{ s}^{-1} \text{ cm}^{-2}$ ). The sample is under 1 V bias at room temperature. The photocurrent is measured according to Figure 3.5b in the three different frequency regimes. **c.** Relative gain evolution with photon energy. The black curve gives the expected gain improvement for ideal carrier multiplication (perfect energy conservation).

The relative gain  $g_\lambda/g_{4400 \text{ nm}}$  is plotted as a function of photon flux and chopping frequency in Figure 3.6. In 3.6a, each point is obtained from the photocurrent measured at 1 kHz of chopping frequency, at room temperature and under 1 V bias. In 3.6b, each laser is set to a photon flux around  $10^{19} \text{ s}^{-1} \text{ cm}^{-2}$  (precisely measured in each case), and the chopping frequency is varied from 2 Hz to 20 kHz (and up to 10 MHz for the QCL). Again, each point is obtained from a photocurrent measurement, realized according to Figure 3.5b in each frequency range.

Both graphs show consistently and over the whole range of explored parameters a very slight improvement of the relative gain by a factor  $< 1.5$  under illumination at 1550 nm, and a much stronger improvement of relative gain by a factor 3 to 4 under illumination at 808 nm. We have here a signature of the MEG effect, with a threshold above  $3E_G$ , as summarized in Figure 3.6c. It is important to point out that we do not report absolute but relative efficiencies here: under illumination with photon

of  $h\nu = 5.5E_G$ , we observe an improvement of the intrinsic efficiency of the detector by a factor  $\simeq 3.5$ , that we attribute to multiple exciton generation. Our observations consequently also suggests that many reports on the photoresponse and dynamics of narrow-bandgap nanomaterials probed with photon energies far above the band-edge may overestimate the actual device performances.

At the time of this study, we did not have a FTIR spectrometer equipped to measure photocurrent spectra. An ultimate confirmation of this effect would be, now that we have such a tool, to compare on the same device the shapes of absorption and photocurrent spectra. For photocurrent and absorption spectra normalized at the band-edge, MEG should appear as a strong deviation of the photocurrent with respect to absorption for high photon energies.

We now have a good picture of the band-edge dynamics and hot carrier effects in HgTe nanocrystals with a narrow bandgap in the Mid-Wave Infrared. I showed that photoconductive devices present fast dynamics with a bandwidth measured around 50 MHz, mostly because the measured photocurrents in a device are an image of the instantaneous carrier density. I found evidence for multiple exciton generation at the device scale, in conditions close to device operation (low frequency illumination, low power). In the following section, I will be interested in another way to probe the photocurrent dynamics in this material, using optical excitation much shorter and more energetic than in our previous experiments.

### 3.3 Transient photocurrent measurements

In this section, I present a transient photocurrent measurement setup. Based on a pulsed source, the goal of this experiment is to create a large number of excited carriers in a biased device, and to study their recombination and transport at longer time scales. This allow us to access to intrinsic material parameters and reveal more information about the band structure of the nanocrystals in a device configuration.

#### 3.3.1 A new, versatile setup to probe transient photocurrent with a large dynamic range

We would like to be able to measure transient photocurrent in devices made of various nanomaterials. Given the range of available materials, we choose to use a UV laser which should be able to excite carriers through the bandgap of most colloidal semiconductor nanomaterials. We are interested in photocurrent transients in the ns to ms range, because sub-ns processes are usually only intra-nanocrystal processes ( $t_{\text{hop}} \sim 1$  ns assuming a mobility of  $10^{-3} \text{ cm}^2\text{V}^{-1}\text{s}^{-1}$ ). We use a 355 nm solid-state laser, producing 1.2 ns long pulses with a repetition rate of 100 Hz, giving us access to a 2 ns to 10 ms time window to resolve the device photocurrent. This is the range of timescales relevant for device operation, giving access to fast processes but also to long-lived photocarriers. Figure 3.7 presents the setup: a high energy pulse (up to 50  $\mu\text{J}$ ) is shone onto a sample. Sample is biased under 10 V or more, and connected to ground through a 50  $\Omega$  current shunt. Voltage drop on the shunt is directly visualized on a GHz oscilloscope. The high energy of the pulse and large bias allows us to avoid any amplification stage and to preserve the large dynamic range of the measurement (ns to ms). At this kind of frequencies, ringing effect in the measurement circuit can become important. The 50  $\Omega$  current shunt is mandatory for impedance matching, and the substrate of the device seems to also have a strong effect on the measurement quality. In particular, silicon substrate must be avoided because of high absorption of silicon at this wavelength. Best results were obtained using interdigitated ITO electrodes on PET substrate, showing only limited ringing (*i.e.* parasitic electrical noise).

This setup is meant to be used in combination to measurements at the bandgap of each material, since according to our previous observations one could expect carrier multiplication and other hot

carrier effects when probing narrow bandgap nanomaterials with high energy photons.

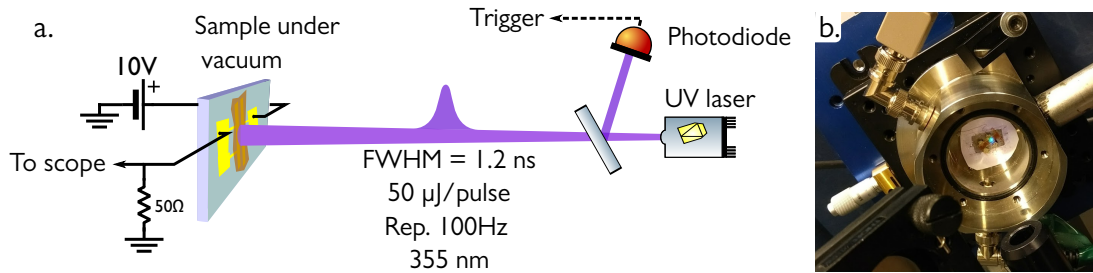


Fig. 3.7 A transient photocurrent setup with high energy, 1 ns laser excitation. **a.** Scheme of the setup. The sample is kept under vacuum with a 10 V bias. Illumination is provided by 355 nm laser producing 1 ns, 50  $\mu\text{J}$  pulses with a 100 Hz repetition rate. The photocurrent is acquired through a 50  $\Omega$  current shunt directly onto an oscilloscope. **b.** Picture of a sample (perovskite film) under measurement in the open sample holder.

### 3.3.2 A tool to probe trap distribution at the device scale in NCs arrays

The typical data we obtain from this experiment is presented in Figure 3.8a. In this case, the device is a photoconductive HgTe MWIR sample. A total of 5 to 10 temporal photocurrent traces are acquired using different time bases, then the data are stitched together to produce the reported curve. This photocurrent trace spans over five orders of magnitude (1 ns to 10  $\mu\text{s}$  here), when the photocurrent changes by two orders of magnitude. Typical signal is around 50 mV at the top of the photocurrent peak, with measurable values down to 0.5 mV reached at very long delay. With a 50  $\Omega$  shunt, this translates into currents of around 1 mA down to 2  $\mu\text{A}$ .

The typical curve presented in Figure 3.8a consists in three parts: at very early times, we see an increase of the photocurrent over  $\sim 1.5$  ns, consistent with the laser pulse duration. The photocurrent decay then consists in two distinctive parts: a fast decay, occurring over the first 10 ns, followed by a much slower contribution, spanning over several  $\mu\text{s}$  and appearing as linear in a log-log representation.

The first contribution is well fitted by an exponential decay of time constant around 1.2 ns. This is around the expected value for hopping time in this material, and can hence be attributed to an instantaneous image of carrier density, as proposed by Gao *et al.* for measurements at even shorter time scale [174, 175]. As a result, this fast decay is due to rapid recombination and trapping of the photogenerated carriers, at the scale of one to two nanocrystals (electron decay in a bandgap state or transfer to a bigger neighbor nanocrystal, acting as a trap state at the film scale). The time constant extracted from the exponential fit then relates to the lifetime of photogenerated exciton. This is mostly the regime that we probe with QCL illumination (at very different wavelength and photon flux). The second regime though, is a specificity of this particular measurement as it is not observed at the band-edge.

The second, longer contribution is characteristic of self-decelerated processes and follows a power law:  $I_{\text{photo}} \propto t^\alpha$ , with here  $\alpha = -0.3$ . This power dependence of transient photocurrent in amorphous (disordered) semiconductors have been studied in the 1980's, notably by Orenstein and Kastner [196, 197]. In their work on  $\text{As}_2\text{Se}_3$ , they describe that the power law dependency of the photocurrent can be interpreted in terms of multiple-trapping transport: trapped carriers (say, holes) prevent the recombination of electrons that contribute to a long-lived photocurrent. Overtime, they are slowly released from their trap states (which can be, in our case, bandgap states or states located in bigger, less confined nanocrystals). As they get released, they are allowed to recombine with an electron, diminishing the overall photocurrent. Because some traps are located deeper than others, they have very different de-trapping times, leading to the observed power-law decay. As a result, the exponent of the power law fit can be related to the distribution of trap states in the device. Assuming an

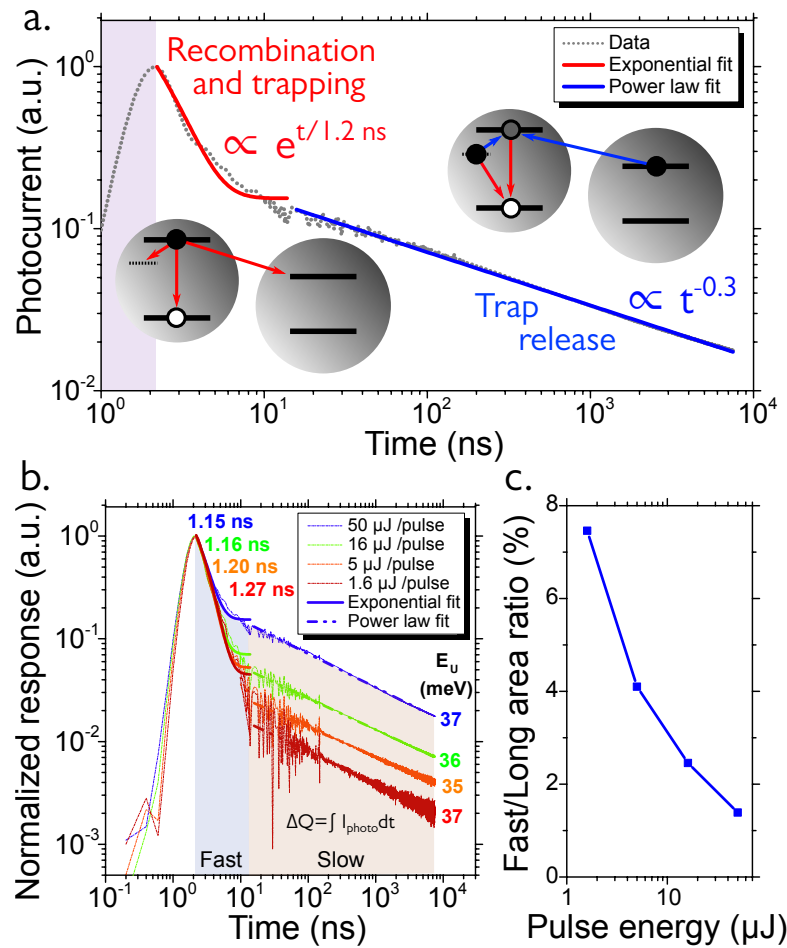


Fig. 3.8 Transient photocurrent measurements on a HgTe MWIR device. **a.** Typical photocurrent evolution. At early times (purple region), photocurrent increases due to the pulse arrival. The photocurrent then consists in two parts: an exponential one relating to fast recombination of carriers and trapping (diminution of  $\Delta n$ ), and a power-law decay extending up to several  $\mu$ s to ms, due to slow trap release. From this slow decay, one can estimation the trap distribution at the nanocrystal film level. Trapping is here only shown for the electron, but also occur for the hole. **b.** Photocurrent temporal traces for a HgTe MWIR film under decreasing pulse energy. Exponential fits and associated time constants (fast decay) as well as power law fits and associated Urbach energies (long decay) are provided. Areas for determinations of exchanged charges  $\Delta Q$  in "fast" and "slow" decay regimes have been highlighted in blue and orange. **c.** Ratio of the integrated areas for "fast" and "slow" decays, as pictured in panel b, measured for increasing pulse energy.

exponentially-decaying trap distribution, we can attribute a characteristic energy for this distribution: the Urbach energy  $E_U$  [198]. We can then relate the power-law exponent  $\alpha$  to Urbach energy through:

$$\alpha = -1 + \frac{k_B T}{E_U} \Rightarrow E_U = \frac{k_B T}{\alpha + 1} \quad (3.4)$$

We demonstrated that this value of Urbach energy can be tuned from around 60 meV to 35 meV in HgTe nanocrystals with a bandgap in the SWIR by playing on the surface chemistry of the nanocrystals, the lowest value (narrowest distribution) being obtained with EDT capping [199]. In our case, with  $\alpha = -0.3$  at room temperature, we get an Urbach energy of  $E_U = 37$  meV, consistent with the previously reported values.

On the same devices, we investigate the effect of pulse energy on the photocurrent temporal trace.

Results are displayed in Figure 3.8b. In this experiment, the pulse energy is tuned from 50  $\mu\text{J}$  to 1.6  $\mu\text{J}$  by the mean of neutral density filters. Interestingly, the Urbach energy extracted from each data set keeps a consistent value of  $35 \pm 5$  meV over the entire range of pulse energies. Time constant extracted from the fast, early decay seems to show a slight acceleration under higher excitation, not significant enough to be really indicative of anything. The most striking effect is the modulation of the two contributions ratios: by integrating the curve in the "fast" 1-10 ns range and the "slow" 10 ns-10  $\mu\text{s}$  range, we get the amount of charges contributing to the photocurrent in each regime  $\Delta Q = \int I_{\text{photo}} dt$ . By taking the ratio of these two quantities, we can estimate how each regime contributes to the total photocurrent. Figure 3.8c shows how this ratio changes with the pulse energy. The first observation to be made is that even under low energy excitation, most of the photocurrent (93%) comes from the slowly decaying part of the transient. Contribution of the early regime is only 7% of the total photocurrent under 1.6  $\mu\text{J}$  excitation, and decreases to reach 1% under 50  $\mu\text{J}$  excitation. In this sense, this experiment is very different from what we see at the band-edge of the material, where the photocurrent does not show any long-lived contribution.

Just as we did earlier, we can estimate the amount of injected excitons by a single pulse. Assuming again a cross section of  $\sigma_{\text{HgTe}} = 10^{-14}$   $\text{cm}^2$ , we have  $\langle N_X \rangle = \sigma_{\text{HgTe}} E_{\text{pulse}} / h\nu$ , with  $E_{\text{pulse}}$  the pulse energy density in  $\text{J}/\text{cm}^2$ . For the 1.6  $\mu\text{J}$  pulse, we get  $\langle N_X \rangle \sim 0.9$ , and  $\langle N_X \rangle \sim 28$  for a 50  $\mu\text{J}$  pulse. In this sense, even at low energy the excitation is orders of magnitude higher than excitation at the band-edge of the material. Given the high amount of injected excitons, the observed modulation of the photocurrent contributions might be a side-effect of fast Auger recombination (occurring around 80 ps after excitation [62] in this material). At high fluence, fast and efficient Auger recombination reduces the proportion of carriers available to contribute to photocurrent, hence modulating the relative contribution of photocurrent coming from carrier density evolution.

More insights about the different processes occurring in these materials under such excitation are definitely needed to understand the complete photophysics timeline. Transient absorption experiments in combination to transient photocurrent measurement in the ps to ns range, for example, would give access to shorter time-scale processes and enable to complete the dynamics picture for this material. Nevertheless, this transient photocurrent experiment gives access to material-related parameters (exciton relaxation and Urbach energy) from device-scale measurements. Moreover, because this experimental setup uses a 355 nm laser, a lot of nanomaterials can be probed, given that they show conduction and photoconduction. In the next section, I will present some of the results we obtained with another kind of nanomaterial.

## 3.4 Probing dynamics in perovskite photodetectors: toward efficient carrier transport

During my PhD, I applied some of the experimental techniques I developed for narrow-bandgap nanocrystals to other kind of nanomaterials, obtained through several collaborations. Among them, I present here some results on perovskite nanocrystals.

### 3.4.1 A new material for visible optoelectronics: perovskite nanocrystals

Cesium lead halide perovskite nanocrystals have encountered a colossal success after the first report by the Kovalenko group in 2015 [200]. Obtained through a typical hot-injection synthesis at high temperature, they display optical feature in the visible range and a very high photoluminescence quantum yield without the need of a shell, thanks to a defect-tolerant structure. Contrary to the other nanomaterials introduced in this section though, perovskite nanocrystals are not a confined system: spectral tunability is obtained through the halide nature and composition (for example,

$\text{CsPb}(\text{Br}_{1-x}\text{I}_x)_3$ . As a rule of thumb, chlorine-rich perovskite NCs will absorb and emit in the blue, Br-rich ones in the green and iodine-rich in the red. This halide composition is either controlled at the synthesis level, but can also be tuned post-synthesis using anion exchange [201, 202]. During my PhD, Wasim Mir from the Angshuman Nag group at IISER Pune came as a visiting student to work around visible light detection based on perovskites nanocrystals. This chapter will include some of the results we got working together, notably on the photocarriers dynamics.

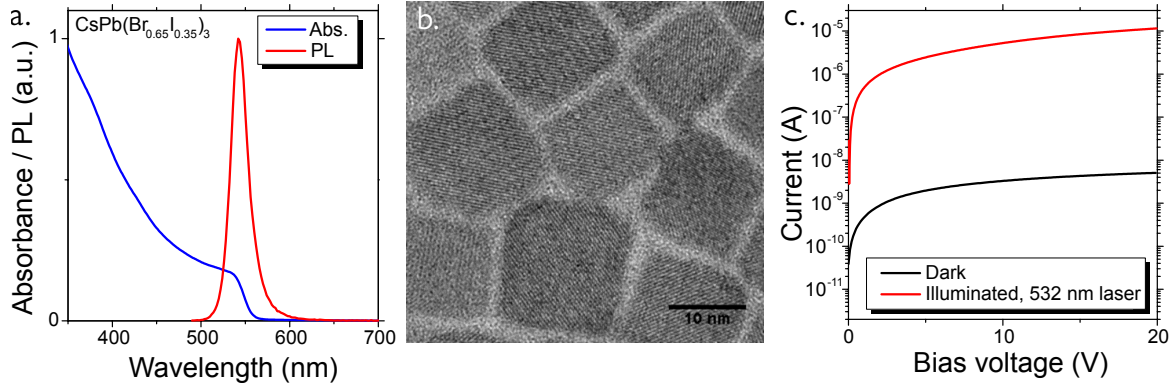


Fig. 3.9 Perovskite nanocrystals for visible optoelectronics. **a.** Absorption and photoluminescence (PL) spectra of  $\text{CsPb}(\text{Br}_{0.65}\text{I}_{0.35})_3$  perovskite nanocrystals. **b.** TEM image of  $\text{CsPb}(\text{Br}_{0.65}\text{I}_{0.35})_3$  perovskite nanocrystals. **c.** Current-voltage characteristics of a  $\text{CsPb}(\text{Br}_{0.65}\text{I}_{0.35})_3$  film treated with methyl acetate, showing conduction in the dark (black curve) and photoconduction under illumination by a 532 nm laser (red curve).

Nanocrystals of cesium lead halide with a 65% bromine to 35% iodine ratio ( $\text{CsPb}(\text{Br}_{0.65}\text{I}_{0.35})_3$ ) were prepared according to literature reports [203, 204], and their optical properties are given in Figure 3.9a. Figure 3.9b shows the typical cubic shape of those perovskite nanocrystals. Device fabrication is not as straightforward as it is for metal chalcogenides: the ligand exchange procedure used to improve the inter-particle coupling and allow charge transport can not be applied here, because the surface chemistry toolbox developed for II-VI materials is totally inefficient for perovskite nanocrystals. Notably, one of our early attempts at obtaining sulfide-capped perovskite nanocrystals using a phase-transfer approach led to conductive and photoconductive films, but XRD data showed that the resulting film was not made of perovskite material, but rather of PbS nanocrystals formed *in-situ* during the ligand exchange process. We then took advantage of a newly reported ligand-stripping strategy developed by the group of J.M. Luther at NREL [204]. The film of perovskite nanocrystals is dipped into a solution of lead acetate in methyl acetate, then annealed. The resulting films show conductive and photoconductive behavior while preserving the perovskite structure, see Figure 3.9c.

### 3.4.2 Transient photocurrents and exciton dissociation in perovskite nanocrystals arrays

We use the same transient photocurrent experimental setup presented in section 3.3 on devices made from cesium lead halide  $\text{CsPb}(\text{Br}_{0.65}\text{I}_{0.35})_3$  perovskite nanocrystals. The transient photocurrent temporal trace, shown in Figure 3.10b, only shows contribution at early time ( $< 100$  ns) in these materials and is well fitted with a double exponential decay of time constants around 1.2 ns and 7.8 ns. Those time constants are very similar to the ones measured with time-resolved photoluminescence experiments [205], indicating that the decay measured with transient photocurrent setup indeed reflects the excitation recombination in the nanocrystals. No contribution of traps to the photocurrent is observed in devices of this material (no long-lived photocurrent regime), confirming its trap tolerance even at the device scale.

Nevertheless, the fact that the photocurrent decay reflects the excitonic relaxation is a signature of a very inefficient exciton dissociation in the material. Indeed, in the ideal photoconductor

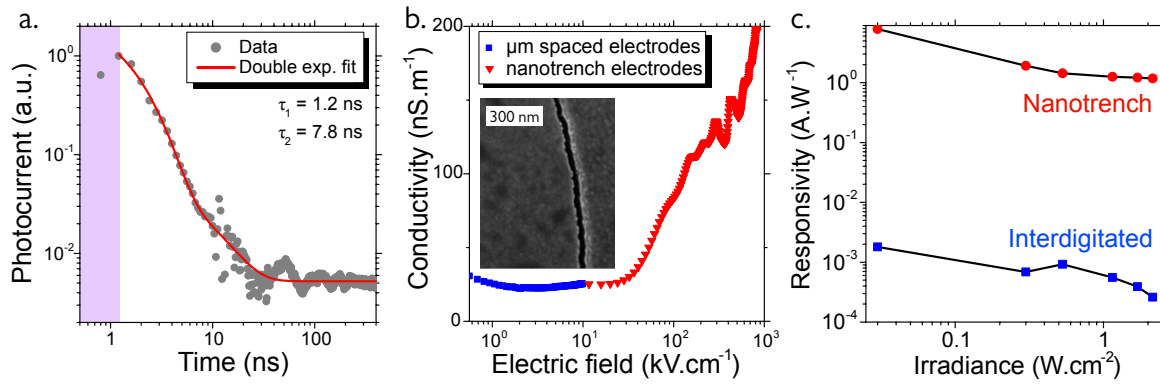


Fig. 3.10 Transient photocurrent on a perovskite nanocrystal device. **a.** Transient photocurrent temporal trace on a  $\text{CsPb}(\text{BrI})_3$  perovskite nanocrystals, showing only a fast, double-exponential decay of the photocurrent. No contribution of traps to photocurrent is found in this sample. Bias is 45 V. **b.** Conductivity evolution with increasing electric field, extracted from device  $I(V)$  characteristics. Blue squares is data from typical interdigitated, 10  $\mu\text{m}$ -spaced electrodes. Red triangles is data from devices on nanotrench ( $\approx 100$  nm spaced) electrodes. Inset: SEM image of nanotrench electrodes. **c.** Responsivity of devices based either on interdigitated electrodes (blue) or nanotrench electrodes (red).

the photogenerated electron/hole pair is splitted under the applied electric field and each carrier is transported toward its electrode. Here, the applied field is too weak to balance the exciton binding energy, so electron/hole pairs mostly recombine in the nanocrystal they were created in. We propose a strategy to enhance the electric field by using nanotrench electrodes: those electrodes are fabricated using a two-step optical lithography process and feature a sub-100 nm spacing with a high aspect ratio ( $\sim 15 \mu\text{m}$  length) [115, 206]. Because of the reduction of electrode spacing by a factor 100 compared to the typical 10  $\mu\text{m}$ -spaced electrodes, the electric field is improved by the same factor under similar bias. Figure 3.10b shows the evolution of conductivity of both interdigitated and nanotrench devices with the applied field. The conductivity is clearly field-independent below an applied field of around  $50 \text{ kVcm}^{-1}$ , and significantly improves over this threshold value. Responsivity of devices under illumination is given in Figure 3.10c: nanotrench devices shows an improvement of a factor 1000 over the interdigitated electrodes. This huge improvement is the combination of more efficient exciton splitting under high field, and apparition of gain effect in nanotrench device. Indeed, due to its small gap, only few (4 to 5) hopping processes are necessary to go from one electrode to the other in this device. As a result, one carrier can circulate several times in the polarization circuit before recombining, contributing several times to the photocurrent [207].

### 3.5 Conclusion

In this chapter, I continued my study on carrier dynamics in mercury telluride, and focused on MWIR-absorbing HgTe 0D nanocrystals. After performing a CW characterization of photoconductive devices, I used a MWIR pulsed Quantum Cascade Laser to investigate the photocurrent dynamics and device bandwidth at the band-edge of the material. I then showed evidences for carrier multiplication effects in HgTe nanocrystals, allowing to reach higher photodetection efficiencies under illumination with high energy photons. I then presented a new, versatile setup to measure transient photocurrents in a wide variety of photoconductive devices. With a very large dynamic range, this setup allows to probe the exciton cooling as trap-assisted transport. As a result, it allows to access material parameters (exciton lifetime and Urbach energy) through a transport measurement. As an example, I showed some results on perovskite nanocrystals, which proved to be an interesting platform to play with exciton dissociation through the use of different devices geometries.

# Chapter 4

## Intraband photodetection with self-doped nanocrystals

---

4.1	<b>HgSe nanocrystals for intraband photodetection: material and early results . . . .</b>	<b>74</b>
4.2	<b>HgSe/HgTe heterostructures: a step toward improved performances . . . . .</b>	<b>81</b>
4.3	<b>Effect of pressure on narrow-bandgap materials . . . . .</b>	<b>88</b>
4.4	<b>Designing a new narrow-bandgap energy landscape: toward colloidal QDIP . . . .</b>	<b>97</b>
4.5	<b>A multi-spectral, intraband-based MWIR photodiode . . . . .</b>	<b>104</b>

---

### Related articles

- A. Robin, C. Livache, S. Ithurria, E. Lacaze, B. Dubertret, and E. Lhuillier, "Surface Control of Doping in Self-Doped Nanocrystals". *ACS Applied Materials and Interfaces* 8, 27122–27128 (2016).
- B. Martinez, C. Livache, L. D. Notemgnou Mouafo, N. Goubet, S. Keuleyan, H. Cruguel, S. Ithurria, H. Aubin, A. Ouerghi, B. Doudin, E. Lacaze, B. Dubertret, M. G. Silly, R. Lobo, J. F. Dayen and E. Lhuillier, "HgSe Self-Doped Nanocrystals as a Platform to Investigate the Effects of Vanishing Confinement", *ACS Applied Materials and Interfaces* 9, 36173–36180 (2017)
- N. Goubet, C. Livache, B. Martinez, X. Z. Xu, S. Ithurria, S. Royer, H. Cruguel, G. Patriarche, A. Ouerghi, M. G. Silly, B. Dubertret, and E. Lhuillier, "Wave-Function Engineering in HgSe/HgTe Colloidal Heterostructures To Enhance Mid-Infrared Photoconductive Properties", *Nano Letters* 18, 4590–4597 (2018)
- C. Livache, N. Goubet, C. Gréboval, B. Martinez, J. Ramade, J. Qu, A. Triboulin, H. Cruguel, B. Baptiste, S. Klotz, G. Fishman, S. Sauvage, F. Capitani and E. Lhuillier, "Effect of Pressure on Interband and Intraband Transition of Mercury Chalcogenide Quantum Dots", *Journal of Physical Chemistry C* 123, 13122–13130 (2019)
- C. Livache, B. Martinez, N. Goubet, C. Gréboval, J. Qu, A. Chu, S. Royer, S. Ithurria, M. G. Silly, B. Dubertret and E. Lhuillier, "A Colloidal Quantum Dot Infrared Photodetector and Its Use for Intraband Detection", *Nature Communications* 10, 2125 (2019)

### Related communications

- "Intraband Nanocrystals for Mid-Wave Infrared Photodetection", eMRS Spring Meeting 2019, Nice, France.

HgSe nanocrystals, as presented in the introduction, are self-doped nanocrystals featuring intraband absorption in the MWIR to LWIR. In the history of infrared devices, going from interband to intraband and intra-subband materials represented a paradigm shift, and allowed to develop alternative detectors and light sources based on wave-function engineering. From the point of view of colloidal materials though, doped intraband nanocrystals are particularly interesting to address low energies (MWIR, LWIR and above). Indeed, narrow bandgap interband nanocrystals require to grow large objects (*i.e.* weakly confined) that are very colloidal unstable and for which the growth is difficult to control.

HgSe nanocrystals are also a very interesting platform to investigate intraband photophysics and transport in few-electrons doped systems. This chapter will include early, exploratory results obtained with simple photoconductive devices of HgSe nanocrystals, especially related to photoconduction dynamics. In the first section, I will also introduce the major drawbacks of such a doped material for device integration.

This chapter will then focus on building heterostructures based on HgSe nanocrystals to overcome the intrinsic limitations of a doped system. I will present two main results: the growth of HgSe/HgTe core-shell heterostructures and the energy-landscape engineering in mixtures of HgSe and HgTe nanocrystals.

Additionally, because it came as an interesting question during the exploration of core-shell materials, this chapter will present results we obtained on the pressure dependency of the energy spectrum in HgSe and HgTe narrow bandgap materials.

Finally, I will present the first intraband-based multicolor infrared detector, based on a HgSe/HgTe material.

## 4.1 HgSe nanocrystals for intraband photodetection: material and early results

### 4.1.1 Self-doped HgSe nanocrystals

As stated earlier in the introductory chapter, it is possible to observe *intraband* transitions in doped nanocrystals. Those transitions typically involve two levels from the conduction band of the nanocrystals, because the high hole effective mass makes that the valence band is a quasi-continuum of states. It requires the first level of the conduction band to be occupied in the ground state. There are several ways of achieving occupation of the first conduction band level: the first demonstrations of intraband absorption relied on electrochemically pumping electrons in CdSe nanocrystals [138]. Saturation of the interband transition can also be realized by optical pumping, as it was demonstrated for PbSe nanocrystals [139] and CdSe/CdS nanocrystals [140], the latter even displaying intraband MWIR photoluminescence. Very recently, intraband absorption has been observed for the first time in 2D CdSe nanoplatelets under high optical excitation [208]. Nevertheless, neither of these techniques are convenient for device integration, where the intraband character of the material should be available in the steady state. More recently, chemical doping of lead sulfide nanocrystals has been presented as a new doped system displaying MWIR to LWIR intraband absorption. Doping PbS nanocrystals with silver successfully leads to occupation of the  $1S_h$  state and to a p-type MWIR absorption in the valence band [209]. Iodine doping, on the other hand, lead to the observation of a n-type character ( $1S_e$  occupation) and transitions in the conduction band, adjustable from the MWIR to LWIR [210].

Mercury selenide nanocrystals are self-doped particles with a populated  $1S_e$  level, and featuring intraband ( $1S_e \rightarrow 1P_e$ ) transition in addition to the interband transition, as pictured in 4.1a [141, 142, 211, 212]. Because of the occupation of the  $1S_e$  level, the  $1S_h \rightarrow 1S_e$  interband transition is usually

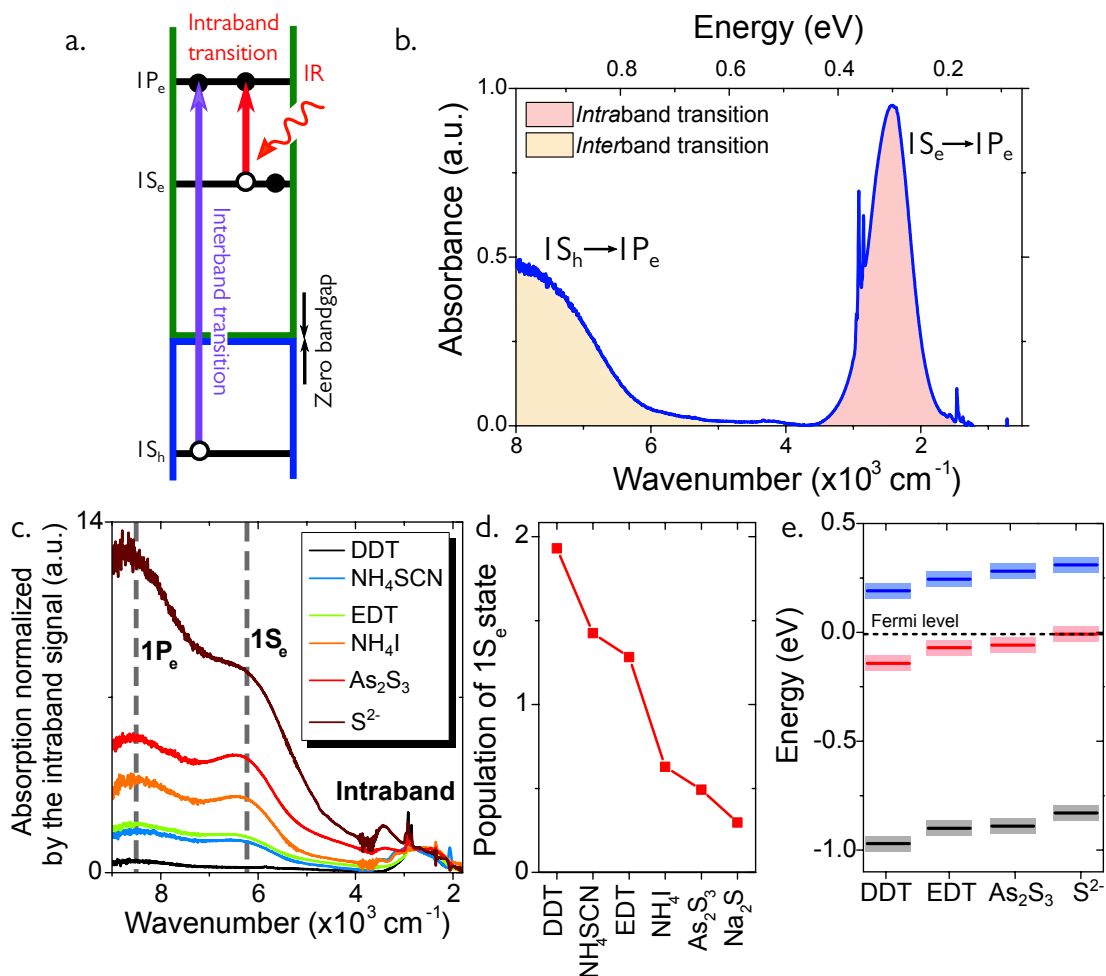


Fig. 4.1 Intraband transitions and control of doping in HgSe nanocrystals. **a.** Scheme of a self-doped HgSe band diagram. The  $1S_e$  state is occupied in the ground state, allowing for low energy  $1S_e \rightarrow 1P_e$  intraband transitions. **b.** Infrared absorption spectrum of  $\approx 5$  nm HgSe nanocrystals, displaying intraband absorption in the MWIR (in red) and interband absorption in the SWIR (in yellow). **c.** Infrared spectra of HgSe nanocrystals capped with different ligands. All spectra are normalized to their intraband contribution. Grey dashed lines indicates the position of  $1S_e$  and  $1P_e$  levels. **d.** Estimated population of the  $1S_e$  state in a single HgSe nanocrystal for different ligands, calculated from the integration of the intraband and interband contributions in each absorption spectrum. **e.** Reconstructed energy spectra for HgSe nanocrystal films capped with four different ligands, using a combination of XPS and infrared spectroscopy (see section 1.2.4).

bleached in these nanoparticles, and the observed interband transition is the ( $1S_e \rightarrow 1P_e$ ). Figure 4.1b shows the typical infrared absorption spectra of a film of HgSe nanocrystals: intraband absorption appears as peak-shaped feature in the MWIR, while interband absorption appears as a broad feature at higher energy. The energy of both transitions is tunable with the nanocrystals mean size, as shown in Figure 1.29. We demonstrated in 2016 that the doping of those HgSe nanocrystals originates from a reduction of the nanocrystals by the environment [143, 213], and that this doping can be tuned by playing on the nanocrystals surface chemistry. This effect can be seen on the optical spectrum of a nanocrystal film, as pictured in Figure 4.1c. In this figure, optical spectra of ligand-capped HgSe nanocrystal are shown normalized by the intraband signal around  $2800 \text{ cm}^{-1}$ . The signature of de-doping is the clear increase of interband absorption: as soon as the original dodecanethiol (DDT) ligand is exchanged toward a transport-compatible ligand, the magnitude of interband increases. A notable observation is the apparition of a feature around  $6000 \text{ cm}^{-1}$ : this is the signature of an unbleaching of the  $1S_h \rightarrow 1S_e$  transition due to doping reduction. By fitting the relative contribution in those spectra, we can evaluate the occupancy of the  $1S_e$  level for the different surface chemistries,

as shown in Figure 4.1d. When the initial DDT ligands lead to a almost-filled  $1S_e$  state (2 electrons per dot), switching to a shorter, transport-compatible ligand leads to a significant reduction of the doping. ethanedithiol reduces the average number of electrons to around  $1 e^-$  per dot, when for  $S^{2-}$  ligand ( $Na_2S$ ) the  $1S_e$  state is almost emptied, and the intraband feature almost disappears from the absorption spectrum. This effect can be explained by a dipole effect: each ligand carry a different dipole, effectively tuning the absolute energy of the bands at the surface of the nanocrystal. For PbS nanocrystals, it has been shown that such dipoles can tune the band energy over almost 1 eV [214–217].

In more recent work, we measured the energy spectrum of ligand-capped HgSe nanocrystals by X-ray photoemission. As pictured in Figure 4.1e, the observed trend is very similar, with a significant shift of the bands upon surface chemistry tuning. While the Fermi level lies in the middle of the intraband ( $1S_e - 1P_e$ ) gap for DDT ligand, it gets closer to the  $1S_e$  level upon switching to shorter ligands, in perfect agreement with the observed reduction of the electron doping [109].

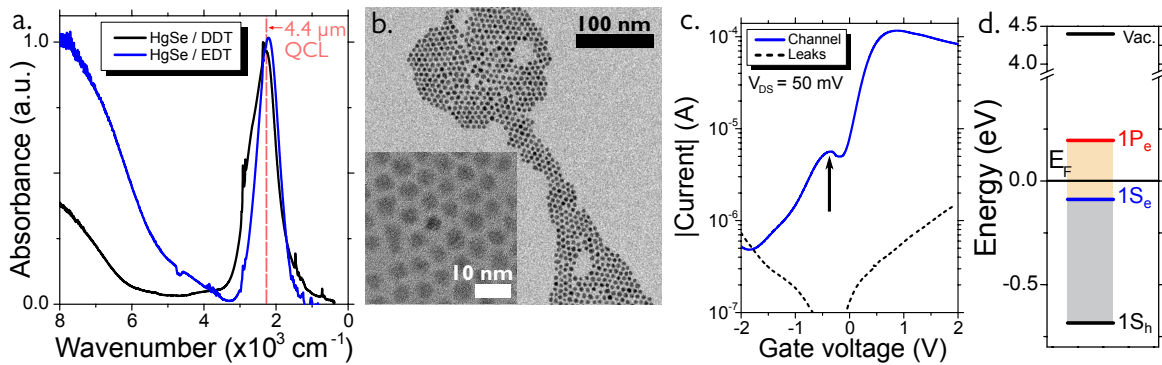


Fig. 4.2 Intraband HgSe nanocrystals around  $2500 \text{ cm}^{-1}$  **a.** Absorbance spectra of HgSe nanocrystals before ligand exchange (DDT-capped, black curve) and after solid-state ligand exchange on film (EDT-capped, blue curve). The C – H absorption lines merge with the high-energy part of the intraband absorption peak. The dashed red line corresponds to the photon energy of our QCL MWIR source. **b.** TEM image of HgSe nanocrystals with intraband absorption around  $2000 \text{ cm}^{-1}$ . Inset: high-resolution TEM image. **c.** Transfer curve of an EDT-capped HgSe device in an electrolytic FET configuration. The curve shows a very clear n-type behavior as well as Pauli blocking (black arrow). Drain-source voltage is set to 50 mV. **d.** Energy diagram of an EDT-capped HgSe film, reconstructed from photoemission and spectroscopy data. Interband gap is pictured in gray and intraband gap in yellow.

Throughout this chapter, I will focus on one particular size of HgSe nanocrystals:  $\simeq 5 \text{ nm}$  HgSe spheres with intraband transition around  $2200 \text{ cm}^{-1}$ , matched with the  $2250 \text{ cm}^{-1}$  emission of our Quantum Cascade Laser MWIR source. Figure 4.2a shows the optical spectra of such a material, before and after ligand exchange toward ethanedithiol (EDT). The reduction of doping upon ligand exchange can again be seen in these spectra: the intraband/interband absorption ratio strongly decreases after the surface chemistry modification, indicating that the nanocrystals are less doped with EDT ligand than with DDT. The position of the intraband is slightly red-shifted after ligand exchange, due to partial wave-function delocalization. The apparent narrowing of the intraband transition is mainly due to the reduction of C – H peak, which appears on the high energy part of the intraband peak in the DDT-capped HgSe spectrum. Figure 4.2b shows TEM pictures of these nanocrystals: their spherical shape as well as good monodispersity allow them to self-organize in honeycomb lattices, as shown in the high-resolution image.

The electron-doped character of these HgSe nanocrystals is confirmed by Field-Effect Transistor (FET) data, as well as by photoemission. In an electrolytic FET configuration, EDT-capped HgSe NCs films display n-type transfer curves, see Figure 4.2c. Contrary to all the previous FET data

presented for interband materials, this transfer curve only displays a very clear electron conduction with no sign of any hole transport, indicative of the strong degenerate doping of those nanocrystals. Typical transfer curves also feature a non-monotonic behavior: when the gate voltage is increased (electron injection), the channel current gradually increases, then drops before increasing further. This is believed to be due to Pauli blocking: the  $1S_e$  level being a two-electrons state (including spin degeneracy), there is a gate voltage for which this level is filled for a majority of nanocrystals, making that the number of available  $1S_e$  states for nearest-neighbour hopping is reduced, and that the overall mobility of the film drops. Adding more electrons populates the  $1P_e$  levels, restoring the electrons mobility due to the increased number of available states to hop to [142]. Finally, photoemission on the Tempo beamline of Synchrotron Soleil confirms that the material is indeed degenerately n-doped: the reconstructed energy diagram of EDT-capped nanocrystals given in Figure 4.2d shows the Fermi level lying between the  $1S_e$  and  $1P_e$  levels in the steady state.

#### 4.1.2 Transport, photodetection and key limitations of pure HgSe nanocrystal arrays

As stated earlier, HgSe NCs films are very exciting for intraband-based MWIR detectors. Nevertheless, it is very clear from the first experiments that a straightforward approach leads to numerous problems. Photoconductive devices from HgSe can be obtained by drop-casting particles from hexane:octane (9:1) mixture, then exchanging their ligands toward EDT using the same approach as described earlier. Because we know that a ligand exchange can have a dramatic effect on the material doping, we have shown in Figure 4.2a that exchange toward EDT only lead to a partial reduction of the doping and preserve the intraband absorption.

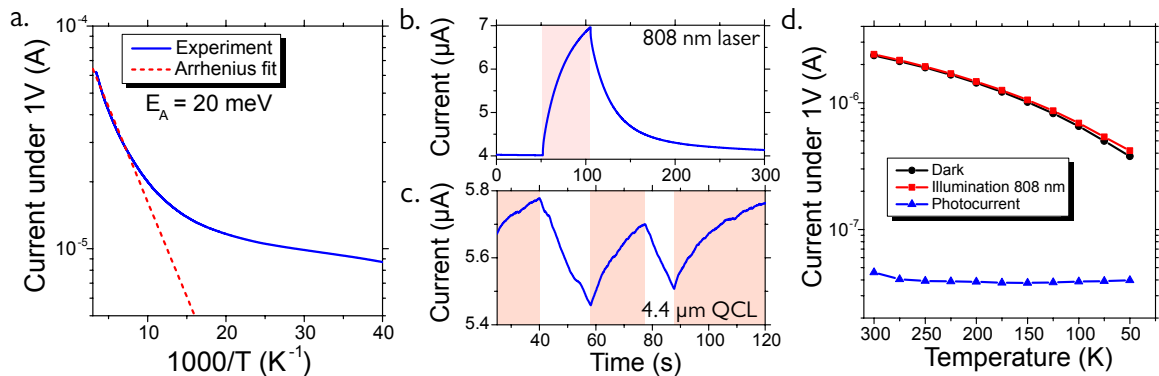


Fig. 4.3 Electrical properties of HgSe films. **a.** Evolution of the current under  $V_{DS} = 1$  V while cooling down the EDT-capped HgSe device. An Arrhenius fit at high temperature allows to extract a low activation energy of around 20 meV. **b.** Temporal trace of the device current (under  $V_{DS} = 1$  V) under interband illumination by a 808 nm laser (highlighted area), displaying very slow dynamics. **c.** Temporal trace of the device current (under  $V_{DS} = 1$  V) under intraband illumination by a 4.4  $\mu m$  (2250  $cm^{-1}$ ) Quantum Cascade Laser (QCL) MWIR source (highlighted area). **d.** Evolution of dark current (black circles), current under 808 nm illumination (red squares) and photocurrent (blue triangles) with temperature.

We are now interested in the performance of those HgSe photoconductive devices, and particularly to their signal to noise ratio, activation energy (*i.e.* how much the dark current is reduced when the device is cooled down) and photoresponse bandwidth. Figure 4.3a presents the dependence of the dark current with temperature when cooling down such a device: the activation energy, measured here around 20 meV, is extremely weak for a photodetector around 250 meV. The consequence of such a low activation energy is that cooling down the device will barely improve its detectivity. For the sake of comparison, HgTe photoconductive interband devices at the same wavelength such as presented earlier (see section 3.1.2), feature activation energies around 90 to 120 meV. Moreover, as pictured in Figure

4.3b and c, the photoresponse of these devices under either interband (808 nm laser) or intraband (4.4  $\mu\text{m}$  QCL) illumination is extremely slow, with response times of the order of several seconds. The fact that the response is symmetrical (*i.e.*, turn-on and turn-off times are comparable) may indicate that the observed photoresponse in this system is *bolometric* rather than due to photocharge transport. In other words, the observed photoresponse is likely due to heating of the film upon light absorption. Finally, Figure 4.3d presents the evolution of dark current, current under 808 nm illumination and photocurrent with temperature: on the 300 K to 50 K range, there is almost no improvement of the device performances. To sum up, intraband-based MWIR photoconductive devices made from HgSe suffer from:

- A high dark current, due to degenerate doping of nanocrystals and occupation of the  $1S_e$  states. This issue is well known for epitaxially-grown doped Quantum Wells or Quantum Dots featuring intraband transitions in QWIP and QDIPS;
- A low activation energy (almost no reduction of dark current upon cooling);
- A low responsivity, leading to poor signal-to-noise ratios;
- A slow ( $> 1$  s) photocurrent dynamics.

All these issues relate to the fact that the system is *degenerately doped*: the electrons in the conduction band are needed to get intraband optical absorption, but they are highly detrimental from the dark current perspective. From these observations, it is clear that, as is, HgSe NCs are not as mature as their interband HgTe counterpart for integration into infrared detectors. Nevertheless, they are an interesting platform to probe transport and infrared phototransport, because they give access to a very different regime of doping than what is usually observed in nanomaterials. In the following of this chapter, I will present several results shining light on the physical processes in those materials, as well as strategies to improve the performances of those HgSe devices to the level of their interband counterparts.

### 4.1.3 HgSe under gate control: toward faster photoresponse?

The first step I took toward a better understanding of the physical processes in films of HgSe nanocrystals was to apply the same strategy as we used earlier for HgTe nanoplatelets: looking at photocurrent dynamics under Fermi level control *via* the use of an electrolytic gate (see section 2.3 and Figure 2.7). With this experiment, I wanted to see the effect of doping reduction (under negative gate bias) or augmentation (under positive gate bias) on the photocurrent dynamics. I firstly used illumination at 808 nm (excitation of the interband transition of HgSe). Because, as stated earlier in section 4.1.2, HgSe nanocrystals show a slow, weak photoresponse (which could be only bolometric), we use here a fairly low frequency measurement. The dark current is measured for 10 s, then light is switched on mechanically for 25 s. Temporal traces of the device current under negative gate biases (hole injection) are shown in Figure 4.4. There are two notable effects of the hole injection: a reduction of the dark (and total) current, due to the reduction of majority carrier (electrons) density; as well as a clear acceleration of the photocurrent. For the sake of comparison, current temporal traces under electron injection are shown in Figure 4.4: they display weak and slow photocurrent regardless of the gate bias. Modulation (*i.e.*,  $I_{\text{light}}/I_{\text{dark}}$  ratio) extracted from the temporal data is given in Figure 4.4c: values significantly different from 1 are only achieved under hole injection. In this range of gate biases, response times of the photocurrent are presented in Figure 4.4d. The "ON" time, or rising time, is measured here by an exponential fit of the rising part of the curve (our mechanical chopper having a  $\simeq 200$  ms rising time). The "OFF" time, or falling time, is measured to be the time  $t_{\text{OFF}}$  where  $I(t_{\text{OFF}}) - I_{\text{dark}} < 90\%(I_{\text{light}} - I_{\text{dark}})$  (the dark current recovers 90% of its original value), and set to 25 s if it never recovers as much. As a result, we observe that improvement of the modulation occurs while the overall time response of the detector is accelerated.

This can be interpreted as a transition from bolometric response, where photocurrent is due to thermal activation of electrons under heating the film with the laser; to a "quantum" photoresponse, where photocurrent is due to electron band-to-band transition under photon absorption and transport of electrons in their excited state.

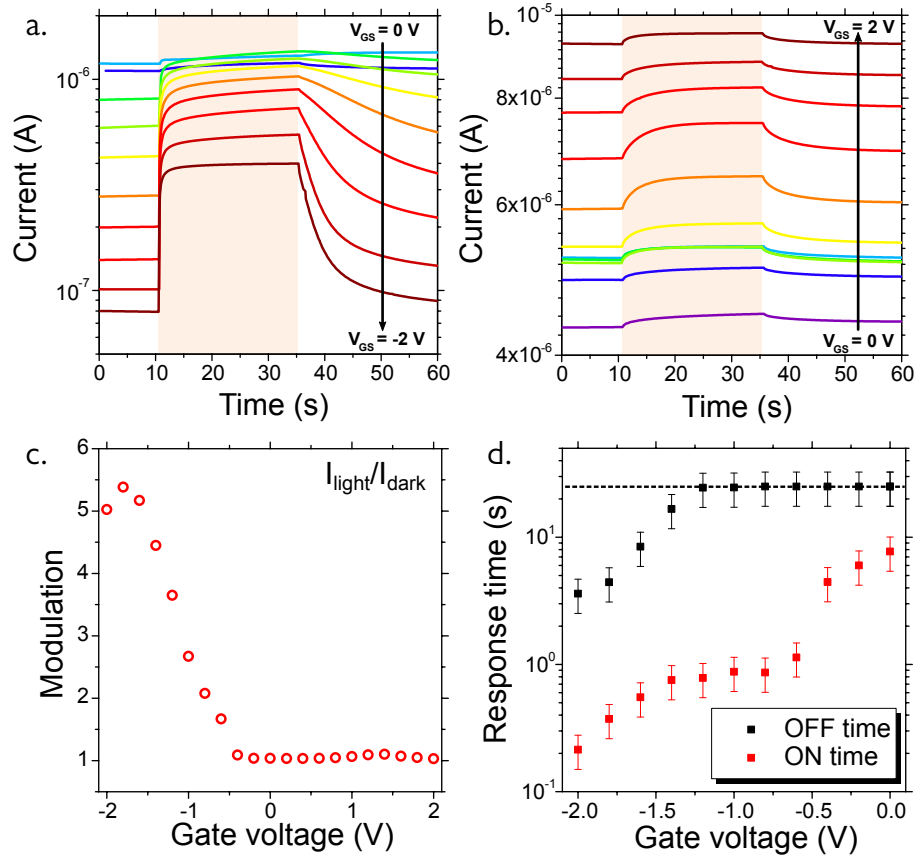


Fig. 4.4 Gate effect on the photocurrent dynamics in HgSe nanocrystals. **a.** Evolution of an HgSe NC film photocurrent temporal trace under low frequency excitation and under hole injection. The 808 nm laser is switched on at  $t = 10$  s and switched off at  $t = 35$  s. The gate bias is swept from 0 V (purple curve) to  $-2$  V (brown curve). **b.** Evolution of temporal traces under low frequency excitation and electron injection. The gate bias is swept from 0 V (purple curve) to  $+2$  V (brown curve). **c.** Evolution of modulation (*i.e.*,  $I_{light}/I_{dark}$  ratio) under gate control. **d.** Evolution of the rise (red) and fall (black) times under gate control, in the regime where the modulation significantly differs from 1. The rise time is measured with an exponential fit of the curve between  $t = 10$  s and  $t = 30$  s, and the fall time is determined by the time it takes for the device to recover 90% of its original dark current (or loose 90% of the photocurrent).

This strategy nevertheless did not enable to get meaningful results from intraband excitation of the device under gate bias, because of the very low signal to noise ratios and the incompatibility of our gating strategy (electrolyte) with cooling. More insights about gate effect on HgSe nanocrystals might be obtained by using Fourier-Transform Infrared spectroscopy (FTIR) and monitor the interband and intraband absorption of a device under electron or hole injection, but this requires the use of alternative, high-speed and low-temperature compatible gating strategies. This topic is currently under investigation by our group, where we notably explore conventional dielectrics ( $\text{SiO}_2$ ) or ionic solids such as  $\text{LaF}_3$  [218].

#### 4.1.4 The need for uncoupling optical and transport properties in intraband materials

At this point, it became very clear that the limitations encountered during my experiments are intrinsically linked to the doped aspect of the material. While doping is definitely required to access intraband transitions, transport in doped nanostructures is by nature driven by those "dark" carriers. Moreover, if we picture what is happening in a HgSe nanocrystal upon light absorption, it is unclear that whether the overall current should increase after promotion of an electron from a  $1S_e$  to a  $1P_e$  level. As this is an unipolar effect, there is only marginal changes in the carrier density of the nanocrystal (as opposed to interband systems). The mobility of this promoted electron might be higher though, as it is higher in the nanocrystal conduction band. Those observations are not limited to HgSe nanocrystals: other electron-doped systems presenting optical absorption in the MWIR to LWIR have been found to present the same performance issues with slow photocurrent and low signal to noise ratios. This is notably the case for  $Ag_2Se$  nanocrystals [150–152], ITO nanocrystals [219] or iodine-doped PbS nanocrystals [210].

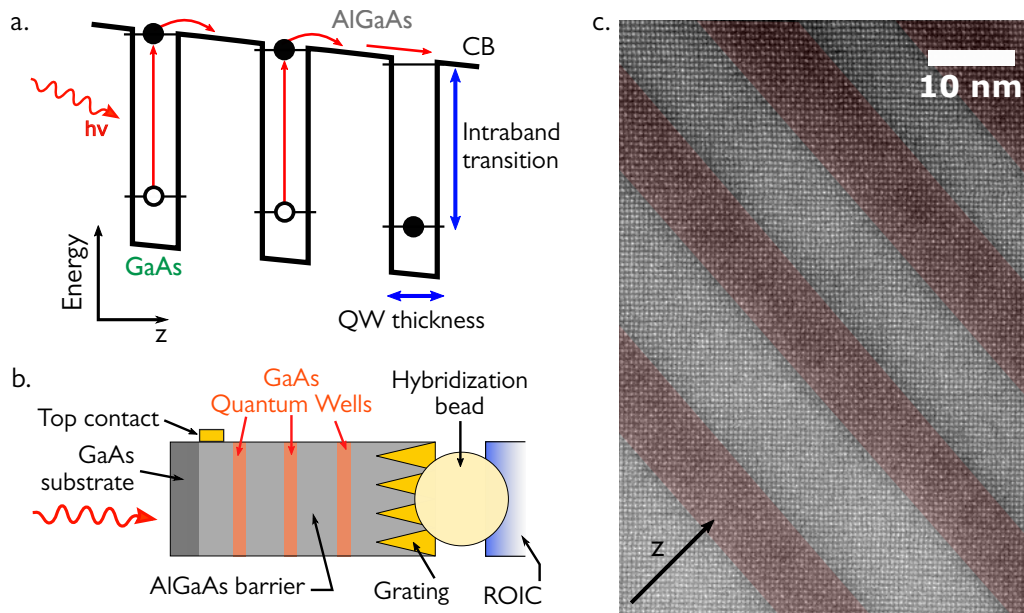


Fig. 4.5 Working principle of an intraband Quantum Well Infrared Photodetector (QWIP). **a.** Schematic band diagram of the conduction band of a QWIP made of multiple doped GaAs Quantum Wells (QW) separated by an AlGaAs barrier. The confined, doped quantum wells feature intraband transitions in the infrared. Electrons promoted to the excited levels of the QW are collected and transported in the AlGaAs barrier. **b.** Scheme of a simple QWIP pixel made of GaAs/AlGaAs equipped with its optical coupling grating and hybridized to a read-out integrated circuit (ROIC). **c.** TEM image of a GaAs/AlGaAs multiple quantum well structure. Doped GaAs quantum wells have been highlighted in red and the growth axis  $z$  is indicated.

When we consider how such issues were tamed with epitaxial material, we must look back to the birth of intraband and inter-subband detectors, which proved to be an alternative to interband-based photodetectors in the infrared (see section 1.3.2). In the 80's and 90's, physicists built the Quantum-Well Infrared Photodetector, or QWIP [126, 220]. An epitaxial Quantum Well (QW) consists in a thin layer of an electron-doped material (GaAs, for example) grown between two layers of a lattice-matched barrier (AlGaAs, here). The energy diagram of such a QWIP heterostructure is presented in Figure 4.5a: because it is doped, the GaAs QW features *intraband* transition between the first levels of its conduction band, and hence absorbs infrared light. The promoted electrons are then transferred to the AlGaAs barrier, and transported in this wide-bandgap material. First devices based on those epitaxially-grown quantum wells were showing poor performance because of the large tunnel current

flowing into the structure, leading to a large dark current. It is only after optimizing the QW-barrier alignment and increasing the barrier length, effectively uncoupling transport and optical absorption, that QWIP devices were able to compete with interband-based devices [124, 220]. Figure 4.5b gives a simplified picture of such a QWIP device. Because of their geometry, the bare heterostructure cannot absorb the normally incident light, so a grating have to be etched at the surface of each pixel to provide efficient light coupling. Figure 4.5c shows a microscopic image of the active material, revealing the very clean, epitaxial growth of the two material.

From this perspective came the realization that good performances with HgSe nanocrystals could be achieved if we found a way to, as it has been successfully done with epitaxial materials, uncouple optical absorption from carrier transport. This requires the design of a new, hybrid material where HgSe nanocrystals take care of the intraband, MWIR absorption, and where the promoted electrons can be transferred to a wider bandgap material. In the following sections, we will be interested in realizing and testing the performances of such materials. The first attempt as creating such an hybrid material was to grow a shell of HgTe on HgSe nanocrystals.

## 4.2 HgSe/HgTe heterostructures: a step toward improved performances

As stated earlier, we want to build a material where optical and transport properties are decoupled by design, in order to reduce the influence of the high doping level of HgSe nanocrystals on the transport properties of the material. Our first approach is to create epitaxially-connected HgSe/HgTe core-shell nanostructures, where the optical properties will be driven by HgSe while transport will occur through HgTe. While the idea of growing a wide-bandgap protective shell of CdSe or CdS on HgSe or HgS doped nanocrystals has been explored before as a strategy to boost the intraband photoluminescence, it ultimately lead to the disappearing of the intraband feature [66, 67]. Moreover, the impact of such an heterostructure on the transport properties of nanocrystal assemblies has never been discussed. In this section, I will firstly introduce the model we used to predict the band alignment and energy diagram of such heterostructures, then I will discuss the synthesis of such materials and their integration into photoconductive devices.

### 4.2.1 Simulation of the core/shell phase diagram

The choice of HgTe as a shelling material is motivated by the fact that HgSe and HgTe present the same crystalline structure and a limited lattice mismatch of around 6% ( $a_{\text{HgSe}} = 0.6085$  nm and  $a_{\text{HgTe}} = 0.6453$  nm). I have shown in the first chapters that HgTe nanocrystals behave like intrinsic semiconductors and feature interband transitions, fast phototransport and good activation energies: we hope that by growing an HgTe shell onto HgSe doped nanocrystals, we can benefit from the combined qualities of the two materials: the intraband absorption of HgSe and the good transport properties of HgTe.

The first task is to explore the band-alignment phase diagram of such heterostructure by the mean of numerical simulation. To do so, we consider a simple concentric spherical core-shell geometry: a HgSe core of radius  $R_{\text{HgSe}}$  on top of which is grown a HgTe shell of thickness  $R_{\text{HgTe}}$ . We need to solve the envelope function equation in this spherical geometry:

$$\left[ \nabla \left( -\frac{\hbar^2}{2m^*(r)} \nabla \right) + V(r) \right] \psi(r) = E\psi(r) \quad (4.1)$$

Where  $m^*(r)$  is the effective mass profile,  $V(r)$  the energy band profile and  $E$  the eigenenergy

associated to the envelope function  $\psi(r)$ . Parameters used for numerical solving of the Schrodinger equation are provided in table 4.1. We make the assumption that the correction of the effective mass profile is negligible compared to that of the energy band profile, and write  $m^*(r) \simeq \text{cst}$ . This is supported by the values given in table 4.1 and by the fact that the error bar on the effective masses in HgTe and HgSe is probably larger than the effective mass difference between HgTe and HgSe. We then write:

$$\left[ -\frac{\hbar^2}{2m^*} \left( \frac{2}{r} \frac{\partial}{\partial r} + \frac{\partial^2}{\partial r^2} \right) + V(r) \right] \psi(r) = E\psi(r) \quad (4.2)$$

At that time, we chosed to use the value reported by Chen *et al.* for HgSe and HgTe valence band offset [111]: they report a value of 0.8 eV, measured by electrochemistry. This model is only qualitative because we neglect any band non-parabolicity as well as dielectric confinement, and assume a perfect spherical geometry. For discrete values of  $R_{\text{HgSe}}$  and  $R_{\text{HgTe}}$ , we numerically solve Equation 4.1 using the shooting method described by Harrison [14]. We start by building the energy potential profiles  $V(r)$ : the boundaries of the nanoparticles are defined by a 2 eV barrier representing the nanocrystal/ligands interface and ensuring the confinement of the wave-functions inside the nanocrystal. We then use the following discretization:

$$\psi(r + dr) = \frac{r \left[ 2m^* \frac{(dr)^2}{\hbar^2} (V(r) - E) + 2 \right] \psi(r) + (dr - r)\psi(r - dr)}{r + dr} \quad (4.3)$$

Where we use a  $dr = 0.1$  nm step. We set  $\psi(0) = 1$  to ensure the confinement of the wave-function in the structure, as well as  $\psi(1) = 1$ , an arbitrary condition that will be corrected when the wave-function gets normalized. The next step is to run the simulation, *i.e.* calculating the wave-function profile for an arbitrary energy  $E$ . The energy is then changed by dichotomy until the wave-function converge toward zero outside the heterostructure: the energy for which this condition is realized is the eigen energy of the wave-function. More details can be found about this procedure in our precedent work on CdSe/ZnS nanoplatelets [113].

Material parameter	Description	Value	Reference
$m_{e, \text{HgSe}}^*$	Electron effective mass in HgSe	$0.06 m_0$	[221, 222]
$m_{e, \text{HgTe}}^*$	Electron effective mass in HgTe	$0.035 m_0$	[223, 224]
$m_{h, \text{HgSe}}^*$	Hole effective mass in HgSe	$0.2 m_0$	[225]
$m_{h, \text{HgTe}}^*$	Hole effective mass in HgTe	$0.5 m_0$	[223, 224]
$V_{\text{VB, HgSe}}$	HgSe valence band energy <i>vs</i> vacuum	-5.5 eV	[111]
$V_{\text{VB, HgTe}}$	HgTe valence band energy <i>vs</i> vacuum	-4.7 eV	[111]
$V_{\text{Offset}}$	Valence band offset between HgSe and HgTe	0.8 eV	[111]

Table 4.1: Material parameter inputs for numerical solving of equation 4.1.

Figure 4.6 summarizes the result of such simulations. In the central panel are identified four main distinct regimes that can be achieved by varying  $R_{\text{HgSe}}$  and  $R_{\text{HgTe}}$ . Each regime is illustrated by a simulation result showing the electron and hole wave-functions. There are two main indications in each of these panels:

- The energy of the  $1S_e$  level relatively to the Fermi level of the system (at  $-4.7$  eV *vs* vacuum) indicates if the whole heterostructure is doped: the  $1S_e$  level must lie below the Fermi level to observe electron doping and the associated intraband transition.

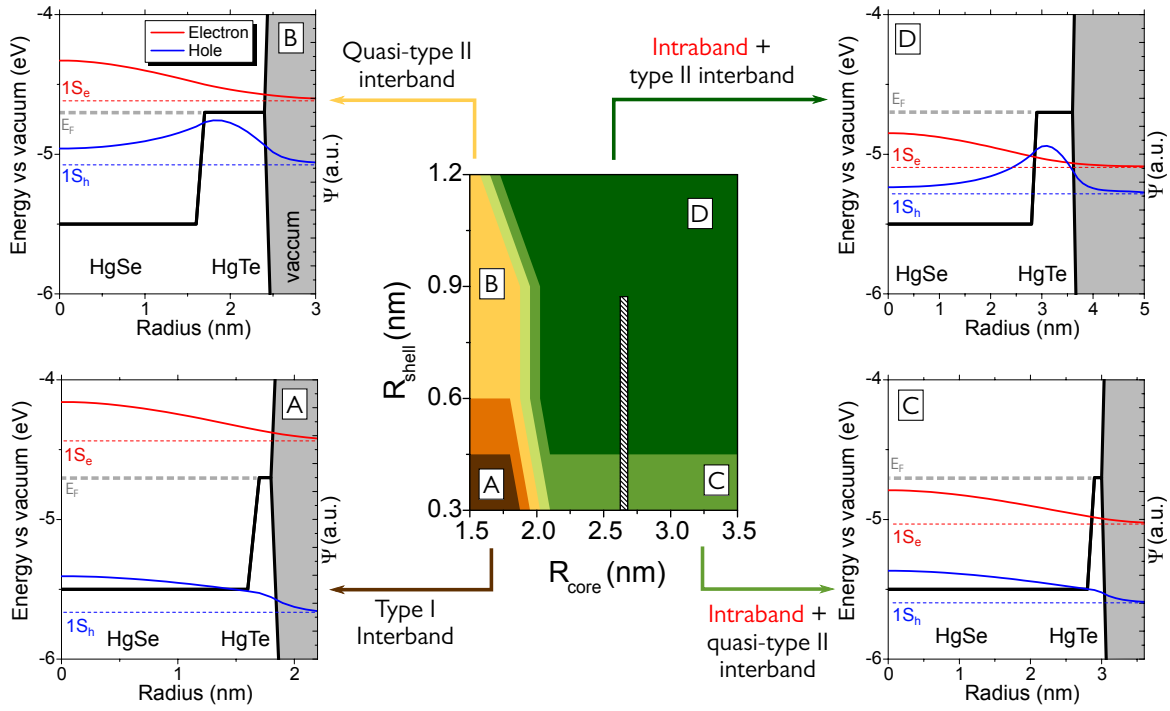


Fig. 4.6 Phase diagram for HgSe/HgTe core/shell heterostructures. The central panel shows the four different possible band-alignments when the size of the HgSe core and HgTe shell are changed. Each surrounding graph corresponds to a simulation of a given situation, identified by letters **A**, **B**, **C** and **D** in the central panel. In each of those four panels, the thick black lines represent the conduction and valence bands of bulk HgSe and HgTe. Conduction and valence bands overlap in bulk HgTe and HgSe due to their semi-metal character ( $E_G = 0$ ). Electron and hole wave-functions (from  $1S_e$  and  $1S_h$  states) are pictured in red and blue lines, respectively, and are shifted to their effective eigen energy, given by the colored dashed line. The thick, dashed grey line represents the Fermi level of the heterostructure. Finally, the stripped area in the central panel corresponds to the range of heterostructures grown in this chapter.

- From the shape of the electron and hole wave-functions can be deduced the associated electron and hole density distributions (given by  $(R_{\text{HgSe}} + R_{\text{HgTe}})^2 |\psi(r)|^2$ ), *i.e.* the electron and hole spatial localization in the heterostructure.

For small  $R_{\text{HgSe}}$  values ( $R_{\text{HgSe}} < 2$  nm, *i.e.* small HgSe cores), the quantum confinement pushes the  $1S_e$  too high (above the Fermi level) and no doping should be observed: there is no intraband absorption. This is consistent with the experimental observation that very small HgSe nanocrystal never display any intraband feature [109]. As a result, those materials only feature interband transition. The nature of those interband transitions depends on the thickness of the HgTe shell. For thin shells (panel 4.6A), we first predict a type-I band alignment with electron and holes delocalized over the whole material. For thicker shells (panel 4.6B), the hole should localize in the HgTe core while the electron stays delocalized, achieving a quasi-type II band alignment.

For larger HgSe radii ( $R_{\text{HgSe}} > 2$  nm), the  $1S_e$  level lies below the Fermi level, indicating that the structure is doped and should display intraband absorption. For thin shells (panel 4.6C), the hole is delocalized and the electron localized in HgSe, so we expect a quasi-type II interband absorption. For thicker HgTe shells (panel 4.6D), the hole localizes in HgTe while the electron is still localized in HgSe, realizing a full type-II heterostructure. This last situations is the most interesting for our application: it combines intraband absorption with a poor electron and hole wave-function overlap, preventing detrimental recombination. This is the targeted heterostructure we will grow in the next section.

### 4.2.2 Growth of HgSe/HgTe heterostructures

The chemical synthesis of the HgSe/HgTe heterostructures was performed by Nicolas Goubet [226]. Growing such material is a challenge, because mercury chalcogenides are soft compounds, do not sustain high temperatures and quickly sinter. The starting point of this synthesis is to grow the desired HgSe cores, with a diameter around 5 nm to present intraband absorption matched with the emission of our 4.4  $\mu\text{m}$  QCL. Most reports about shelling mercury chalcogenide materials employ the colloidal atomic layer deposition method (c-ALD) [180], allowing to grow a shell layer-by-layer at room temperature by successively exposing the material to ions and cations forming the shell. Nevertheless, the high oxygen sensitivity of tellurium makes that this procedure is not well suited for the growth of multilayer HgTe shells.

Alternatively, we use a re-growth technique schematized in Figure 4.7a. A  $\text{HgI}_2$  mercury precursor in oleylamine is degassed and previously synthesized HgSe nanocrystals are introduced at 50°C. Under argon atmosphere, the temperature is increased to 80°C and a TOP:Te solution in oleylamine is injected drop-wise over 60 minutes. Thanks to the low reactivity of  $\text{HgI}_2$  [131] and relative bulkiness of TOP:Te, the growth of HgTe should preferentially occur on the HgSe seeds rather than through side nucleation. After 60 minutes, the reaction is quenched with dodecanethiol (DDT) and the resulting nanocrystals are washed.

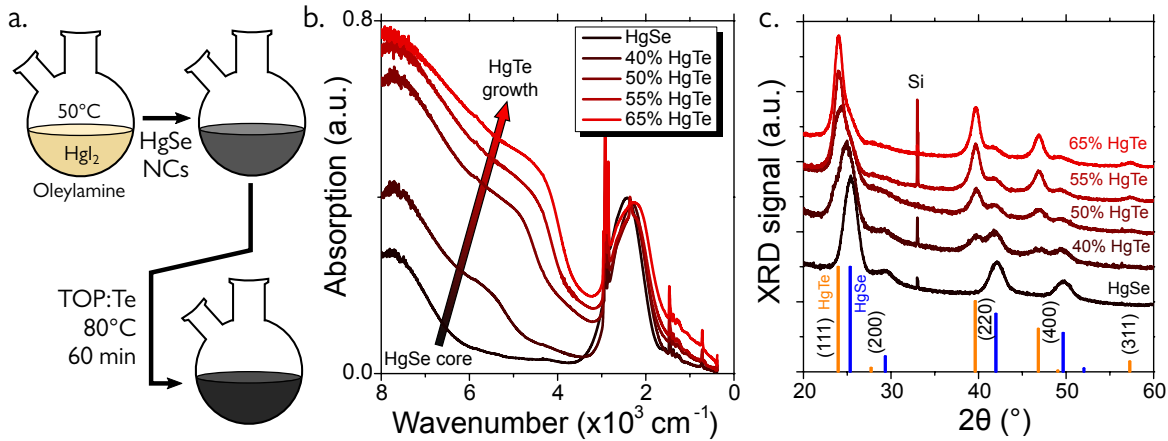


Fig. 4.7 HgSe/HgTe heterostructures: synthesis and characterization. **a.** Schematic synthesis of the HgSe/HgTe heterostructures in mild conditions. **b.** Absorption spectra of the heterostructures after growth of HgTe. The different HgTe contents corresponds to different initial quantities of  $\text{HgI}_2$  precursor from 0.1 to 0.4 mmol, determined on the final nanoparticles by Energy Dispersive X-ray spetrometry (EDX). **c.** Powder X-ray diffraction diagrams for the different heterostructured nanocrystals. Reference diffraction lines for HgSe and HgTe are given in blue and yellow, respectively.

Figure 4.7b shows the optical spectra of such heterostructures. The starting HgSe cores presents intraband absorption around  $2500\text{ cm}^{-1}$  (300 meV) and interband absorption around  $7000\text{ cm}^{-1}$  (840 meV). The successive spectra presented in this figure correspond to increasing HgTe amount (*i.e.* increasing shell thickness), controlled through the concentration of the TOP:Te precursor. Ranging from 0.1 to 0.4 mmol, it leads to Te/Se ratios of 40 to 65%, measured by Energy Dispersive X-ray spetrometry (EDX) and X-ray diffraction on the final materials. Upon HgTe shell growth, the optical spectrum of the material is affected: the intraband feature stays mostly untouched, only displaying a small broadening and red-shift toward lower energies, attributable to the slight wave-function extension into the HgTe shell. For low HgTe content, a de-bleaching of the  $1S_h \rightarrow 1S_e$  interband transition in HgSe is observed around  $5500\text{ cm}^{-1}$  (680 meV), similar to what is observed upon ligand exchange. This suggests a slight de-doping of the HgSe nanocrystals. Upon higher HgTe incorporation, this interband feature red-shifts to saturate around  $4000\text{ cm}^{-1}$  (500 meV), which might be the signature of the expected type-II transition. Another hypothesis to explain the apparent red-shift of this interband

transition involves the interfacial pressure due to a lattice mismatch between HgSe and HgTe: I will discuss this further in the next section. X-ray diffraction, presented in Figure 4.7c, confirms the incorporation of HgTe, as evidenced by the appearance of new diffraction peaks.

Transmission Electronic Microscopy (TEM) images of the materials are given in Figure 4.8. HgSe cores used as seeds for the synthesis present spherical shape and a  $5.2 \pm 0.7$  nm mean diameter, see Figure 4.8a. Upon growth of HgTe, the shape of the particles becomes less regular and their mean size increases to  $6.4 \pm 1.3$  nm in this particular image. While the overall shape of the particles strongly deviates from the expected and simulated spherical core-shell heterostructure, High-Angle Annular Dark-Field imaging in a Scanning-Transmission Electron Microscope (HAADF-STEM) performed by Gilles Patriarche at C2N reveals that nanocrystals present both Se and Te elements at the single-particle level, indicating that the heterostructures are epitaxially connected, see Figure 4.8c and d. This indicates that at least a significant fraction of our heterostructured nanocrystals are Janus-like nanoparticles rather than actual core-shell.

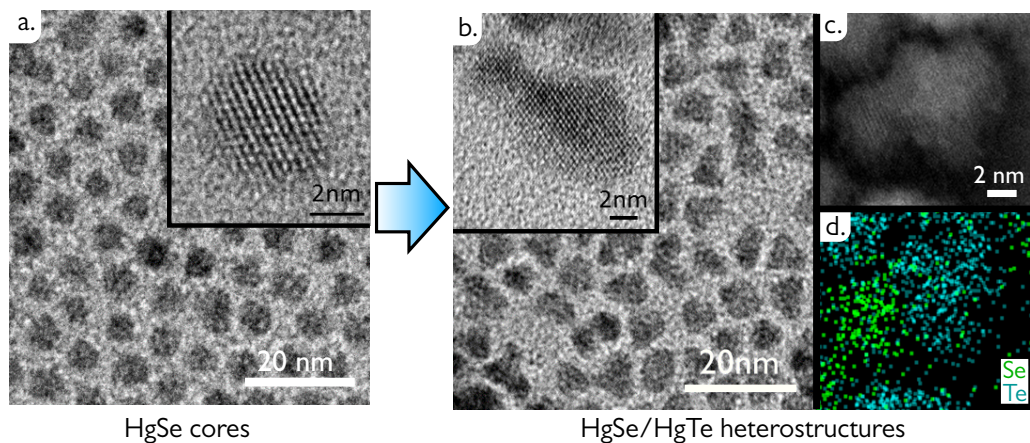


Fig. 4.8 Electronic microscopy images of HgSe/HgTe heterostructures. **a.** TEM image of HgSe core-only nanocrystals. Inset: high-resolution image of a single nanocrystal. **b.** TEM image of resulting HgSe/HgTe nanocrystals after the growth of HgTe on HgSe cores. Inset: high-resolution image. **c.** HAADF STEM image of a single HgSe/HgTe heterostructure with **d.** the localization of Se (green) and Te (blue) in the particle.

After successfully synthesizing those HgSe/HgTe heterostructures, we integrated them into photoconductive devices to determine the impact of such a HgTe "shell" on transport, phototransport and ultimately, MWIR detection performances.

### 4.2.3 Transport and improved MWIR performances in HgSe/HgTe heterostructures

To get an accurate idea of how the heterostructure affects the transport properties of the nanocrystals, I built devices from both HgSe core material and the HgSe/HgTe heterostructures. Both materials are drop-cast onto interdigitated electrodes from a hexane:octane solution, and cross-linked with a solid-state ligand exchange toward ethanedithiol (EDT).

I first measured transport properties of both materials in dark conditions. Field effect transistor measurements made in an electrolyte gate configuration shows a dramatic change in the shape of the transfer curve between the core-only material and the heterostructure, see Figure 4.9a. While the transfer curve of the core material displays the pure n-type behavior expected for self-doped HgSe nanocrystals (see section 4.1.1 and Figure 4.2c), the transfer curve of the heterostructured material shows ambipolar characteristics, with conduction of both electron and holes. In that sense, this transfer curve resembles a lot that of HgTe nanocrystals (see Figure 3.1c, for example). To quantify

the effect of HgTe on transport, we look at the hole mobility, and more precisely at the  $\mu_e/\mu_h$  electron to hole mobility ratio. By taking the derivative of the transfer curves, we can evaluate this ratio for pure HgSe, HgTe and core/shell devices. Figure 4.9b shows that there is a clear drop in the  $\mu_e/\mu_h$  ratio between the pure HgSe material and all the heterostructured materials synthesized during this project. For the sake of comparison, the  $\mu_e/\mu_h$  ratio for pure HgTe nanocrystals featuring interband transition around  $4000\text{ cm}^{-1}$  has been provided.

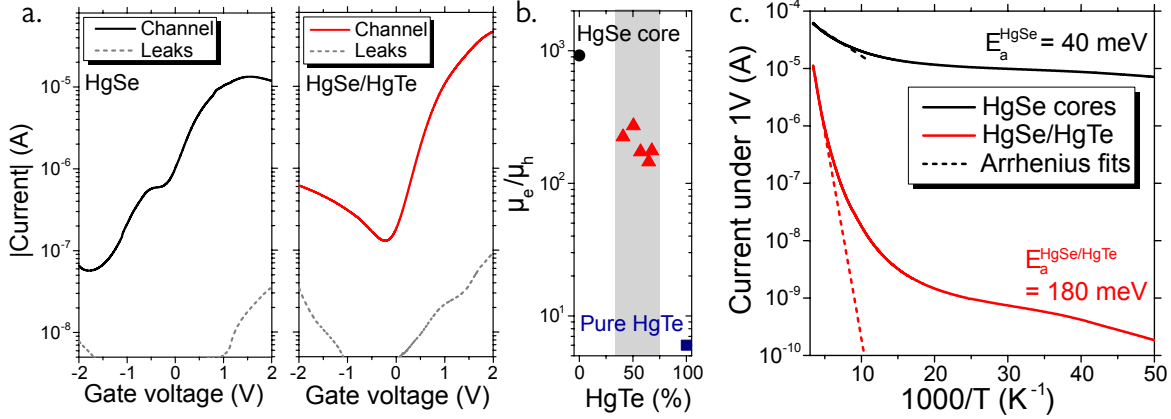


Fig. 4.9 Dark current reduction in HgSe/HgTe heterostructures. **a.** Field-effect transistor transfer curves of HgSe core nanocrystals (left) and HgSe/HgTe heterostructures (right) in an ion-gel gating configuration. Both materials are capped with EDT ligands. Drain voltages are respectively of 50 mV and 400 mV. **b.** Ratio of electron/hole mobilities for pure HgSe (black circle) and HgTe materials (blue square) and for several heterostructured nanocrystals (red triangles). Mobility ratios are determined using the derivative of the transfer curves. **c.** Evolution of devices dark current under 1 V polarization in the case of EDT-capped HgSe (black) and HgSe/HgTe (red). An Arrhenius fit is provided at high temperature, allowing the extraction of a dark current activation energy  $E_a$ .

Activation energies of both devices have also been measured by cooling down the samples in the dark and under 1 V bias, see Figure 4.9c. The activation energy relates on how the dark current of a device is reduced when the operating temperature is lowered, and is a critical figure of merit for an infrared-sensing material. Just as reported earlier, the HgSe core-only material features a fairly low activation energy of around  $40 \pm 20$  meV. The HgSe/HgTe heterostructured material, on the other hand, features an impressively larger  $180 \pm 20$  meV activation energy, with the dark current dropping by three orders of magnitude between 300 K and 100 K. By looking at the dark current only, this is a very strong performance improvement compared to the pure HgSe material. Not only the dark current is reduced at room temperature, but the activation energy is significantly increased, meaning that the dark current drops by several orders of magnitude at cryogenic temperatures. Interestingly, the value of 180 meV is higher than half of the intraband optical bandgap in HgSe ( $E_{\text{Intraband}} \simeq 300$  meV), indicating that the HgTe shell is indeed involved in the carrier transport.

From the transport point of view, it looks like the material behaves like an undoped (or very lightly doped) material, while preserving the intraband optical absorption. We now need to know if we still observe MWIR photocurrent in those devices.

In that scope, we use our  $4.4\ \mu\text{m}$  ( $2270\text{ cm}^{-1}$ ) Quantum Cascade Laser to resonantly excite the intraband transition in HgSe. By using this very narrow optical source, we make sure that any observed photocurrent origins from absorption in the MWIR intraband transition of HgSe material. The experiment is schematized in Figure 4.10a: the QCL working in quasi-CW is optically chopped at low frequency and sent onto our devices, enclosed in a cryostat. Photocurrent is either directly measured by the source-meter, or amplified and visualized on a oscilloscope. Temporal traces of the photocurrent are provided in Figure 4.10b for pure HgSe cores (measured at 100 Hz) and in Figure 4.10c for the HgSe/HgTe heterostructures (measured at 1 kHz). While the pure HgSe material displays

the same very slow, symmetrical photoresponse as described earlier, the HgSe/HgTe heterostructured material is much faster, with rising and falling times measured around 50  $\mu\text{s}$ , limited by the speed of the optical chopper blade. Another way of presenting the same effect is to plot the frequency dependence of the photocurrent, see Figure 4.10d: HgSe core nanocrystals photocurrent continuously decreases with increased frequency while the HgSe/HgTe photocurrent is flat over the 1 Hz to 1 kHz window.

We then evaluated the responsivity and detectivity of those two devices at room temperature and under low frequency (10 Hz) excitation with a 982°C blackbody equipped with a 1.9  $\mu\text{m}$  Ge filter. The noise of those devices is found to be  $1/f$ -limited for both materials. The detectivity is found to be more than 30 times higher for heterostructures than for pure HgSe material, even in conditions where the heterostructure does not benefit from all their advantages (detectivity measured at room temperature and at 1 Hz).

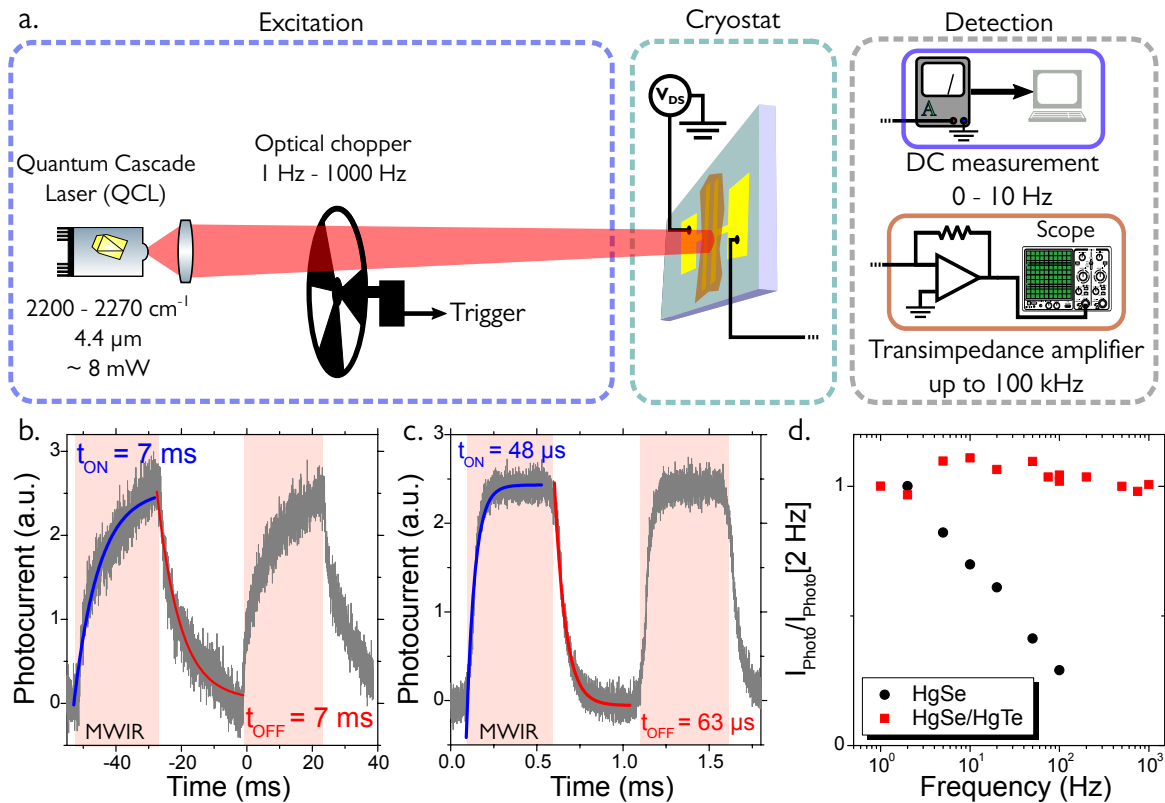


Fig. 4.10 Acceleration of the photoresponse in HgSe/HgTe heterostructures. **a.** Scheme of the experiment: a 4.4  $\mu\text{m}$  QCL is used to resonantly excite the intraband transition in HgSe nanocrystals. The light is optically chopped and the device photocurrent is either measured by the source-meter (for chopping frequencies  $< 10$  Hz) or amplified and sent to an oscilloscope. **b.** Photocurrent temporal trace in a EDT-capped HgSe device under MWIR intraband excitation at 100 Hz. Turn-ON and turn-OFF times are extracted from exponential fits (in blue and red). **c.** Photocurrent temporal trace in a EDT-capped HgSe/HgTe device under MWIR intraband excitation at 1 kHz. **d.** Frequency dependence of the photocurrent in HgSe and HgSe/HgTe-based devices, under illumination in the MWIR. The photocurrent is normalized at low frequency for each data set.

Heterostructuring HgSe with HgTe is hence a valid approach to improve the material optoelectronic properties. By growing an epitaxially-connected HgTe "shell" on HgSe nanoparticles, we observe a dramatic effect on the transport properties of the material, while the key optical property of the HgSe nanoparticles (namely, the presence of intraband absorption in the MWIR due to electron doping) is preserved. Charge transport in this new material is very similar to what is measured in arrays of intrinsic, weakly coupled nanocrystals (see chapters 2 and 3). As a result, this material seems to solve the three main issues encountered while building HgSe-based photodetector devices:

- Dark current shows significant reduction, even at room temperature
- Activation energy is improved up to 180 meV, higher than half of the optical intraband bandgap of HgSe.
- The photocurrent shows fast dynamics.

#### 4.2.4 Perspectives for HgSe/HgTe nanocrystals

These results can be seen as a signature of a successful electron transfer from HgSe to HgTe after photon absorption, and transport through an array of (intrinsic) HgTe-like nanoparticles. The devices made with those nanocrystals are nevertheless not extraordinary efficient, and need to be improved: responsivity of the devices is notably fairly low (around 10  $\mu\text{A}/\text{W}$ ) because of low absorption (films in those devices are  $\sim 50$  nm thick, resulting in  $\sim 1$  % light absorption in the MWIR). However, the synthesis of those particles being still quite challenging, the produced amounts of nanocrystals remain limited. In the last section of this chapter, I will present a different, yet similar approach allowing to achieve even higher performances with HgSe-based photodetection.

In the process of understanding the band diagram of such heterostructured nanoparticles, we stumbled around a question: since HgTe grows epitaxially onto HgSe, and since there is a small 6% lattice mismatch between the two crystal structures, what is the effect of interfacial pressure at the HgSe/HgTe interface, and can it explain the observed changes in the optical properties of the nanocrystals? To answer these questions and go further into the global comprehension of nanoscale mercury chalcogenide systems, we looked into the effect of pressure on several nanocrystals. The next section is dedicated to such investigations.

### 4.3 Effect of pressure on narrow-bandgap materials

The question of pressure effect on mercury chalcogenide nanocrystals came from our work on HgSe/HgTe nanocrystals, as presented earlier. While the effect of temperature on the optical spectrum of HgSe and HgTe has been quite extensively studied, mostly because of their interest for infrared detection requiring low-temperature operation [109, 118, 188], the effect of pressure on those nanocrystals has never been reported. The unusual band diagram of bulk HgTe and HgSe (inverted band diagram, semi-metal nature, ...) makes that mercury chalcogenide nanocrystals are an interesting platform to study these effects. Interestingly, in their bulk phase, pressure effect in HgTe and HgSe has been investigated in the last century [227, 228]. More recently, topological insulators have motivated the study of HgTe thin films under strain [229]. The peculiar band diagram of HgTe and HgSe makes that even under nanocrystal form, they do not behave like traditional II-VI semiconductor nanocrystals (CdSe, CdS, ...). For example, their interband transition ( $1S_h \rightarrow 1S_e$ ) red-shifts at low temperature instead of the expected blue-shift.

Moreover, knowledge about the pressure effect on the nanostructures is mandatory to get a good understanding of the interfacial effects occurring while growing heterostructures with mercury chalcogenides: due to lattice mismatch, interfacial strain appears when epitaxially growing two materials on top of each other. In this section, I will present theoretical and experimental results obtained in collaboration with Francesco Capitani at the SMIS beamline of Soleil Synchrotron and Sébastien Sauvage at C2N, who provided  $\mathbf{k}\cdot\mathbf{p}$  simulation.

### 4.3.1 Evaluation of the interfacial pressure in HgSe/HgTe nanocrystals

In a first approach, we wanted to evaluate the impact of lattice mismatch in HgSe/HgTe core-shell nanocrystals optical properties: as I presented in the last section, while growing HgTe on top of HgSe, we see a strong shift of the interband absorption (see Figure 4.7b) from around  $5500 \text{ cm}^{-1}$  to  $4000 \text{ cm}^{-1}$ , corresponding to a 180 meV red-shift. We mostly attribute this red-shift to hole delocalization in the HgTe shell, but we want to evaluate how much of this spectrum modification can be explained by pressure effects at the HgSe/HgTe interface. For a spherical core/shell nanoparticle geometry, the interfacial pressure is given by [230]:

$$P_i = \frac{2\varepsilon Y_{\text{core}} Y_{\text{shell}} \times \left( \frac{R_{\text{shell}}^3}{R_{\text{core}}^3} - 1 \right)}{[2Y_{\text{shell}}(1 - 2\nu_{\text{core}}) + Y_{\text{core}}(1 + \nu_{\text{shell}})] \frac{R_{\text{shell}}^3}{R_{\text{core}}^3} - 2[Y_{\text{shell}}(1 - 2\nu_{\text{core}}) - Y_{\text{core}}(1 - 2\nu_{\text{shell}})]} \quad (4.4)$$

Where  $Y_{c/s}$  and  $\nu_{c/s}$  are the Young modulus and the Poisson ratio of the core and shell materials, and  $\varepsilon$  is the lattice mismatch (6 %). Since the two materials (HgSe core and HgTe shell) are very similar structurally speaking, we assume that  $Y_{\text{core}} = Y_{\text{shell}} = 40 \text{ GPa}$  [231] and  $\nu_{\text{core}} = \nu_{\text{shell}} = 0.46$  [232]. Equation 4.4 then becomes:

$$P_i = \frac{2\varepsilon Y_{\text{HgX}}}{3(1 - \nu_{\text{HgX}})} \left( 1 - \frac{R_{\text{core}}^3}{R_{\text{shell}}^3} \right) \simeq 1.4 \text{ GPa} \quad (4.5)$$

We can then evaluate the effect of this interfacial pressure on the bandgap of HgSe nanocrystals. Using a deformation potential of  $a_P = 4.9 \text{ meV/kbar}$  reported for bulk HgSe [233], we have:

$$\delta E_G = a_P P_i = 68 \text{ meV} \quad (4.6)$$

Which is too low to explain the observed 180 meV red-shift. Moreover, the shape of the particles deviates strongly from this spherical core-shell model, as seen by TEM imaging, so we can expect the interfacial pressure to be even lower considering the small surface of contact between the HgSe and HgTe coupled nanoparticles. As a result, this red-shift of the interband transition can be attributed mostly to the hole delocalization in HgTe. Nevertheless, it is important to quantify precisely the effect of this kind of interfacial pressure, notably for future use of alternative shelling materials.

### 4.3.2 Fourier-transform Infrared Spectroscopy under pressure at Soleil synchrotron

To investigate the effect of hydrostatic pressure on the optical properties of HgTe and HgSe nanocrystals, we used the high pressure infrared spectroscopy setup of SMIS beamline at Soleil synchrotron. The setup is presented in Figure 4.11. In a synchrotron, low energy infrared photons are created through *bremstrahlung* due to deceleration of the electron beam. Because of their low energy, production of these photons does not requires to alter the electron beam trajectory: they are emitted even when the beam travels in a straight line, due to continuous deceleration of the electrons. As a result, they can be collected by bringing a mirror sufficiently close to the electron beam. While a synchrotron source does not produce significantly more photons than a typical lab FTIR glow-bar source, the beam *brilliance* is much higher because of a low angular divergence.

The experiment, described in Figure 4.11a, relies on a modified commercial FTIR to produce high order infrared "white light" from the synchrotron infrared beam passing through a Michelson

interferometer. This light is then coupled into a Cassegrain microscope focusing the light into the 150  $\mu\text{m}$  hole of the high pressure Diamond Anvil Cell (DAC) containing our sample, and focused onto a nitrogen-cooled MCT MWIR-LWIR detector. The output of the detector is then sent back into the FTIR to lock its signal to the mirror displacement and perform the Fourier transform necessary to obtain the absorbance spectrum of our sample. The Diamond Anvil Cell is schematized in Figure 4.11b: it consists in two diamonds cut with a 150  $\mu\text{m}$  flat, facing each other. A stainless steel gasket, shown in Figure 4.11c is embedded into the cell between the two diamond flats. Our nanocrystal sample is contained within that gasket, drop-cast from colloidal solution onto a clear NaCl layer used to fill the voids and efficiently transmit the pressure. The pressure is increased in the DAC by inflating a metallic membrane with helium, pushing the diamonds together. The pressure is monitored by following the fluorescence signal of a ruby microcrystal included within the NaCl window, inside the DAC. Our experiments explore a low range of pressure, mainly between 0 and 5 GPa, and up to 12 GPa.

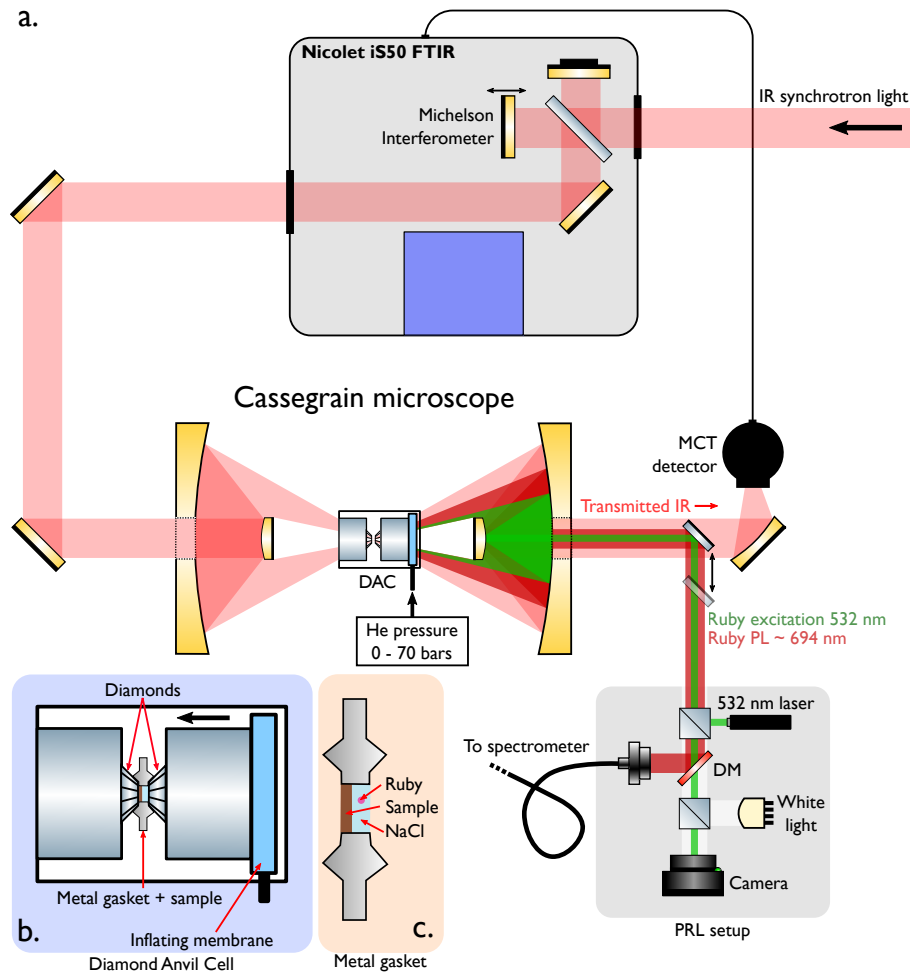


Fig. 4.11 Experimental setup for high-pressure infrared spectroscopy on SMIS beamline at Soleil synchrotron. **a.** Scheme of the optical setup, comprising of a commercial FTIR spectrometer, a Cassegrain microscope, an external MCT detector and a pressure-monitoring setup based on ruby photoluminescence measurement (Pressure by Ruby Photoluminescence, PRL). DAC: diamond anvil cell. DM: dichroic mirror. **b.** Scheme of the diamond anvil cell used to induce high pressure at the sample location, between the two diamonds' flats. **c.** Scheme of the metal gasket introduced between the two diamonds and containing the nanocrystal sample as well as the pressure-monitoring ruby.

In this section, I present the effect of pressure on both HgTe and HgSe materials. Two sizes of HgTe nanocrystals and three sizes of HgSe nanocrystals have been studied in this work to get an accurate picture of the pressure effect on the nanocrystal's energy diagrams.

### 4.3.3 HgTe nanocrystals under pressure: a story of gap-opening

HgTe nanocrystals crystallize in a cubic zinc-blende ( $F\bar{4}3M$ ) structure. In its bulk form, HgTe transforms into a cinnabar phase ( $P3_121$ ) at 1.4 GPa [234, 235], which is a fairly low pressure: our previous calculations shows that it is in the expected range of interfacial pressure for shell growth, see Equation 4.5. This cinnabar phase is stable up to 8 GPa in the bulk, then the material undergoes another phase transition toward rock-salt structure [236]. It is not clear how those phase transitions are affected once the material is under nanocrystal form, so I firstly present high-pressure X-Ray Diffraction results obtained with the IMPMC lab, allowing to indentify phase transitions in our material. To get a good understanding of the material behavior under high pressure, we study two different sizes of nanocrystals: HgTe "4k" with a band-edge around  $4000\text{ cm}^{-1}$  (500 meV), and HgTe "6k" with a band-edge around  $6000\text{ cm}^{-1}$  (740 meV).

#### Phase transition

The high-pressure XRD experiment done at IMPMC lab with Benoit Baptiste and Stefan Klotz employs the same Diamond Anvil Cells (DAC) presented earlier. We use HgTe 4k to determine the pressure threshold for phase transition in HgTe nanocrystals: X-ray diffractograms are presented in Figure 4.12a. The zinc-blende structure is clearly identified at low pressure and remain stable up to at least 3 GPa. Under 5.5 GPa of pressure, a clear phase change is observed: the new phase corresponds to a cinnabar phase. This pressure is much higher than the 1.4 GPa threshold pressure reported for bulk HgTe [234, 235]: this change of threshold toward higher pressure has already been observed for CdSe nanocrystals, and attributed to a nucleation barrier delaying the phase transition [237].

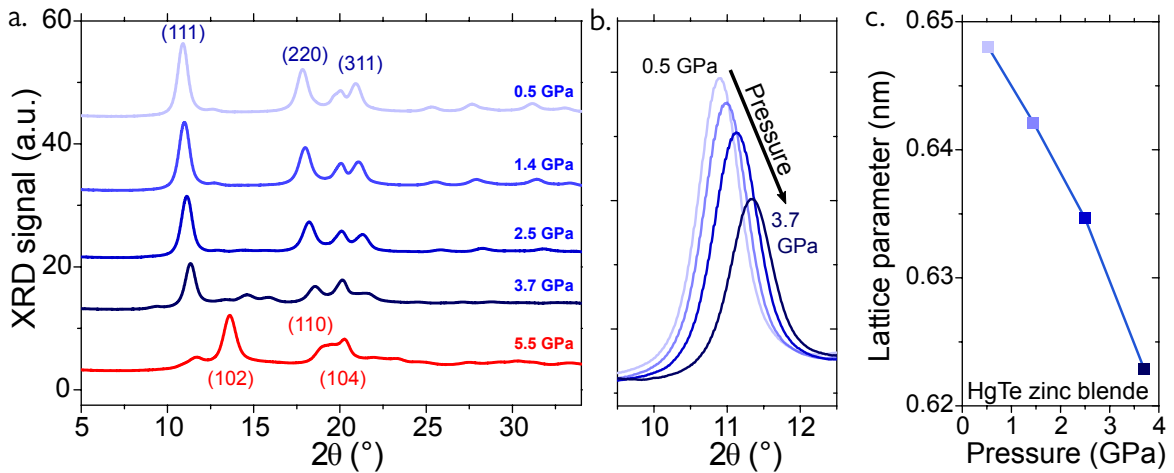


Fig. 4.12 Phase transition in HgTe nanocrystals under pressure. **a.** X-ray powder diffractograms for HgTe "4k" nanocrystals (with band-edge around  $4000\text{ cm}^{-1}$ ) under increasing pressure. Phase transition occur between 3.7 GPa (last blue curve) and 5.5 GPa (red curve). **b.** Zoom on the [111] Bragg reflection peak for HgTe nanocrystals in the zinc-blende phase. **c.** Lattice parameter of HgTe zinc-blende phase under increasing pressure, extracted from the [111] Bragg reflection.

By looking at the [111] Bragg reflection, we can extract the lattice parameter on HgTe in the zinc-blende phase, and follow its evolution with pressure (see Figure 4.12b and c). We obtain a pressure coefficient of  $da/dP = -6.4 \times 10^{-3}\text{ nm/GPa}$ , and an average lattice parameter  $a \simeq 0.645\text{ nm}$ . We can then calculate the bulk modulus at zero pressure  $B_{\text{HgTe}} = -dP/(3da/a) \simeq 33\text{ GPa}$ , very close to the value of 34 GPa expected for bulk HgTe. With a Poisson coefficient  $\nu_{\text{HgTe}} = 0.288$  [238], we obtain a Young modulus of  $Y_{\text{HgTe}} = 3B_{\text{HgTe}}(1 - 2\nu_{\text{HgTe}}) = 42\text{ GPa}$ , again close to the commonly admitted 40 GPa for bulk HgTe.

### Pressure effect in the zinc-blende domain

We then explore the effect of pressure on optical properties of HgTe nanocrystals. Since the cinnabar phase does not present any narrow-bandgap, we are only interested in the low pressure regime where the material stays in the zinc-blende phase and where the band diagram of HgTe is known. The signature of the phase change is visible in the optical spectrum of HgTe: the spectrum becomes featureless around 3 GPa, and only shows a strong, continuous baseline increase for higher pressures [239]. It is important to note that for every sample studied in this section, the effect of pressure is reversible (with notable hysteresis) and does not seem to lead to any sintering effect.

The evolution of both HgTe 4k and 6k spectra under pressure is pictured in Figures 4.13a and b, and consistently shows a blue shift of the  $1S_h \rightarrow 1S_e$  interband transition under increasing pressure. The band-edge energy of both nanocrystal samples are extracted from the FTIR spectra and plotted in Figure 4.13c against the cell pressure. In the 1 to 2 GPa range, a linear fit of the bandgap evolution with pressure is provided, allowing to extract  $dE_{\text{inter}} \simeq 60$  meV/GPa for both sizes of nanocrystals.

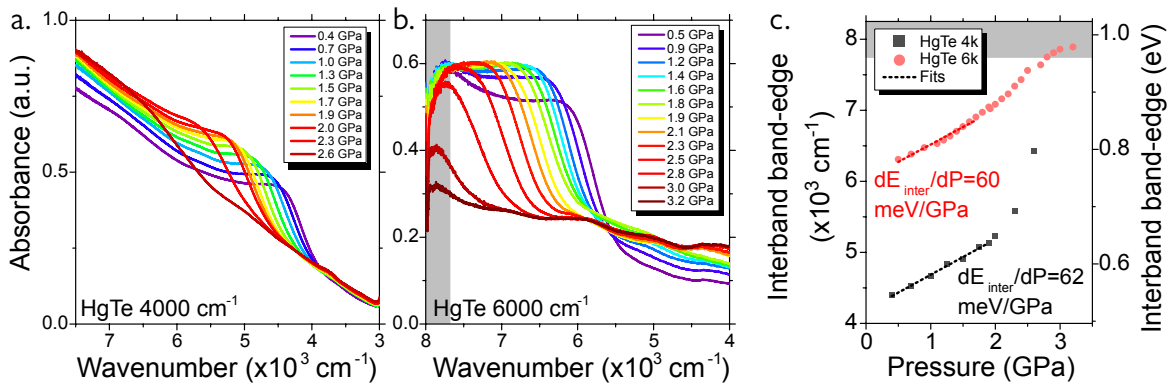


Fig. 4.13 HgTe nanocrystals under pressure: infrared spectroscopy. **a.** Infrared spectra under increasing pressure of HgTe "4k" nanocrystals, with a band-edge around  $4000 \text{ cm}^{-1}$  at ambient pressure. Final pressure is 2.7 GPa. **b.** Infrared spectra under increasing pressure of HgTe "6k" nanocrystals, with a band-edge around  $6000 \text{ cm}^{-1}$  at ambient pressure. Final pressure is 3.2 GPa. **c.** Evolution of the band-edge energy for both HgTe nanocrystals (4k and 6k). Linear fits are provided at low pressure (0-2 GPa).

To understand the origin of this blue shift, we firstly use a simple, infinite well quantum box model. In such a model, the interband transition energy is given by:

$$E_{\text{inter}}(P) = E_{1S_e} - E_{1S_h} = E_{\text{bulk}}(P) + \frac{3\hbar^2\pi^2}{2m_h^*(P)(2R_{\text{QD}}(P))^2} + \frac{3\hbar^2\pi^2}{2m_e^*(P)(2R_{\text{QD}}(P))^2} \quad (4.7)$$

Where  $E_{\text{bulk}}(P)$  is the bulk bandgap of HgTe (0 at ambient pressure),  $m_h^*(P)$  and  $m_e^*(P)$  are the effective hole and electron masses in the parabolic model, and  $R_{\text{QD}}(P)$  the nanocrystal mean radius. Considering such an expression, one can expect the applied pressure to have an effect on the bulk bandgap, the effective masses (*i.e.* the bands curvature), and the nanocrystal mean radius.

We first consider the nanocrystal radius: under compression, nanocrystals shrink. Thanks to XRD measurements, we can estimate that under 1 GPa, the nanocrystals radius is reduced by  $\varepsilon = P/(3B_{\text{HgTe}}) = 1\%$ . A size reduction leading to an increase of confinement, a blue shift of the interband transition is expected: we can quantify it using Equation 4.7:

$$\frac{\Delta E_{\text{inter}}(P)}{E_{\text{inter}}(P=0)} = 2 \frac{\Delta R_{\text{QD}}(P)}{R_{\text{QD}}(P=0)} \approx 2\% \quad (4.8)$$

Which is much smaller than the observed  $\sim 10\%$  shift at 1 GPa. As a result, a significant contribution of the shift is brought by either a change in effective masses or a change in the bulk bandgap of HgTe. To discriminate between the two, we need a deeper understanding of the HgTe band structure behavior under pressure.

### HgTe nanocrystals under strain through $\mathbf{k}\cdot\mathbf{p}$ simulation

To get a deeper understanding of the physical processes at play, we asked Sébastien Sauvage from C2N to perform  $\mathbf{k}\cdot\mathbf{p}$  simulation on HgTe under compressive strain. He uses a 8-bands  $\mathbf{k}\cdot\mathbf{p}$  formalism, and as a starting point he fits the DFT-calculated band structure proposed by Svane *et al.* with the 8-bands  $\mathbf{k}\cdot\mathbf{p}$  model. Strain is introduced as a deformation potential in the structure, chosen to be  $\gamma_{\text{HgTe}} = -2.4$  eV between  $\Gamma_8$  and  $\Gamma_6$  bands to quantitatively fit the experimentally observed shifts. I will discuss the slight difference between this value and the one reported in literature later in this section.

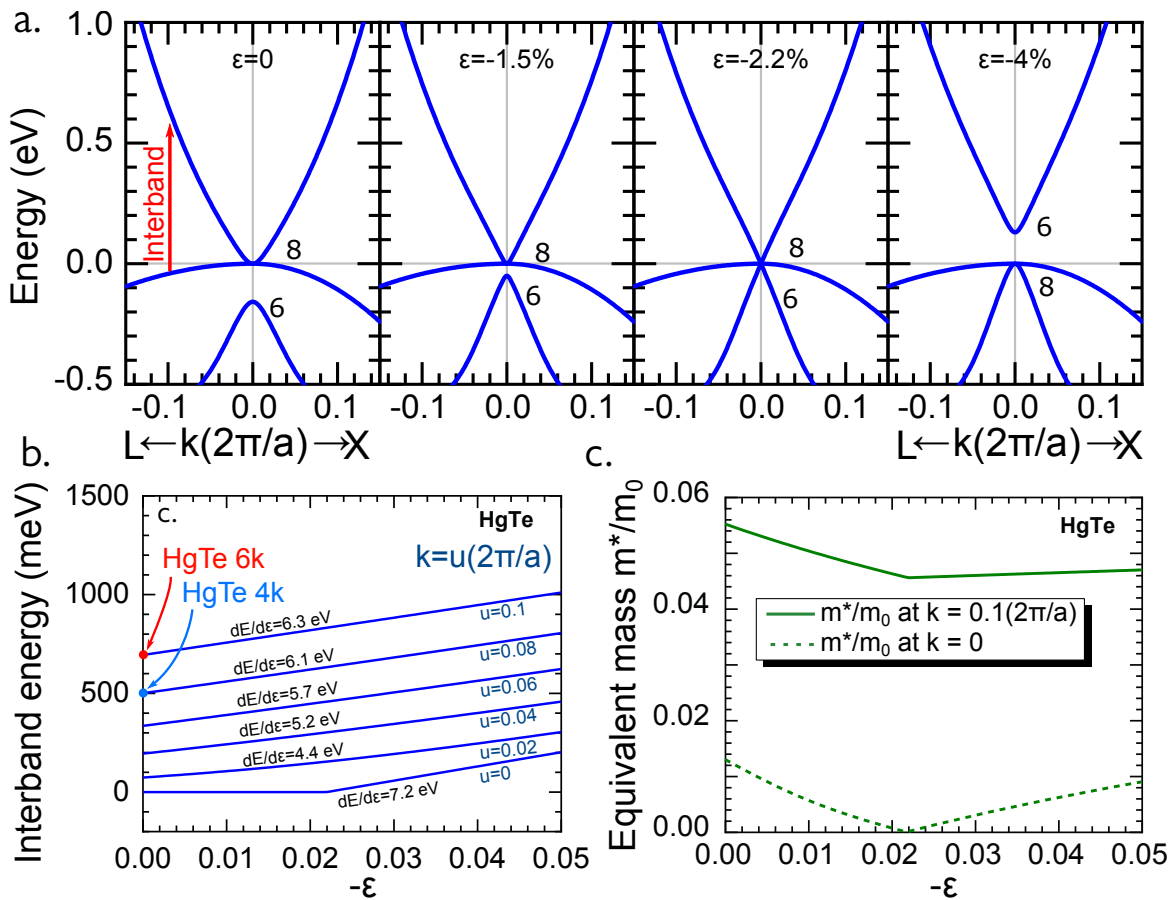


Fig. 4.14  $\mathbf{k}\cdot\mathbf{p}$  simulations: HgTe under compressive strain. **a.** Band diagram (energy as a function of the Brillouin zone wave vector  $\mathbf{k}$ ) of bulk HgTe calculated for different values of strain  $\varepsilon$ , from 0 to -4 %. The bandgap remains closed at  $\Gamma$  point up to -2.2 % strain. We simulate a quantum dot by slicing the band diagrams at  $k \neq 0$ . **b.** Simulated evolution of the interband transition energy in HgTe nanocrystals under strain: interband energy is calculated from slices of the band diagrams at  $k = u \times 2\pi/a$ . The wave vector  $\mathbf{k}$  is here along the  $\Gamma - L$  direction. Curves corresponding to the experimentally studied materials (HgTe 4k and 6k) have been highlighted at zero strain. **c.** Simulated evolution of the equivalent mass in HgTe under compressive strain, at the zone center  $\Gamma$  (dashed line) and at  $k = 10\%(2\pi/a)$  along  $\Gamma - L$  (thick line). The equivalent mass is the mass  $m^*$  that gives the  $\mathbf{k}\cdot\mathbf{p}$ -calculated energy  $E(k)$  of the conduction band at the  $\mathbf{k}$  point through the formula  $E(k) = E(k=0) + \hbar^2 k^2 / (2m^*)$ .

Figure 4.14a presents the band structure of bulk HgTe under increasing strain, around the center of the Brillouin zone. The deformation  $\varepsilon = da/a$  is negative to simulate compressive strain. Whenever strain is applied to the structure, the bands start to deform. Particularly, the conduction  $\Gamma_8$  band curvature increases (*i.e.* the electron effective mass decreases for strains below 2.2 %). The valence  $\Gamma_6$  band shifts upward as soon as strain is applied, but this should have no effect on the interband absorption of the material since the relevant valence band (of higher energy) is the  $\Gamma_8$  band. For a 2.2 % strain, the  $\Gamma_6$  band touches both  $\Gamma_8$  bands at the  $\Gamma$  point. Below this critical value, the bandgap of the bulk material remains null because it is defined by the two  $\Gamma_8$  bands, touching at  $\Gamma$  point. Above this critical value of  $|\varepsilon| = 2.2$  %, the band ordering is swapped: the  $\Gamma_6$  band moves above the Fermi level and becomes the conduction band, while the  $\Gamma_8$  band becomes a valence band. A direct bandgap opens at the  $\Gamma$  point between the conduction and valence bands of strained HgTe. From that point of view, the band diagram of HgTe under sufficient strain becomes non-inverted and looks like a typical II-VI semiconductor band diagram.

In this simulation, the interband transition in a HgTe nanocrystal is defined by taking a slice in the band diagram at discrete wave vectors from the family:

$$\mathbf{k}_{\pm 1 \pm 1 \pm 1} = \frac{\pi}{R_{\text{QD}}}(\pm 1, \pm 1, \pm 1) \quad (4.9)$$

In practice, we look for  $\mathbf{k}$  vectors along the  $\Gamma - L$  direction and take slices at different  $u$  such as  $k = u \times 2\pi/a$ . From the non-strained band diagram, we find that HgTe 4k with a 500 meV bandgap corresponds to  $u = 0.08$ , and that HgTe 6k with a 740 meV bandgap corresponds to  $u = 0.1$ . Figure 4.14b shows the evolution of the interband energy  $E_{\text{inter}}(\varepsilon)$  for different values of  $u$  under increasing compressive strain. At the center of the Brillouin zone (*i.e.* at  $u = 0$ ), the two regimes of pressure effect are clearly identified with a constant, null bandgap up to  $\varepsilon = -2.2$  % (in the effective mass regime), then a continuous increase of the interband energy in the gap opening regime. For  $u \neq 0$  though (the case corresponding to actual confined nanocrystals), those two regimes are indistinguishable: the increase of bandgap energy is linear for the whole range of explored strain. In other words, away from the center of the Brillouin zone, the two regimes have the same quantitative effect despite having different physical origins.

The equivalent mass, *i.e.* the effective mass  $m^*$  that gives the  $\mathbf{k} \cdot \mathbf{p}$ -calculated energy  $E(k)$  of the conduction band at the  $\mathbf{k}$  point through the formula  $E(k) = E(k=0) + \hbar^2 k^2 / (2m^*)$ , has been plotted for  $u = 0$  and  $u = 0.1$  in Figure 4.14c. The two regimes are clearly identified here: the equivalent mass decreases below a 2.2 % strain, then the gap opens at 2.2 % strain and the effective mass slowly increases to retrieve its original value, compensating the effect of bandgap opening.

This simulation reproduces well the experimental results, because it predicts a quasi-linear blue shift of the HgTe nanocrystal interband transition, see Figure 4.14, and because the slope of this shift with strain is poorly dependent on the nanocrystal size (*i.e.* on  $u$ ). The extracted slopes  $dE_{\text{inter}}/d\varepsilon$  are provided in Figure 4.14, and can be converted to meV/GPa using the measured bulk modulus of HgTe nanocrystals through:

$$\frac{dE_{\text{inter}}}{dP} = \frac{dE_{\text{inter}}}{d\varepsilon} \times \frac{1}{3B_{\text{HgTe}}} \quad (4.10)$$

Leading to the  $\sim 60$  meV/GPa measured experimentally. The value of the deformation potential  $\gamma_{\text{HgTe}} = -2.4$  eV between  $\Gamma_8$  and  $\Gamma_6$  have been chosen to reproduce this expected rate of variation with pressure. It differs significantly from the reported value by Latussek *et al.* [240] for HgTe/HgCdTe superlattices ( $\gamma_{\text{Latussek}} = -3.69$  eV). This difference likely results from the presence of ligands in our material, making that the medium does not "feel" the pressure effect as fast as a bulk medium due to a significant damping of the strain into the ligand shells.

### 4.3.4 HgSe intraband nanocrystals under pressure

The pressure dependence of the HgSe intraband transition was also investigated. In this scope, we prepared three HgSe samples displaying intraband absorption at  $3000\text{ cm}^{-1}$  (HgSe "3k", 370 meV),  $2500\text{ cm}^{-1}$  (HgSe "2.5k", 300 meV) and  $1000\text{ cm}^{-1}$  (HgSe "1k", 120 meV).

HgSe is structurally very similar to HgTe, with a cubic zinc-blende crystalline structure. In the bulk, HgSe undergoes the same phase transitions as HgTe, only with slight differences in the threshold pressures. Again, the signature of the zinc-blende to cinnabar phase transition in the optical spectra of HgSe is, just as for HgTe, a disappearing of any feature followed by a strong increase of the baseline. This transition occurs around 4 to 5 GPa. As we are interested in the narrow-bandgap semiconducting phase, we limit our study to pressures up to 4 GPa in the following.

#### HgSe nanocrystals under pressure: optical properties in the zinc-blende domain

Infrared spectra of the intraband transition in HgSe 2.5k are presented in Figure 4.15a. Initially centered around  $2500\text{ cm}^{-1}$ , this peak red-shifts while the pressure is increased. In addition to this shift toward low energies, the intensity of the absorption peak dramatically decreases. While this behavior is consistently observed for the three sizes of materials we studied, they do not present the same rate of evolution with pressure, see Figure 4.15.

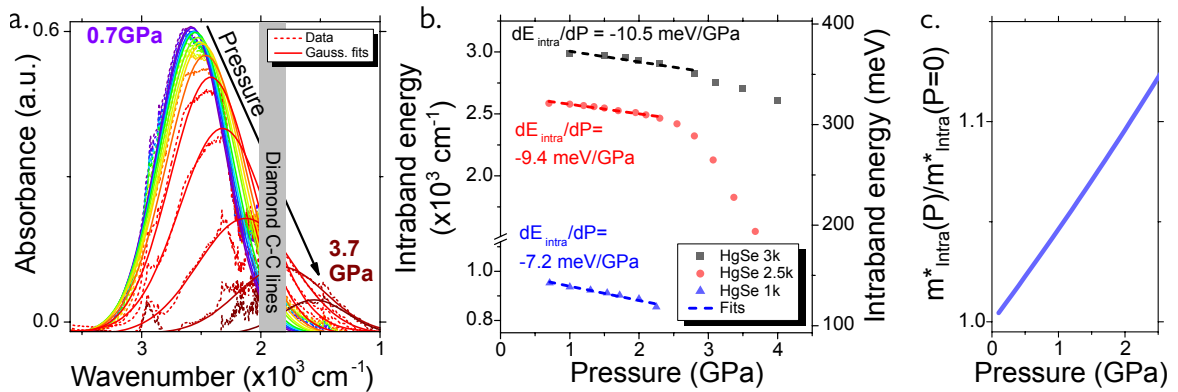


Fig. 4.15 Intraband HgSe nanocrystals under pressure: infrared spectroscopy. **a.** Infrared spectra of the intraband absorption peak in HgSe nanocrystals (around  $2500\text{ cm}^{-1}$  at ambient pressure) under increasing pressure. Raw data are displayed in dashed lines and Gaussian fits in thick lines. Final pressure is 3.7 GPa. **b.** Intraband peak energy extracted from Gaussian fits of the infrared spectra for three different sizes of HgSe nanocrystals ("3k" around  $3000\text{ cm}^{-1}$ , "2.5k" around  $2500\text{ cm}^{-1}$  and "1k" around  $1000\text{ cm}^{-1}$ ). A linear fit is provided in the low pressure regime (0-2 GPa). **c.** Calculated change of the intraband effective mass under pressure for HgSe "2.5k" nanocrystals.

To understand the origin of this red-shift, we can write a parametrized expression for the intraband energy:

$$E_{\text{intra}}(P) = E_{\text{intra}}(P=0) + \frac{\hbar^2 k^2}{2m^*_{\text{intra}}(P)} \quad \text{with} \quad k = \frac{\sqrt{3}\pi}{2R_{\text{QD}}(P)} \quad (4.11)$$

Where  $m^*_{\text{intra}}(P)$  is the intraband equivalent mass giving the transition  $E_{\text{intra}}(P)$ . We can note that the bulk bandgap of the material does not contribute to this expression, contrary to the HgTe case. Just like HgTe though, we can expect a shrink of the nanocrystal under pressure. This reduction of  $R_{\text{QD}}$  would have the same effect as for HgTe: an increase of confinement, leading to a blue-shift of the

intraband transition. A red shift is observed here, so this size shrinking effect must be counterbalanced by a change in the intraband equivalent mass. We can estimate this change by writing:

$$E_{\text{intra}}(P) \simeq E_{\text{intra}}(P = 0) + P \cdot \frac{dE_{\text{intra}}(P)}{dP} \quad (4.12)$$

Where we relate the nanocrystal radius to pressure through the bulk modulus of HgSe  $B_{\text{HgSe}}$  with  $R_{\text{QD}}(P) \simeq R_{\text{QD}}(P = 0)[1 - P/(3B_{\text{HgSe}})]$ . We obtain the following expression:

$$\frac{m_{\text{intra}}^*(P)}{m_{\text{intra}}^*(P = 0)} = \frac{R_{\text{QD}}^2(P = 0)E_{\text{intra}}(P = 0)}{R_{\text{QD}}^2(P)E_{\text{intra}}(P)} \simeq \left[ \left( 1 + \frac{dE_{\text{intra}}(P)}{dP} \cdot \frac{P}{E_{\text{intra}}(P = 0)} \right) \left( 1 - \frac{P}{3B_{\text{HgSe}}} \right) \right]^{-2} \quad (4.13)$$

Using the experimentally measured  $dE_{\text{intra}}(P)/dP = -9.4$  meV/GPa for HgSe 2.5k, we can estimate the change in the intraband equivalent mass using equation 4.13. The result is given in Figure 4.15c: the intraband equivalent mass increases under pressure, leading to a flattening of the bands and to a narrowing of the intraband transition. At 2 GPa, the relative increase of the equivalent mass is around 10 %.

The other manifestation of the pressure is a strong reduction of the intraband signal for the three sizes of studied nanocrystals. This effect can be attributed to a doping reduction consequent with the opening of the bandgap: if the gap opening has no visible effect on the intraband transition, it pushes the conduction band higher in energy, away from the Fermi level. The consequence of this upward shift is that the population of the  $1S_e$  level is reduced as the pressure is increased, leading to the progressive disappearing of the associated intraband transition.

### Consequences for HgSe-based heterostructures

From such experiments, we can draw several conclusion on HgSe sensibility to interfacial pressure in core/shell heterostructures. The first obvious point is that in the zinc-blende structure of HgSe must be preserved to observe intraband transitions: the zinc-blende to cinnabar transition, occurring around 4 GPa, is observed as a total loss of any clear feature in the infrared spectrum. This limits the choice of shelling materials to materials presenting a limited lattice mismatch with HgSe, or to very thin shells. Furthermore, even in the zinc-blende structure, the effect of increasing pressure on the intraband contribution in HgSe is non-negligible, since a continuous red-shift and decrease of the intraband absorption peak is observed due to the bulk bandgap opening and depopulation of the  $1S_e$  level.

The consequence for HgSe-based heterostructures is that very careful control over the interfacial pressure is required to preserve the intrand transition of the HgSe core materials. This notably explains the strong reduction or disappearance of the intraband contribution in HgSe/CdS core shell-structures [66]. In our study of HgSe/HgTe "core/shell" particles, the fact that the growth of HgTe was more Janus-like than shell-like probably helped reducing the interfacial pressure, leading to a limited red-shift and de-doping of the HgSe nanoparticles.

As a result, this problem of interfacial pressure sensitivity of HgSe, combined with the challenge brought by the synthesis of such core-shell objects, makes that there are very few tunable parameters for the chemical design and production of HgSe heterostructures. In the next section, I present an alternative technique to engineer heterostructures at the device scale rather than at the nanoparticle level.

## 4.4 Designing a new narrow-bandgap energy landscape: toward colloidal QDIP

To go further in the concept of uncoupling optical and transport properties, we propose a new approach where we want to use a mixture of nanocrystals to reproduce the energy landscape of epitaxially-grown Quantum Well or Quantum Dot Infrared photodetectors. While nanocrystals are almost exclusively used as a single population with a very fine control of the size dispersion, mixing different populations of NC has been recently explored as a new approach to control the average doping at the whole device scale [241] or to engineer new optoelectronic properties in light-emitting devices [242] and solar cells [243, 244].

In this section, I will present how we engineered efficient charge transport between doped intraband HgSe nanocrystals and HgTe nanocrystals by copying the energy landscape of QWIP/QDIP devices.

### 4.4.1 Reproducing the QDIP energy landscape by mixing nanocrystals: building the CQDIP

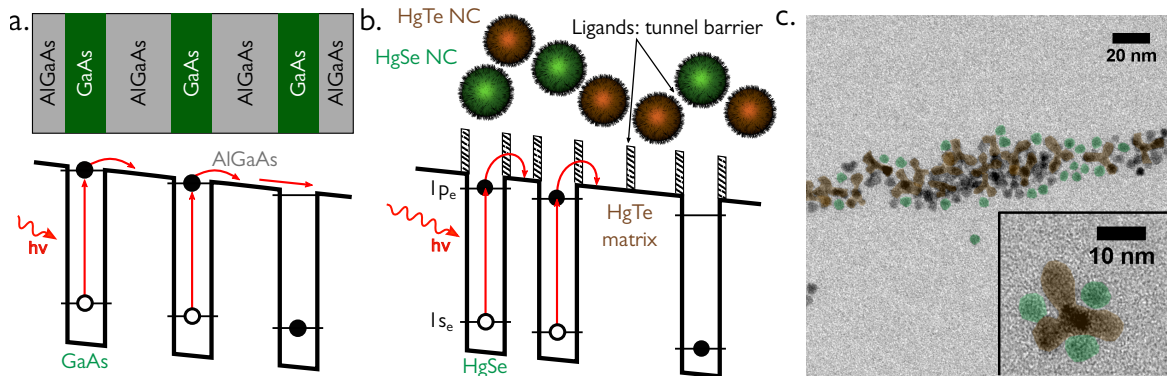


Fig. 4.16 From epitaxial Quantum Well/Dot Infrared photodetector to colloidal QDIP **a.** Energy landscape of a GaAs/AlGaAs Quantum Well Infrared Photodetector (QWIP). Doped GaAs quantum wells provide infrared absorption, and the excited electrons are transferred to the wide bandgap AlGaAs barrier. **b.** Scheme of the energy landscape of an HgSe and HgTe nanocrystals mixture. Doped HgSe nanocrystals provide intraband absorption, and HgTe nanocrystals form the transport matrix. **c.** TEM image of mixed HgSe (green) and HgTe (brown) nanocrystals. Inset: High-resolution TEM image showing one HgTe tetrapod surrounded by three HgSe spheres.

The main idea of this section is that we want to reproduce, with colloidal materials, the energy landscape of QWIP or QDIP detectors. The idea is to create a c-QDIP, a colloidal Quantum Dot Infrared Photodetector. In a Quantum Well Infrared Photodetector, as discussed earlier, infrared absorption is provided by the degenerately doped Quantum Wells (QW) featuring intraband transitions (GaAs, typically). Because those QW are epitaxially grown, they need to be confined by a barrier material, AlGaAs in our example. As shown in Figure 4.16a, such devices are engineered so that two levels are located in the QW, a ground level and an excited level. The excited level is made resonant with the barrier, so that the promoted electron can be efficiently transferred to the wide-bandgap, undoped barrier material. This strategy allows to uncouple photon absorption (due to QW) and carrier transport (mostly done in the barrier material) and to achieve reasonably low dark current despite relying on doped materials for intraband absorption. Devices are constituted of multiple quantum wells for enhanced absorption, but the QW are uncoupled from each other to prevent tunneling, which would be detrimental from the dark current point of view. As a result, both the energy of the ground and excited states as well as the QW spacing must be precisely controlled in such devices.

The Quantum Dot Infrared Photodetector, or QDIP, is the 0-D counterpart of QWIP. It relies on epitaxially grown, confined Quantum Dots. Its principle of operation is nevertheless the same as the QWIP: the excited levels of the Quantum Dots are engineered to be resonant with the surrounding barrier.

As pictured in Figure 4.16b, we can reproduce a similar energy landscape and working principle with HgSe and HgTe mixed nanocrystals and build a colloidal Quantum Dot Infrared Photodetector or CQDIP. HgSe is our "Quantum Well" or "Quantum Dot" material, while our transport matrix would be the HgTe nanocrystal network. In a random mix of particles, we can expect to observe a strong reduction of the dark current once the ratio of HgSe nanocrystals falls behind the percolation threshold: in other words, when it is not possible to create a current path only using HgSe nanocrystals.

As seen on TEM pictures shown in Figure 4.16c, HgSe and HgTe nanocrystals have fairly different shapes. HgTe usually presents tetrapodic shapes while HgSe are small spheres. The two kinds of nanocrystals nevertheless self-assemble fairly well and can be brought in intimate contact even with long capping ligands, as seen in the inset of Figure 4.16c.

The important parameters to control in the CQDIP hybrid structure are pictured in Figure 4.17a. Just like in the QWIP or QDIP heterostructures, we want the excited level of our HgSe nanocrystals (HgSe  $1P_e$  level) to be resonant with the conduction band of our transport material, constituted by HgTe nanocrystals (HgTe  $1S_e$  levels). The energy mismatch between those two levels is noted  $\Delta E$  in the following, defined as  $\Delta E = (E_{\text{HgTe } 1S_e} - E_{\text{HgSe } 1P_e})$ . The distance between two HgSe absorbers should also be controlled: we call  $\Delta L$  the average distance between two HgSe nanocrystals in a mixed film.

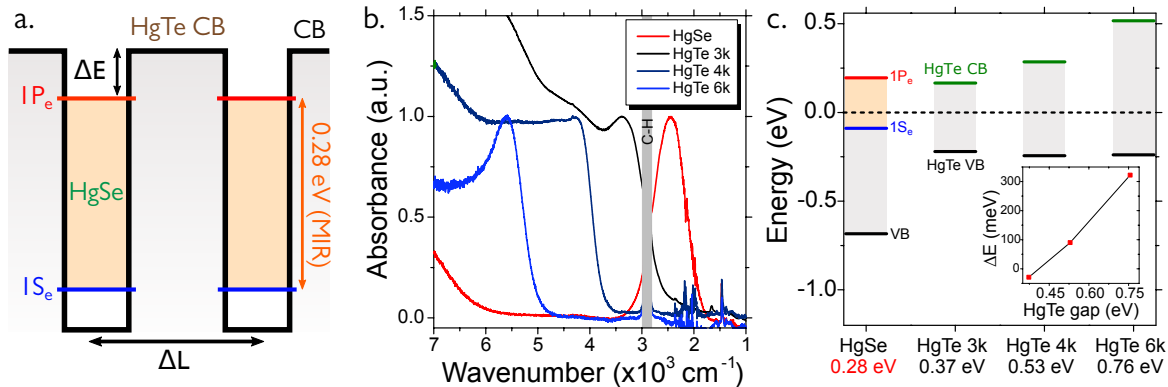


Fig. 4.17 Control of the energy landscape of the HgSe/HgTe CQDIP. **a.** Scheme of the desired energy landscape. The intraband absorption of HgSe is fixed to 280 meV. The important parameters to control are the energy difference between the excited level of HgSe (HgSe  $1P_e$ ) and the conduction band of HgTe (HgTe  $1S_e$ ):  $\Delta E = (E_{\text{HgTe } 1S_e} - E_{\text{HgSe } 1P_e})$ ; as well as the average distance between two HgSe absorbers  $\Delta L$ . **b.** Infrared spectrum of the materials used in this section: HgSe nanocrystals and three sizes of HgTe nanocrystals: 3k (band-edge around  $3000 \text{ cm}^{-1}$ ), 4k (band-edge around  $4000 \text{ cm}^{-1}$ ) and 6k (band-edge around  $6000 \text{ cm}^{-1}$ ). **c.** Control of  $\Delta E$ : energy spectrum of HgSe nanocrystals and three different sizes of HgTe nanocrystals, measured by photoemission on EDT-exchanged films. Inset: energy difference  $\Delta E$  (see panel **a**) for the three different sizes of HgTe nanocrystals.

Figure 4.17b presents the four materials of interest for this section. For the sake of simplicity, and also to match our MWIR  $4.4 \mu\text{m}$  light source, we fixed the size of HgSe nanocrystals. In the following, HgSe nanocrystals present intraband absorption around  $2500 \text{ cm}^{-1}$ , or 280 meV. I used three different sizes of HgTe nanocrystals to create hybrid CQDIP materials: HgTe 3k with a bandgap around  $3000 \text{ cm}^{-1}$ , HgTe 4k with a bandgap around  $4000 \text{ cm}^{-1}$  and HgTe 6k with a bandgap around  $6000 \text{ cm}^{-1}$ . I reconstructed the energy diagram of those four materials from photoemission measurements and optical spectroscopy in Figure 4.17c. We can evaluate the  $\Delta E$  energy distance from

HgSe  $1P_e$  to HgTe  $1S_e$  from those isolated materials measurements, considering that Fermi levels of the materials align whenever they are mixed together and intimately brought in contact through ligand exchange. The inset of Figure 4.17c shows that the smallest value of  $\Delta E$  is obtained for HgTe 3k ( $\Delta E_{3k} = -28$  meV), while the  $1S_e$  levels of HgTe 4k and 6k are above the  $1P_e$  level of HgSe ( $\Delta E_{4k} = 90$  meV and  $\Delta E_{6k} = 320$  meV, respectively).

The other tunable parameter is the average distance  $\Delta L$  between two HgSe nanocrystals in a film made from a HgSe/HgTe mix. This parameter is controlled *via* the HgSe ratio in the initial mix. In a first step, two solutions of HgSe and HgTe nanocrystals are diluted so their absorbance at 415 nm matches. This ensures a similar concentration in mercury atoms in the solutions [188]. They are then mixed together in a volume ratio  $x_V = V_{\text{HgSe}} / (V_{\text{HgSe}} + V_{\text{HgTe}})$ . Assuming a 50/50 stoichiometry and similar atomic densities for the two nanocrystals, we can express the HgSe nanocrystal ratio as:

$$x_{\text{HgSe}} = \frac{V_{\text{HgSe}}}{V_{\text{HgSe}} + \frac{v_{\text{HgSe NC}}}{v_{\text{HgTe NC}}} V_{\text{HgTe}}} \quad (4.14)$$

Where  $v_{\text{HgSe NC}}/v_{\text{HgTe NC}}$  is the individual nanoparticles volumic ratio. Using TEM images, I estimated this ratio to be around 1/3 for a HgSe (5 nm sphere) / HgTe 4k ( $\approx 12$  nm tetrapod) mix. Figure 4.18a gives the resulting values of  $x_{\text{HgSe}}$  for several volumic ratios. There is a reasonably good match between those calculated values and those obtained with EDX elementary analysis (based on Se/Te ratios corrected with the same expression as 4.14).

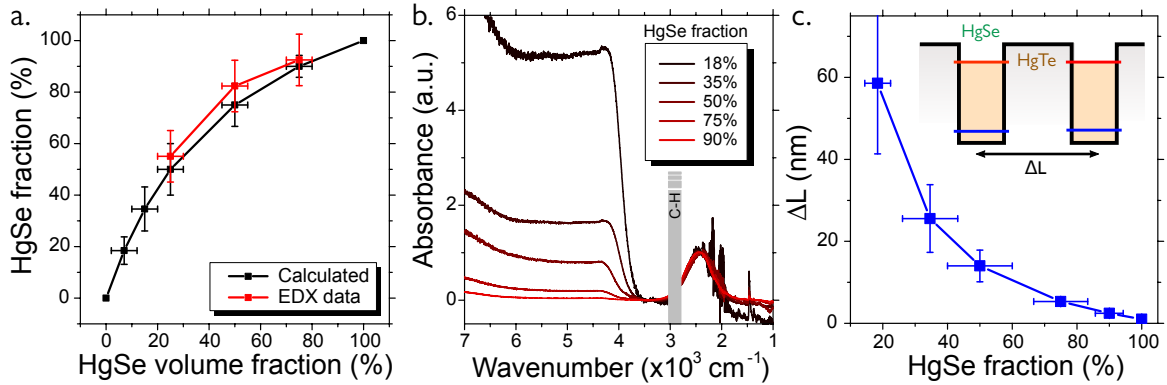


Fig. 4.18 Control of the HgSe nanocrystals spacing in the CQDIP. **a.** Calculated HgSe nanocrystal ratio  $x_{\text{HgSe}}$  from the volumic mixing ratio. Calculation is done assuming a 1 to 3 ratio for the HgSe to HgTe nanoparticle volume (black points). Experimental EDX data (based of the Se to Te ratio) is given in red. **b.** Optical spectra of HgSe/HgTe mixtures with varying HgSe content. **c.** Calculated average distance  $\Delta L$  between two HgSe nanocrystals for the different HgSe/HgTe 4k mixtures.

Infrared spectra of HgSe/HgTe 4k material are presented in Figure 4.18b. As expected, the intraband to interband absorption ratio scales linearly with the  $N_{\text{HgTe}}/N_{\text{HgSe}} = 1 - 1/x_{\text{HgSe}}$  nanocrystals ratio. From here, we can estimate the average distance between two HgSe nanocrystals in a charge percolation path. This can be thought as a one-dimensional situation, where on average two HgSe nanocrystals are separated by  $N_{\text{HgTe}}/N_{\text{HgSe}}$  nanocrystals. The distance  $\Delta L$  is then:

$$\Delta L = (l_{\text{ligands}} + 2R_{\text{HgTe}}) \times \frac{N_{\text{HgTe}}}{N_{\text{HgSe}}} = (l_{\text{ligands}} + 2R_{\text{HgTe}}) \times \left(1 - \frac{1}{x_{\text{HgSe}}}\right) \quad (4.15)$$

Where  $N_{\text{HgTe}}/N_{\text{HgSe}}$  is the HgTe to HgSe nanocrystals ratio,  $l_{\text{ligands}}$  is the capping ligands length (taken as 0.5 nm) and  $2R_{\text{HgTe}}$  is the mean HgTe nanocrystal size. Figure 4.18c gives the estimated

$\Delta L$  for HgSe/HgTe 4k with different HgSe fractions: by tuning the HgSe nanocrystal fractions from 100 % to 18 %, we tune the average inter-HgSe distance from  $\sim 1$  nm to  $\sim 60$  nm.

By changing the constituents of the mix and their relative proportions, we are able to finely control and optimize the absorption and transport properties of this hybrid material. I went on to build devices from those materials to find the optimized configuration leading to good MWIR photodetection performances.

#### 4.4.2 Optimization of the hybrid material for intraband photodetection in the MWIR

Basic photoconductive devices can be built from those mixed HgSe/HgTe solutions. Solutions are drop-cast from hexane:octane onto interdigitated electrodes, and the films are cross-linked by a ligand exchange toward ethanedithiol (EDT). Since all the solution absorbances are normalized, devices of similar thicknesses are built by using the same number of deposition and exchange step for all variations of the material constituents and fractions. Solutions containing HgTe 3k are deposited through dip-coating instead of drop-casting, since the colloidal stability of HgTe 3k is not good enough in the hexane:octane drop-casting solvent. Devices have a  $\sim 100$  nm thickness, and they are transferred into a close-cycle cryostat directly after deposition.

The main figure of merit I choose to use for optimization of the HgSe/HgTe CQDIP material is the photocurrent over dark current ratio  $I_{\text{photo}}/I_{\text{dark}}$ , taken in the same illumination conditions for all studied devices. It is a good figure of merit because it should scale as the detectivity (it is a signal to noise ratio), while being easier to evaluate. The measurement principle is given in Figure 4.19a. Each sample is enclosed in a cryostat and illumination is provided specifically on the HgSe intraband absorption peak by our 4.4  $\mu\text{m}$  ( $2280\text{ cm}^{-1}$ ) Quantum Cascade Laser (QCL). Acquisition of the signal-to-noise ratio  $I_{\text{photo}}/I_{\text{dark}}$  is done by optically chopping the laser at 1 Hz and continuously acquiring the current temporal traces. Figure 4.19b gives two examples of such temporal traces, for a HgSe (35 %) / HgTe 4k mix and a pure HgTe material. While there is an obvious effect of the laser illumination on the HgSe-containing sample, with sharp, 1 Hz-modulated current peaks, temporal traces for pure HgTe 4k show no modulation at all under illumination, proof that any observed photocurrent origins from absorption in HgSe nanocrystals and not from a potential sub-bandgap absorption in HgTe nanocrystals.

I then screened the effect of  $\Delta E$  by changing the composition of the mix from HgTe 3k to HgTe 4k and 6k (for which respectively  $\Delta E = -18$  meV, 90 meV and 320 meV), with a fixed HgSe fraction of 35 % ( $\Delta L \simeq 25$  nm). Results are presented in Figure 4.19c. Because this measurement is temperature-resolved, we can understand the effect of  $\Delta E$  variation at high and low temperature regimes. Mixtures with HgTe 4k and HgTe 6k start around the same value at room temperature, but the improvement brought by cooling down is much superior in the case of HgTe 4k. Indeed, while using a barrier material with a large bandgap such as HgTe 6k is good from the dark current point of view, it leads to poor extraction of the carriers generated in HgSe due to the large barrier, especially at low temperature where thermal activation is reduced. The shape of the temperature evolution of the HgTe 3k differs from the first two, with a low signal/noise ratio at high temperature, improving significantly as the device is cooled down. This is due to the narrow bandgap nature of HgTe 3k. Despite the barrier height being well optimized for this material ( $\Delta E_{3k} = -18$  meV), there is a significant number of thermally activated carriers at room temperature in the barrier material (HgTe 3k is an intrinsic, n-type material). As a result, dark current is high in the device because of large thermal activation through the bandgap of the barrier itself. Electron collection from HgSe being efficient in this material, the signal/noise ratio is largely improved at cryogenic temperatures where the number of thermally activated carriers contributing to dark current in HgTe 3k is sufficiently reduced. As a result, we choose to use HgTe 4k as a mixing material for the rest of this study: while featuring a 90 meV barrier, it is the material that performs the best for the whole range of temperatures. As a result and because of

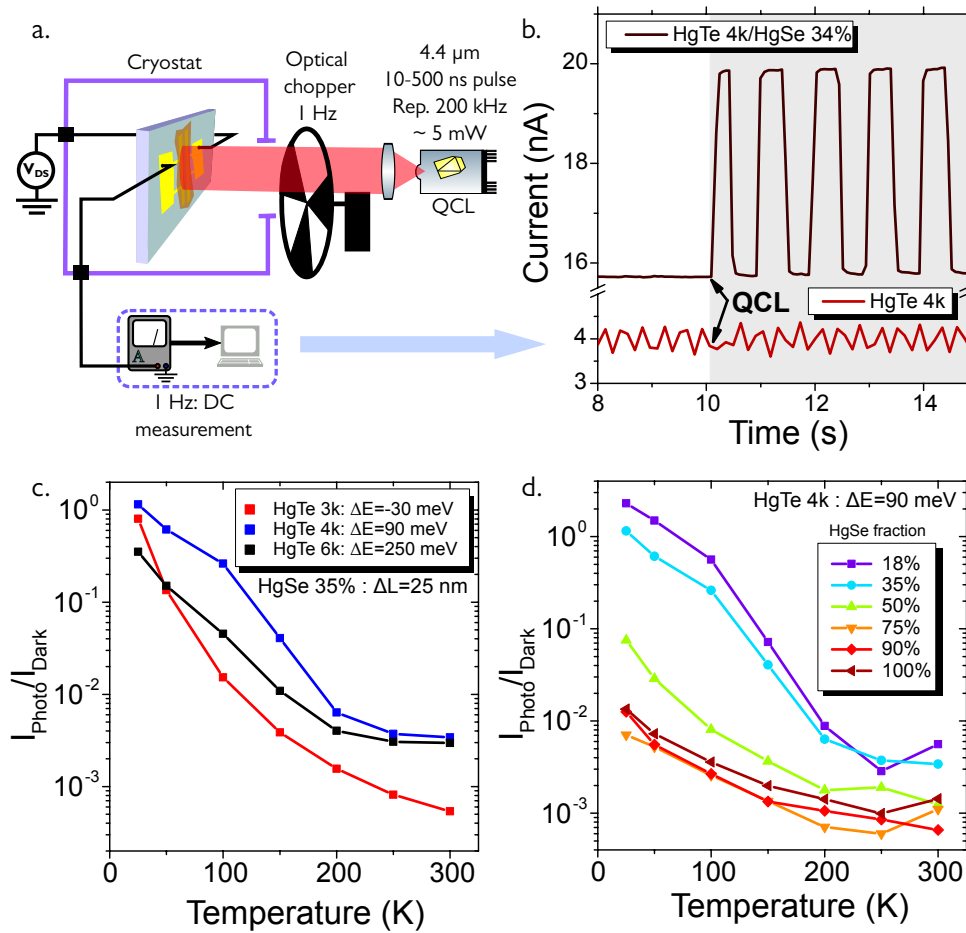


Fig. 4.19 Optimization of the HgSe/HgTe CQDIP parameters. **a.** Scheme of the signal/noise measurement: the sample is enclosed in a cryostat, and illuminated by a 4.4  $\mu\text{m}$  QCL chopped at 1 Hz. The sample is in the dark for 10 s, then illuminated for 25 s before another 30 s of dark. The temporal trace of the current under  $V_{DS} = 1$  V is acquired through the source-meter with a 10 Hz sampling rate. **b.** Example of two temporal traces from which the signal to noise ratio  $I_{\text{photo}}/I_{\text{dark}}$  is determined. The laser is switched one at  $t = 10$  s and is modulated at 1 Hz. Temporal traces are shown for HgSe (35 %) / HgTe 4k and pure HgTe 4k devices. **c.** Optimization of the transport material ( $\Delta E$ ): evolution of the photocurrent over dark current ratio  $I_{\text{photo}}/I_{\text{dark}}$  with temperature, measured on devices made of HgTe 3k, HgTe 4k, and HgTe 6k with the same amount of HgSe (same  $\Delta L$ ). Illumination is provided by a 4.4  $\mu\text{m}$  QCL exciting exclusively the HgSe intraband transition. **d.** Effect of  $\Delta L$ : evolution of the photocurrent over dark current ratio with temperature, measured on six HgTe 4k devices ( $\Delta E = 90$  meV) with different HgSe contents (different  $\Delta L$ ).

the band alignment of our materials, there is a trade-off between the bandgap of the barrier material (which is desired as big as possible) and the barrier height (which is desired as low as possible).

Next, I studied the effect of  $\Delta L$  on the performances of the devices. I present in Figure 4.19d the temperature-resolved signal/noise ratios of HgSe/HgTe 4k devices with decreasing HgSe fraction. For high HgSe fractions, all the curves are mostly superimposed on the pure HgSe one, displaying a low signal/noise ratio and a very poor improvement with temperature (due to very limited reduction of dark current with temperature in HgSe, see section 4.1.2). In this regime, the devices are basically HgSe-driven. Below a 50 % HgSe fraction, there is a clear improvement of the devices signal/noise value, first at low temperature then on the whole temperature range for low HgSe contents. From this point, the transport looks HgTe-driven: this indeed corresponds to the percolation threshold we expected to find. Here again, there is an obvious trade-off because reducing the HgSe content reduces

the overall MWIR absorption in the film. From the signal to noise ratio point-of-view though, our strategy is successful: by mixing together HgTe and HgSe nanocrystals, we see an efficient improvement of the MWIR detection by several orders of magnitude.

I also looked more directly on the dark current dependency on temperature: in pure HgSe devices, the activation energy  $E_A$  of the dark current is fairly low (20 to 40 meV). Cooling curves ( $I_{\text{dark}}(T)$ ) for two devices are presented in Figure 4.20a, and the extracted activation energies for the whole family of HgSe/HgTe 4k devices is given in Figure 4.19b. From both those results, it is very clear that optimized CQDIP material behaves like pure HgTe 4k material from the transport point-of-view: not only the dark current is strongly reduced at room temperature compared to HgSe devices, but the activation energy of the CQDIP devices strongly increases below a 50 % HgSe fraction, to saturate around the activation energy of pure HgTe 4k devices. Evolution of activation energy is well fitted with a sigmoidal law to yield  $x_{\text{threshold}} = 45 \%$ , comparable with percolation thresholds for three-dimensional processes.

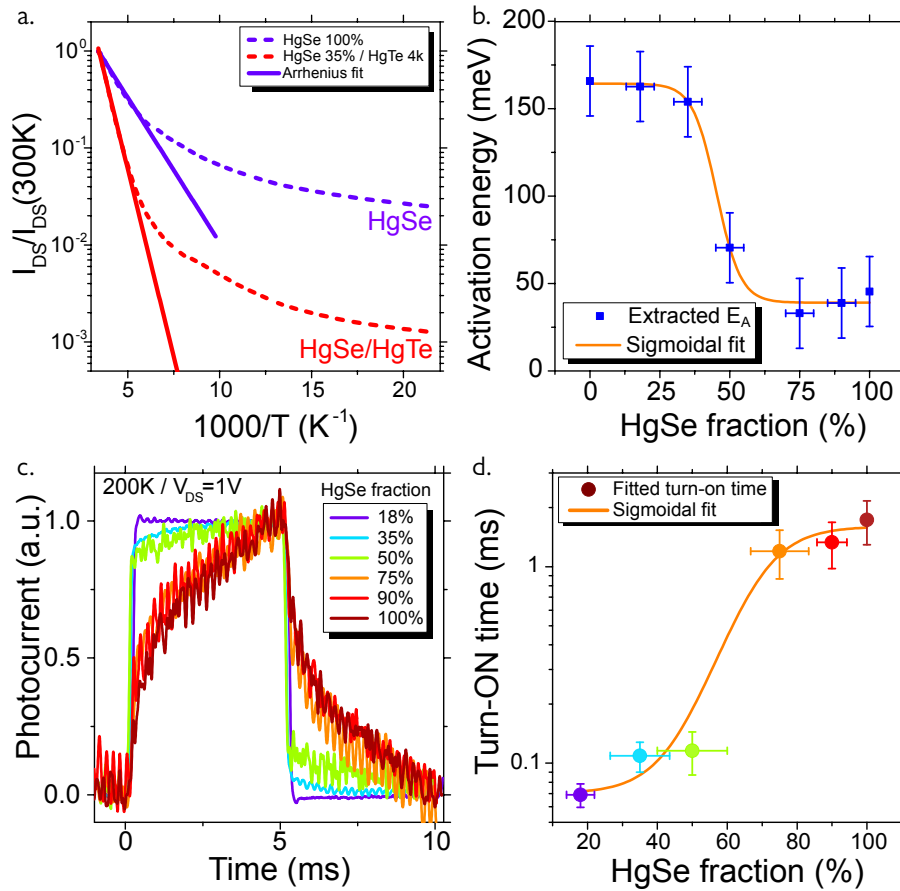


Fig. 4.20 Activation energy and photoresponse dynamics improvement with HgSe/HgTe hybrids. **a.** Evolution of the dark current under  $V_{\text{DS}} = 1$  V with temperature for a pure HgSe device (in purple) and for an optimized HgSe/HgTe 4k device (35 % HgSe, in red). Arrhenius fits is provided at high temperature. **b.** Activation energies extracted from cooling curves  $I(T)$  in the dark, for decreasing HgSe content. A sigmoidal fit is provided, yielding a 45 % threshold. **c.** Photocurrent temporal traces for HgSe/HgTe 4k hybrids. Illumination is provided by a 4.4  $\mu\text{m}$  QCL exciting exclusively the HgSe intraband transition. **d.** Turn-ON times extracted from photocurrent temporal traces. A sigmoidal fit is provided, with a 60 % threshold.

Finally, I looked at the MWIR photocurrent dynamics in the HgSe/HgTe 4k CQDIP devices. For this experiment, the QCL laser is optically chopped at 100 Hz, the photocurrent is converted by a transimpedance amplifier and visualized onto an oscilloscope. Figure 4.20c shows normalized temporal traces of the photocurrent for decreasing fractions of HgSe in the CQDIP mix. Again, for high HgSe fractions the photocurrent features slow rising and falling times, very similar with pure HgSe; while for

low HgSe fractions the photocurrent displays sharp rising and falling times, limited by the speed of the chopper blade. The rising times are again well fitted by a sigmoidal curve, see Figure 4.20d, with a threshold around 60 %.

In both the dark current characterization and photoresponse dynamics, we observe a very consistent signature of the uncoupling between optical properties and transport. While the optimized (*i.e.* HgSe (<40 %) / HgTe 4k) CQDIP devices feature optical absorption and photocurrent in the MWIR (HgSe-driven), their transport properties are clearly driven by the HgTe 4k nanocrystals network with high activation energy and fast photocurrent dynamics. As a result, our strategy allows to overcome the three main drawbacks of pure HgSe devices, by engineering a new energy landscape through careful mixing with HgTe nanocrystals. In this sense, the performances improvement obtained with those CQDIP devices are very similar to that of HgSe/HgTe core-shell nanocrystals presented earlier, with an easier fabrication process and more flexibility: there is no need for epitaxially-connected nanocrystals nor synthesis in the new CQDIP design.

#### 4.4.3 Reduction of apparent doping in the HgSe/HgTe CQDIP

As a final proof for the effective uncoupling between absorption and transport in our HgSe/HgTe 4k CQDIP material, I investigated the apparent doping of the material using both X-ray photoemission and transport measurements in field-effect transistor (FET) configuration. We now from previous data that HgSe nanocrystals are degenerately n-doped, and that HgTe 4k nanocrystals (with a bandgap around  $4000\text{ cm}^{-1}$  or  $500\text{ meV}$ ) are intrinsic semiconductors. In a mixture of those two nanocrystals, we can measure an average, or apparent doping level in the hybrid material.

I firstly used photoemission to measure the Fermi level position in our hybrid materials. Figure 4.21a presents the reconstructed energy diagram of HgTe 4k, HgSe and four mixtures with different HgSe fractions. For each spectrum, the valence band ( $1S_h$  level) position is determined by photoemission and the conduction band levels (HgTe  $1S_e$ , HgSe  $1S_e$  and HgSe  $1P_e$ ) are determined using optical spectroscopy. In pure materials, the Fermi level lies in the middle of the bandgap for HgTe 4k and slightly above the  $1S_e$  level for HgSe, as expected from previous measurements. In the hybrid materials, the reconstructed spectra allow visualizing the average doping in the material: HgTe appears strongly more n-type while HgSe appear strongly de-doped. We see here a signature that the apparent doping seen through photoemission measurement is decoupled from the optical properties because intraband absorption is observed for every HgSe-containing sample. The valence band to Fermi level energy, measured on photoemission spectra, is plotted in Figure 4.21b: from this data, it is very clear that the average Fermi level position shifts downward relatively to the band structure, going continuously from a n-type material to a ambipolar material while the amount of HgSe is decreased.

I then looked at this apparent doping level from the transport point-of-view, using FET characterization. Using the same electrolyte-gating configuration as described before, we can follow the evolution of the devices transfer curves while decreasing the amount of HgSe in the mixture. Figures 4.21c, d and e presents three transfer curves, for pure HgSe, HgSe (35 %) / HgTe 4k mixture and pure HgTe. The shape of those transfer curves are indicative of the material doping, which rapidly switches from n-type only (increase of conductance under electron injection only) to ambipolar (increase of the device conductance under both electron and hole injection). Neutrality point (*i.e.* the gate voltage for which the current is minimized in the transfer curve) and hole/electron mobility ratios  $\mu_h/\mu_e$  have been extracted from each transfer curve and are presented in Figure 4.21f: both those parameters shows an apparent de-doping of the hybrid system, with a shift of the neutrality point toward positive voltages and a continuous increase of the hole mobility (with respect to the electron mobility) in the hybrid material. In this sense, this is another proof that the material behaves almost exactly like the HgTe 4k network from the transport point of view.

As a result, both photoemission and transport measurement in a FET configuration show a

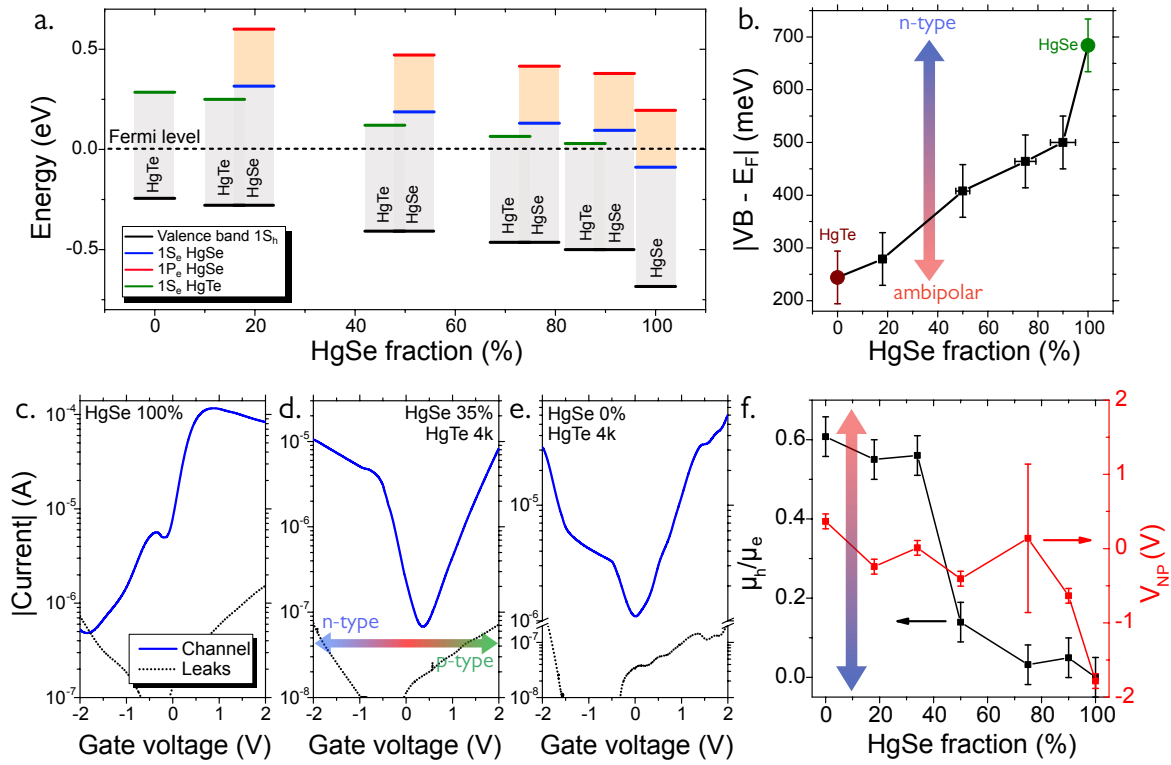


Fig. 4.21 Reduction of the apparent doping in the HgSe/HgTe mix. **a.** Reconstructed apparent energy diagrams of HgTe 4k, HgSe and hybrid fractions. The Fermi level is taken at 0 eV, valence band position is determined using XPS measurements and conduction band levels (HgTe  $1S_e$  in green, HgSe  $1S_e$  in blue, HgSe  $1P_e$  in red) are obtained from optical spectroscopy. **b.** Evolution of the valence-band to Fermi level energy distance  $|VB - E_F|$  for increasing HgTe fraction in the HgSe/HgTe 4k mix. **c, d, e.** Transfer curves (in electrolytic transistor configuration) for a pure HgSe nanocrystal device (**c**), a 35 % HgSe/HgTe 4k device (**d**) and a pure HgTe 4k device (**e**). **f.** Extracted neutrality point (in red) and  $\mu_e/\mu_h$  mobility ratios (in black) from the whole set of transfer curves on HgSe/HgTe 4k devices.

consistent de-doping of the system, indicative of the efficient decoupling of the optical and transport properties in our HgSe/HgTe 4k hybrid material.

Now that we have this promising material, we would like to evaluate its performances into an optimized device. In the next section, I present how we integrated this hybrid HgSe/HgTe 4k material into a MWIR-sensing vertical device.

## 4.5 A multi-spectral, intraband-based MWIR photodiode

In this last section, I present how we integrated our HgSe/HgTe CQDIP hybrid material into a photodiode device. A photodiode, as introduced earlier (see section 1.2.5), allows zero bias operation thanks to a built-in voltage, which is critical to reduce the dark current associated with narrow bandgap materials. The active absorbing material in this diode is our optimized HgSe (35 %) / HgTe 4k mix.

### 4.5.1 Building a mid-wave infrared vertical device

While a significant number of NIR, SWIR or E-SWIR nanocrystal-based diode structures have been proposed in the last decade, there is only few reports for nanocrystals in the MWIR range,

and no report on intraband-based MWIR photodiodes. Because we want to build a vertical device, the first constraint is to find a transparent, conductive material to act as a bottom contact while allowing MWIR light transmission. In the visible to NIR and SWIR, transparent conductive oxides as tin-doped indium oxide (ITO) and fluorine-doped tin oxide (FTO) are widely used, but their transparency degrades strongly in the MWIR where they start to absorb a significant fraction of the incident light. Another issue with those materials is that they are mostly commercially available as a thin film deposited on glass, and glass strongly absorbs in the MWIR. A solution, used notably by the Guyot Sionnest group in Chicago for their HgTe-based MWIR photodiode [162] is to sputter thin films of ITO on sapphire, achieving a  $\sim 50\%$  transparency at  $5\ \mu\text{m}$  ( $2000\ \text{cm}^{-1}$ ). This approach is nevertheless limited, because it is not extendable to longer wavelength.

Instead, we used another approach based on the geometrical patterning of a metallic electrode. We designed a grid-shaped back-electrode consisting in a fine mesh of digits that are all connected together. Figure 4.22a shows the structure of this this patterned electrode, designed to allow transmission of up to 75 % of the incident light (*i.e.* the metal only covers 25 % of the optical area). We then pattern a sapphire substrate (MWIR transparent) using optical lithography and we thermally evaporate 80 nm of aluminum in the resist pattern. Resulting electrodes are presented in Figure 4.22b and c: the fine structure of the digits is well reproduced at the electrode level. Transparency of this electrode + substrate ensemble is measured to be around 70 % over the whole infrared spectrum and up to  $1000\ \text{cm}^{-1}$ , see Figure 4.22d. This strategy is versatile as a wide variety of metals (or conductive oxides) can be patterned this way, and is easily transferable to longer wavelengths.

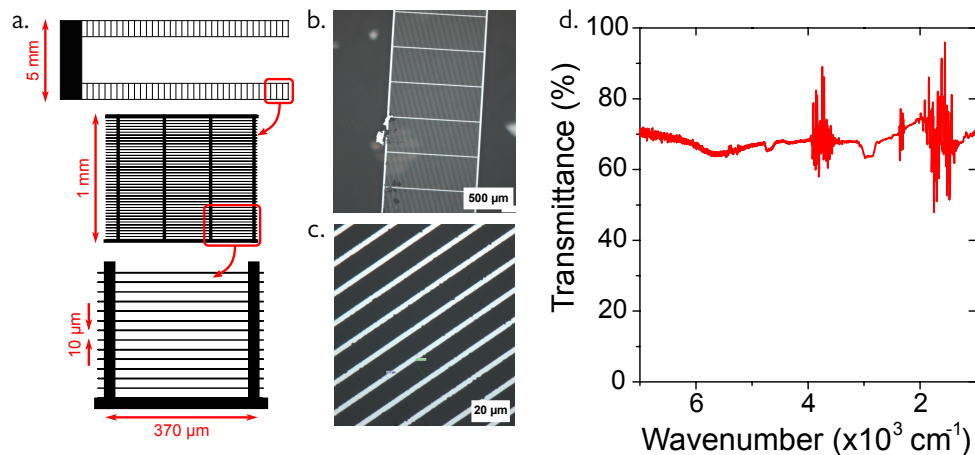


Fig. 4.22 A new transparent electrode for MWIR vertical devices: metallic grid. **a.** Scheme of the metallic grid used as a bottom-contact in our MWIR vertical devices, at three levels of zoom. The smallest features (finest digits) are  $3\ \mu\text{m}$  thick. **b.** Optical microscopy image of an aluminium grid, patterned on sapphire using optical lithography. **c.** Optical image of the fine  $3\ \mu\text{m}$  digits on an aluminum grid. **d.** Infrared transmission spectrum of the aluminium grid electrode. Optical area is limited to the patterned areas.

Another challenge with vertical MWIR devices is that the effort to identify good electron and hole transport (or blocking) layers have not yet been pushed up to the MWIR range. Recently, we identified that the typical  $\text{TiO}_2$  or  $\text{ZnO}$  layers used as an electron transport material for many NIR to SWIR applications with PbS nanocrystals [95, 117] were not well fitted for HgTe material in the SWIR, and lead to an important filtering of the photocurrent [164]. Diodes proposed by the Guyot-Sionnest group use a thin layer of  $\text{Ag}_2\text{Te}$  as a p-doped material to build an heterojunction with n-type HgTe. In our case, the particularity is that in the MWIR, the diode is unipolar: since MWIR sensitivity is due to intraband absorption in HgSe, there is no hole involved in the (MWIR-related) phototransport. To introduce an asymmetry in our device, we choose to use the concept of unipolar barrier introduced by our group for HgTe-based, SWIR photodiodes [163, 164]. This concept has been developed firstly for III-V semiconductors and their heterostructures [245, 246]: in a photodiode structure, an unipolar barrier is a layer designed to filter only one of the carriers, while allowing the other to flow. As a

result, it suppresses strongly the dark current associated with the blocked carrier.

Figure 4.17c predicts a good valence band alignment between HgTe 6k and HgTe 4k, which forms the transport matrix of our active material: we hence choose to use a thin layer of HgTe 6k as an unipolar, electron-filtering layer.

#### 4.5.2 An intraband-based MWIR diode with an unipolar barrier

The structure of the diode is schematized in Figure 4.23a, and consists in a stack of Al/HgTe 6k/(HgSe-HgTe 4k)/Au on sapphire. As explained in the previous paragraph, the aluminium electrode is patterned to be semi-transparent in the infrared and the thin HgTe 6k layer is here to act as an unipolar electron filtering barrier, while HgSe (35 %)/HgTe 4k is our active CQDIP material.

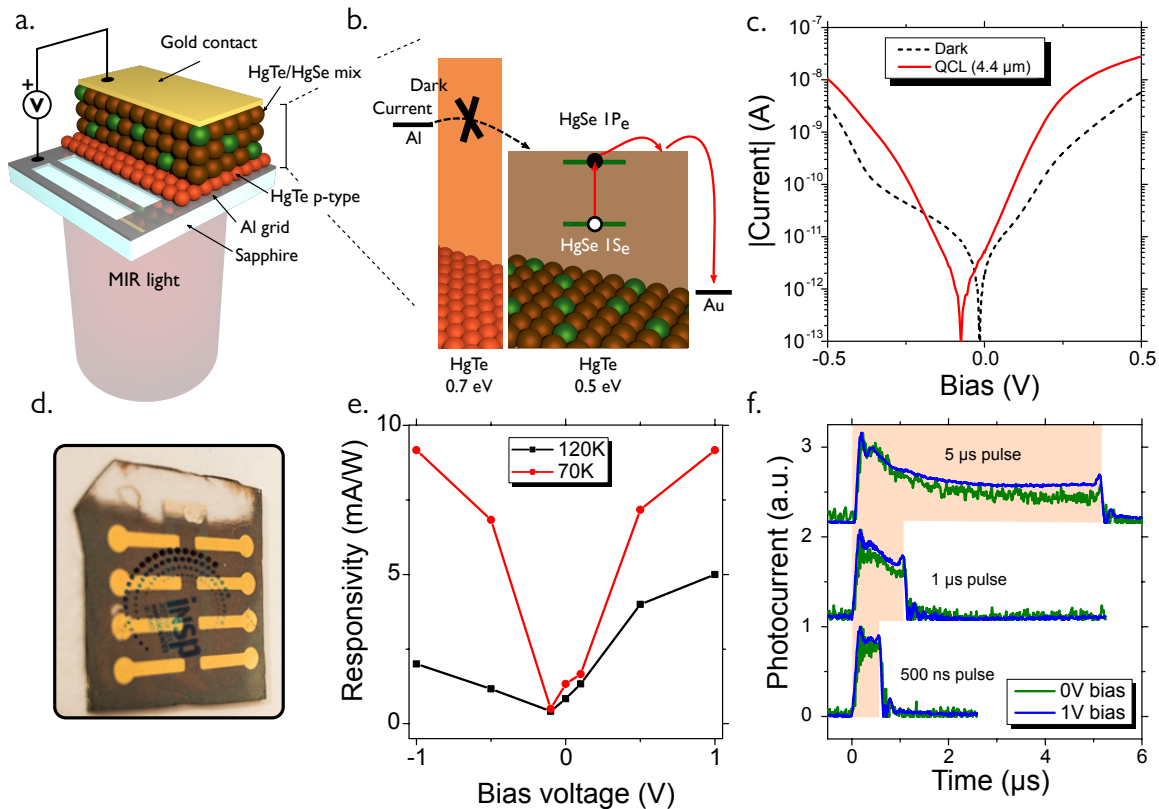


Fig. 4.23 A CQDIP-based intraband photodiode. **a.** Scheme of the device. Illumination is provided from the back-side through the sapphire substrate and patterned electrode. **b.** Scheme of the band alignment in the CQDIP diode structure. HgSe (35 %) / HgTe 4k mix is used as the active material. HgTe 6k nanocrystals are used as an unipolar barrier filtering the dark current injection from the aluminium side. **c.**  $I(V)$  characteristics of the diode at 80 K in the dark and under illumination by a 4.4  $\mu\text{m}$  QCL, at 80 K. **d.** Picture of a device. The device is very reflective, indicative a good film quality. Active area is 1  $\text{mm}^2$ . **e.** Responsivity of the device, measured in front of a calibrated black body at 650°C with a 1.9  $\mu\text{m}$  ( $5200\text{ cm}^{-1}$ ) long-pass filter, at 100 Hz. **f.** Temporal traces of the photocurrent under excitation by short pulses of the 4.4  $\mu\text{m}$  QCL, at 80 K.

The diode is prepared under ambient conditions with the help of Bertille Martinez, a fellow PhD student. HgTe 6k is spin-coated on top of an Al electrode on sapphire, then ligand-exchanged toward EDT by dipping the whole device in a 1 % EDT solution in ethanol for 60 s. The device is rinsed in ethanol, and another layer of HgTe 6k is spin-coated. This step is repeated three times to reach a 30 to 50 nm thickness. The HgSe/HgTe 4k solution is then either spin-coated or drop-cast and cross-linked with EDT using the same solid-state ligand exchange as for HgTe 6k. 8 to 12 layers are

built to achieve a  $\sim 200$  nm thick layer. While film thickness should be maximized to increase light absorption, it is primordial to preserve a good film quality and homogeneity over the whole device to prevent shortcuts, pinholes and excessive noise: there is a trade-off between thickness and film quality. Figure 4.23d shows a picture of a  $1 \text{ cm}^2$  substrate with eight  $1 \text{ mm}^2$  devices.

A schematic band alignment of the device is given in 4.23b: the HgTe 6k layer, thanks to its larger bandgap, prevents injection of dark electronic current from the Al side to the active material. The choice of a thin layer of a relatively narrow bandgap material such as HgTe 6k is motivated by the fact that under illumination, the Al side must provide electrons to refill the HgSe quantum dots. The operating range of the diode can be defined as the range of biases for which the energy drop over the HgTe 6k unipolar barrier remains small compared to the barrier height. In practice, the critical electric field is around  $70 \text{ kVcm}^{-1}$  for our devices, corresponding to a 1.8 V bias. The hole dark current, resulting from thermal activation in HgTe 6k and HgTe 4k, is reduced by operating the device at cryogenic temperatures.

In the following, we define the bias reference as the Al side. In the dark, the  $I(V)$  characteristics display an asymmetric shape, see Figure 4.23c. Under selective excitation of the HgSe intraband transition by our  $4.4 \text{ }\mu\text{m}$  QCL, we observe a clear increase of the current as well as the apparition of a negative open circuit voltage. Operation of the diode under positive biases for MWIR illumination is in good agreement with the band structure of the device presented in 4.23b (extraction of intraband electrons on the gold side).

I determined the device responsivity under broadband excitation by a calibrated blackbody, equipped with a  $1.9 \text{ }\mu\text{m}$  germanium filter. As a result, the excitation spectral window lies between  $5200 \text{ cm}^{-1}$  and  $2000 \text{ cm}^{-1}$  (cut-off of the device absorption). A scheme of the experiment is given in 4.24a. For a black body at the temperature  $T_{\text{BB}}$ , the total power received by the device is given by:

$$P_{\text{opt}} = T \times A_d \pi \sin^2 \alpha \int_{\lambda_{\text{Ge}}}^{\lambda_{\text{cut-off}}} \frac{2hc^2}{\lambda^5} \frac{1}{\exp\left(\frac{hc}{\lambda k T_{\text{BB}}}\right) - 1} d\lambda \quad (4.16)$$

Where  $T$  is the transmission of the cryostat windows,  $A_d$  is the detector area and  $\alpha$  is the half-angle of view defined by the detector and the black body aperture. The photocurrent is measured by optically chopping the black body flux and feeding the detector signal into a lock-in amplifier. The devices sees the black body aperture with a  $2^\circ$  half-angle, while the total half-angle field of view of the detector is  $15^\circ$  (defined by the external 300 K ZnSe window of the cryostat). As pictured in Figure 4.23e, responsivity under broadband excitation is around  $1 \text{ mA/W}$  at zero bias and reaches up to  $10 \text{ mA/W}$  under higher biases. Finally, using the MWIR QCL source I checked that the fast photocurrent dynamics demonstrated with the HgSe/HgTe hybrid material are preserved in the vertical device: Figure 4.23f shows that we perfectly resolve QCL pulses down to at least 500 ns, both in short-circuit conditions or under 1 V bias. The fast nature of this CQDIP-based MWIR detector will be exploited in the last part of this section.

Finally, I quantified the specific detectivity of our devices. As introduced earlier (see 1.2.5), the specific detectivity  $D^*$  is the ultimate figure of merit of a photodetector. For a detector of optical area  $A_d$ , it can be calculated from the responsivity  $\mathcal{R}$  and the dark current spectral density  $S_I$  as:

$$D^* = \frac{\mathcal{R} \sqrt{A_d}}{S_I} \quad (4.17)$$

Figure 4.24a explains how we measured both the responsivity (*i.e.*, signal) and the dark current spectral density (*i.e.*, the noise) on the same device, at cryogenic temperatures. In such nanocrystal-based device, noise is never limited by thermal or generation/recombination noise [119]. As a result,

it cannot be expressed analytically as in conventional semiconductors, and must be experimentally characterized. Noise measurement is done by measuring the spectral components of the dark current with a low-frequency spectrum analyzer. It is usually a complex task because of the high number of electrically noisy apparatus in a physical chemistry lab, making the measured noise room-limited rather than device-limited. To get an accurate reading on the actual device noise level, special care has to be taken to avoid any ground loop, cable lengths should be as short and symmetric as possible, and a good shielding of the device is mandatory. For those reasons, low temperature noise characterization is particularly tricky because of the long cables and need of noisy pumps for cooling. We use low-noise current amplifiers as well as battery-based bias sources to avoid the introduction of any additional noise in the measurement. Figure 4.23b shows the measured device dark current spectral density for a 0 V bias and at 80 K: the baseline of the curve is clearly  $1/f^{1/2}$ -limited (*i.e.* the noise is  $1/f$  limited), indicating that we are indeed limited by the device noise. The structure in the noise data is mainly due to 50 Hz room noise and its harmonics.

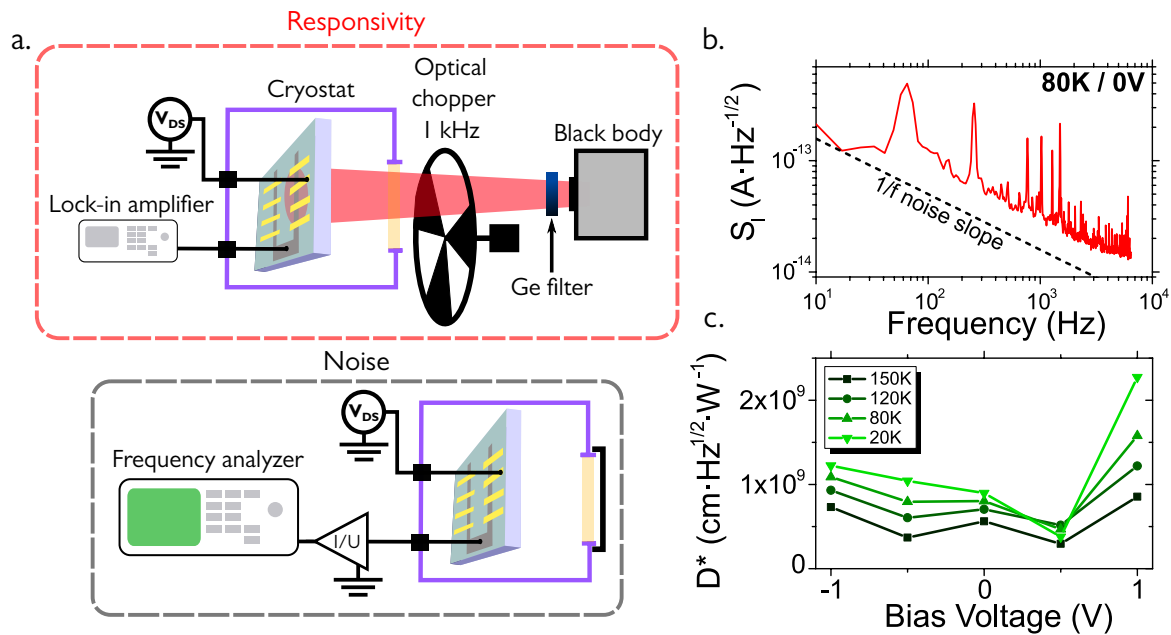


Fig. 4.24 CQDIP-based intraband diode: detectivity evaluation. **a.** Scheme of responsivity and noise measurements. Responsivity is measured under illumination by a  $650^\circ\text{C}$  equipped with a  $1.9 \mu\text{m}$  germanium long-pass filter. Photocurrent measurement is done at 1 kHz using a lock-in amplifier. The dark current spectral density (noise) is measured in the dark, under polarization by a battery. The dark current is amplified using a transimpedance amplifier which output is fed into a frequency analyzer. **b.** Dark current spectral density measured at 80 K and in short-circuit conditions. The  $1/f$  noise slope (or  $1/f^{1/2}$  current spectral density slope) is pictured with a dash line. **c.** Device specific detectivity  $D^*$ , measured at 1 kHz and for a  $1.9 \mu\text{m} - 5 \mu\text{m}$  spectral window.

For the detectivity calculation, both the responsivity and the noise are taken at 1 kHz. Resulting values are presented in Figure 4.24c: under broadband illumination and at cryogenic temperatures, we report a  $D^* \simeq 10^9$  Jones at zero bias. This value slightly increases to reach 1.5 to  $2 \times 10^9$  Jones under 1 V operation. While these values do not reach the performances of HgTe-based interband diodes around the same wavelengths [162], this constitutes a record performance for nanocrystal-based intraband detectors.

This photodiode device being made of three materials active in the infrared (HSe, HgTe 4k and HgTe 6k in the unipolar barrier), it is very difficult to deconvolute the effect of each material on the final performances of the device from broadband measurements: in the next paragraph, I focus on the spectral characterization of this multi-spectral device.

### 4.5.3 Spectral characterization

Investigation of the spectral response of the diode is extremely valuable to understand its behavior. At the time of this study, I set up a photocurrent spectroscopy experiment based on our new FTIR setup. A FTIR spectrometer is not a scanning instrument like classical UV-visible spectrometers, but it produces modulated infrared light *via* a Michelson interferometer and a moving mirror. As a result, the IR beam in a FTIR is modulated in time. By exposing our device to the output light and feeding the device output back into the FTIR, the signal is synchronized with the mirror movement and the Fourier transform can be calculated, yielding the photocurrent spectrum of the device. In other words, we use our device as an external detector for the FTIR. Practically speaking, we use a transimpedance amplifier to bias the diode and convert its photocurrent into a voltage signal that can be used by the FTIR pre-amplifier (see appendix A). This experiment has one major drawback though: because of the high mirror speed in the interferometer, the device photocurrent dynamics must be sufficiently fast ( $> 1$  kHz) for the measured spectrum to accurately represent the actual spectral dependence of the photocurrent.

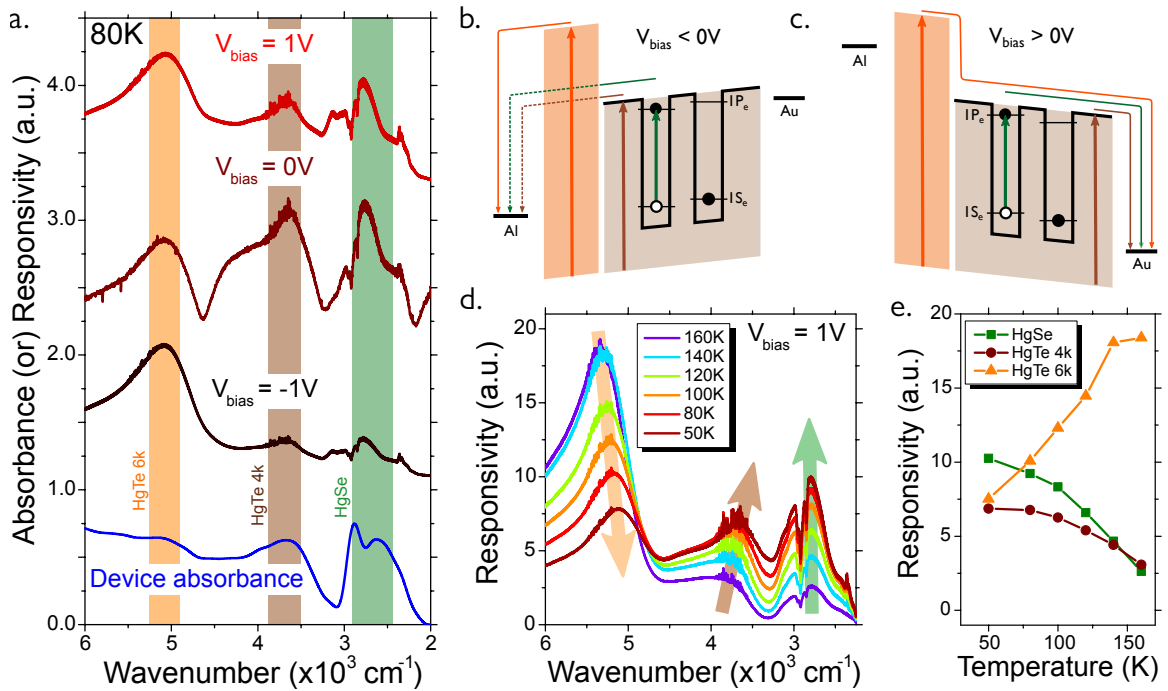


Fig. 4.25 Intraband diode spectral characterization. **a.** Spectral responsivity of the device at 80 K (from photocurrent spectra) for 0 V, -1 V and 1 V biases applied on the diode. Device absorbance, measured in the same conditions, is given in blue. Spectral contributions of HgSe (green), HgTe 4k (brown) and HgTe 6k (orange) have been highlighted. **b.** Scheme of the diode band structure under negative bias. **c.** Scheme of the diode band structure under positive bias. **d.** Spectral responsivity of the device measured for decreasing temperature, under 1 V bias. Evolution of the spectral contribution of HgSe (green), HgTe 4k (brown) and HgSe 6k (orange) have been highlighted with arrows pointing in the direction of cooling. **e.** Evolution of the relative responsivities with temperature for the three materials constituting the diode device.

Photocurrent spectra ( $I_{\text{photo}}(\nu)$ ) are measured by using the FTIR source spectrum (photon flux  $\phi_{\text{IR}}(\nu)$ ) as a background. If  $V(\nu)$  is the raw detector spectral signal (after Fourier transform), then  $I_{\text{photo}}(\nu) = V(\nu)/\phi_{\text{IR}}(\nu)$  and the device spectral responsivity (in arbitrary units) is  $\mathcal{R}(\nu) \propto I_{\text{photo}}(\nu)/(h\nu)$ . The spectral responsivity of the device at 80 K is given in Figure 4.25a for several biases, as well as the device absorbance, measured in transmission in the exact same conditions as the photocurrent spectra. The device spectral responsivity clearly shows three contributions to the photocurrent: HgSe intraband contribution appears in the low energy part of the spectrum as

a peaked feature, HgTe 4k around  $3800\text{ cm}^{-1}$  as a broadband feature and HgTe 6k around  $5200\text{ cm}^{-1}$ . This spectrum shows dramatic changes with bias: under negative bias, the responsivity is very clearly dominated by the HgTe 6k signal while for zero volt or positive biases, there is a clear responsivity signal coming from both HgSe and HgTe 4k. This is explained by the presence of the HgTe 6k unipolar barrier, as schematized in Figure 4.25b and c: under negative bias, extraction of photocharges generated in HgSe/HgTe mix is very limited because they are filtered by the wide bandgap HgTe 6k unipolar barrier, while charges generated in the barrier can easily be collected at the Al electrode. Under positive bias, photocharges generated both in the barrier and in the HgSe/HgTe hybrid material are efficiently extracted. The zero bias situation likely corresponds to a point where charges from HgSe/HgTe mix are collected due to the built-in voltage, but those generated in HgTe 6k do not diffuse far enough to be efficiently collected. Here again, we observe a strong asymmetry of the device operation with bias, which confirms both the rectifying behavior of the diode and the positive bias operation as the way to maximize the intraband (MWIR) performances.

In Figure 4.25a, we notice that the HgSe-related photocurrent contribution is slightly blue-shifted with respect to the intraband absorption: at 80 K, the maximum of intraband absorption lies around  $2620\text{ cm}^{-1}$  (disregarding the C-H absorption peak) while maximum of intraband photocurrent is found around  $2780\text{ cm}^{-1}$ . This represents a  $160\text{ cm}^{-1}$  or 20 meV blue-shift. The fact that this shift is only observed on the HgSe contribution (HgTe 4k and HgTe 6k responsivity features match their absorption maxima) suggests that the charge extraction from the HgSe nanocrystals to the HgTe 4k network is slightly non-optimal and that high-energy photocarriers are more easily transferred to HgTe than the ones resonant with the  $1P_e$  level. This is fully consistent with photoemission measurements (see Figure 4.17c) which predicted a 90 meV offset between HgSe  $1P_e$  and HgTe  $1S_e$  levels at room temperature. This slight blue-shift of the device MWIR responsivity relatively to absorption also explains the relatively low modulation observed under QCL monochromatic illumination at  $2270\text{ cm}^{-1}$ : the laser is matched to the red part of the intraband absorption peak at room temperature. The spectral match of the device spectral responsivity and the QCL is hence strongly affected by the combination of (i) the blue-shift of the HgSe intraband absorption resulting from cooling down the device and (ii) the observed blue-shift between the device intraband responsivity and absorption.

Evolution of the device spectral responsivity with temperature, measured under 1 V bias, is illustrated in Figure 4.25d. Again, the responsivity spectra show strong modulation with the device operating temperature. Particularly, HgTe 6k contribution, which is predominant at high temperatures, is strongly reduced while cooling the device. On the contrary, spectral contribution of the HgSe/HgTe 4k active material increases while lowering the device operating temperature. Figure 4.25e summarizes the responsivity evolution of the three contributions with temperature. Interestingly, while both HgTe 4k and HgTe 6k spectral contributions red-shift while the device is cooled (in Figure 4.25d), accordingly to the red-shift of their actual bandgap, we do not observe any shift of the MWIR intraband responsivity contribution despite the absorption spectra of the device showing a very clear blue-shift of the intraband peak, see appendix A. If we think of this HgSe/HgTe 4k material in term of band alignment, we anticipate that the energy mismatch  $\Delta E$  defined earlier is reduced while cooling down the materials, since HgTe 4k interband bandgap red-shifts and HgSe intraband bandgap blue-shifts at low temperatures. As a result, the CQDIP material becomes better matched at low temperature. Because electrons generated in HgSe only contribute to the photocurrent through HgTe 4k, the measured intraband contribution in the responsivity spectra can be seen as the convolution of the HgSe intraband absorption spectrum with a notch spectral window characterized by the energy mismatch between HgTe 4k and HgSe. This is a possible explanation for the relative increase in responsivity observed for the HgSe contribution in Figure 4.25e: HgSe-related responsivity increases faster than HgTe 4k-related responsivity due to a better match between the intraband absorption of HgSe and the extraction efficiency window.

Spectral characterization is definitely a powerful tool to understand the behavior of our devices. Being constituted by three materials active in the IR, our diode is essentially a multi-spectral photodetector. I showed that the relative contributions of those three materials to the overall device spectral

responsivity, from SWIR to MWIR, can be tuned by either the bias of the detector or the temperature of operation. I also identified that the spectral mismatch between absorption and responsivity in the MWIR part of the device spectrum is a critical point to address in future devices developments. Finally, this study confirms that ideal working conditions for good MWIR detection performances in our diode are around the liquid nitrogen temperature and with a 1 V bias. In the last part of this chapter, I will evaluate the potency of our intraband photodetector for thermal imaging in the MWIR.

#### 4.5.4 First attempts at thermal sensing

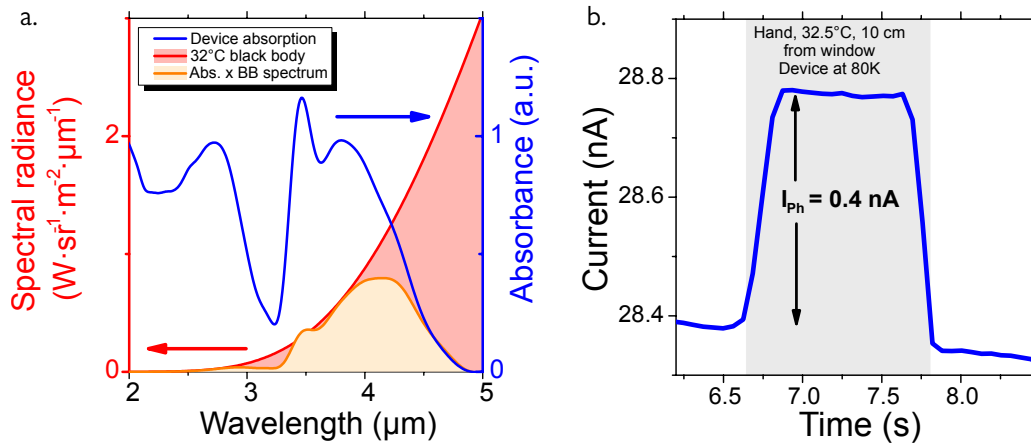


Fig. 4.26 Evaluation of the device performances for thermal imaging. **a.** Spectral radiance of a 32°C black body (human hand), in red. Device absorption at 80 K in the 2 μm - 5 μm window is pictured in blue. The product of device absorption and human hand spectral radiance is indicated in orange. **b.** Exposition of the device to a hand at 80 K, 10 cm from the cryostat window. The device is cooled to 80 K and under 1 V bias a 0.4 nA photocurrent is measured.

Because the ultimate goal of this type of device is to be used as cheap thermal imagers, after identifying the optimal operation point of our MWIR-sensing, intraband-based photodiode, I evaluated its capability to perform thermal detection. The first way of doing this is to expose the device to a cold black body to estimate the Net-Equivalent Temperature Difference (NETD), the minimal black body temperature difference being measurable with the device. To do so, we expose the device to a hand (a 32.5°C black-body). The temperature contrast is given by the ambient 20°C lab temperature. The spectral radiance of such a low temperature black-body is plotted in Figure 4.26a. The absorption spectrum of our device only matches with the black-body emission in its intraband MWIR part, as witnessed by the shape of the product of device absorption and black-body spectral radiance in Figure 4.26a. Using such a cold black-body is hence a good way to characterize the intraband-related responsivity of our diode. Figure 4.26b shows the device current under 1 V of applied bias and at 80 K. Exposure of the diode to a hand 10 cm away from the cryostat window produces a clear 0.4 nA photocurrent. The optical power radiated at the device position is obtained by using the black-body formula 4.16. Assuming that the half-angle of view is only limited by the cryostat window, we have  $\alpha = 14^\circ$  and:

$$P_{\text{opt}} = T \times A_d \pi \sin^2 \alpha \int_2^5 \frac{\mu\text{m}}{\mu\text{m}} S(\lambda, T_{\text{BB}}) d\lambda = 77 \text{ nW} \quad (4.18)$$

Where  $S(\lambda, T_{\text{BB}})$  is the black-body spectral radiance at 32.5°C. The associated responsivity is then  $\mathcal{R} = 5.2 \text{ mA/W}$ , which is a decent fraction of what is measured with the 650°C black-body.

We can then estimate the NETD as:

$$\text{NETD} = \frac{\Delta T}{\Delta I_{\text{photo}}/I_n} \quad (4.19)$$

Where  $\Delta T$  is the temperature difference associated with the photocurrent  $\Delta I_{\text{photo}}$  and  $I_n$  is the RMS noise of the device. From Figure 4.26b, we have  $\Delta T = 12.5^\circ\text{C}$  and  $\Delta I_{\text{photo}} = 0.4 \text{ nA}$ . The spectral dark current density have been measured to be  $3 \text{ fA/Hz}^{1/2}$  under 1 V and at 80 K, for a 1 kHz operation. Hence with a 1 kHz bandwidth, we have  $I_n=0.9 \text{ pA}$  and  $\text{NETD} = 35 \text{ mK}$ .

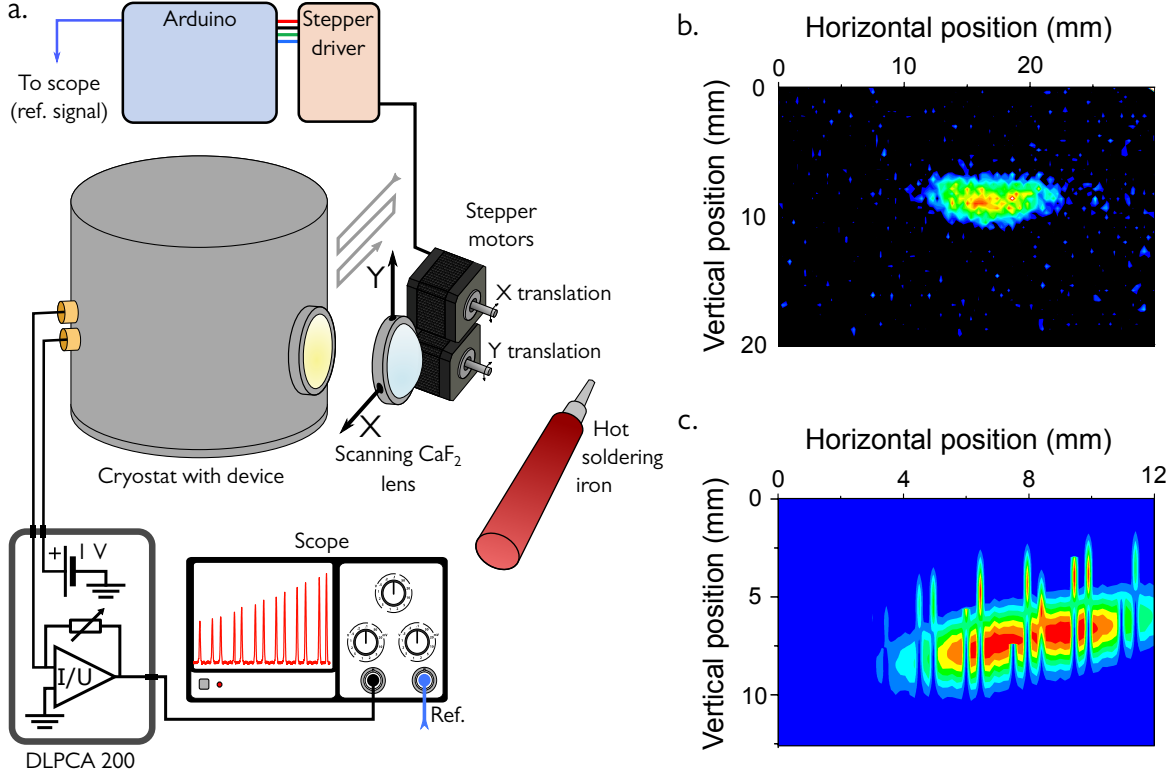


Fig. 4.27 First attempts at single-pixel imaging. **a.** Scheme of the imaging experiment: the sample is kept at 80 K in the cryostat, and a hot ( $300^\circ\text{C}$ ) soldering iron is placed  $\sim 50 \text{ cm}$  away. A  $\text{CaF}_2$  lens is scanned in front of the cryostat window using a home-made X-Y motorized translation stage. Motors are controlled through an Arduino micro-controller, photocurrent is measured using a transimpedance amplifier and an oscilloscope in continuous acquisition mode. **b.** Soldering iron thermal picture reconstructed from temporal data acquired on the oscilloscope at 2.5 kHz. **c.** Soldering iron image reconstructed using temporal data acquired directly through the source-meter at 1.4 kHz.

I then took advantage of the device fast dynamics to build a single-pixel scanning imager. The original idea was proposed by Tang *et al.* from the Guyot-Sionnest group with their HgTe-based MWIR photodiode [161]. The principle is to use the single-pixel device to produce a 2D image by scanning its position in the focal plane of a lens. The device being kept at 80 K in a cryostat, it is much simpler to scan the lens position instead of the pixel one. Figure 4.27a provides a scheme of the experiment: a 30 mm  $\text{CaF}_2$  lens is mounted in a home-made motorized X-Y translation stage and positioned so its focal plane lies approximately at the device position. The hot object we want to image is the tip of a  $300^\circ\text{C}$  soldering iron placed  $\sim 50 \text{ cm}$  away from the cryostat window. Two stepper motors for X and Y movement are controlled through an Arduino board to move the lens in a zig-zag pattern with  $\sim 80 \mu\text{m}$  minimum step size and a 4 cm by 4 cm maximal movement in X and Y directions. Because of the device fast response, the scanning speed can be fast without worrying about image distortion: with 1 ms per step (limited by the motor drivers), a  $300 \times 200$  "pixels" image is scanned in 60 s.

Acquisition of the device photocurrent is challenging: to preserve the fast scanning speed, communication between instruments must be kept minimal. Results presented here are only preliminary, but show that this technique is quite promising for reasonably fast construction of 2D images from a single pixel device. Figure 4.27b is reconstructed from data acquired using an oscilloscope, measuring the output of a transimpedance amplifier connected to the biased device. A reference signal indicating the motors directions is needed to reconstruct the final image. While the image produced by this technique is fairly noisy (mostly because of strong electrical noise from the motor drivers), we still identify very clearly the hot spot defined by the soldering iron tip, and the transition with the cold plastic sleeve. The image from Figure 4.27c is acquired using the buffer capabilities of a Keithley 2634b source-meter, and shows much crispier contrast. Nevertheless, the lack of reference on the motor positions makes that image reconstruction is painful and produces a lot of artefacts.

Those results are only very preliminary, and a lot of work remains to be done to achieve good image quality. A key improvement in the acquisition part is needed to achieve a fast scanning with real-time image reconstruction, as the heavy post-processing needed right now prevents any feedback on the image focus or centering.

## Conclusions

This chapter was mostly focused on the use of HgSe nanocrystals for alternative MWIR sensing. With intraband absorption in the MWIR, HgSe doped nanocrystals offer a paradigm shift from interband-based devices toward the exploitation of low energy intraband transitions, relaxing a significant number of material constraints. Nevertheless, devices made from pure HgSe nanocrystals suffer from three major drawbacks: a low signal/noise ratio, weak activation energy and a slow photoreponse, making them incompatible with MWIR photodetection needs. We identified two strategies to improve the material performances by engineering charge transfer toward HgTe nanocrystals. In a first approach, we synthesized HgSe/HgTe "core-shell" nanocrystals, in which we observed a strong decoupling of the optical and transport properties. This allowed to build photoconductive devices with improved performances, at the price of a rather complex synthetic effort.

Along the way, we were interested by the effect of pressure on the nanocrystals growth. Indeed, building core-shell nanocrystals implies dealing with interfacial pressure that can have a strong effect on the nanocrystals optical spectra. Using a combination of high pressure infrared spectroscopy and  $\mathbf{k}\cdot\mathbf{p}$  simulations, we studied the effect of pressure on both HgTe and HgSe nanocrystals. The main conclusions from this study is that there is a very narrow range of tunable parameters for growing HgSe-based core/shell materials, because of phase transition in HgSe and high sensitivity of the intraband transition to pressure, even in the low pressure range.

We hence turned to an alternative design, where the heterostructure is not realized at the nanoparticle level but rather at the device scale. To do so, we were inspired by QWIP and QDIP devices and tried to reproduce similar energy landscape by mixing two populations of HgTe and HgSe nanocrystals. Doing so, we obtained a hybrid material displaying intraband (*i.e.* HgSe-like) optical properties in which transport is mostly driven by HgTe, effectively uncoupling absorption and charge transport and achieving high signal to noise ratios, good activation energies and high photoresponse dynamics. We then integrated this material into the first intraband-based MWIR photodiode.

This approach is very promising for device design, because it can be used for a wide variety of materials and applications: a very similar concept have been used to build high efficiency infrared LEDs by mixing two populations of PbS NCs [242]. We can hope that using concepts from intraband and intra-subband epitaxial devices and doped nanocrystals (HgSe, HgS, Ag<sub>2</sub>Se...), it might be possible in the years to come to go even further and build the colloidal equivalent of Quantum Cascade devices, pushing the wave-function engineering up to the device scale by carefully arranging networks of nanocrystals.



# Conclusion and perspectives

In the first two result chapters, we used mercury telluride nanocrystals to build infrared sensing devices in the NIR (with HgTe nanoplatelets) and the MWIR (with HgTe quantum dots). After giving evidence for a strong tunability of the majority carrier in HgTe nanoplatelets with surface chemistry control, I studied carrier dynamics under gate control in NIR photoconductors made from those objects. I then used time-resolved photoemission to shine light on the intrinsic limitations of the material, and measured majority carrier dynamics around 100 ns. Mercury telluride nanoplatelets offer promising opportunities to build new NIR sensing devices, and pave the way to new 2D materials with narrower bandgaps to address redder parts of the infrared spectrum.

I then switched to HgTe quantum dots with absorption in the MWIR, and showed that they can achieve photodetection with a bandwidth larger than 20 MHz under illumination at their band-edge. I also showed that multiple exciton generation is efficient in this material, and can be observed with illumination in the NIR thanks to the narrow bandgap of those nanocrystals. Finally, I built a transient photocurrent setup allowing to probe, in a wide variety of nanocrystal-based devices, photocurrent dynamics over a large temporal window. This experiment enables to extract material-related parameters (exciton lifetime and Urbach energy) from measurements at the device scale.

In the last chapter, I introduce mercury selenide nanocrystals as a new platform to investigate intraband transitions in colloidal nanomaterials. This material features optical properties that are extremely interesting in terms of MWIR-LWIR photodetection applications. I started working with this material since my arrival at the lab, and from early results, it was clear that HgSe NCs suffer from major drawbacks in terms of transport: HgSe devices, because of their high doping level, features low signal to noise ratios, low activation energies and display slow photoresponse. From those observations, it was clear that we needed a way to uncouple optical and transport properties in this material so that the high doping level, required for the observation of intraband transitions, could not drive the transport properties of the devices. I then presented two successful approaches: designing HgSe/HgTe core-shell heterostructures where the electron excited in HgSe can be transferred to HgTe for transport, and mimicking the energy landscape of III-V semiconductors by carefully mixing HgSe and HgTe nanocrystals. The latter is probably the most promising, because it is versatile enough to be applied to a wide range of materials. From this metamaterial, we build the first intraband-based MWIR photodiode presenting reasonable performances, and give very preliminary results for thermal detection with this device.

A nearby perspective for this work is to improve this intraband diode: there is a lot of unoptimized parameters in this first generation. I see several ways of optimization:

- The spectral mismatch between absorption and photocurrent should be solved by slightly adjusting the confinement of the two original materials in the binary mix.
- The material itself should be better matched with our MWIR QCL by taking into account the spectral mismatch between absorption and photocurrent, as well as the blue-shift of absorption with cooling.
- The layer of active material is currently quite thin (150-200 nm), leading to poor absorption of incident light. This layer should be made thicker, and for that thickness increase to be effective, the electron diffusion length (*i.e.*, electron mobility) should also be increased to match with the film thickness. A way of doing this is to use nanocrystals inks, that achieve higher carrier mobility and enable the building of thick, homogeneous films over large scales [247].
- Demonstration of thermal imaging with this device should be pushed further by improving the

signal acquisition and synchronization with the motors movements. Integration of the QDIP material into simple  $10 \times 10$  pixel matrices, as we demonstrated for HgTe 4k [247] can also be considered. The issue of operating temperature can be addressed with, for example, single or multiple-stage Peltier coolers as demonstrated by Sergei Yakunin in recent work [248].

- Finally, thanks to our recent collaboration with NIT (New Imaging Technology), we can think of embedding our QDIP material on top of their logarithmic-response CMOS detectors (up to 10 MPx matrices with built-in high dynamic range). We already demonstrated that this strategy is successful with HgTe 6k materials, efficiently increasing the response of the CMOS detectors to the SWIR. This would obviously require an optimized material and operation at low temperature (at least with Peltier cooling).

The quest for wave-function engineering at the device level relied up to now on the realization of bandlike transport, which is not likely to occur even in well-assembled networks of nanocrystals [81]. Recent results, including our work on HgSe/HgTe mixed nanocrystals, suggest that one can engineer heterostructures, local doping and heterojunctions at the device level without worrying too much about disorder and interfaces [49, 242, 243, 249]. If this is indeed the case, it opens an incredible amount of possibilities to build light-emitting or detector devices in the infrared range. With some imagination, one can for example hope to reproduce similar band-alignments such as in a Quantum Cascade Laser, only by carefully assembling layers of doped and intrinsic nanocrystals.

# Appendix A

## Material and Methods

### Nanocrystal synthesis

**Disclaimer:** mercury compounds are highly toxic and must be handled with special care.

#### HgTe nanocrystals

**1 M TOP:Te precursor:** 2.54 g of Te powder is mixed in 20 mL of TOP in a three neck flask. The flask is kept under vacuum at room temperature for 5 min and then the temperature is raised to 100 °C. Furthermore, degassing of flask is conducted for the next 20 min. The atmosphere is switched to Ar and the temperature is raised to 275°C. The solution is stirred until a clear orange coloration is obtained. The flask is cooled down to room temperature and the color switches to yellow. Finally, this solution is transferred to an Ar filled glove box for storage.

**HgTe 2k:** 27 mg of HgCl<sub>2</sub> and 10 mL of oleylamine are degassed under vacuum at 120°C in a 50 mL three-neck flask. A pre-heated solution made of 100 µL of TOP:Te and 9.9 mL of oleylamine is injected into the flask. One has to note that pre-heating is essential to synthesize nanocrystals with low size dispersion. The solution color quickly changes from light yellow to dark-brown. After 3 min, the reaction is quenched with an injection of a solution of 1 mL of dodecanethiol and 9 mL of toluene. The temperature quickly drops to 70-80°C. Resulting solution is precipitated with addition of 90 mL ethanol and then centrifuged. The precipitate is redispersed in chloroform and four drops of dodecanethiol are added. A second washing step is carried out with 80 mL of methanol. The stability of the final colloidal solution is improved by redispersing the nanocrystals in chloroform.

**HgTe 3k:** 513 mg of HgCl<sub>2</sub> is added to 60 mL of oleylamine in a 100 mL round flask. The solution is placed under vacuum and heated to 110 °C for 1 h. The temperature is then decreased to 100 °C and atmosphere is switched to argon. 1.9 mL of TOP:Te (1 M) with 10 mL of oleylamine is added to the mercury solution. The solution color gradually turns to dark brown and the reaction is quenched after 3 min with the injection of a solution made of 1 mL of dodecanethiol and 9 mL of toluene. The flask is cooled down and the nanocrystals are then precipitated with ethanol. After centrifugation, the nanocrystals are redispersed in chloroform. The washing step is repeated one more time before using the nanocrystals.

**HgTe 4k:** 513 mg of HgCl<sub>2</sub> is added to 60 mL of oleylamine in a 100 mL round flask. The solution is placed under vacuum and heated to 110°C for 1 h. Then, the temperature is decreased to 80 °C and solution placed under Ar atmosphere. 1.9 mL of TOP:Te (1 M) with 10 mL of oleylamine is added to the mercury solution. The solution color gradually turns to dark brown and the reaction is made during 3 min. A solution made of 1 mL of dodecanethiol and 9 mL of toluene is quickly added to quench the reaction. The nanocrystals are then precipitated with ethanol. After centrifugation, the nanocrystals are redispersed in chloroform. The washing step is repeated one more time. The solution is filtered with a 0.2 µm filter and redispersed in 6 mL of chloroform.

**HgTe 6k:** 513 mg of  $\text{HgCl}_2$  is added to 60 mL of oleylamine in a 100 mL round flask. The solution is placed under vacuum and heated to  $110^\circ\text{C}$  for 1 h. Then, the temperature is decreased to  $60^\circ\text{C}$  and the solution is placed under Ar atmosphere. 1.9 mL of TOP:Te (1 M) with 10 mL of oleylamine is added to the mercury solution. The solution color gradually turns to dark brown and the reaction is made during 3 min. A solution made of 1 mL of dodecanethiol and 9 mL of toluene is quickly added to quench the reaction. The nanocrystals are then precipitated with ethanol. After centrifugation, the nanocrystals are redispersed in chloroform. The washing step is repeated one more time. The solution is redispersed in chloroform and filtered with a  $0.2\ \mu\text{m}$  filter. Two additional washing steps are applied with final redispersion in chloroform.

## HgSe nanocrystals

**1 M TOP:Se precursor:** 1.57 g of Se is mixed with 20 mL of TOP in a flask. Dissolution of Se powder is helped by sonication for 1 hour. The resulting solution is colorless.

**HgSe 1k:** 0.5 g of mercury acetate are dissolved in 10 mL of oleic acid and 25 mL of oleylamine. The solution is degassed under vacuum at  $100^\circ\text{C}$  during 60 min. The atmosphere is switched to argon. At  $110^\circ\text{C}$ , 0.65 g of  $\text{SeS}_2$  dissolved in 5 mL of OLA is injected to the mercury solution. The solution rapidly turns from yellow to dark, indicating the formation of HgSe material. After 1 Min, the reaction is quenched by adding 1 mL of dodecanethiol and cooled to room temperature with water bath. The nanocrystals are then precipitated with ethanol. After centrifugation, the nanocrystals are redispersed in chloroform. The washing step is repeated one more time.

**HgSe 2.5k:** This is the well-known *Adrien synthesis*. 500 mg of mercury acetate is dissolved in 10 mL of oleic acid and 25 mL of oleylamine. The solution is degassed under vacuum at  $100^\circ\text{C}$  during 1 h. The atmosphere is switched to argon. At  $110^\circ\text{C}$ , 1 mL of TOP:Se (1 M) is injected to the mercury solution. The solution rapidly turns from yellow to dark, indicating the formation of HgSe material. After 1 Min, the reaction is quenched by to addition of 1 mL of dodecanethiol and cooled to room temperature with a water bath. The nanocrystals are then precipitated with ethanol. After centrifugation, the nanocrystals are redispersed in chloroform. The washing step is repeated one more time. The solution is filtered with a  $0.2\ \mu\text{m}$  filter and redispersed in chloroform.

**HgSe 3k:** 500 mg of mercury acetate are dissolved in 10 mL of oleic acid and 25 mL of oleylamine. The solution is degassed under vacuum at  $100^\circ\text{C}$  during 60 min. The atmosphere is switched to argon. At  $110^\circ\text{C}$ , 1.6 mL of TOP:Se (1 M) is injected to the mercury solution. The solution rapidly turns from yellow to dark, indicating the formation of HgSe material. After 1 Min, the reaction is quenched by adding 1 mL of dodecanethiol and cooled to room temperature with air flux. The nanocrystals are then precipitated with ethanol. After centrifugation, the nanocrystals are redispersed in chloroform. The washing step is repeated one more time. The solution is filtered with a  $0.2\ \mu\text{m}$  filter and redispersed in 6 mL of chloroform. Two size selection precipitations are carried out by adding ethanol and keeping the precipitate each time.

## Electrodes and FET fabrication

### Interdigitated electrodes for photoconductive devices

1 mm glass slides cut in half are cleaned by sonication in acetone and rinsed with isopropanol, then receive a 5 min oxygen plasma cleaning. An adhesion primer (TI Prime) is spin-coated onto each substrate and annealed for 2 min at  $120^\circ\text{C}$  before AZ5214E resist is spin-coated and baked at  $110^\circ\text{C}$  for 90 s. A MJB4 mask aligner is used to expose the substrates to UV light for 1.5 s through a

lithography mask. Substrates are then baked at 125°C for 2 min to invert the resist and flood-exposed for 40 s. AZ726 developer is used to develop the resist: the samples are dipped in the solution for 20 s before being rinsed in pure water for 10 s. Patterned substrates are dried and cleaned with 5 min of oxygen plasma to remove resist residues. In a thermal evaporator, 5 nm of chromium are deposited as an adhesion promoter before 80 nm of gold is evaporated. Lift-off is conducted in an acetone bath for at least one hour. Electrodes are formed with 25 pairs of 2.5 mm long fingers, spaced by 20  $\mu\text{m}$ .

## Aluminium grid electrodes on sapphire

Sapphire substrates ( $2 \times 2 \text{ cm}^2$ ) are sonicated in acetone and cleaned with acetone and isopropanol before being exposed to an oxygen plasma for 5 min. Adhesion promoter (TI Prime) is spin coated on the substrate and annealed at 120 °C for 2 min. Then, the UV sensitive photoresist is spin coated on the substrate and is baked at 110 °C for 90 s, then a MJB4 mask aligner is used to expose the slides to UV light through a quartz mask (1.5 s exposition). After a 125 °C bake for 2 min and a 40 s flood exposure, substrates are developed using AZ726 developer for 20 s and rinsed with distilled water. After a 5 min plasma cleaning, 80 nm of aluminium are deposited using a thermal evaporator. Lift-off is conducted overnight in an acetone bath. Resulting electrodes are shown in Figure 4.22.

## Electrolyte-gated field effect transistors

**Electrolyte preparation** The electrolyte is prepared in a nitrogen-free glove-box. 0.5 g of  $\text{LiClO}_4$  are mixed with 2.3 g of polyethyleneglycol (PEG,  $\text{MW} = 6 \text{ kg}\cdot\text{mol}^{-1}$ ). The resulting mix is heated at 170 °C for 2 h until the solution turns clear, then cooled down overnight before use.

**FET devices** In a nitrogen-filled glove-box, the  $\text{LiClO}_4$ -PEG electrolyte is heated up at 90 °C until it turns clear. The resulting viscous gel is brushed on top of a device, see Figure 1.16. The polymer gel is allowed to cool down overnight. The device is measured under probes or in a specially designed box with a Keithely 2634b dual channel source-meter. The transfer curve is measured under a 50to500 mV drain-source bias, with a  $1 \text{ mVs}^{-1}$  gate bias sweep rate.

## Low-temperature absorption/photocurrent spectra

**Photocurrent spectra:** The device is enclosed in a closed-cycle cryostat and cooled down to the desired temperature. The head of the cryostat is brought in the sample compartment of a Fischer iS50 FTIR spectrometer (see Figure A.1) and illumination is provided from the backside of the device by the focused Globar source through two ZnSe windows (one on the outer cryostat enclosure and one on the shield), and through a hole in the sample holder. The photocurrent is amplified using a Femto DLPCA-200 transimpedance amplifier which also serves as a bias source. Output of the amplifier is sent back to the FTIR spectrometer. All interferograms are normalized to the source spectrum, acquired with a flat-response DTGS detector in the same range of wavenumbers (see section 4.5.3).

**Absorption spectra:** because the device is transparent enough, we can measure absorption spectra of devices mounted in photocurrent spectrum configuration in the sample compartment. In this configuration, we use the FTIR DTGS detector to measure the transmitted IR. Figure A.1d presents absorption spectra of a device for decreasing temperatures. Contributions of the three materials constituting the device (HgSe, HgTe 4k, HgTe 6k) are clearly identified, as well the shift in energy of their respective transitions at low temperature. Energy of HgTe 6k interband transition, HgTe 4k interband transition and HgSe intraband transition have been extracted and are plotted in graph A.1e.

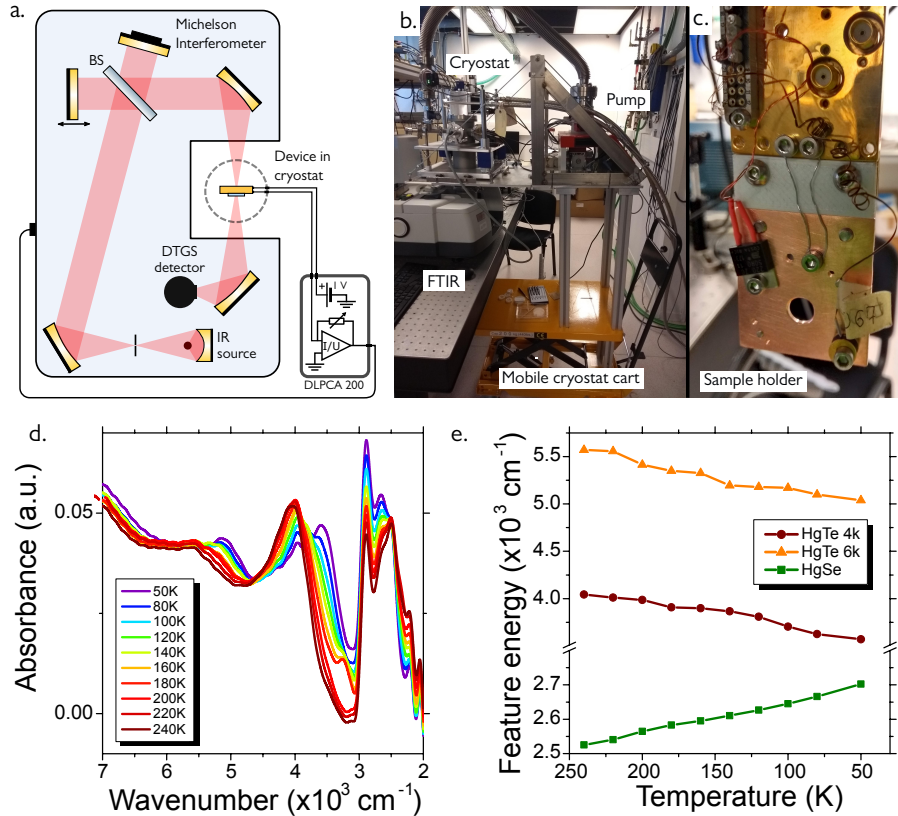


Fig. A.1 Experimental setup for low temperature photocurrent and absorption spectra. **a.** Scheme of the setup. The cryostat is placed in the FTIR sample compartment, with the sample holder aligned on the IR beam. Photocurrent spectra is acquired through a Femto DLPCA-200 transimpedance amplifier which output is fed into the FTIR. Absorption spectrum of the device is measured in transmission mode with the FTIR DTGS detector in the same conditions as for the photocurrent spectrum. **b.** Picture of the experimental setup. The cryostat support is built to be easily moved to over experiments. **c.** Picture of a thermally decoupled sample holder, equipped with three electrical contacts (on the backside) as well as heater and temperature probe. **d.** Absorption spectra of a QDIP diode device fro decreasing temperatures. Spectra have been smoothed to remove interferences due to device high reflectivity. **e.** Energy of the three materials optical features (HgTe 6k interband energy, HgTe 4k interband energy, HgSe 2.5k intraband energy), extracted from absorption spectra.

# List of publications

## Journal Articles

### First Author Articles

1. [C. Livache](#), B. Martinez, N. Goubet, C. Gréboval, J. Qu, A. Chu, S. Royer, S. Ithurria, M. G. Silly, B. Dubertret, E. Lhuillier, “A colloidal quantum dot infrared photodetector and its use for intraband detection”, *Nature Communications* 10, 2125 (2019).
2. [C. Livache](#), N. Goubet, C. Gréboval, B. Martinez, J. Ramade, J. Qu, A. Triboulin, H. Cruguel, B. Baptiste, S. Klotz, G. Fishman, S. Sauvage, F. Capitani, E. Lhuillier, “Effect of Pressure on Interband and Intraband Transition of Mercury Chalcogenides Quantum Dots”, *The Journal of Physical Chemistry C* (2019).
3. [C. Livache](#), B. J. Ryan, U. Ramesh, V. Steinmetz, C. Gréboval, A. Chu, T. Brulé, S. Ithurria, G. Prévot, T. Barisien, A. Ouerghi, M. G. Panthani, E. Lhuillier, “Optoelectronics of methyl-terminated germanane”, *Applied Physics Letters* 115, 52106 (2019).
4. [C. Livache](#), N. Goubet, B. Martinez, A. Jagtap, J. Qu, S. Ithurria, M. G. Silly, B. Dubertret, E. Lhuillier, “Band edge dynamics and multiexciton generation in narrow band gap HgTe nanocrystals”, *ACS Applied Materials & Interfaces* 10, 11880–11887 (2018).
5. [C. Livache](#), B. Martinez, N. Goubet, J. Ramade, E. Lhuillier, “Road map for nanocrystal based infrared photodetectors”, *Frontiers in Chemistry* 6 (2018).
6. [C. Livache](#), E. Izquierdo, B. Martinez, M. Dufour, D. Pierucci, S. Keuleyan, H. Cruguel, L. Becerra, J. L. Fave, H. Aubin, A. Ouerghi, E. Lacaze, M. Silly, B. Dubertret, S. Ithurria, E. Lhuillier, “Charge dynamics and optoelectronic properties in HgTe colloidal quantum wells”, *Nano Letters* 17, 4067–4074 (2017).

### Other Articles

7. J. Ramade, J. Qu, A. Chu, C. Gréboval, [C. Livache](#), N. Goubet, B. Martinez, G. Vincent, E. Lhuillier, "Potential of Colloidal Quantum Dot based Solar Cell for Near-Infrared Active Detection", *ACS Photonics*, ASAP, (2019).
8. B. Martinez, R. Plamont, C. Gréboval, P. Rastogi, Y. Prado, J. Qu, A. Chu, [C. Livache](#), X. Xu, H. Cruguel, S. Ithurria, M. G. Silly, N. Goubet, E. Lhuillier, “Azobenzene as Light-Activable Carrier Density Switches in Nanocrystals”, *The Journal of Physical Chemistry C* 123, 27257-27263 (2019).
9. A. Chu, C. Gréboval, N. Goubet, B. Martinez, [C. Livache](#), J. Qu, P. Rastogi, F. A. Bresciani, Y. Prado, S. Suffit, S. Ithurria, G. Vincet, E. Lhuillier, “Near Unity Absorption in Nanocrystal Based Short Wave Infrared Photodetectors using Guided Mode Resonators”, *ACS Photonics* 6, 2553-2561 (2019).
10. M. Dufour, E. Izquierdo, [C. Livache](#), B. Martinez, M. G. Silly, T. Pons, E. Lhuillier, C. Delerue, S. Ithurria, “Doping as a Strategy to Tune Color of 2D Colloidal Nanoplatelets”, *ACS Applied Materials & Interfaces* 11, 10128–10134 (2019).

11. A. Chu, B. Martinez, S. Ferré, V. Noguier, C. Gréboval, C. Livache, J. Qu, Y. Prado, N. Casaretto, N. Goubet, H. Cruguel, L. Dudy, M. G. Silly, G. Vincent, E. Lhuillier, “HgTe Nanocrystals for SWIR Detection and Their Integration up to the Focal Plane Array”, *ACS Applied Materials & Interfaces* 11, 33116–33123 (2019).
12. C. Gréboval, U. Noumbe, N. Goubet, C. Livache, J. Ramade, J. Qu, A. Chu, B. Martinez, Y. Prado, S. Ithurria, A. Ouerghi, H. Aubin, J.F. Dayen, E. Lhuillier, “Field effect transistor and photo transistor of narrow band gap nanocrystal arrays using ionic glasses”, *Nano Letters* (2019).
13. C. Gréboval, E. Izquierdo, C. Livache, B. Martinez, M. Dufour, N. Goubet, N. Moghaddam, J. Qu, A. Chu, J. Ramade, H. Aubin, H. Cruguel, M.G. Silly, E. Lhuillier, S. Ithurria, “Impact of dimensionality and confinement on the electronic properties of mercury chalcogenide nanocrystals”, *Nanoscale* 11, 3905–3915 (2019).
14. B. Martinez, J. Ramade, C. Livache, N. Goubet, A. Chu, C. Gréboval, J. Qu, W. L. Watkins, L. Becerra, E. Dandeu, J.L. Fave, C. Méthivier, E. Lacaze, E. Lhuillier, “HgTe Nanocrystal Inks for Extended Short-Wave Infrared Detection”, *Advanced Optical Materials*, 1900348 (2019).
15. U. N. Noubé, C. Gréboval, C. Livache, T. Brule, B. Doudin, A. Ouerghi, E. Lhuillier, J.F. Dayen, “Ionic Glass-Gated 2D Material-Based Phototransistor: MoSe<sub>2</sub> over LaF<sub>3</sub> as Case Study”, *Advanced Functional Materials*, 1902723 (2019).
16. J. Qu, C. Livache, B. Martinez, C. Gréboval, A. Chu, E. Meriggio, J. Ramade, H. Cruguel, X. Z. Xu, A. Proust, F. Volatron, G. Cabailh, N. Goubet, E. Lhuillier, “Transport in ITO Nanocrystals with Short-to Long-Wave Infrared Absorption for Heavy-Metal-Free Infrared Photodetection”, *ACS Applied Nano Materials* 2, 1621–1630 (2019).
17. D. Pierucci, J. Zribi, C. Livache, C. Gréboval, M. G. Silly, J. Chaste, G. Patriarche, D. Montarnal, E. Lhuillier, A. Ouerghi, B. Mahler, “Evidence for a narrow bandgap phase in 1T’ WS<sub>2</sub> nanosheet”, *Applied Physics Letters* 115, 32102 (2019).
18. S. A. Rezvani, M. Suzuki, P. Malevich, C. Livache, J. V. de Montgolfier, Y. Nomura, N. Tsurumachi, A. Baltuska, T. Fuji, “Millijoule femtosecond pulses at 1937 nm from a diode-pumped ring cavity Tm:YAP regenerative amplifier”, *Optics Express* 26, 29460–29470 (2018).
19. A. Chu, C. Livache, S. Ithurria, E. Lhuillier, “Electronic structure robustness and design rules for 2D colloidal heterostructures”, *Journal of Applied Physics* 123, 035701 (2018).
20. N. Goubet, A. Jagtap, C. Livache, B. Martinez, H. Portalès, X. Z. Xu, R. P. Lobo, B. Dubertret, E. Lhuillier, “Terahertz HgTe nanocrystals: beyond confinement”, *Journal of the American Chemical Society* 140, 5033–5036 (2018).
21. N. Goubet, C. Livache, B. Martinez, X. Z. Xu, S. Ithurria, S. Royer, H. Cruguel, G. Patriarche, A. Ouerghi, M. Silly, B. Dubertret, E. Lhuillier, “Wave-function engineering in HgSe/HgTe colloidal heterostructures to enhance mid-infrared photoconductive properties”, *Nano Letters* 18, 4590–4597 (2018).
22. E. Izquierdo, M. Dufour, A. Chu, C. Livache, B. Martinez, D. Amelot, G. Patriarche, N. Lequeux, E. Lhuillier, S. Ithurria, “Coupled HgSe colloidal quantum wells through a tunable barrier: a strategy to uncouple optical and transport band gap”, *Chemistry of Materials* 30, 4065–4072 (2018).
23. A. Jagtap, C. Livache, B. Martinez, J. Qu, A. Chu, C. Gréboval, N. Goubet, E. Lhuillier, “Emergence of intraband transitions in colloidal nanocrystals”, *Optical Materials Express* 8, 1174–1183 (2018).

24. A. Jagtap, B. Martinez, N. Goubet, A. Chu, C. Livache, C. Gréboval, J. Ramade, D. Amelot, P. Troussset, A. Triboulin, S. Ithurria, M.G. Silly, B. Dubertret, E. Lhuillier, “Design of a unipolar barrier for a nanocrystal-based short-wave infrared photodiode”, *ACS Photonics* 5, 4569–4576 (2018).
25. A. Jagtap, N. Goubet, C. Livache, A. Chu, B. Martinez, C. Gréboval, J. Qu, E. Dandeu, L. Becerra, N. Witkowski, S. Ithurria, F. Mathevet, M. Silly, B. Dubertret, E. Lhuillier, “Short wave infrared devices based on HgTe nanocrystals with air stable performances”, *The Journal of Physical Chemistry C* 122, 14979–14985 (2018).
26. B. Martinez, C. Livache, E. Meriggio, X. Z. Xu, H. Cruguel, E. Lacaze, A. Proust, S. Ithurria, M. G. Silly, G. Cabailh, F. Volatron, E. Lhuillier, “Polyoxometalate as control agent for the doping in HgSe self-doped nanocrystals”, *The Journal of Physical Chemistry C* 122, 26680–26685 (2018).
27. W. J. Mir, C. Livache, N. Goubet, B. Martinez, A. Jagtap, A. Chu, N. Coutard, H. Cruguel, T. Barisien, S. Ithurria, A. Nag, B. Dubertret, A. Ouerghi, M. Silly, E. Lhuillier, “Strategy to overcome recombination limited photocurrent generation in CsPbX<sub>3</sub> nanocrystal arrays”, *Applied Physics Letters* 112, 113503 (2018).
28. J. Qu, N. Goubet, C. Livache, B. Martinez, D. Amelot, C. Gréboval, A. Chu, J. Ramade, H. Cruguel, S. Ithurria, M. Silly, E. Lhuillier, “Intraband mid-infrared transitions in Ag<sub>2</sub>Se nanocrystals: potential and limitations for Hg-Free low-cost photodetection”, *The Journal of Physical Chemistry C* 122, 18161–18167 (2018).
29. H. Cruguel, C. Livache, B. Martinez, S. Pedetti, D. Pierucci, E. Izquierdo, M. Dufour, S. Ithurria, H. Aubin, A. Ouerghi, E. Lacaze, M. Silly, B. Dubertret, E. Lhuillier, “Electronic structure of CdSe-ZnS 2D nanoplatelets”, *Applied Physics Letters* 110, 152103 (2017).
30. B. Martinez, C. Livache, N. Goubet, E. Izquierdo, M. G. Silly, S. Ithurria, E. Lhuillier, “Optoelectronics Using 2D Colloidal Nanocrystals from Wide Band Gap to Narrow Band Gap Materials”, *physica status solidi c* 14, 1700138 (2017).
31. B. Martinez, C. Livache, N. Goubet, A. Jagtap, H. Cruguel, A. Ouerghi, E. Lacaze, M. G. Silly, E. Lhuillier, “Probing Charge Carrier Dynamics to Unveil the Role of Surface Ligands in HgTe Narrow Band Gap Nanocrystals”, *The Journal of Physical Chemistry C* 122, 859–865 (2017).
32. B. Martinez, C. Livache, L. D. Notemgnou Mouafo, N. Goubet, S. Keuleyan, H. Cruguel, S. Ithurria, H. Aubin, A. Ouerghi, B. Doudin, E. Lacaze, B. Dubertret, M. Silly, R.P.S.M. Lobo, J.F. Dayen, E. Lhuillier, “HgSe self-doped nanocrystals as a platform to investigate the effects of vanishing confinement”, *ACS Applied Materials & Interfaces* 9, 36173–36180 (2017).
33. W. J. Mir, A. Assouline, C. Livache, B. Martinez, N. Goubet, X. Z. Xu, G. Patriarche, S. Ithurria, H. Aubin, E. Lhuillier, “Electronic properties of (SbBi)<sub>2</sub>Te<sub>3</sub> colloidal heterostructured nanoplates down to the single particle level”, *Scientific Reports* 7, 9647 (2017).
34. A. Robin, C. Livache, S. Ithurria, E. Lacaze, B. Dubertret, E. Lhuillier, “Surface control of doping in self-doped nanocrystals”, *ACS Applied Materials & Interfaces* 8, 27122–27128 (2016).

## Conference Proceedings

1. B. Martinez, C. Livache, A. Chu, C. Gréboval, H. Cruguel, N. Goubet, E. Lhuillier, "Designing Photovoltaic Devices Using HgTe Nanocrystals for Short and Mid-Wave Infrared Detection", *physica status solidi (a)*, 1900449 (2019).
2. C. Livache, N. Goubet, B. Martinez, E. Izquierdo, C. Gréboval, S. Ithurria, E. Lhuillier, “HgTe, the Most Tunable Colloidal Material: from the Strong Confinement Regime to THz Material”, *MRS Advances* 3, 2913–2921 (2018).

3. C. Livache, B. Martinez, A. Robin, N. Goubet, B. Dubertret, H. Wang, S. Ithurria, H. Aubin, E. Lhuillier, "Investigation of the Self-Doping Process in HgSe Nanocrystals", *physica status solidi (a)* 215, 1700294 (2018).
4. M. Bertille, C. Livache, A. Robin, H. Cruguel, S. Royer, X. Xu, H. Aubin, S. Ithurria, E. Lhuillier, "Intraband transition in self-doped narrow band gap colloidal quantum dots", *SPIE photonic west* (2017).
5. C. Livache, B. Martinez, E. Izquierdo, M. Dufour, H. Cruguel, S. Royer, X. Z. Xu, S. Ithurria, E. Lhuillier, "Shape and confinement control in mid and far infrared nanocrystals", *Quantum Dots and Nanostructures: Growth, Characterization, and Modeling XIV*, Vol. 10114 (International Society for Optics and Photonics, 2017), 101140B.
6. B. Martinez, C. Livache, A. Robin, H. Cruguel, S. Royer, X. Z. Xu, H. Aubin, S. Ithurria, E. Lhuillier, "Intraband transition in self-doped narrow band gap colloidal quantum dots", *Quantum Sensing and Nano Electronics and Photonics XIV*, Vol. 10111 (International Society for Optics and Photonics, 2017), 101112S.

## Patent

- E. Lhuillier, N. Goubet, A. Jagtap, C. Livache, Y. P. Lin, "Nanocristaux dans le domaine Terahertz, infrarouge lointain, matériau hétérostructuré pourvu d'une caractéristique d'absorption intrabande et utilisations correspondantes" WO 2019/068814 A1

# References

- [1] G.-É. L. T. d. B. Du Châtelet, *Dissertation sur la nature et la propagation du feu*. 1744 (cit. on p. xi).
- [2] W. Herschel, “Experiments on the Refrangibility of the Invisible Rays of the Sun. By William Herschel, LL. D. F. R. S.”, *Philosophical Transactions of the Royal Society of London*, vol. 90, pp. 284–292, 1800 (cit. on p. xi).
- [3] S. P. Langley, “The Bolometer and Radiant Energy”, *Proceedings of the American Academy of Arts and Sciences*, vol. 16, pp. 342–358, 1880 (cit. on p. xi).
- [4] E. A. Newman and P. H. Hartline, “Integration of visual and infrared information in bimodal neurons in the rattlesnake optic tectum”, *Science*, vol. 213, no. 4509, pp. 789–791, 1981 (cit. on p. xi).
- [5] A. Rose, *Concepts in photoconductivity and allied problems*. London, UK: Interscience Publishers, 1963 (cit. on pp. xi, 25).
- [6] L. Esaki, “Long Journey into Tunneling”, *Science*, vol. 183, no. 4130, pp. 1149–1155, 1974 (cit. on pp. xi, 5).
- [7] C. B. Murray, D. J. Norris, and M. G. Bawendi, “Synthesis and characterization of nearly monodisperse CdE (E = sulfur, selenium, tellurium) semiconductor nanocrystallites”, *Journal of the American Chemical Society*, vol. 115, no. 19, pp. 8706–8715, 1993 (cit. on pp. xi, 5, 7).
- [8] E. H. Sargent, “Colloidal quantum dot solar cells”, *Nature Photonics*, no. 6, pp. 133–135, 2012 (cit. on p. 2).
- [9] V. Rinnerbauer, K. Hingerl, M. Kovalenko, and W. Heiss, “Effect of quantum confinement on higher transitions in HgTe nanocrystals”, *Applied Physics Letters*, vol. 89, no. 19, p. 193114, 2006 (cit. on p. 2).
- [10] L. I. Berger, *Semiconductor Materials*. CRC Press, 1996, 488 pp. (cit. on p. 2).
- [11] A. L. Efros and A. L. Efros, “Interband Absorption of Light in a Semiconductor Sphere”, *Soviet Physics Semiconductors*, vol. 16, no. 7, pp. 772–775, 1982 (cit. on p. 3).
- [12] L. E. Brus, “Electron–electron and electron-hole interactions in small semiconductor crystallites: The size dependence of the lowest excited electronic state”, *The Journal of Chemical Physics*, vol. 80, no. 9, pp. 4403–4409, 1984 (cit. on p. 4).
- [13] W. L. Wilson, P. F. Szajowski, and L. E. Brus, “Quantum Confinement in Size-Selected, Surface-Oxidized Silicon Nanocrystals”, *Science*, vol. 262, no. 5137, pp. 1242–1244, 1993 (cit. on p. 4).
- [14] P. Harrison, *Quantum Wells, Wires and Dots*, 2nd. Hoboken, NJ: Wiley, 2005 (cit. on pp. 5, 82).
- [15] M. A. Reed, J. N. Randall, R. J. Aggarwal, R. J. Matyi, T. M. Moore, and A. E. Wetsel, “Observation of discrete electronic states in a zero-dimensional semiconductor nanostructure”, *Physical Review Letters*, vol. 60, no. 6, pp. 535–537, 1988 (cit. on p. 5).
- [16] V. A. Shchukin, N. N. Ledentsov, P. S. Kop’ev, and D. Bimberg, “Spontaneous Ordering of Arrays of Coherent Strained Islands”, *Physical Review Letters*, vol. 75, no. 16, pp. 2968–2971, 1995 (cit. on p. 5).
- [17] J. M. Pietryga, Y.-S. Park, J. Lim, A. F. Fidler, W. K. Bae, S. Brovelli, and V. I. Klimov, “Spectroscopic and Device Aspects of Nanocrystal Quantum Dots”, *Chemical Reviews*, vol. 116, no. 18, pp. 10513–10622, 2016 (cit. on pp. 6, 9, 11, 12, 43, 64).

- [18] D. V. Talapin, S. K. Poznyak, N. P. Gaponik, A. L. Rogach, and A. Eychmüller, “Synthesis of surface-modified colloidal semiconductor nanocrystals and study of photoinduced charge separation and transport in nanocrystal-polymer composites”, *Physica E: Low-dimensional Systems and Nanostructures*, vol. 14, no. 1, pp. 237–241, 2002 (cit. on p. 6).
- [19] M. A. Boles, D. Ling, T. Hyeon, and D. V. Talapin, “The surface science of nanocrystals”, *Nature Materials*, vol. 15, no. 2, pp. 141–153, 2016 (cit. on p. 7).
- [20] M. Nirmal, D. J. Norris, M. Kuno, M. G. Bawendi, A. L. Efros, and M. Rosen, “Observation of the “Dark Exciton” in CdSe Quantum Dots”, *Physical Review Letters*, vol. 75, no. 20, pp. 3728–3731, 1995 (cit. on p. 7).
- [21] I. Moreels, Y. Justo, B. De Geyter, K. Haestraete, J. C. Martins, and Z. Hens, “Size-Tunable, Bright, and Stable PbS Quantum Dots: A Surface Chemistry Study”, *ACS Nano*, vol. 5, no. 3, pp. 2004–2012, 2011 (cit. on p. 7).
- [22] M. A. Hines and P. Guyot-Sionnest, “Bright UV-Blue Luminescent Colloidal ZnSe Nanocrystals”, *The Journal of Physical Chemistry B*, vol. 102, no. 19, pp. 3655–3657, 1998 (cit. on p. 7).
- [23] A. L. Rogach, S. V. Kershaw, M. Burt, M. T. Harrison, A. Kornowski, A. Eychmüller, and H. Weller, “Colloidally Prepared HgTe Nanocrystals with Strong Room-Temperature Infrared Luminescence”, *Advanced Materials*, vol. 11, no. 7, pp. 552–555, 1999 (cit. on pp. 7, 34).
- [24] M. V. Kovalenko, E. Kaufmann, D. Pachinger, J. Roither, M. Huber, J. Stangl, G. Hesser, F. Schäffler, and W. Heiss, “Colloidal HgTe Nanocrystals with Widely Tunable Narrow Band Gap Energies: From Telecommunications to Molecular Vibrations”, *Journal of the American Chemical Society*, vol. 128, no. 11, pp. 3516–3517, 2006 (cit. on pp. 7, 34).
- [25] L. Liu, Q. Wu, Y. Ding, H. Liu, and B. Zhang, “Synthesis of HgSe quantum dots through templates controlling and gas-liquid transport with emulsion liquid membrane system”, *Colloids and Surfaces A: Physicochemical and Engineering Aspects*, vol. 240, no. 1–3, pp. 135–139, 2004 (cit. on p. 7).
- [26] P. Howes, M. Green, C. Johnston, and A. Crossley, “Synthesis and shape control of mercury selenide (HgSe) quantum dots”, *Journal of Materials Chemistry*, vol. 18, no. 29, pp. 3474–3480, 2008 (cit. on p. 7).
- [27] S. Keuleyan, E. Lhuillier, and P. Guyot-Sionnest, “Synthesis of Colloidal HgTe Quantum Dots for Narrow Mid-IR Emission and Detection”, *Journal of the American Chemical Society*, vol. 133, no. 41, pp. 16 422–16 424, 2011 (cit. on pp. 7, 34, 35, 38).
- [28] M. Green and H. Mirzai, “Synthetic routes to mercury chalcogenide quantum dots”, *Journal of Materials Chemistry C*, vol. 6, no. 19, pp. 5097–5112, 2018 (cit. on p. 7).
- [29] M. A. Hines and P. Guyot-Sionnest, “Synthesis and Characterization of Strongly Luminescing ZnS-Capped CdSe Nanocrystals”, *The Journal of Physical Chemistry*, vol. 100, no. 2, pp. 468–471, 1996 (cit. on pp. 7, 13).
- [30] W. Lu, J. Fang, K. L. Stokes, and J. Lin, “Shape Evolution and Self Assembly of Monodisperse PbTe Nanocrystals”, *Journal of the American Chemical Society*, vol. 126, no. 38, pp. 11 798–11 799, 2004 (cit. on p. 7).
- [31] G. H. Carey, A. L. Abdelhady, Z. Ning, S. M. Thon, O. M. Bakr, and E. H. Sargent, “Colloidal Quantum Dot Solar Cells”, *Chemical Reviews*, vol. 115, no. 23, pp. 12 732–12 763, 2015 (cit. on p. 7).
- [32] P. Reiss, M. Carrière, C. Lincheneau, L. Vaure, and S. Tamang, “Synthesis of Semiconductor Nanocrystals, Focusing on Nontoxic and Earth-Abundant Materials”, *Chemical Reviews*, vol. 116, no. 18, pp. 10 731–10 819, 2016 (cit. on p. 7).
- [33] M. A. Malik, P. O’Brien, and N. Revaprasadu, “A Novel Route for the Preparation of CuSe and CuInSe<sub>2</sub> Nanoparticles”, *Advanced Materials*, vol. 11, no. 17, pp. 1441–1444, 1999 (cit. on p. 7).

- [34] P. M. Allen and M. G. Bawendi, “Ternary I-III-VI Quantum Dots Luminescent in the Red to Near-Infrared”, *Journal of the American Chemical Society*, vol. 130, no. 29, pp. 9240–9241, 2008 (cit. on p. 7).
- [35] H. McDaniel, N. Fuke, J. M. Pietryga, and V. I. Klimov, “Engineered CuInSexS<sub>2-x</sub> Quantum Dots for Sensitized Solar Cells”, *The Journal of Physical Chemistry Letters*, vol. 4, no. 3, pp. 355–361, 2013 (cit. on p. 7).
- [36] J. Joo, J. S. Son, S. G. Kwon, J. H. Yu, and T. Hyeon, “Low-Temperature Solution-Phase Synthesis of Quantum Well Structured CdSe Nanoribbons”, *Journal of the American Chemical Society*, vol. 128, no. 17, pp. 5632–5633, 2006 (cit. on p. 8).
- [37] S. Ithurria and B. Dubertret, “Quasi 2D Colloidal CdSe Platelets with Thicknesses Controlled at the Atomic Level”, *Journal of the American Chemical Society*, vol. 130, no. 49, pp. 16 504–16 505, 2008 (cit. on p. 8).
- [38] S. Ithurria, M. D. Tessier, B. Mahler, R. P. S. M. Lobo, B. Dubertret, and A. L. Efros, “Colloidal nanoplatelets with two-dimensional electronic structure”, *Nature Materials*, vol. 10, no. 12, pp. 936–941, 2011 (cit. on p. 8).
- [39] M. Nasilowski, B. Mahler, E. Lhuillier, S. Ithurria, and B. Dubertret, “Two-Dimensional Colloidal Nanocrystals”, *Chemical Reviews*, vol. 116, no. 18, pp. 10 934–10 982, 2016 (cit. on pp. 8, 13, 14).
- [40] M. D. Tessier, C. Javaux, I. Maksimovic, V. Lorient, and B. Dubertret, “Spectroscopy of Single CdSe Nanoplatelets”, *ACS Nano*, vol. 6, no. 8, pp. 6751–6758, 2012 (cit. on p. 8).
- [41] Y. V. Vandyshev, V. S. Dneprovskii, V. I. Klimov, and D. K. Okorokov, “Lasing on a transition between quantum-well levels in a quantum dot”, *ZhETF Pisma Redaktsiiu*, vol. 54, p. 441, 1991 (cit. on p. 9).
- [42] H.-J. Eisler, V. C. Sundar, M. G. Bawendi, M. Walsh, H. I. Smith, and V. Klimov, “Color-selective semiconductor nanocrystal laser”, *Applied Physics Letters*, vol. 80, no. 24, pp. 4614–4616, 2002 (cit. on p. 9).
- [43] I. Moreels, G. Rainò, R. Gomes, Z. Hens, T. Stöferle, and R. F. Mahrt, “Nearly Temperature-Independent Threshold for Amplified Spontaneous Emission in Colloidal CdSe/CdS Quantum Dot-in-Rods”, *Advanced Materials*, vol. 24, no. 35, OP231–OP235, 2012 (cit. on p. 9).
- [44] F. Fan, O. Voznyy, R. P. Sabatini, K. T. Bicanic, M. M. Adachi, J. R. McBride, K. R. Reid, Y.-S. Park, X. Li, A. Jain, R. Quintero-Bermudez, M. Saravanapavanantham, M. Liu, M. Korkusinski, P. Hawrylak, V. I. Klimov, S. J. Rosenthal, S. Hoogland, and E. H. Sargent, “Continuous-wave lasing in colloidal quantum dot solids enabled by facet-selective epitaxy”, *Nature*, vol. 544, no. 7648, pp. 75–79, 2017 (cit. on pp. 9, 13).
- [45] P. Geiregat, A. J. Houtepen, L. K. Sagar, I. Infante, F. Zapata, V. Grigel, G. Allan, C. Delerue, D. Van Thourhout, and Z. Hens, “Continuous-wave infrared optical gain and amplified spontaneous emission at ultralow threshold by colloidal HgTe quantum dots”, *Nature Materials*, vol. 17, no. 1, pp. 35–42, 2018 (cit. on pp. 9, 35).
- [46] J. M. Caruge, J. E. Halpert, V. Wood, V. Bulović, and M. G. Bawendi, “Colloidal quantum-dot light-emitting diodes with metal-oxide charge transport layers”, *Nature Photonics*, vol. 2, no. 4, pp. 247–250, 2008 (cit. on p. 9).
- [47] V. Wood and V. Bulović, “Colloidal quantum dot light-emitting devices”, *Nano Reviews*, vol. 1, no. 1, p. 5202, 2010 (cit. on p. 9).
- [48] E. Jang, S. Jun, H. Jang, J. Lim, B. Kim, and Y. Kim, “White-Light-Emitting Diodes with Quantum Dot Color Converters for Display Backlights”, *Advanced Materials*, vol. 22, no. 28, pp. 3076–3080, 2010 (cit. on p. 9).
- [49] X. Gong, Z. Yang, G. Walters, R. Comin, Z. Ning, E. Beauregard, V. Adinolfi, O. Voznyy, and E. H. Sargent, “Highly efficient quantum dot near-infrared light-emitting diodes”, *Nature Photonics*, vol. 10, no. 4, pp. 253–257, 2016 (cit. on pp. 9, 116).

- [50] V. Wood, M. J. Panzer, J. Chen, M. S. Bradley, J. E. Halpert, M. G. Bawendi, and V. Bulović, “Inkjet-Printed Quantum Dot–Polymer Composites for Full-Color AC-Driven Displays”, *Advanced Materials*, vol. 21, no. 21, pp. 2151–2155, 2009 (cit. on p. 9).
- [51] B. Guzelturk, Y. Kelestemur, M. Olutas, S. Delikanli, and H. V. Demir, “Amplified Spontaneous Emission and Lasing in Colloidal Nanoplatelets”, *ACS Nano*, vol. 8, no. 7, pp. 6599–6605, 2014 (cit. on p. 9).
- [52] C. She, I. Fedin, D. S. Dolzhenkov, A. Demortière, R. D. Schaller, M. Pelton, and D. V. Talapin, “Low-Threshold Stimulated Emission Using Colloidal Quantum Wells”, *Nano Letters*, vol. 14, no. 5, pp. 2772–2777, 2014 (cit. on p. 9).
- [53] J. Q. Grim, S. Christodoulou, F. Di Stasio, R. Krahn, R. Cingolani, L. Manna, and I. Moreels, “Continuous-wave biexciton lasing at room temperature using solution-processed quantum wells”, *Nature Nanotechnology*, vol. 9, no. 11, pp. 891–895, 2014 (cit. on p. 9).
- [54] M. Dufour, E. Izquierdo, C. Livache, B. Martinez, M. G. Silly, T. Pons, E. Lhuillier, C. Delerue, and S. Ithurria, “Doping as Strategy to Tune Color of 2D colloidal Nanoplatelets”, *ACS Applied Materials & Interfaces*, 2019 (cit. on p. 9).
- [55] A. H. Khan, V. Pinchetti, I. Tanghe, Z. Dang, B. Martín-García, Z. Hens, D. Van Thourhout, P. Geiregat, S. Brovelli, and I. Moreels, “Tunable and Efficient Red to Near-Infrared Photoluminescence by Synergistic Exploitation of Core and Surface Silver Doping of CdSe Nanoplatelets”, *Chemistry of Materials*, 2019 (cit. on p. 9).
- [56] E. Izquierdo, A. Robin, S. Keuleyan, N. Lequeux, E. Lhuillier, and S. Ithurria, “Strongly confined HgTe 2D nanoplatelets as narrow near infrared emitters”, *Journal of the American Chemical Society*, vol. 138, no. 33, pp. 10 496–10 501, 2016 (cit. on pp. 9, 11, 20, 36, 45).
- [57] V. I. Klimov, A. A. Mikhailovsky, D. W. McBranch, C. A. Leatherdale, and M. G. Bawendi, “Quantization of Multiparticle Auger Rates in Semiconductor Quantum Dots”, *Science*, vol. 287, no. 5455, pp. 1011–1013, 2000 (cit. on p. 11).
- [58] A. A. Bakulin, S. Neutzner, H. J. Bakker, L. Ottaviani, D. Barakel, and Z. Chen, “Charge Trapping Dynamics in PbS Colloidal Quantum Dot Photovoltaic Devices”, *ACS Nano*, vol. 7, no. 10, pp. 8771–8779, 2013 (cit. on p. 11).
- [59] A. Jain, O. Voznyy, M. Korkusinski, P. Hawrylak, and E. H. Sargent, “Ultrafast Carrier Trapping in Thick-Shell Colloidal Quantum Dots”, *The Journal of Physical Chemistry Letters*, vol. 8, no. 14, pp. 3179–3184, 2017 (cit. on p. 11).
- [60] N. Taghipour, P. L. Hernandez Martinez, A. Ozden, M. Olutas, D. Dede, K. Gungor, O. Erdem, N. K. Perkgoz, and H. V. Demir, “Near-Unity Efficiency Energy Transfer from Colloidal Semiconductor Quantum Wells of CdSe/CdS Nanoplatelets to a Monolayer of MoS<sub>2</sub>”, *ACS Nano*, 2018 (cit. on p. 11).
- [61] Y.-S. Park, W. K. Bae, J. M. Pietryga, and V. I. Klimov, “Auger Recombination of Biexcitons and Negative and Positive Trions in Individual Quantum Dots”, *ACS Nano*, vol. 8, no. 7, pp. 7288–7296, 2014 (cit. on p. 11).
- [62] C. Melnychuk and P. Guyot-Sionnest, “Slow Auger Relaxation in HgTe Colloidal Quantum Dots”, *The Journal of Physical Chemistry Letters*, vol. 9, no. 9, pp. 2208–2211, 2018 (cit. on pp. 11, 70).
- [63] B. O. Dabbousi, J. Rodriguez-Viejo, F. V. Mikulec, J. R. Heine, H. Mattoussi, R. Ober, K. F. Jensen, and M. G. Bawendi, “(CdSe)/ZnS Core-Shell Quantum Dots: Synthesis and Characterization of a Size Series of Highly Luminescent Nanocrystallites”, *The Journal of Physical Chemistry B*, vol. 101, no. 46, pp. 9463–9475, 1997 (cit. on p. 13).
- [64] Y. Justo, P. Geiregat, K. van Hoecke, F. Vanhaecke, C. De Mello Donega, and Z. Hens, “Optical Properties of PbS/CdS Core/Shell Quantum Dots”, *The Journal of Physical Chemistry C*, vol. 117, no. 39, pp. 20 171–20 177, 2013 (cit. on p. 13).

- [65] L. K. Sagar, W. Walravens, Q. Zhao, A. Vantomme, P. Geiregat, and Z. Hens, “PbS/CdS Core/Shell Quantum Dots by Additive, Layer-by-Layer Shell Growth”, *Chemistry of Materials*, vol. 28, no. 19, pp. 6953–6959, 2016 (cit. on p. 13).
- [66] L. K. Sagar, W. Walravens, J. Maes, P. Geiregat, and Z. Hens, “HgSe/CdE (E = S, Se) Core/Shell Nanocrystals by Colloidal Atomic Layer Deposition”, *The Journal of Physical Chemistry C*, vol. 121, no. 25, pp. 13 816–13 822, 2017 (cit. on pp. 13, 81, 96).
- [67] Z. Deng and P. Guyot-Sionnest, “Intraband Luminescence from HgSe/CdS Core/Shell Quantum Dots”, *ACS Nano*, vol. 10, no. 2, pp. 2121–2127, 2016 (cit. on pp. 13, 81).
- [68] H. S. Zhou, I. Honma, H. Komiyama, and J. W. Haus, “Coated semiconductor nanoparticles: The cadmium sulfide/lead sulfide system’s synthesis and properties”, *The Journal of Physical Chemistry*, vol. 97, no. 4, pp. 895–901, 1993 (cit. on p. 13).
- [69] S. Kim, B. Fisher, H.-J. Eisler, and M. Bawendi, “Type-II Quantum Dots: CdTe/CdSe(Core/Shell) and CdSe/ZnTe(Core/Shell) Heterostructures”, *Journal of the American Chemical Society*, vol. 125, no. 38, pp. 11 466–11 467, 2003 (cit. on p. 13).
- [70] S. A. Ivanov, A. Piryatinski, J. Nanda, S. Tretiak, K. R. Zavadil, W. O. Wallace, D. Werder, and V. I. Klimov, “Type-II core/shell CdS/ZnSe nanocrystals: Synthesis, electronic structures, and spectroscopic properties”, *Journal of the American Chemical Society*, vol. 129, no. 38, pp. 11 708–11 719, 2007 (cit. on p. 13).
- [71] E. Lifshitz, M. Brumer, A. Kigel, A. Sashchiuk, M. Bashouti, M. Sirota, E. Galun, Z. Burshtein, A. Q. Le Quang, I. Ledoux-Rak, and J. Zyss, “Air-Stable PbSe/PbS and PbSe/PbSexS1-x Core-Shell Nanocrystal Quantum Dots and Their Applications”, *The Journal of Physical Chemistry B*, vol. 110, no. 50, pp. 25 356–25 365, 2006 (cit. on p. 13).
- [72] A. C. Bartnik, F. W. Wise, A. Kigel, and E. Lifshitz, “Electronic structure of PbSe/PbS core-shell quantum dots”, *Physical Review B*, vol. 75, no. 24, p. 245 424, 2007 (cit. on p. 13).
- [73] X. Peng, M. C. Schlamp, A. V. Kadavanich, and A. P. Alivisatos, “Epitaxial Growth of Highly Luminescent CdSe/CdS Core/Shell Nanocrystals with Photostability and Electronic Accessibility”, *Journal of the American Chemical Society*, vol. 119, no. 30, pp. 7019–7029, 1997 (cit. on p. 13).
- [74] C.-Y. Chen, C.-T. Cheng, C.-W. Lai, Y.-H. Hu, P.-T. Chou, Y.-H. Chou, and H.-T. Chiu, “Type-II CdSe/CdTe/ZnTe (core-shell-shell) quantum dots with cascade band edges: The separation of electron (at CdSe) and hole (at ZnTe) by the CdTe layer”, *Small (Weinheim an Der Bergstrasse, Germany)*, vol. 1, no. 12, pp. 1215–1220, 2005 (cit. on p. 13).
- [75] T. Franzl, T. A. Klar, S. Schietinger, A. L. Rogach, and J. Feldmann, “Exciton Recycling in Graded Gap Nanocrystal Structures”, *Nano Letters*, vol. 4, no. 9, pp. 1599–1603, 2004 (cit. on p. 13).
- [76] D. Choi, B. Yoon, D.-K. Kim, H. Baik, J.-H. Choi, and K. S. Jeong, “Major Electronic Transition Shift from Bandgap to Localized Surface Plasmon Resonance in CdxHg1-xSe Alloy Nanocrystals”, *Chemistry of Materials*, vol. 29, no. 19, pp. 8548–8554, 2017 (cit. on p. 13).
- [77] Y. Gao, M. Li, S. Delikanli, H. Zheng, B. Liu, C. Dang, T. C. Sum, and H. V. Demir, “Low-threshold lasing from colloidal CdSe/CdSeTe core/alloyed-crown type-II heteronano-platelets”, *Nanoscale*, 2018 (cit. on p. 13).
- [78] Y.-S. Park, J. Lim, and V. I. Klimov, “Asymmetrically strained quantum dots with non-fluctuating single-dot emission spectra and subthermal room-temperature linewidths”, *Nature Materials*, p. 1, 2019 (cit. on p. 13).
- [79] P. T. K. Chin, C. de Mello Donegá, S. S. van Bavel, S. C. J. Meskers, N. A. J. M. Sommerdijk, and R. A. J. Janssen, “Highly Luminescent CdTe/CdSe Colloidal Heteronano-crystals with Temperature-Dependent Emission Color”, *Journal of the American Chemical Society*, vol. 129, no. 48, pp. 14 880–14 886, 2007 (cit. on p. 13).

- [80] B. Mahler, B. Nadal, C. Bouet, G. Patriarche, and B. Dubertret, “Core/Shell Colloidal Semiconductor Nanoplatelets”, *Journal of the American Chemical Society*, vol. 134, no. 45, pp. 18 591–18 598, 2012 (cit. on p. 14).
- [81] P. Guyot-Sionnest, “Electrical Transport in Colloidal Quantum Dot Films”, *The Journal of Physical Chemistry Letters*, vol. 3, no. 9, pp. 1169–1175, 2012 (cit. on pp. 15, 116).
- [82] N. F. Mott, “Conduction in Non-Crystalline Materials”, *Philosophical Magazine*, vol. 19, no. 160, pp. 835–852, 1969 (cit. on p. 16).
- [83] A. L. Efros and B. I. Shklovskii, “Coulomb gap and low temperature conductivity of disordered systems”, *Journal of Physics C: Solid State Physics*, vol. 8, no. 4, pp. L49–L51, 1975 (cit. on p. 16).
- [84] D. Yu, C. Wang, B. L. Wehrenberg, and P. Guyot-Sionnest, “Variable Range Hopping Conduction in Semiconductor Nanocrystal Solids”, *Physical Review Letters*, vol. 92, no. 21, p. 216 802, 2004 (cit. on p. 16).
- [85] N. Y. Morgan, C. A. Leatherdale, M. Drndić, M. V. Jarosz, M. A. Kastner, and M. Bawendi, “Electronic transport in films of colloidal CdSe nanocrystals”, *Physical Review B*, vol. 66, no. 7, p. 075 339, 2002 (cit. on p. 16).
- [86] M. V. Jarosz, V. J. Porter, B. R. Fisher, M. A. Kastner, and M. G. Bawendi, “Photoconductivity studies of treated CdSe quantum dot films exhibiting increased exciton ionization efficiency”, *Physical Review B*, vol. 70, no. 19, p. 195 327, 2004 (cit. on p. 16).
- [87] D. Yu, C. Wang, and P. Guyot-Sionnest, “N-Type Conducting CdSe Nanocrystal Solids”, *Science*, vol. 300, no. 5623, pp. 1277–1280, 2003 (cit. on p. 17).
- [88] D. V. Talapin and C. B. Murray, “PbSe Nanocrystal Solids for n- and p-Channel Thin Film Field-Effect Transistors”, *Science*, vol. 310, no. 5745, pp. 86–89, 2005 (cit. on p. 17).
- [89] Y. Liu, M. Gibbs, J. Puthussery, S. Gaik, R. Ihly, H. W. Hillhouse, and M. Law, “Dependence of Carrier Mobility on Nanocrystal Size and Ligand Length in PbSe Nanocrystal Solids”, *Nano Letters*, vol. 10, no. 5, pp. 1960–1969, 2010 (cit. on pp. 17, 18).
- [90] D. V. Talapin, J.-S. Lee, M. V. Kovalenko, and E. V. Shevchenko, “Prospects of Colloidal Nanocrystals for Electronic and Optoelectronic Applications”, *Chemical Reviews*, vol. 110, no. 1, pp. 389–458, 2010 (cit. on p. 17).
- [91] M. V. Kovalenko, M. Scheele, and D. V. Talapin, “Colloidal Nanocrystals with Molecular Metal Chalcogenide Surface Ligands”, *Science*, vol. 324, no. 5933, pp. 1417–1420, 2009 (cit. on p. 17).
- [92] A. Nag, D. S. Chung, D. S. Dolzhenkov, N. M. Dimitrijevic, S. Chattopadhyay, T. Shibata, and D. V. Talapin, “Effect of Metal Ions on Photoluminescence, Charge Transport, Magnetic and Catalytic Properties of All-Inorganic Colloidal Nanocrystals and Nanocrystal Solids”, *Journal of the American Chemical Society*, vol. 134, no. 33, pp. 13 604–13 615, 2012 (cit. on p. 17).
- [93] A. Nag, M. V. Kovalenko, J.-S. Lee, W. Liu, B. Spokoyny, and D. V. Talapin, “Metal-free Inorganic Ligands for Colloidal Nanocrystals: S<sup>2-</sup>, HS<sup>-</sup>, Se<sup>2-</sup>, HSe<sup>-</sup>, Te<sup>2-</sup>, HTe<sup>-</sup>, TeS<sub>3</sub><sup>2-</sup>, OH<sup>-</sup>, and NH<sub>2</sub><sup>-</sup> as Surface Ligands”, *Journal of the American Chemical Society*, vol. 133, no. 27, pp. 10 612–10 620, 2011 (cit. on pp. 17, 18).
- [94] A. T. Fafarman, W.-k. Koh, B. T. Diroll, D. K. Kim, D.-K. Ko, S. J. Oh, X. Ye, V. Doan-Nguyen, M. R. Crump, D. C. Reifsnyder, C. B. Murray, and C. R. Kagan, “Thiocyanate-Capped Nanocrystal Colloids: Vibrational Reporter of Surface Chemistry and Solution-Based Route to Enhanced Coupling in Nanocrystal Solids”, *Journal of the American Chemical Society*, vol. 133, no. 39, pp. 15 753–15 761, 2011 (cit. on p. 17).
- [95] J. Tang, K. W. Kemp, S. Hoogland, K. S. Jeong, H. Liu, L. Levina, M. Furukawa, X. Wang, R. Debnath, D. Cha, K. W. Chou, A. Fischer, A. Amassian, J. B. Asbury, and E. H. Sargent, “Colloidal-quantum-dot photovoltaics using atomic-ligand passivation”, *Nature Materials*, vol. 10, no. 10, p. 765, 2011 (cit. on pp. 17, 105).

- [96] A. H. Ip, S. M. Thon, S. Hoogland, O. Voznyy, D. Zhitomirsky, R. Debnath, L. Levina, L. R. Rollny, G. H. Carey, A. Fischer, K. W. Kemp, I. J. Kramer, Z. Ning, A. J. Labelle, K. W. Chou, A. Amassian, and E. H. Sargent, “Hybrid passivated colloidal quantum dot solids”, *Nature Nanotechnology*, vol. 7, no. 9, p. 577, 2012 (cit. on p. 18).
- [97] G. H. Carey, L. Levina, R. Comin, O. Voznyy, and E. H. Sargent, “Record Charge Carrier Diffusion Length in Colloidal Quantum Dot Solids via Mutual Dot-To-Dot Surface Passivation”, *Advanced Materials*, vol. 27, no. 21, pp. 3325–3330, 2015 (cit. on p. 18).
- [98] X. Lan, O. Voznyy, A. Kiani, F. P. García de Arquer, A. S. Abbas, G.-H. Kim, M. Liu, Z. Yang, G. Walters, J. Xu, M. Yuan, Z. Ning, F. Fan, P. Kanjanaboos, I. Kramer, D. Zhitomirsky, P. Lee, A. Perelgut, S. Hoogland, and E. H. Sargent, “Passivation Using Molecular Halides Increases Quantum Dot Solar Cell Performance”, *Advanced Materials*, vol. 28, no. 2, pp. 299–304, 2016 (cit. on p. 18).
- [99] B. Sun, O. Voznyy, H. Tan, P. Stadler, M. Liu, G. Walters, A. H. Proppe, M. Liu, J. Fan, T. Zhuang, J. Li, M. Wei, J. Xu, Y. Kim, S. Hoogland, and E. H. Sargent, “Pseudohalide-Exchanged Quantum Dot Solids Achieve Record Quantum Efficiency in Infrared Photovoltaics”, *Advanced Materials*, vol. 29, no. 27, n/a–n/a, 2017 (cit. on p. 18).
- [100] J. Jang, D. S. Dolzhenkov, W. Liu, S. Nam, M. Shim, and D. V. Talapin, “Solution-Processed Transistors Using Colloidal Nanocrystals with Composition-Matched Molecular “Solders”: Approaching Single Crystal Mobility”, *Nano Letters*, vol. 15, no. 10, pp. 6309–6317, 2015 (cit. on p. 18).
- [101] J. Jang, W. Liu, J. S. Son, and D. V. Talapin, “Temperature-dependent Hall and field-effect mobility in strongly coupled all-inorganic nanocrystal arrays”, *Nano Letters*, vol. 14, no. 2, pp. 653–662, 2014 (cit. on p. 19).
- [102] S. J. Oh, N. E. Berry, J.-H. Choi, E. A. Gaulding, T. Paik, S.-H. Hong, C. B. Murray, and C. R. Kagan, “Stoichiometric Control of Lead Chalcogenide Nanocrystal Solids to Enhance Their Electronic and Optoelectronic Device Performance”, *ACS Nano*, vol. 7, no. 3, pp. 2413–2421, 2013 (cit. on p. 19).
- [103] S. H. Kim, K. Hong, W. Xie, K. H. Lee, S. Zhang, T. P. Lodge, and C. D. Frisbie, “Electrolyte-Gated Transistors for Organic and Printed Electronics”, *Advanced Materials*, vol. 25, no. 13, pp. 1822–1846, 2013 (cit. on p. 19).
- [104] E. Lhuillier, A. Robin, S. Ithurria, H. Aubin, and B. Dubertret, “Electrolyte-Gated Colloidal Nanoplatelets-Based Phototransistor and Its Use for Bicolor Detection”, *Nano Letters*, vol. 14, no. 5, pp. 2715–2719, 2014 (cit. on pp. 19, 40).
- [105] E. Lhuillier, S. Pedetti, S. Ithurria, H. Heuclin, B. Nadal, A. Robin, G. Patriarche, N. Lequeux, and B. Dubertret, “Electrolyte-Gated Field Effect Transistor to Probe the Surface Defects and Morphology in Films of Thick CdSe Colloidal Nanoplatelets”, *ACS Nano*, vol. 8, no. 4, pp. 3813–3820, 2014 (cit. on p. 19).
- [106] E. Lhuillier, S. Ithurria, A. Descamps-Mandine, T. Douillard, R. Castaing, X. Z. Xu, P.-L. Taberna, P. Simon, H. Aubin, and B. Dubertret, “Investigating the n- and p-Type Electrolytic Charging of Colloidal Nanoplatelets”, *The Journal of Physical Chemistry C*, vol. 119, no. 38, pp. 21 795–21 799, 2015 (cit. on pp. 19, 50).
- [107] C. Livache, E. Izquierdo, B. Martinez, M. Dufour, D. Pierucci, S. Keuleyan, H. Cruguel, L. Becerra, J. L. Fave, H. Aubin, A. Ouerghi, E. Lacaze, M. G. Silly, B. Dubertret, S. Ithurria, and E. Lhuillier, “Charge Dynamics and Optoelectronic Properties in HgTe Colloidal Quantum Wells”, *Nano Letters*, vol. 17, no. 7, pp. 4067–4074, 2017 (cit. on pp. 20, 24, 25).
- [108] T. Chen, K. V. Reich, N. J. Kramer, H. Fu, U. R. Kortshagen, and B. I. Shklovskii, “Metal-insulator transition in films of doped semiconductor nanocrystals”, *Nature Materials*, vol. 15, no. 3, pp. 299–303, 2016 (cit. on p. 21).

- [109] B. Martinez, C. Livache, L. D. Notemgnou Mouafo, N. Goubet, S. Keuleyan, H. Cruguel, S. Ithurria, H. Aubin, A. Ouerghi, B. Doudin, E. Lacaze, B. Dubertret, M. G. Silly, R. P. S. M. Lobo, J.-F. Dayen, and E. Lhuillier, “HgSe Self-Doped Nanocrystals as a Platform to Investigate the Effects of Vanishing Confinement”, *ACS Applied Materials & Interfaces*, vol. 9, no. 41, pp. 36 173–36 180, 2017 (cit. on pp. 21, 37, 76, 83, 88).
- [110] H. Liu, S. Keuleyan, and P. Guyot-Sionnest, “N- and p-Type HgTe Quantum Dot Films”, *The Journal of Physical Chemistry C*, vol. 116, no. 1, pp. 1344–1349, 2012 (cit. on pp. 21, 36).
- [111] M. Chen and P. Guyot-Sionnest, “Reversible Electrochemistry of Mercury Chalcogenide Colloidal Quantum Dot Films”, *ACS Nano*, vol. 11, no. 4, pp. 4165–4173, 2017 (cit. on pp. 21, 82).
- [112] D. Spittel, J. Poppe, C. Meerbach, C. Ziegler, S. G. Hickey, and A. Eychmüller, “Absolute Energy Level Positions in CdSe Nanostructures from Potential-Modulated Absorption Spectroscopy (EMAS)”, *ACS Nano*, 2017 (cit. on p. 21).
- [113] H. Cruguel, C. Livache, B. Martinez, S. Pedetti, D. Pierucci, E. Izquierdo, M. Dufour, S. Ithurria, H. Aubin, A. Ouerghi, E. Lacaze, M. G. Silly, B. Dubertret, and E. Lhuillier, “Electronic structure of CdSe-ZnS 2D nanoplatelets”, *Applied Physics Letters*, vol. 110, no. 15, p. 152 103, 2017 (cit. on pp. 22, 82).
- [114] Rosencher and Vinter, *Optoélectronique*. Paris: Dunod, 2002, 608 pp. (cit. on pp. 24, 26, 27).
- [115] E. Lhuillier, J.-F. Dayen, D. O. Thomas, A. Robin, B. Doudin, and B. Dubertret, “Nanoplatelets Bridging a Nanotrench: A New Architecture for Photodetectors with Increased Sensitivity”, *Nano Letters*, vol. 15, no. 3, pp. 1736–1742, 2015 (cit. on pp. 25, 50, 72).
- [116] H. Wang, E. Lhuillier, Q. Yu, A. Zimmers, B. Dubertret, C. Ulysse, and H. Aubin, “Transport in a Single Self-Doped Nanocrystal”, *ACS Nano*, vol. 11, no. 2, pp. 1222–1229, 2017 (cit. on pp. 25, 37).
- [117] C.-H. M. Chuang, P. R. Brown, V. Bulović, and M. G. Bawendi, “Improved performance and stability in quantum dot solar cells through band alignment engineering”, *Nature Materials*, vol. 13, no. 8, p. 796, 2014 (cit. on pp. 26, 105).
- [118] E. Lhuillier, S. Keuleyan, P. Rekemeyer, and P. Guyot-Sionnest, “Thermal properties of mid-infrared colloidal quantum dot detectors”, *Journal of Applied Physics*, vol. 110, no. 3, p. 033 110, 2011 (cit. on pp. 28, 35, 38, 88).
- [119] H. Liu, E. Lhuillier, and P. Guyot-Sionnest, “1/f noise in semiconductor and metal nanocrystal solids”, *Journal of Applied Physics*, vol. 115, no. 15, p. 154 309, 2014 (cit. on pp. 28, 38, 107).
- [120] Y. Lai, H. Li, D. K. Kim, B. T. Diroll, C. B. Murray, and C. R. Kagan, “Low-Frequency (1/f) Noise in Nanocrystal Field-Effect Transistors”, *ACS Nano*, vol. 8, no. 9, pp. 9664–9672, 2014 (cit. on p. 28).
- [121] A. Rogalski, “Infrared detectors: An overview”, *Infrared Physics and Technology*, vol. 43, pp. 187–210, 2002 (cit. on p. 30).
- [122] A. Rogalski, *Infrared Detectors, Second Edition*. CRC Press, 2010, 900 pp. (cit. on p. 30).
- [123] A. Rogalski, “HgCdTe infrared detector material: History, status and outlook”, *Reports on Progress in Physics*, vol. 68, no. 10, p. 2267, 2005 (cit. on p. 32).
- [124] A. Rogalski, “History of infrared detectors”, *Opto-Electronics Review*, vol. 20, no. 3, pp. 279–308, 2012 (cit. on pp. 32, 81).
- [125] A. Rogalski, “Quantum well photoconductors in infrared detector technology”, *Journal of Applied Physics*, vol. 93, no. 8, pp. 4355–4391, 2003 (cit. on p. 33).
- [126] H. Schneider and H. C. Liu, *Quantum Well Infrared Photodetectors: Physics and Applications*. Springer, 2006, 258 pp. (cit. on pp. 33, 80).
- [127] L. Gendron, M. Carras, A. Huynh, V. Ortiz, C. Koeniguer, and V. Berger, “Quantum cascade photodetector”, *Applied Physics Letters*, vol. 85, no. 14, pp. 2824–2826, 2004 (cit. on p. 33).

- [128] H. C. Liu and F. Capasso, Eds., *Intersubband Transitions in Quantum Wells: Physics and Devices*, Springer US, 1998 (cit. on p. 33).
- [129] A. Rogalski, P. Martyniuk, and M. Kopytko, “InAs/GaSb type-II superlattice infrared detectors: Future prospect”, *Applied Physics Reviews*, vol. 4, no. 3, p. 031 304, 2017 (cit. on p. 33).
- [130] A. Svane, N. E. Christensen, M. Cardona, A. N. Chantis, M. van Schilfhaarde, and T. Kotani, “Quasiparticle band structures of beta-HgS, HgSe, and HgTe”, *Physical Review B*, vol. 84, no. 20, p. 205 205, 2011 (cit. on p. 34).
- [131] N. Goubet, A. Jagtap, C. Livache, B. Martinez, H. Portalès, X. Z. Xu, R. P. S. M. Lobo, B. Dubertret, and E. Lhuillier, “Terahertz HgTe Nanocrystals: Beyond Confinement”, *Journal of the American Chemical Society*, vol. 140, no. 15, pp. 5033–5036, 2018 (cit. on pp. 35, 37, 84).
- [132] S. Keuleyan, E. Lhuillier, V. Brajuskovic, and P. Guyot-Sionnest, “Mid-infrared HgTe colloidal quantum dot photodetectors”, *Nature Photonics*, vol. 5, no. 8, pp. 489–493, 2011 (cit. on pp. 35, 38, 60).
- [133] M. Chen, H. Yu, S. V. Kershaw, H. Xu, S. Gupta, F. Hetsch, A. L. Rogach, and N. Zhao, “Fast, Air-Stable Infrared Photodetectors based on Spray-Deposited Aqueous HgTe Quantum Dots”, *Advanced Functional Materials*, vol. 24, no. 1, pp. 53–59, 2013 (cit. on pp. 35, 38).
- [134] A. L. Rogach, A. Eychmüller, S. G. Hickey, and S. V. Kershaw, “Infrared-Emitting Colloidal Nanocrystals: Synthesis, Assembly, Spectroscopy, and Applications”, *Small*, vol. 3, no. 4, pp. 536–557, 2007 (cit. on p. 35).
- [135] S. Keuleyan, J. Kohler, and P. Guyot-Sionnest, “Photoluminescence of Mid-Infrared HgTe Colloidal Quantum Dots”, *The Journal of Physical Chemistry C*, vol. 118, no. 5, pp. 2749–2753, 2014 (cit. on pp. 35, 43).
- [136] N. M. Abdelazim, Q. Zhu, Y. Xiong, Y. Zhu, M. Chen, N. Zhao, S. V. Kershaw, and A. L. Rogach, “Room Temperature Synthesis of HgTe Quantum Dots in an Aprotic Solvent Realizing High Photoluminescence Quantum Yields in the Infrared”, *Chemistry of Materials*, vol. 29, no. 18, pp. 7859–7867, 2017 (cit. on p. 35).
- [137] É. O’Connor, A. O’Riordan, H. Doyle, S. Moynihan, A. Cuddihy, and G. Redmond, “Near-infrared electroluminescent devices based on colloidal HgTe quantum dot arrays”, *Applied Physics Letters*, vol. 86, no. 20, p. 201 114, 2005 (cit. on p. 35).
- [138] C. Wang, M. Shim, and P. Guyot-Sionnest, “Electrochromic nanocrystal quantum dots”, *Science*, vol. 291, no. 5512, pp. 2390–2392, 2001 (cit. on pp. 36, 74).
- [139] B. L. Wehrenberg, C. Wang, and P. Guyot-Sionnest, “Interband and Intraband Optical Studies of PbSe Colloidal Quantum Dots”, *The Journal of Physical Chemistry B*, vol. 106, no. 41, pp. 10 634–10 640, 2002 (cit. on pp. 36, 74).
- [140] K. S. Jeong and P. Guyot-Sionnest, “Mid-Infrared Photoluminescence of CdS and CdSe Colloidal Quantum Dots”, *ACS Nano*, vol. 10, no. 2, pp. 2225–2231, 2016 (cit. on pp. 36, 74).
- [141] Z. Deng, K. S. Jeong, and P. Guyot-Sionnest, “Colloidal Quantum Dots Intraband Photodetectors”, *ACS Nano*, vol. 8, no. 11, pp. 11 707–11 714, 2014 (cit. on pp. 36, 74).
- [142] E. Lhuillier, M. Scarafagio, P. Hease, B. Nadal, H. Aubin, X. Z. Xu, N. Lequeux, G. Patriarche, S. Ithurria, and B. Dubertret, “Infrared Photodetection Based on Colloidal Quantum-Dot Films with High Mobility and Optical Absorption up to THz”, *Nano Letters*, vol. 16, no. 2, pp. 1282–1286, 2016 (cit. on pp. 36, 74, 77).
- [143] A. Robin, C. Livache, S. Ithurria, E. Lacaze, B. Dubertret, and E. Lhuillier, “Surface Control of Doping in Self-Doped Nanocrystals”, *ACS Applied Materials & Interfaces*, vol. 8, no. 40, pp. 27 122–27 128, 2016 (cit. on pp. 37, 75).
- [144] B. Askenazi, A. Vasanelli, A. Delteil, Y. Todorov, L. C. Andreani, G. Beaudoin, I. Sagnes, and C. Sirtori, “Ultra-strong light–matter coupling for designer Reststrahlen band”, *New Journal of Physics*, vol. 16, no. 4, p. 043 029, 2014 (cit. on p. 37).

- [145] K. S. Jeong, Z. Deng, S. Keuleyan, H. Liu, and P. Guyot-Sionnest, “Air-Stable n-Doped Colloidal HgS Quantum Dots”, *The Journal of Physical Chemistry Letters*, vol. 5, no. 7, pp. 1139–1143, 2014 (cit. on p. 37).
- [146] G. Shen and P. Guyot-Sionnest, “HgS and HgS/CdS Colloidal Quantum Dots with Infrared Intraband Transitions and Emergence of a Surface Plasmon”, *The Journal of Physical Chemistry C*, vol. 120, no. 21, pp. 11 744–11 753, 2016 (cit. on p. 37).
- [147] M. H. Hudson, M. Chen, V. Kamysbayev, E. M. Janke, X. Lan, G. Allan, C. Delerue, B. Lee, P. Guyot-Sionnest, and D. V. Talapin, “Conduction Band Fine Structure in Colloidal HgTe Quantum Dots”, *ACS Nano*, 2018 (cit. on p. 37).
- [148] C. Livache, B. Martinez, N. Goubet, J. Ramade, and E. Lhuillier, “Road Map for Nanocrystal Based Infrared Photodetectors”, *Frontiers in Chemistry*, vol. 6, p. 575, 2018 (cit. on p. 38).
- [149] A. Sahu, L. Qi, M. S. Kang, D. Deng, and D. J. Norris, “Facile Synthesis of Silver Chalcogenide (Ag<sub>2</sub>E; E = Se, S, Te) Semiconductor Nanocrystals”, *Journal of the American Chemical Society*, vol. 133, no. 17, pp. 6509–6512, 2011 (cit. on p. 38).
- [150] M. Park, D. Choi, Y. Choi, H.-b. Shin, and K. S. Jeong, “Mid-Infrared Intraband Transition of Metal Excess Colloidal Ag<sub>2</sub>Se Nanocrystals”, *ACS Photonics*, vol. 5, no. 5, pp. 1907–1911, 2018 (cit. on pp. 38, 80).
- [151] J. Qu, N. Goubet, C. Livache, B. Martinez, D. Amelot, C. Gréboval, A. Chu, J. Ramade, H. Cruguel, S. Ithurria, M. G. Silly, and E. Lhuillier, “Intraband Mid-Infrared Transitions in Ag<sub>2</sub>Se Nanocrystals: Potential and Limitations for Hg-Free Low-Cost Photodetection”, *The Journal of Physical Chemistry C*, vol. 122, no. 31, pp. 18 161–18 167, 2018 (cit. on pp. 38, 80).
- [152] S. B. Hafiz, M. R. Scimeca, P. Zhao, I. J. Paredes, A. Sahu, and D.-K. Ko, “Silver Selenide Colloidal Quantum Dots for Mid-Wavelength Infrared Photodetection”, *ACS Applied Nano Materials*, 2019 (cit. on pp. 38, 80).
- [153] M. Böberl, M. V. Kovalenko, S. Gamerith, E. J. W. List, and W. Heiss, “Inkjet-Printed Nanocrystal Photodetectors Operating up to 3  $\mu$ m Wavelengths”, *Advanced Materials*, vol. 19, no. 21, pp. 3574–3578, 2007 (cit. on p. 38).
- [154] E. Lhuillier, S. Keuleyan, P. Zolotavin, and P. Guyot-Sionnest, “Mid-Infrared HgTe/As<sub>2</sub>S<sub>3</sub> Field Effect Transistors and Photodetectors”, *Advanced Materials*, vol. 25, no. 1, pp. 137–141, 2013 (cit. on p. 38).
- [155] P. Guyot-Sionnest and J. A. Roberts, “Background limited mid-infrared photodetection with photovoltaic HgTe colloidal quantum dots”, *Applied Physics Letters*, vol. 107, no. 25, p. 253 104, 2015 (cit. on pp. 38, 39).
- [156] M. Chen, H. Lu, N. M. Abdelazim, Y. Zhu, Z. Wang, W. Ren, S. V. Kershaw, A. L. Rogach, and N. Zhao, “Mercury Telluride Quantum Dot Based Phototransistor Enabling High-Sensitivity Room-Temperature Photodetection at 2000 nm”, *ACS Nano*, vol. 11, no. 6, pp. 5614–5622, 2017 (cit. on p. 38).
- [157] X. Tang, X. Tang, and K. W. C. Lai, “Scalable Fabrication of Infrared Detectors with Multi-spectral Photoresponse Based on Patterned Colloidal Quantum Dot Films”, *ACS Photonics*, vol. 3, no. 12, pp. 2396–2404, 2016 (cit. on pp. 38, 40).
- [158] M. E. Cryer and J. E. Halpert, “300 nm Spectral Resolution in the Mid-Infrared with Robust, High Responsivity Flexible Colloidal Quantum Dot Devices at Room Temperature”, *ACS Photonics*, vol. 5, no. 8, pp. 3009–3015, 2018 (cit. on p. 38).
- [159] N. Huo, S. Gupta, and G. Konstantatos, “MoS<sub>2</sub>-HgTe Quantum Dot Hybrid Photodetectors beyond 2  $\mu$ m”, *Advanced Materials*, vol. 29, no. 17, p. 1 606 576, 2017 (cit. on p. 38).
- [160] M. Chen, L. Shao, S. V. Kershaw, H. Yu, J. Wang, A. L. Rogach, and N. Zhao, “Photocurrent Enhancement of HgTe Quantum Dot Photodiodes by Plasmonic Gold Nanorod Structures”, *ACS Nano*, vol. 8, no. 8, pp. 8208–8216, 2014 (cit. on p. 39).

- [161] X. Tang, M. M. Ackerman, and P. Guyot-Sionnest, “Thermal Imaging with Plasmon Resonance Enhanced HgTe Colloidal Quantum Dot Photovoltaic Devices”, *ACS Nano*, vol. 12, no. 7, pp. 7362–7370, 2018 (cit. on pp. 39, 112).
- [162] M. M. Ackerman, X. Tang, and P. Guyot-Sionnest, “Fast and Sensitive Colloidal Quantum Dot Mid-Wave Infrared Photodetectors”, *ACS Nano*, vol. 12, no. 7, pp. 7264–7271, 2018 (cit. on pp. 39, 60, 105, 108).
- [163] A. Jagtap, B. Martinez, N. Goubet, A. Chu, C. Livache, C. Gréboval, J. Ramade, D. Amelot, P. Troussset, A. Triboulin, S. Ithurria, M. G. Silly, B. Dubertret, and E. Lhuillier, “Design of a Unipolar Barrier for a Nanocrystal-Based Short-Wave Infrared Photodiode”, *ACS Photonics*, vol. 5, no. 11, pp. 4569–4576, 2018 (cit. on pp. 39, 105).
- [164] B. Martinez, J. Ramade, C. Livache, N. Goubet, A. Chu, C. Greboval, J. Qu, W. Watkins, L. Becerra, E. Dandeu, J. L. Fave, C. Méthivier, E. Lacaze, and E. Lhuillier, “HgTe nanocrystals ink for extended short wave infrared detection”, *Submitted*, 2019 (cit. on pp. 39, 105).
- [165] A. Jagtap, N. Goubet, C. Livache, A. Chu, B. Martinez, C. Gréboval, J. Qu, E. Dandeu, L. Becerra, N. Witkowski, S. Ithurria, F. Mathevet, M. G. Silly, B. Dubertret, and E. Lhuillier, “Short Wave Infrared Devices Based on HgTe Nanocrystals with Air Stable Performances”, *The Journal of Physical Chemistry C*, vol. 122, no. 26, pp. 14979–14985, 2018 (cit. on p. 39).
- [166] X. Tang, M. M. Ackerman, G. Shen, and P. Guyot-Sionnest, “Towards Infrared Electronic Eyes: Flexible Colloidal Quantum Dot Photovoltaic Detectors Enhanced by Resonant Cavity”, *Small*, vol. 15, no. 12, p. 1804920, 2019 (cit. on p. 39).
- [167] J. Ramade, J. Qu, A. Chu, C. Greboval, C. Livache, N. Goubet, B. Martinez, G. Vincet, and E. Lhuillier, “Potential of colloidal quantum dot based solar cell for near-infrared active imaging”, (cit. on p. 39).
- [168] X. Tang, M. M. Ackerman, M. Chen, and P. Guyot-Sionnest, “Dual-band infrared imaging using stacked colloidal quantum dot photodiodes”, *Nature Photonics*, vol. 13, no. 4, p. 277, 2019 (cit. on p. 40).
- [169] S. A. Rezvani, M. Suzuki, P. Malevich, C. Livache, J. V. de Montgolfier, Y. Nomura, N. Tsurumachi, A. Baltuška, and T. Fuji, “Millijoule femtosecond pulses at 1937 nm from a diode-pumped ring cavity Tm:YAP regenerative amplifier”, *Optics Express*, vol. 26, no. 22, pp. 29460–29470, 2018 (cit. on p. 43).
- [170] S. V. Kershaw and A. L. Rogach, “Carrier Multiplication Mechanisms and Competing Processes in Colloidal Semiconductor Nanostructures”, *Materials*, vol. 10, no. 9, p. 1095, 2017 (cit. on p. 43).
- [171] E. Rosencher, *Optoelectronics*. Cambridge, UK ; New York, NY: Cambridge University Press, 2002, 744 pp. (cit. on p. 43).
- [172] C. Main and D. Nesheva, *Transient Photocurrent Techniques as a Means of Characterising Amorphous Semiconductors*. 2001 (cit. on p. 43).
- [173] D. Auston, “Impulse response of photoconductors in transmission lines”, *IEEE Journal of Quantum Electronics*, vol. 19, no. 4, pp. 639–648, 1983 (cit. on p. 44).
- [174] A. F. Fidler, J. Gao, and V. I. Klimov, “Electron-hole exchange blockade and memory-less recombination in photoexcited films of colloidal quantum dots”, *Nature Physics*, vol. 13, no. 6, pp. 604–610, 2017 (cit. on pp. 44, 68).
- [175] J. Gao, A. F. Fidler, and V. I. Klimov, “Carrier multiplication detected through transient photocurrent in device-grade films of lead selenide quantum dots”, *Nature Communications*, vol. 6, p. 8185, 2015 (cit. on pp. 44, 68).
- [176] W. M. M. Lin, D. Bozyigit, O. Yarema, and V. Wood, “Transient Photovoltage Measurements in Nanocrystal-Based Solar Cells”, *The Journal of Physical Chemistry C*, vol. 120, no. 23, pp. 12900–12908, 2016 (cit. on p. 44).

- [177] N. Kholmicheva, P. Moroz, E. Bastola, N. Razgoniaeva, J. Bocanegra, M. Shaughnessy, Z. Porach, D. Khon, and M. Zamkov, “Mapping the Exciton Diffusion in Semiconductor Nanocrystal Solids”, *ACS Nano*, vol. 9, no. 3, pp. 2926–2937, 2015 (cit. on p. 44).
- [178] G. M. Akselrod, F. Prins, L. V. Poulikakos, E. M. Y. Lee, M. C. Weidman, A. J. Mork, A. P. Willard, V. Bulović, and W. A. Tisdale, “Subdiffusive Exciton Transport in Quantum Dot Solids”, *Nano Letters*, vol. 14, no. 6, pp. 3556–3562, 2014 (cit. on p. 44).
- [179] E. Izquierdo, M. Dufour, A. Chu, C. Livache, B. Martinez, D. Amelot, G. Patriarche, N. Lequeux, E. Lhuillier, and S. Ithurria, “Coupled HgSe Colloidal Quantum Wells through a Tunable Barrier: A Strategy To Uncouple Optical and Transport Band Gap”, *Chemistry of Materials*, vol. 30, no. 12, pp. 4065–4072, 2018 (cit. on p. 46).
- [180] S. Ithurria and D. V. Talapin, “Colloidal Atomic Layer Deposition (c-ALD) using Self-Limiting Reactions at Nanocrystal Surface Coupled to Phase Transfer between Polar and Nonpolar Media”, *Journal of the American Chemical Society*, vol. 134, no. 45, pp. 18 585–18 590, 2012 (cit. on pp. 47, 84).
- [181] S. Yamamoto and I. Matsuda, “Time-Resolved Photoelectron Spectroscopies Using Synchrotron Radiation: Past, Present, and Future”, *Journal of the Physical Society of Japan*, vol. 82, no. 2, p. 021 003, 2013 (cit. on p. 51).
- [182] B. F. Spencer, D. M. Graham, S. J. O. Hardman, E. A. Seddon, M. J. Cliffe, K. L. Syres, A. G. Thomas, S. K. Stubbs, F. Sirotti, M. G. Silly, P. F. Kirkham, A. R. Kumarasinghe, G. J. Hirst, A. J. Moss, S. F. Hill, D. A. Shaw, S. Chattopadhyay, and W. R. Flavell, “Time-resolved surface photovoltage measurements at n-type photovoltaic surfaces: Si(111) and ZnO(10-10)”, *Physical Review B*, vol. 88, no. 19, p. 195 301, 2013 (cit. on p. 51).
- [183] N. Bergeard, M. G. Silly, D. Krizmancic, C. Chauvet, M. Guzzo, J. P. Ricaud, M. Izquierdo, L. Stebel, P. Pittana, R. Sergo, G. Cautero, G. Dufour, F. Rochet, and F. Sirotti, “Time-resolved photoelectron spectroscopy using synchrotron radiation time structure”, *Journal of Synchrotron Radiation*, vol. 18, no. 2, pp. 245–250, 2011 (cit. on p. 53).
- [184] M.-H. Chiu, C. Zhang, H.-W. Shiu, C.-P. Chuu, C.-H. Chen, C.-Y. S. Chang, C.-H. Chen, M.-Y. Chou, C.-K. Shih, and L.-J. Li, “Determination of band alignment in the single-layer MoS<sub>2</sub>/WSe<sub>2</sub> heterojunction”, *Nature Communications*, vol. 6, p. 7666, 2015 (cit. on p. 54).
- [185] D. Pierucci, H. Henck, J. Avila, A. Balan, C. H. Naylor, G. Patriarche, Y. J. Dappe, M. G. Silly, F. Sirotti, A. T. C. Johnson, M. C. Asensio, and A. Ouerghi, “Band Alignment and Minigaps in Monolayer MoS<sub>2</sub>-Graphene van der Waals Heterostructures”, *Nano Letters*, vol. 16, no. 7, pp. 4054–4061, 2016 (cit. on p. 54).
- [186] O. Lang, A. Klein, C. Pettenkofer, W. Jaegermann, and A. Chevy, “Band lineup of lattice mismatched InSe/GaSe quantum well structures prepared by van der Waals epitaxy: Absence of interfacial dipoles”, *Journal of Applied Physics*, 1998 (cit. on p. 54).
- [187] A. Yeltik, S. Delikanli, M. Olutas, Y. Kelestemur, B. Guzelturk, and H. V. Demir, “Experimental Determination of the Absorption Cross-Section and Molar Extinction Coefficient of Colloidal CdSe Nanoplatelets”, *The Journal of Physical Chemistry C*, vol. 119, no. 47, pp. 26 768–26 775, 2015 (cit. on p. 56).
- [188] E. Lhuillier, S. Keuleyan, and P. Guyot-Sionnest, “Optical properties of HgTe colloidal quantum dots”, *Nanotechnology*, vol. 23, no. 17, p. 175 705, 2012 (cit. on pp. 56, 66, 88, 99).
- [189] C. Gréboval, E. Izquierdo, C. Livache, B. Martinez, M. Dufour, N. Goubet, N. Moghaddam, J. Qu, A. Chu, J. Ramade, H. Aubin, H. Cruguel, M. Silly, E. Lhuillier, and S. Ithurria, “Impact of dimensionality and confinement on the electronic properties of mercury chalcogenide nanocrystals”, *Nanoscale*, vol. 11, no. 9, pp. 3905–3915, 2019 (cit. on p. 57).
- [190] N. F. Mott and E. A. Davis, *Electronic Processes in Non-Crystalline Materials*, ser. Oxford Classic Texts in the Physical Sciences. Oxford, New York: Oxford University Press, 2012, 608 pp. (cit. on p. 61).

- [191] D. J. Binks, “Multiple exciton generation in nanocrystal quantum dots – controversy, current status and future prospects”, *Physical Chemistry Chemical Physics*, vol. 13, no. 28, pp. 12 693–12 704, 2011 (cit. on p. 64).
- [192] A. J. Nozik, “Quantum dot solar cells”, *Physica E: Low-dimensional Systems and Nanostructures*, vol. 14, no. 1, pp. 115–120, 2002 (cit. on p. 64).
- [193] R. J. Ellingson, M. C. Beard, J. C. Johnson, P. Yu, O. I. Micic, A. J. Nozik, A. Shabaev, and A. L. Efros, “Highly Efficient Multiple Exciton Generation in Colloidal PbSe and PbS Quantum Dots”, *Nano Letters*, vol. 5, no. 5, pp. 865–871, 2005 (cit. on p. 64).
- [194] O. E. Semonin, J. M. Luther, S. Choi, H.-Y. Chen, J. Gao, A. J. Nozik, and M. C. Beard, “Peak External Photocurrent Quantum Efficiency Exceeding 100% via MEG in a Quantum Dot Solar Cell”, *Science*, vol. 334, no. 6062, pp. 1530–1533, 2011 (cit. on p. 64).
- [195] A. Al-Otaify, S. V. Kershaw, S. Gupta, A. L. Rogach, G. Allan, C. Delerue, and D. J. Binks, “Multiple exciton generation and ultrafast exciton dynamics in HgTe colloidal quantum dots”, *Physical Chemistry Chemical Physics*, vol. 15, no. 39, pp. 16 864–16 873, 2013 (cit. on p. 64).
- [196] J. Orenstein and M. Kastner, “Photocurrent Transient Spectroscopy: Measurement of the Density of Localized States in As<sub>2</sub>Se<sub>3</sub>”, *Physical Review Letters*, vol. 46, no. 21, pp. 1421–1424, 1981 (cit. on p. 68).
- [197] J. Orenstein, M. A. Kastner, and V. Vaninov, “Transient photoconductivity and photo-induced optical absorption in amorphous semiconductors”, *Philosophical Magazine Part B*, vol. 46, pp. 23–62, 1982 (cit. on p. 68).
- [198] P. Guyot-Sionnest, E. Lhuillier, and H. Liu, “A mirage study of CdSe colloidal quantum dot films, Urbach tail, and surface states”, *The Journal of Chemical Physics*, vol. 137, no. 15, p. 154 704, 2012 (cit. on p. 69).
- [199] B. Martinez, C. Livache, N. Goubet, A. Jagtap, H. Cruguel, A. Ouerghi, E. Lacaze, M. G. Silly, and E. Lhuillier, “Probing Charge Carrier Dynamics to Unveil the Role of Surface Ligands in HgTe Narrow Band Gap Nanocrystals”, *The Journal of Physical Chemistry C*, vol. 122, no. 1, pp. 859–865, 2018 (cit. on p. 69).
- [200] L. Protesescu, S. Yakunin, M. I. Bodnarchuk, F. Krieg, R. Caputo, C. H. Hendon, R. X. Yang, A. Walsh, and M. V. Kovalenko, “Nanocrystals of Cesium Lead Halide Perovskites (CsPbX<sub>3</sub>, X = Cl, Br, and I): Novel Optoelectronic Materials Showing Bright Emission with Wide Color Gamut”, *Nano Letters*, vol. 15, no. 6, pp. 3692–3696, 2015 (cit. on p. 70).
- [201] G. Nedelcu, L. Protesescu, S. Yakunin, M. I. Bodnarchuk, M. J. Grotevent, and M. V. Kovalenko, “Fast Anion-Exchange in Highly Luminescent Nanocrystals of Cesium Lead Halide Perovskites (CsPbX<sub>3</sub>, X = Cl, Br, I)”, *Nano Letters*, vol. 15, no. 8, pp. 5635–5640, 2015 (cit. on p. 71).
- [202] Q. A. Akkerman, V. D’Innocenzo, S. Accornero, A. Scarpellini, A. Petrozza, M. Prato, and L. Manna, “Tuning the Optical Properties of Cesium Lead Halide Perovskite Nanocrystals by Anion Exchange Reactions”, *Journal of the American Chemical Society*, vol. 137, no. 32, pp. 10 276–10 281, 2015 (cit. on p. 71).
- [203] S. Yakunin, L. Protesescu, F. Krieg, M. I. Bodnarchuk, G. Nedelcu, M. Humer, G. De Luca, M. Fiebig, W. Heiss, and M. V. Kovalenko, “Low-threshold amplified spontaneous emission and lasing from colloidal nanocrystals of caesium lead halide perovskites”, *Nature Communications*, vol. 6, p. 8056, 2015 (cit. on p. 71).
- [204] E. M. Sanchez, A. R. Marshall, J. A. Christians, S. P. Harvey, P. N. Ciesielski, L. M. Wheeler, P. Schulz, L. Y. Lin, M. C. Beard, and J. M. Luther, “Enhanced mobility CsPbI<sub>3</sub> quantum dot arrays for record-efficiency, high-voltage photovoltaic cells”, *Science Advances*, vol. 3, no. 10, eaao4204, 2017 (cit. on p. 71).

- [205] W. J. Mir, C. Livache, N. Goubet, B. Martinez, A. Jagtap, A. Chu, N. Coutard, H. Cruguel, T. Barisien, S. Ithurria, A. Nag, B. Dubertret, A. Ouerghi, M. G. Silly, and E. Lhuillier, “Strategy to overcome recombination limited photocurrent generation in CsPbX<sub>3</sub> nanocrystal arrays”, *Applied Physics Letters*, vol. 112, no. 11, p. 113 503, 2018 (cit. on p. 71).
- [206] J.-F. Dayen, V. Faramarzi, M. Pauly, N. T. Kemp, M. Barbero, B. P. Pichon, H. Majjad, S. Begin-Colin, and B. Doudin, “Nanotrench for nano and microparticle electrical interconnects”, *Nanotechnology*, vol. 21, no. 33, p. 335 303, 2010 (cit. on p. 72).
- [207] G. Konstantatos and E. H. Sargent, “PbS colloidal quantum dot photoconductive photodetectors: Transport, traps, and gain”, *Applied Physics Letters*, vol. 91, no. 17, p. 173 505, 2007 (cit. on p. 72).
- [208] B. T. Diroll, M. Chen, I. Coropceanu, K. R. Williams, D. V. Talapin, P. Guyot-Sionnest, and R. D. Schaller, “Polarized near-infrared intersubband absorptions in CdSe colloidal quantum wells”, *Nature Communications*, vol. 10, no. 1, pp. 1–9, 2019 (cit. on p. 74).
- [209] D. M. Kroupa, B. K. Hughes, E. M. Miller, D. T. Moore, N. C. Anderson, B. D. Chernomordik, A. J. Nozik, and M. C. Beard, “Synthesis and Spectroscopy of Silver-Doped PbSe Quantum Dots”, *Journal of the American Chemical Society*, vol. 139, no. 30, pp. 10 382–10 394, 2017 (cit. on p. 74).
- [210] I. Ramiro, O. Ozdemir, S. Christodoulou, S. Gupta, M. Dalmases, and G. Konstantatos, “Intra-band Photresponse in the Mid-and Long-Wave Infrared by Robust Heavily Doped PbS Colloidal Quantum Dots Films”, *To be published*, 2019 (cit. on pp. 74, 80).
- [211] B. Yoon, J. Jeong, and K. S. Jeong, “Higher Quantum State Transitions in Colloidal Quantum Dot with Heavy Electron Doping”, *The Journal of Physical Chemistry C*, vol. 120, no. 38, pp. 22 062–22 068, 2016 (cit. on p. 74).
- [212] J. Jeong, B. Yoon, Y.-W. Kwon, D. Choi, and K. S. Jeong, “Singly and Doubly Occupied Higher Quantum States in Nanocrystals”, *Nano Letters*, vol. 17, no. 2, pp. 1187–1193, 2017 (cit. on p. 74).
- [213] A. Robin, “Opto-électronique de boîtes et puits quantiques colloïdaux - Application au photo-transport”, thesis, Paris 6, 2016 (cit. on p. 75).
- [214] P. R. Brown, D. Kim, R. R. Lunt, N. Zhao, M. G. Bawendi, J. C. Grossman, and V. Bulović, “Energy Level Modification in Lead Sulfide Quantum Dot Thin Films through Ligand Exchange”, *ACS Nano*, vol. 8, no. 6, pp. 5863–5872, 2014 (cit. on p. 76).
- [215] A. J. Houtepen, Z. Hens, J. S. Owen, and I. Infante, “On the Origin of Surface Traps in Colloidal II–VI Semiconductor Nanocrystals”, *Chemistry of Materials*, 2016 (cit. on p. 76).
- [216] D. M. Kroupa, M. Vörös, N. P. Brawand, B. W. McNichols, E. M. Miller, J. Gu, A. J. Nozik, A. Sellinger, G. Galli, and M. C. Beard, “Tuning colloidal quantum dot band edge positions through solution-phase surface chemistry modification”, *Nature Communications*, vol. 8, p. 15 257, 2017 (cit. on p. 76).
- [217] B. Kundu and A. J. Pal, “Ligand-Mediated Energy-Level Modification in PbS Quantum Dots as Probed by Density of States (DOS) Spectra”, *The Journal of Physical Chemistry C*, vol. 122, no. 21, pp. 11 570–11 576, 2018 (cit. on p. 76).
- [218] C. Gréboval, U. Noumbe, N. Goubet, C. Livache, J. Ramade, J. Qu, A. Chu, B. Martinez, Y. Prado, S. Ithurria, A. Ouerghi, H. Aubin, J.-F. Dayen, and E. Lhuillier, “Field-Effect Transistor and Photo-Transistor of Narrow-Band-Gap Nanocrystal Arrays Using Ionic Glasses”, *Nano Letters*, vol. 19, no. 6, pp. 3981–3986, 2019 (cit. on p. 79).
- [219] J. Qu, C. Livache, B. Martinez, C. Gréboval, A. Chu, E. Meriggio, J. Ramade, H. Cruguel, X. Z. Xu, A. Proust, F. Volatron, G. Cabailh, N. Goubet, and E. Lhuillier, “Transport in ITO Nanocrystals with Short- to Long-Wave Infrared Absorption for Heavy-Metal-Free Infrared Photodetection”, *ACS Applied Nano Materials*, vol. 2, no. 3, pp. 1621–1630, 2019 (cit. on p. 80).

- [220] C. Kwong-kit, *The Physics Of Quantum Well Infrared Photodetectors*. World Scientific, 1997, 434 pp. (cit. on pp. 80, 81).
- [221] G. B. Wright, A. J. Strauss, and T. C. Harman, “Nonparabolic Conduction Band in HgSe and HgSe(0.5)Te(0.5)”, *Physical Review*, vol. 125, no. 5, pp. 1534–1536, 1962 (cit. on p. 82).
- [222] D. G. Seiler, R. R. Galazka, and W. M. Becker, “Band Structure of HgSe: Band Parameter Determinations from Effective-Mass Data, and Concentration Dependence and Anisotropy of Beating Effects in the Shubnikov-de Haas Oscillations”, *Physical Review B*, vol. 3, no. 12, pp. 4274–4285, 1971 (cit. on p. 82).
- [223] G. Nimtz, B. Schlicht, and R. Dornhaus, *Narrow-gap semiconductors*. Springer, 1983, OCLC: 476671694 (cit. on p. 82).
- [224] L. Śniadower, V. I. Ivanov-Omsky, and Z. Dziuba, “Determination of the Effective Mass of Electrons in HgTe”, *Physica status solidi (b)*, vol. 8, no. 1, K43–K45, 1965 (cit. on p. 82).
- [225] T. C. Harman and A. J. Strauss, “Band Structure of HgSe and HgSe–HgTe Alloys”, *Journal of Applied Physics*, vol. 32, no. 10, pp. 2265–2270, 1961 (cit. on p. 82).
- [226] N. Goubet, C. Livache, B. Martinez, X. Z. Xu, S. Ithurria, S. Royer, H. Cruguel, G. Patriarche, A. Ouerghi, M. Silly, B. Dubertret, and E. Lhuillier, “Wave-Function Engineering in HgSe/HgTe Colloidal Heterostructures To Enhance Mid-infrared Photoconductive Properties”, *Nano Letters*, vol. 18, no. 7, pp. 4590–4597, 2018 (cit. on p. 84).
- [227] S.-i. Katsuki and M. Kunimune, “Effect of Pressure on the Band Structure of HgTe: Pseudopotential Calculation”, *Journal of the Physical Society of Japan*, vol. 31, no. 2, pp. 337–341, 1971 (cit. on p. 88).
- [228] T. Huang and A. L. Ruoff, “Pressure-induced phase transitions of HgSe”, *Physical Review B*, vol. 27, no. 12, pp. 7811–7812, 1983 (cit. on p. 88).
- [229] C. Brüne, C. X. Liu, E. G. Novik, E. M. Hankiewicz, H. Buhmann, Y. L. Chen, X. L. Qi, Z. X. Shen, S. C. Zhang, and L. W. Molenkamp, “Quantum Hall Effect from the Topological Surface States of Strained Bulk HgTe”, *Physical Review Letters*, vol. 106, no. 12, p. 126 803, 2011 (cit. on p. 88).
- [230] S. Ithurria, P. Guyot-Sionnest, B. Mahler, and B. Dubertret, “Mn<sup>2+</sup> as a Radial Pressure Gauge in Colloidal Core/Shell Nanocrystals”, *Physical Review Letters*, vol. 99, no. 26, p. 265 501, 2007 (cit. on p. 89).
- [231] I. V. Kurilo, V. P. Alekhin, I. O. Rudyi, S. I. Bulychev, and L. I. Osypshin, “Mechanical Properties of ZnTe, CdTe, CdHgTe and HgTe Crystals from Micromechanical Investigation”, *Physica status solidi (a)*, vol. 163, no. 1, pp. 47–58, 1997 (cit. on p. 89).
- [232] U. Rössler, Ed., *II-VI and I-VII Compounds; Semimagnetic Compounds*, ser. Condensed Matter, Berlin Heidelberg: Springer-Verlag, 1999 (cit. on p. 89).
- [233] S.-H. Wei and A. Zunger, “Predicted band-gap pressure coefficients of all diamond and zincblende semiconductors: Chemical trends”, *Physical Review B*, vol. 60, no. 8, pp. 5404–5411, 1999 (cit. on p. 89).
- [234] A. San-Miguel, N. G. Wright, M. I. McMahon, and R. J. Nelmes, “Pressure evolution of the cinnabar phase of HgTe”, *Physical Review. B, Condensed Matter*, vol. 51, no. 14, pp. 8731–8736, 1995 (cit. on p. 91).
- [235] N. G. Wright, M. I. McMahon, R. J. Nelmes, and A. San-Miguel, “Crystal structure of the cinnabar phase of HgTe”, *Physical Review B*, vol. 48, no. 17, pp. 13 111–13 114, 1993 (cit. on p. 91).
- [236] A. Werner, H. D. Hochheimer, K. Strössner, and A. Jayaraman, “High-pressure x-ray diffraction studies on HgTe and HgS to 20 GPa”, *Physical Review B*, vol. 28, pp. 3330–3334, 1983 (cit. on p. 91).

- [237] S. H. Tolbert and A. P. Alivisatos, “Size Dependence of a First Order Solid-Solid Phase Transition: The Wurtzite to Rock Salt Transformation in CdSe Nanocrystals”, *Science*, vol. 265, no. 5170, pp. 373–376, 1994 (cit. on p. 91).
- [238] I. Düz, I. Erdem, S. Ozdemir Kart, and V. Kuzucu, “First principles investigations of HgX (X=S, Se and Te)”, *Archives of Materials Science and Engineering*, vol. Vol. 79, nr 1 2016 (cit. on p. 91).
- [239] C. Livache, N. Goubet, C. Gréboval, B. Martinez, J. Ramade, J. Qu, A. Triboulin, H. Cruguel, B. Baptiste, S. Klotz, G. Fishman, S. Sauvage, F. Capitani, and E. Lhuillier, “Effect of Pressure on Interband and Intraband Transition of Mercury Chalcogenide Quantum Dots”, *The Journal of Physical Chemistry C*, vol. 123, no. 20, pp. 13 122–13 130, 2019 (cit. on p. 92).
- [240] V. Latussek, C. R. Becker, G. Landwehr, R. Bini, and L. Ulivi, “Deformation potentials of the semimetal HgTe”, *Physical Review B*, vol. 71, no. 12, p. 125 305, 2005 (cit. on p. 94).
- [241] H. Yang, E. Wong, T. Zhao, J. D. Lee, H. L. Xin, M. Chi, B. Fleury, H.-Y. Tang, E. A. Gaulding, C. R. Kagan, and C. B. Murray, “Charge Transport Modulation in PbSe Nanocrystal Solids by AuxAg<sub>1-x</sub> Nanoparticle Doping”, *ACS Nano*, vol. 12, no. 9, pp. 9091–9100, 2018 (cit. on p. 97).
- [242] S. Pradhan, F. D. Stasio, Y. Bi, S. Gupta, S. Christodoulou, A. Stavrinadis, and G. Konstantatos, “High-efficiency colloidal quantum dot infrared light-emitting diodes via engineering at the supra-nanocrystalline level”, *Nature Nanotechnology*, vol. 14, no. 1, p. 72, 2019 (cit. on pp. 97, 113, 116).
- [243] Z. Yang, J. Z. Fan, A. H. Proppe, F. P. G. de Arquer, D. Rossouw, O. Voznyy, X. Lan, M. Liu, G. Walters, R. Quintero-Bermudez, B. Sun, S. Hoogland, G. A. Botton, S. O. Kelley, and E. H. Sargent, “Mixed-quantum-dot solar cells”, *Nature Communications*, vol. 8, no. 1, p. 1325, 2017 (cit. on pp. 97, 116).
- [244] B. Sun, O. Ouellette, F. P. G. de Arquer, O. Voznyy, Y. Kim, M. Wei, A. H. Proppe, M. I. Saidaminov, J. Xu, M. Liu, P. Li, J. Z. Fan, J. W. Jo, H. Tan, F. Tan, S. Hoogland, Z. H. Lu, S. O. Kelley, and E. H. Sargent, “Multibandgap quantum dot ensembles for solar-matched infrared energy harvesting”, *Nature Communications*, vol. 9, no. 1, p. 4003, 2018 (cit. on p. 97).
- [245] G. R. Savich, J. R. Pedrazzani, D. E. Sidor, S. Maimon, and G. W. Wicks, “Dark current filtering in unipolar barrier infrared detectors”, *Applied Physics Letters*, vol. 99, no. 12, p. 121 112, 2011 (cit. on p. 105).
- [246] P. Martyniuk, M. Kopytko, and A. Rogalski, “Barrier infrared detectors”, *Opto-Electronics Review*, vol. 22, no. 2, pp. 127–146, 2014 (cit. on p. 105).
- [247] B. Martinez, J. Ramade, C. Livache, N. Goubet, A. Chu, C. Gréboval, J. Qu, W. L. Watkins, L. Becerra, E. Dandeu, J. L. Fave, C. Méthivier, E. Lacaze, and E. Lhuillier, “HgTe Nanocrystal Inks for Extended Short-Wave Infrared Detection”, *Advanced Optical Materials*, p. 1 900 348, 2019 (cit. on pp. 115, 116).
- [248] S. Yakunin, B. M. Benin, Y. Shynkarenko, O. Nazarenko, M. I. Bodnarchuk, D. N. Dirin, C. Hofer, S. Cattaneo, and M. V. Kovalenko, “High-resolution remote thermometry and thermography using luminescent low-dimensional tin-halide perovskites”, *Nature Materials*, p. 1, 2019 (cit. on p. 116).
- [249] C. Livache, B. Martinez, N. Goubet, C. Gréboval, J. Qu, A. Chu, S. Royer, S. Ithurria, M. G. Silly, B. Dubertret, and E. Lhuillier, “A colloidal quantum dot infrared photodetector and its use for intraband detection”, *Nature Communications*, vol. 10, no. 1, p. 2125, 2019 (cit. on p. 116).



---

**Sujet : Nanocristaux colloïdaux confinés pour l'optoélectronique infrarouge: dynamique des porteurs et transitions intrabande**

---

**Résumé :** Les nanocristaux colloïdaux sont des objets cristallins obtenus par voie chimique. Ces objets étant confinés, leurs propriétés optiques dépendent de leur taille, et peuvent donc être ajustées à la demande. Les nanocristaux de tellure de mercure et de sélénure de mercure possèdent notamment des propriétés d'absorption dans l'infrarouge: l'énergie de bande interdite (interbande) des nanocristaux de HgTe peut-être variée du SWIR au MWIR, tandis que les nanocristaux de HgSe, grâce à un auto-dopage électronique dégénéré, présentent des transitions intrabande ajustables du MWIR au LWIR. Un contrôle fin de la chimie de surface de ces objets permet de les intégrer dans des dispositifs électroniques et de créer des détecteurs infrarouge à bas-coût. Dans mon travail de thèse, je me suis intéressé à différentes manières de sonder la dynamique des porteurs dans ces dispositifs, soit *via* la mesure du photocourant, soit par des observations directes de la relaxation des porteurs photogénérés. A partir d'études sur la dynamique dans HgSe, j'ai identifié les limitations apportées par le fort dopage de ces nanocristaux: le transport est dominé par la forte densité électronique, conduisant à des faibles performances pour la détection IR. En reprenant les concepts développés pour les hétérostructures de semi-conducteurs III-V, je propose différentes approches fructueuses pour découpler les propriétés optiques et le transport de charges dans des dispositifs de détection MWIR à base de nanocristaux de HgSe.

**Mots clés :** Nanocristaux, infrarouge, optoélectronique, dynamique, quantum dots

---

**Subject : Quantum-confined nanocrystals for infrared optoelectronics: carrier dynamics and intraband transitions**

---

**Abstract:** Colloidal nanocrystals are crystalline objects grown by colloidal chemistry approaches. Thanks to quantum confinement, their optical properties depend on their size, and can then be tuned accordingly. Using mercury selenide and mercury telluride, we grow infrared-absorbing nanocrystals. While HgTe nanocrystals interband gap can be tuned from the NIR to the MWIR, HgSe nanocrystals display self-doping and intraband transitions in the MWIR to LWIR. With a careful control of their surface chemistry, those nanocrystals can be integrated into electrical devices to create cheap infrared photodetectors. In my PhD work, I am interested in probing carrier dynamics in those devices using various time-resolved techniques, either based on photocurrent measurements or on direct observation of the photocarriers relaxation. From dynamic study of HgSe intraband devices, I identify the issue brought by the degenerative doping level of those nanocrystals: transport is driven by the doping of this material, resulting in very poor IR-sensing performances. By taking inspiration from the III-V semiconductor developments, I propose several successful approaches to uncouple optical and transport properties in HgSe-based, MWIR detectors.

**Keywords :** Nanocrystals, infrared, optoelectronics, dynamics, quantum dots